

INAUGURAL – DISSERTATION

zur Erlangung der Doktorwürde

der

Naturwissenschaftlich-Mathematischen

Gesamtfakultät

der

Ruprecht-Karls-Universität

Heidelberg

vorgelegt von

Hacı Osman Güvenç

aus Kayseri, Türkei

Tag der mündlichen Prüfung

26.03.2013

**Label-free Detection
of Biospecific Interactions
in Peptide Arrays
Using Core-shell Nanoparticle Films**

Gutachter:

Prof. (apl.) Dr. Reiner Dahint

Prof. Dr. Joachim Spatz

ABSTRACT

A novel nanostructured material with mutually coupled optical and biological functionalities was developed to facilitate the label-free read-out of biospecific binding events in high-density peptide arrays. The nanostructured material consists of a monolayer of dielectric nanoparticle cores deposited on a planar substrate and coated with a metal shell. Upon reflection of white light, these core-shell nanoparticle films exhibit pronounced plasmonic extinction peaks in a wide wavelength regime. Upon molecule adsorption the peaks shift to longer wavelengths due to the change in the refractive index close to the surface, thus, providing a label-free detection mechanism.

The optical properties of the biosensor surfaces were analyzed with three different instrumental set-ups; (i) a standard UV-Vis reflection set-up, (ii) a LSPR imaging set-up based on a scanning unit and (iii) a homemade CCD-based fast read-out system for simultaneous analysis of extended surface areas. The UV-Vis reflection set-up was used to evaluate the performance and sensitivity of the proposed and prepared biosensor surfaces by nonspecific adsorption of proteins whereas the others were used to detect biomolecular reactions in an array format. In particular, biospecific interactions in high density peptide arrays were investigated.

To optimize the wavelength shift induced by protein adsorption, various features were changed in the biosensor configuration, and the impact of these parameters on biosensor performance was tested. Metal shell thickness and roughness, the layer structure of the underlying substrate and the metal shell material (Au or Ag) were found to have an impact on biosensor performance. The most significant improvement, however, was obtained when operating biosensors with rough metal shells, prepared by seeding and consecutive electroless plating, at long wavelength plasmonic resonances. Here, an approximately five-fold increase in sensitivity towards

protein adsorption could be achieved with respect to state-of-the art core-shell nanoparticle sensors. Also, the use of densely-packed monolayer films prepared by a so-called floating technique proved to be advantageous in the analysis of high-density arrays compared to films generated by statistical adsorption of nanoparticles.

The optical homogeneity of the core-shell nanoparticle film was found to be another crucial parameter in label-free detection of specific interactions in high density peptide arrays. Core-shell nanoparticle films with improved optical homogeneity were obtained by changing the shell preparation technique from seeding and consecutive electroless metal plating to sputter coating. In collaboration with the Cancer Research Center (DKFZ) Heidelberg high density peptide arrays were transferred to the core-shell nanoparticle film by cleavage from a synthesis slide preserving spot size and lateral distances. Both the CCD-based fast read-out system and the scanning unit were used to detect protein/peptide interactions in these arrays and yielded consistent results in terms of wavelength shift. The antibody-stained peptide arrays were estimated to contain slightly more than 1 ng/mm² of protein which resulted in 3.6 nm wavelength shift. In future experiments, the use of biosensors with seeded and plated metal shells, operated at long wavelength plasmonic resonances, should provide even higher sensitivity in array analysis.

Core-shell nanoparticle films were also used to enhance the intensity of weak Raman signals of molecules, in this case methylene blue (MB) and fibrinogen via electromagnetic and chemical amplification mechanisms due to their strong surface plasmon resonance (SPR) response in Surface Enhanced Raman Scattering (SERS).

KURZFASSUNG

Ein neues nanostrukturiertes Material mit gekoppelter optischer und biologischer Funktionalität wurde entwickelt, um die markierungsfreie Detektion von biospezifischen Bindungsereignissen in hochdichten Peptidarrays zu ermöglichen. Das Material besteht aus einer Monolage von dielektrischen Nanopartikeln, die auf einer ebenen Substratoberfläche abgeschieden und mit einer Metall-Hülle überzogen werden. Wird an diesen Oberflächen weißes Licht reflektiert, entstehen deutliche Plasmonenresonanz-Peaks, die sich über einen breiten Wellenlängenbereich erstrecken. Bei der Adsorption von Biomolekülen verschiebt sich diese Plasmonenresonanz durch die Änderung des Brechungsindex in der Nähe der Oberfläche zu größeren Wellenlängen, was für die markierungsfreie Detektion von Bindungsereignissen genutzt werden kann.

Die optischen Eigenschaften einer auf Basis des nanostrukturierten Materials konzipierten Biosensor-Oberfläche wurden in drei verschiedenen experimentellen Aufbauten analysiert und verglichen: (i) mit einem herkömmlichen UV-Vis Reflektions-Aufbau, (ii) mit einem LSPR-Bildgebungs-Aufbau auf Basis einer Scan-Einheit und (iii) mit einem eigens entwickelten CCD-Auslese-System zur simultanen Analyse von größeren Oberflächen-Bereichen. Der UV-Vis Reflektions-Aufbau wurde zur Bestimmung der Leistungsfähigkeit und Sensitivität von verschiedenen hergestellten Biosensor-Oberflächen genutzt, an denen Proteine unspezifisch adsorbiert wurden. Die anderen beiden Aufbauten wurden im Speziellen zum markierungsfreien Nachweis von Bindungsereignissen an hoch-komplexen Peptidarrays genutzt.

Um die Wellenlängenverschiebung bei der Adsorption von Biomolekülen an den Sensor-Oberflächen zu optimieren, wurden diverse Parameter im Biosensor-Aufbau variiert und ihr Einfluss auf die Leistungsfähigkeit des Sensors untersucht. Insbesondere die Dicke und Rauheit der Metall-

Beschichtung, die Schichtstruktur der Substratoberfläche und das Material der Metallhülle (Ag oder Au) wurden als Parameter mit Einfluss auf die Biosensor-Leistung identifiziert. Eine entscheidende Verbesserung der Wellenlängenverschiebung von langwelligen Plasmonenresonanzen gelang durch die Herstellung rauer Metall-Hüllen mittels stromloser Metallabscheidung („seeding“ und „plating“). Dabei konnte im Vergleich zu Kern-Hülle- („Core-Shell“) Nanopartikel-Strukturen, die den gegenwärtigen Stand der Technik repräsentieren, ein ungefähr fünffacher Anstieg der Sensitivität auf Proteinadsorption erzielt werden. Zudem zeigte sich die Verwendung von dicht-gepackten Partikel-Monolagen, die mit Hilfe einer Langmuir-Blodgett- ähnlichen Technik (sogenanntes „Floating“) hergestellt werden, als besser geeignet für die Analyse von Bindungsereignissen in hoch-komplexen Peptidarrays als vergleichbare Filme aus statistisch adsorbierten Nanopartikeln.

Die optische Homogenität der Core-Shell-Nanopartikel-Filme wurde als weiterer entscheidender Parameter für die markierungsfreie Detektion von spezifischen Wechselwirkungen von Proteinen mit Peptidarrays identifiziert. Core-Shell-Strukturen mit verbesserter optischer Einheitlichkeit konnten durch das Aufbringen der Metall-Hülle im Sputter-Verfahren an Stelle der stromlosen Stromabscheidung erhalten werden.

In Zusammenarbeit mit dem Deutschen Krebsforschungszentrum (DKFZ) in Heidelberg konnten hochdichte Peptidarrays auf die optimierten Core-Shell“-Sensoroberflächen übertragen werden. Die Synthese der Peptidarrays erfolgte dabei auf der Standard-Syntheseoberfläche an einem spaltbaren Peptidlinker. Erst nach Synthese aller Peptide des Arrays wurde der Peptidlinker gespalten und der gesamte Array unter Erhalt der Ortsinformation auf die Sensoroberfläche übertragen. Sowohl der CCD-basierte Schnellauslese-Aufbau als auch die LSPR-Scan-Einheit wurden verwendet, um die Wechselwirkung von Proteinen und Peptiden zu verfolgen, wobei ähnliche Werte im Hinblick auf die Wellenlängenverschiebung der Plasmonenresonanz-Peaks bei

Proteinadsorption erhalten wurden. Für Antikörper-konjugierte Peptide eines Arrays mit einer ungefähren Massendichte von 1 ng/mm^2 Protein wurde eine Wellenlängenverschiebung von 3.6 nm erhalten. In zukünftigen Experimenten könnten mittels stromloser Stromabscheidung hergestellte Biosensoren sogar noch höhere Nachweisempfindlichkeiten liefern, sofern die langwelligen Plasmonenresonanzen zur Verfolgung der Resonanzverschiebung herangezogen werden können.

Zusätzlich wurden gezeigt, dass Core-Shell“-Nanopartikel-Filme aufgrund ihrer starken Plasmonenresonanz auch zur Verstärkung schwacher Raman-Signale von Methylenblau (MB) und Fibrinogen über elektromagnetische und chemische Verstärkungs-Mechanismen geeignet sind.

TABLE OF CONTENTS

ABSTRACT.....	I
KURZFASSUNG	III
LIST OF FIGURES.....	XI
LIST OF TABLES.....	XVIII
1 INTRODUCTION	1
2 THEORY.....	5
2.1 Surface Plasmon Resonance	5
2.1.1 Propagating Surface Plasmons (PSPs)	5
2.1.2 Localized Surface Plasmons (LSPs)	9
2.1.3 Excitation of Propagating Surface Plasmons	10
2.1.4 Methods of SPR Measurements	13
2.1.5 Core-Shell Nanoparticles as SPR Sensor	15
2.1.6 Sensitivity of Surface Plasmon Resonance Sensors	16
2.1.7 Surface Plasmon Resonance in Biosensing	20
2.2 Surface Enhanced Raman Scattering (SERS)	23
2.2.1 Raman Scattering.....	23
2.2.2 Mechanisms of SERS	25
2.3 Floating Self-Assembly.....	28
2.4 Electroless Metal Plating.....	30
2.5 High Density Peptide Arrays	33
2.5.1 Lithographic Synthesis.....	33
2.5.2 SPOT Synthesis.....	34
2.5.3 Particle-based Synthesis.....	35
3 BIOSENSOR SURFACE ANALYSIS METHODS	39
3.1 UV-Vis Spectroscopy	39
3.1.1 Light Source.....	39
3.1.2 Spectrometer.....	39
3.1.3 Optical Fiber	41
3.2 Surface Plasmon Resonance Imaging (SPRi)	42

3.2.1	Light Source.....	42
3.2.2	Monochromator.....	42
3.2.3	Charge Coupled Device (CCD) Camera.....	43
3.3	X-Ray Photoelectron Spectroscopy (XPS).....	45
3.3.1	Principles	45
3.3.2	Instrumentation	48
3.4	Scanning Electron Microscopy (SEM).....	49
3.4.1	Principle of SEM.....	49
3.4.2	Instrumentation	50
4	EXPERIMENTAL.....	53
4.1	Materials	53
4.1.1	Preparation of Stock Solutions	54
4.2	Preparation of Substrates	54
4.3	Adsorption of Dielectric Nanoparticles on Substrate.....	55
4.3.1	By Incubation	55
4.3.2	By Spin-coating.....	55
4.3.3	By Self-assembly Floating.....	56
4.4	Metal Seed Decoration of Dielectric Nanoparticles.....	57
4.4.1	Gold Nanoparticle Preparation as Seed Solution	57
4.4.2	Silver Nanoparticle Preparation as Seed Solution.....	58
4.5	Electroless Plating of Surfaces	59
4.5.1	Electroless Gold Plating.....	59
4.5.2	Electroless Silver Plating	59
4.6	Protein Adsorption on Biosensor Surfaces for Evaluation of their Performance in UV-Vis Experiments.....	59
4.6.1	Fibrinogen Adsorption	60
4.6.2	Covalent Coupling of Antibodies	60
4.6.3	Spotting Antibody Arrays.....	61
4.7	Peptide Array Synthesis & Layout.....	61
4.7.1	Peptide Array Transfer & Purification	63
4.7.2	Blocking with EG7-SH	63
4.7.3	Immunostaining.....	63
4.8	UV-Vis Spectroscopy Reflection Measurements	64

4.9	XPS Measurements.....	65
4.10	Au Shell Sputter Coating.....	66
4.11	Raman Measurements.....	67
5	RESULTS AND DISCUSSIONS.....	69
5.1	Preparation of Label-free Biosensors.....	70
5.1.1	Deposition of Dielectric Nanoparticles on Substrates	70
5.1.2	Seed Nanoparticle Decoration on Dielectric Silica Nanoparticles.....	76
5.1.3	Electroless Plating of Surfaces	77
5.2	Optical Response of Biosensor Surfaces upon Protein Adsorption .	80
5.2.1	Fibrinogen Adsorption on Biosensor Surfaces for Sensitivity Measurements.....	81
5.2.2	Sputter Coating of a Au shell on Dielectric Nanoparticles.....	101
5.3	Label-free Detection of Protein Binding on Biosensor Surfaces by SPR Imaging and SPR Wavelength Shift.....	104
5.3.1	Detection Protein Arrays on Biosensor Surfaces by SPR Intensity Imaging	109
5.3.2	Label-free Detection of High Complexity Peptide Arrays	118
5.4	Wavelength Averaging of Long Wavelength Peak for Better Sensitivity.. ..	133
5.5	Use of Core-shell Nanoparticles as Surface Enhanced Raman Scattering (SERS) Substrates	146
5.5.1	SERS of MB on Core-Shell Nanoparticles.....	146
5.5.2	SERS of Fibrinogen	154
6	SUMMARY AND CONCLUSIONS.....	157
7	REFERENCES.....	161
8	APPENDIX.....	171
8.1	Abbreviations	171
8.2	List of Aminoacids	173
8.3	Acknowledgement.....	174
8.4	Eidesstattliche Erklärung	176

LIST OF FIGURES

Figure 1. Schematic illustration of a propagating surface plasmon ^[13]	6
Figure 2. Real part of the dielectric constant of Au, Ag and Al as a function of wavelength ^[12]	7
Figure 3. Distribution of the magnetic field amplitude for a surface plasmon at two different wavelengths at the gold/dielectric interface ^[15]	8
Figure 4. Illustration of a localized surface plasmon resonance (LSPR) ^[13]	9
Figure 5. Dispersion curve of light and the surface plasmon on a planar metal-dielectric interface ^[21]	10
Figure 6. Excitation of surface plasmons in the A) Kretschmann and B) Otto geometry of the attenuated total reflection (ATR) method ^[12]	11
Figure 7. Excitation of surface plasmons by a grating coupler ^[12]	12
Figure 8. Densely packed monodisperse SiO ₂ nanoparticles on a Au film.	12
Figure 9. Reflected light intensity as a function of A) wavelength and B) incident angle for a refractive index of n_s and $n_s + \Delta n$ ^[12]	13
Figure 10. SPR response curves of a plain gold surface (blue curve) and after adsorption of a ~5 nm layer of protein (red curve). In SPR imaging, at a fixed angle and wavelength (dotted line), binding is measured as the local change in reflectivity ($\Delta\%R$) ^[27]	14
Figure 11. Measured SPR response over a narrow range of n near that for water. ($n=1.330$) ^[37]	16
Figure 12. Schematic diagram of a bilayer structure involving an adsorbate thickness d and refractive index n_{ads} on the metal surface of the SPR sensor which is in contact with a solution of refractive index n_s (Scheme was redrawn from Jung et al. ^[37])	17
Figure 13. SPR response versus adsorbate thickness, d , where $n_{ads}=1.330$, $n_s=1.340$ and $\lambda=825\text{nm}$. INSET: Calculated SPR response in a homogenous solution for $\lambda=825\text{nm}$ and m was calculated to be 107 per RIU ^[37]	18
Figure 14. Preparation of a biosensor surface. A) carboxyl functionalization of the biosensor surface, B) activation of carboxyl groups, C) immobilization of antibody via peptide bonding, D) target molecule detection	22
Figure 15. Model for illustration of Stokes, Rayleigh and anti-Stokes Raman scattering.....	24
Figure 16. Energy level diagram for a molecule adsorbed on a metal surface. The occupied and unoccupied molecular orbitals are broadened into resonances by their interaction with the metal states; orbital occupancy is determined by the Fermi energy ^[55] . Possible charge transfer excitations are from a) HOMO to LUMO, b) HOMO of molecule to metal, c) metal to LUMO of the molecule.	26
Figure 17. Electroless gold plating with hydroxylamine (redrawn according to the scheme by Brown et al. ^[72])	31
Figure 18. Lithographic peptide array synthesis. a) Lithographic mask defines the area on a 2D solid support. b) Transient protecting group is removed through	

irradiation. c) C-terminally activated monomers are coupled to the only deprotected structures. d) Excess monomer is washed away ^[77]	34
Figure 19. SPOT synthesis ^[77] . a) A spotter positions the C-terminally activated amino acid derivatives to defined areas on a solid support. b) They are coupled to the support in parallel. c) Excess monomer is washed away. d) The transient protecting group is removed for the next cycle.....	35
Figure 20. Positioning amino acid particles with a laser printer ^[82] . a) A laser printer positions Fmoc-amino acid-OPfp esters embedded within solid toner particles onto a solid support derivatised with free amino acid groups. b) The particles are melted and coupled c) Excess monomer is washed away. d) The Fmoc protecting group is removed.....	36
Figure 21. The peptide laser printer with 20 different cartridges ^[82]	36
Figure 22. Schematic of a laser printer ^[82] . An LED light source illuminates and neutralizes selected areas of the OPC drum, which has been evenly charged by a corona. Triboelectrically charged micro particles (bearing the same charge as the non-neutralized areas of the OPC drum) are transferred only to the neutralized areas. The such generated particle pattern is transferred from the OPC drum to a functionalized glass slide by a strong electrical field applied to the solid support.	37
Figure 23. Diagram of a multichannel spectrometer based on a grating spectrograph with an array detector. Radiation from the tungsten or deuterium source is made parallel and reduced in size by the lens and diaphragm. Radiation transmitted by the sample enters the spectrograph through slit S. Collimating mirror M_1 , makes the beam parallel before it strikes the grating G. The grating disperses the radiation into its component wavelengths which are then focused by focusing mirror M_2 onto the photodiode or CCD array A. The output from the array detector is then processed by the computer data system ^[87]	40
Figure 24. Optical fiber based total internal reflection. Light transmission (1) in an optical fiber occurs by total internal reflection for which the transmitting fiber is coated with outer cladding material (3) that has lower refractive index than the inner core material (2) ^[88]	41
Figure 25. Configuration of the Czerny-Turner grating monochromator ($\lambda_1 > \lambda_2$) ^[87] . 43	
Figure 26. Illustration of the readout operation of a CCD. The charge trapped in one pixel is transferred to the next pixel by changing the voltage levels of neighboring pixels. By repeating this cycle on adjacent pixels, the charges associated with each pixel are sequentially read out into a charge amplifier, which creates a varying output voltage signal ^[89]	44
Figure 27. Basic principle of XPS	45
Figure 28. C1s signal in the XP spectrum of fibrinogen on Au shell-silica core surface showing the chemical shifts for C=O (287.9 eV) and C-O (285.9 eV) with respect to C-C normalized to 284.6 eV	47
Figure 29. Schematic of a typical electron spectrometer showing all necessary components ^[90]	48
Figure 30. Diagram of SEM column and specimen chamber ^[95]	50
Figure 31. Self-assembly floating of nanoparticles: transfer of the nanoparticles to aqueous media by a transfer glass slide (A), formation of a monolayer of	

nanoparticles at the air/liquid interface (B), lifting off the monolayer with a Au substrate (C) and densely packed monolayer adsorption on the Au substrate (D).....	57
Figure 32. UV-Vis spectra of Au and Ag nanoparticle seeds in aqueous solution. .	58
Figure 33. Sketch of the optical set-up for A)UV-Vis reflection measurements. Inset: cross-section of the reflection probe and B) LSPR imaging set-up ^[8]	64
Figure 34. a) and b) are SEM images of silica nanoparticle film deposited on a flat Au film by incubation. Also shown are UV-Vis spectra of the Au shell-silica core nanoparticle film recorded with c) the standard UV-Vis reflection set-up and d) the 50 μ m resolution scanning unit. The Au shell was prepared by seeding and consecutive electroless plating.	71
Figure 35. SEM images of dielectric silica particles on a flat Au film prepared by spin-coating.	72
Figure 36. a) and b) are SEM images of a monolayer silica nanoparticle film on a flat Au film deposited by floating assembly. Also shown are UV-Vis spectra of the Au shell-silica core nanoparticle film recorded with c) the standard UV-Vis reflection set-up and d) the 50 μ m resolution scanning unit. The Au shell was prepared by seeding and consecutive electroless plating.....	74
Figure 37. SEM image of monolayer silica nanoparticle film over a large surface area (estimated area 15 x 10 mm).	75
Figure 38. SEM image of silica nanoparticle film on a flat Au film decorated with a) Au nanoparticle and b) Ag nanoparticle seeds, respectively.	76
Figure 39. SEM images of silica nanoparticle films deposited on a flat Au film for different plating times: a) no plating (only seeds), b) 1 min plating, c) 3 min plating, d) 5 min plating, and e) 10 min plating.	78
Figure 40. SEM image of silica nanoparticle film after electroless silver plating. ...	79
Figure 41. Schematic illustration of substrates used in biosensor configuration variation, focusing on different dielectric layers: I) SiO ₂ nanoparticles, II) SiO ₂ nanoparticles on a SiO ₂ planar film and III)SiO ₂ plane film. Corresponding UV-Vis spectra are given below.	82
Figure 42. UV-Vis spectra of the biosensor surface (Au shell-silica core) taken after seeding and various times of electroless gold plating	83
Figure 43. UV-Vis spectra of a biosensor surface (Au shell-silica nanoparticle core) before and after fibrinogen adsorption. The Au shell was prepared by seeding and 180 s electroless plating.	84
Figure 44. Wavelength shift of various biosensor surfaces upon fibrinogen adsorption for different times of electroless plating.....	85
Figure 45. N1s signal area difference in XPS spectra taken before and after fibrinogen adsorption for different biosensor surfaces.	86
Figure 46. UV-Vis spectra of biosensor surfaces before and after fibrinogen adsorption. Au film thickness A) 30 nm, B) 100 nm.	87
Figure 47. UV-Vis spectra of the biosensor (configuration II in Figure 41) before and after fibrinogen adsorption.	89
Figure 48. UV-Vis spectra of the biosensor surface (configuration III in Figure 41) before and after fibrinogen adsorption and corresponding SEM image.	90
Figure 49. UV-Vis spectra of a A) Au shell-silica core, B) Ag shell-silica core nanoparticle film biosensor surface before and after fibrinogen adsorption. ...	92

Figure 50. XPS spectrum of the Ag3d signal of a Ag shell-silica core biosensor surface.	93
Figure 51. XPS spectra of C1s signal of Au shell-silica core and Ag shell-silica core biosensor surfaces before and after fibrinogen adsorption.	94
Figure 52. XPS spectra of the N1s signal of a Ag shell-silica core nanoparticle film before and after fibrinogen adsorption and comparison of the N1s signal area for Au shell- and Ag shell-silica core nanoparticle films. Shown is the difference in peak area with respect to the situation before and after fibrinogen adsorption.	95
Figure 53. UV-Vis spectra of Au shell-silica core nanoparticle film before antibody binding, after antibody binding, after nonspecific antigen binding and after specific antigen binding.	96
Figure 54. UV-Vis spectra of Ag shell-silica core nanoparticle film before antibody binding, after antibody binding, after nonspecific antigen binding and after specific antigen binding.	97
Figure 55. N1s signal area difference between before antibody coupling and after specific antigen coupling for Ag shell-silica core and Au shell-silica core biosensor surfaces.	98
Figure 56. SEM images of a) a Au-coated PVDF membrane and b) the same substrate with a dielectric silica nanoparticle film deposited on it.	99
Figure 57. UV-Vis spectra of a Au shell-silica core nanoparticle film on a PVDF membrane before and after fibrinogen adsorption.	99
Figure 58. SEM image of a Au shell-silica core nanoparticle film deposited on a PI foil (left) and UV-Vis spectra of Au shell-silica core the nanoparticle film before and after fibrinogen adsorption.	100
Figure 59. SEM image of a Au shell-silica core nanoparticle film prepared by sputter coating the Au shell (20 nm thickness). Inset: Au shell coated silica nanoparticles which were removed from the surface.	101
Figure 60. Wavelength shift of biosensor surfaces for different shell thickness... ..	102
Figure 61. UV-Vis spectra of biosensor surfaces prepared by sputter coating of the Au shell at different shell thickness.	102
Figure 62. UV-Vis spectra of the biosensor (configuration II in Figure 33) prepared by sputter coating of Au shell before and after fibrinogen adsorption.	103
Figure 63. Fast read-out set-up and its components.	105
Figure 64. Quantum efficiency curve for A) Sensicam UV measured by PCO and B) transmission curve for fused silica measured by Laser Components.	106
Figure 65. Transmission curves of A) UV-VIS CoastalOpt® SLR Lens and B) Makro Planar 2/100mm ZF provided by the companies.	106
Figure 66. A) Fluorescence image and B) SPR intensity image (2.5s exposure time) of the antibody array spotted on biosensor surface as measured at 600 nm wavelength.	109
Figure 67. SPR curves for antibody spots and background generated from the SPR images at different wavelengths.	110
Figure 68. SPR intensity images of an antibody array on an A) Au shell-silica core film (2.6 ng/mm ² protein) and B) Ag shell-silica core film (0.13 ng/mm ² protein) measured at at 650 nm wavelength. (5 s integration time for A and 7.5 s for B)	111

Figure 69. SPR images of an antibody array spotted on a biosensor surface (same sample) measured at different wavelengths A) 360 nm B) 600 nm and C) 800 nm (5 s integration time). (A Au core-silica-shell nanoparticle layer on 30 nm flat Au film was used in the experiments.).....	112
Figure 70. SPR image of biosensor surface at 500nm and A) SPR wavelength shift and B) UV-Vis reflection spectra of the protein spot and background.....	113
Figure 71. SPR images of fibrinogen spots on A) Au shell-silica core and B) Ag shell-silica core at 550 nm (2 s integration time for each)	114
Figure 72. UV-Vis reflection spectra of fibrinogen spot and background on A) Au shell-silica core and B) Ag shell-silica core, and SPR wavelength shift spectra of fibrinogen spot and background on C) Au shell-silica core and D) Ag shell-silica core.....	115
Figure 73. SPR images of fibrinogen spots on a A) Au coated PVDF membrane based and B) PI-foil based biosensor. (10 s exposure for A and 1.5 s exposure for B).....	117
Figure 74. Transfer of peptide arrays. I) The synthesis surface is placed face-down on the biosensor surface. II) The synthesis surface is left on the biosensor for the desired transfer time. III) Separation of the surfaces. (Redrawn according to experimental set up by C. Schirwitz ^[78]).....	119
Figure 75. Fluorescence image of the transferred array on a biosensor surface. The image was obtained by staining the array with the DyLight 680 conjugated antibody. The biosensor surface consists of an Au shell silica-core nanoparticle film A glass slide coated with a 30 nm flat Au film and 40 nm SiO ₂ served as the substrate.....	120
Figure 76. SPR images of the Au shell silica-core nanoparticle film on the biosensor surface to which the peptide array in Table 1 was transferred. Wavelengths: A) 550 nm, B) 600 nm and C) 650 nm. A glass slide coated with a 30 nm flat Au film and 40 nm SiO ₂ served as the substrate.	121
Figure 77. LSPR image of an Au shell-silica core nanoparticle film after antibody staining of the transferred peptide array taken at a step size of 100 μ m. The color indicates the intensity of the extinction peak observed at wavelengths: A) 550 nm, B) 600 nm and C) 650 nm. A glass slide coated with a 30 nm flat Au film and 40 nm SiO ₂ served as the substrate.	122
Figure 78. SPR images of a Au shell-silica core nanoparticle film on 30 nm flat Au with sputter-coated Au shell (~20nm) at different wavelengths A) 550 nm, B) 600nm and C) 650nm	123
Figure 79. LSPR image of a Au shell-silica core nanoparticle film (taken at a step size of 100 μ m) with sputter-coated Au shell (~20 nm) on 30 nm flat Au at wavelengths A)550 nm, B) 600nm and C)650 nm in comparison to Figure 78.	124
Figure 80. A) Fluorescence image of a peptide array stained with dye-labeled secondary antibody on an Au shell-silica core nanoparticle film and B) SPR image at 535 nm. A 40 nm SiO ₂ layer on a 30 nm flat Au film served as the substrate (4 s integration time for B).....	125
Figure 81. SPR wavelength shift spectra of background and protein spot.....	125

Figure 82. A) LSPR intensity image of Au shell-silica core nanoparticle film after peptide array transfer and antibody staining. B) UV-Vis spectra of protein spot and corresponding background.(The step size was 50 μ m).....	126
Figure 83. A) Fluorescence image of a peptide array stained with dye-labeled secondary antibody on a Au shell-silica core nanoparticle film and B) SPR image at 530 nm. A 40 nm SiO ₂ layer on a 30 nm flat Au film served as the substrate (10 s integration time for B).....	127
Figure 84. SPR wavelength shift spectra of background and protein spot.....	127
Figure 85. A) LSPR image of a Au shell-silica core nanoparticle film after peptide array transfer and antibody staining. B) UV-Vis spectra of protein spot and corresponding background. (The step size was 50 μ m)	128
Figure 86. A) Fluorescence image of antibody array at different concentrations and B) SPR image of the nanoparticle film with the same antibody array at 500nm.	129
Figure 87. SPR wavelength shift spectra of background and protein spot.....	130
Figure 88. A) LSPR intensity image of an Au shell-silica core nanoparticle film with spotted antibody array (1ng/mm ² protein). B) UV-Vis spectra of protein spot and corresponding background are shown (The step size was 50 μ m).	131
Figure 89. Sensor sensitivity, S_n , as a function of wavelength for the structure: BK7 glass prism, surface plasmon active metal layer (gold and silver with 50 nm thickness), gaseous sensed medium ($n_s=1$) ^[106]	134
Figure 90. Distribution of the wavelength maxima of a biosensor surface for A) the short wavelength peak before protein adsorption, and B) the short wavelength peak after protein adsorption, C) the long wavelength peak before protein adsorption and D) the long wavelength peak after protein adsorption. (Configuration I in Figure 41 was used with a Au metal shell prepared by seeding and 180 s electroless gold plating) The histograms were generated from the LSPR image of the biosensor surface recorded by the scanning unit. The scanned area was 1x1 mm with 25 μ m step size. Full Width at Half Maximum (FWHM) values were calculated to be A) 3.4 nm B) 3.7 nm, C) 28.2 nm and D) 16.5 nm. They were determined from the histograms by fitting the data with a Gaussian function. Bin size was set to 1 nm for A and B, 2 nm for C and D.	135
Figure 91. Wavelength shifts of the short and the long wavelength peak upon protein adsorption on the biosensor surface as deduced from Figure 90.	136
Figure 92. Fluorescence image of ATTO 680 conjugated anti-HA IgG antibody ...	137
Figure 93. LSPR intensity image of Au shell-silica core nanoparticle film after antibody adsorption at 610 nm, and the four selected antibody spots for wavelength averaging. (The step size of the scan is 25 μ m)	138
Figure 94. Distribution of the wavelength maxima of a biosensor surface after antibody adsorption for four different spots and their corresponding area before antibody adsorption. (16 pixels for each histogram, bin size is 5 nm for after antibody adsorption column and 1 nm for before antibody adsorption column)	139
Figure 95. LSPR intensity images of the Au shell-silica core nanoparticle film A) before antibody spotting, B) after antibody spotting, and LSPR wavelength images C) before antibody spotting for the marked areas of image A and D) after antibody spotting for the marked areas of image B. The LSPR wavelength	

images were obtained from the histograms in Figure 94. Color codes in A and B show the peak intensity, in C and D the peak position determined for each step of scanning. LSPR intensity images were recorded at 610 nm with a step size of 25 μm . (White squares correspond to areas before and after antibody adsorption and black square corresponds to background where there was no antibody present)(Center to center distance in C and D was reduced and the images were magnified to show the details of the analysis)	140
Figure 96. LSPR wavelength images after the wavelength averaging process for A) before antibody spotting and B) after antibody spotting. C) displays the difference between B) and A). (Center to center distance in images was reduced and the images were magnified to show the details of the analysis as in Figure 95)	142
Figure 97. A) LSPR intensity image and B) LSPR wavelength image of the four protein spots. The color code is only valid for B.....	143
Figure 98. UV-Vis spectra of Au shell-silica core nanoparticle films taken after seeding and various times of electroless gold plating and the wavelength of the Raman excitation line.....	147
Figure 99. SERS spectrum of 10^{-4} M MB on a Au shell-silica core nanoparticle film (600s electroless gold plating) and Raman spectrum of background prior to molecule adsorption. (10 s accumulation time for each spectrum)($\sim 6 \times 10^{10}$ molecule/ mm^2).....	148
Figure 100. 1621cm^{-1} peak peak area/accumulation time for different time of electroless gold plating.	149
Figure 101. A) Real and B) imaginary part of the dielectric permittivity of Ag, C) Real and D) imaginary part of the dielectric permittivity of Au. Values are decomposed into the Drude, ϵ_{Drude} , and interband, χ , contributions.....	151
Figure 102. SERS spectra of 10^{-4} M MB on Au shell-silica core and Ag shell-silica core nanoparticle films. 10 s accumulation time were selected for each spectrum and a baseline correction was performed. ($\sim 6 \times 10^{10}$ molecule/ mm^2)	152
Figure 103. 1621cm^{-1} peak area/accumulation time for Au shell-silica core and Ag shell-silica core nanoparticle films.	152
Figure 104. SERS spectra of fibrinogen on Ag shell-silica core and Au shell-silica core nanoparticle films (20 s accumulation time were selected for each spectrum and a baseline correction was performed)	154

LIST OF TABLES

Table 1. Layout of peptide transfer array. The array consist of various HA permutations, all of which are CAA-terminated. The wild type sequence is YPYDVDPDYA.	62
Table 2. Standard XPS measurement parameters.....	66
Table 3. Au shell sputter coating parameters	66
Table 4. Tentative peak assignment of Raman frequencies observed in the SERS spectrum of MB and the structure of MB.(ν = <i>symmetric stretching</i> , ν_{as} = <i>asymmetric streching</i>) ^[127]	148
Table 5. Tentative peak assignment of Raman frequencies observed in SERS spectrum of fibrinogen ^[135-137]	155

1 INTRODUCTION

In recent years, array concepts have become popular and powerful tools to facilitate highly parallel and rapid identification of binding events in basic research, diagnostics and drug discovery^[1,2]. Generally, the interaction analysis is assisted by labeling one of the binding molecules with additional markers. Introducing a label might, however, cause changes in molecular conformation, blocking of the active binding epitopes, steric hindrance and inaccessibility of the labeling site. To overcome the related obstacles due to labeling, label-free detection techniques such as surface plasmon resonance (SPR), ellipsometry, atomic force microscopy (AFM), interferometry, reflectometry and gravimetry have been used to follow the interactions in protein microarrays^[3,4]. Surface plasmon resonance (SPR) has served as an optical tool in chemical, physical and biological investigations to characterize the interactions of molecules at the surface of a metallized dielectric in a *label-free* format. It uses refractive index changes to detect adsorbed molecules. In other words, molecular interactions can be followed by the wavelength shifts of the plasmon peaks upon adsorption of molecules (SPR wavelength shift). Another way to detect the interaction of the biomolecules is SPR imaging based on the contrast differences between the biomolecule array and the bare surface (without protein). Moreover, different types of surfaces and configurations can be used for optical detection of molecular interactions based on SPR such as propagating surface plasmons in plain metal films^[5] and localized surface plasmon resonance (LSPR) in metal nanoparticles^[6] and metal-coated nanospheres^[7-9].

In this thesis, a novel nanostructured material with mutually coupled optical and biological functionalities in order to facilitate the label-free readout of biospecific binding events in high density peptide arrays was developed. For this purpose, a monolayer of metal-coated dielectric nanoparticles (core-shell nanoparticle) was prepared on a metallized

substrate. The combination of optically responsive core-shell nanoparticle films and innovative combinatorial peptide synthesis shall provide high-density arrays with an intrinsic label-free readout mechanism for parallel biospecific interaction analysis. In close cooperation with the Cancer Research Center (DKFZ) Heidelberg, high density peptides were generated on optimized optically responsive core-shell nanoparticle films for label-free detection of peptide-antibody specific interactions using a home built charge-coupling device (CCD) based set-up.

The surface-bound dielectric core-metal shell nanoparticle films were used to detect biomolecular interactions in a label-free format which uses both SPR and LSPR^[7]. Particularly, the core-shell nanoparticle film was improved and optimized in terms of dielectric core adsorption, metal shell coating and the type of substrate used for detection of biomolecular reactions in an array format. Moreover, for detection of protein binding to high density peptide arrays, a fast read-out set-up was established based on a CCD camera which can perform SPR imaging and SPR wavelength shift measurements.

In the second chapter of the thesis, the theory behind the principles of SPR (propagating and localized surface plasmons), the measurement methods for SPR and the use of SPR in biosensing are going to be introduced. Use of core-shell nanoparticles for SPR sensors will be followed by the use of these particles for enhancement of Raman signals. Later on, the preparation techniques for core nanoparticle adsorption and the metal shell deposition will be discussed. Finally, the peptide array preparation techniques which are SPOT, lithographic and particle based-synthesis are briefly introduced.

In the third part of the thesis, the instrumental analysis techniques and the methods which were used to evaluate and analyze the prepared core-shell nanoparticle films are introduced in terms of their basic principles. The fourth chapter of the thesis provides the details of the experimental work related to the preparation, analysis and evaluation of the surfaces.

In the results and discussion part, chapter five, representative results of the experiments are presented and discussed. Furthermore, the new fast read-out set-up based on CCD camera was introduced and used for SPR imaging and SPR wavelength shift measurements. Subsequently, wavelength averaging technique is introduced to achieve better sensitivity by compensating the optical inhomogeneity of the long wavelength peak. In the last part of the results section, the core-shell nanoparticles were used to enhance the Raman signals of the chosen analytes: methylene blue and fibrinogen.

In the conclusion section, chapter six, the results of this thesis are summarized.

2 THEORY

2.1 Surface Plasmon Resonance

In the last twenty years, the physical phenomenon of surface plasmon resonance (SPR) has been used as an optical tool in chemical, physical and biological investigations to characterize the interactions of molecules at the surface of a metallized dielectric in a *label-free* format. SPR, being a *label-free detection* method, uses refractive index changes to detect adsorbed molecules. In the following chapter, the principles of propagating surface plasmons and localized surface plasmons are introduced, and the necessary conditions to excite surface plasmons are discussed. Different methods to measure surface plasmon resonance are described and the application of surface plasmons to biosensing and enhancing Raman signals are summarized.

2.1.1 Propagating Surface Plasmons (PSPs)

Propagating surface plasmons (PSPs) are oscillations of free electrons propagating along the interface between a metal and a dielectric medium as shown in Figure 1^[10,11]. The propagation constant of a surface plasmon, k_{sp} , propagating at the interface between a dielectric and a metal may be derived by solving Maxwell's equations using the modal method^[12], and is given by the following expression in Equation 1:

$$k_{sp} = \frac{\omega}{c} \sqrt{\frac{\epsilon_m \epsilon_d}{\epsilon_m + \epsilon_d}} \quad (\text{Equation 1})$$

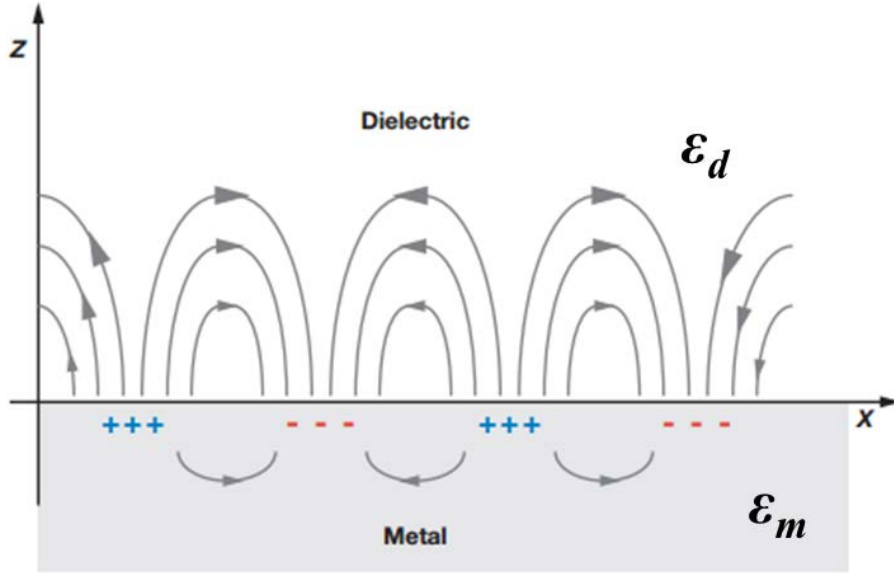


Figure 1. Schematic illustration of a propagating surface plasmon^[13].

where c is the speed of light in vacuum, ω the angular frequency, ϵ_m the complex dielectric constant (permittivity) of the metal ($\epsilon_m = \epsilon_m' + \epsilon_m''$) and ϵ_d the complex dielectric constant of the dielectric ($\epsilon_d = \epsilon_d' + \epsilon_d''$). For lossless metals and dielectrics, the imaginary parts of the dielectric constants are $\epsilon_m'' = \epsilon_d'' = 0$. Since the dielectric constants of dielectric materials are usually positive, propagating surface plasmons are generated if $\epsilon_m' < 0$ and $\epsilon_m' < -\epsilon_d'$. For metals following the free electron model^[12],

$$\epsilon_m = \epsilon_0 \left(1 - \frac{\omega_p^2}{\omega^2 + i\omega\nu} \right) \text{ (Equation 2)}$$

where ν is the collision frequency and ω_p is the plasma frequency which is given by:

$$\omega_p = \sqrt{\frac{Ne^2}{\epsilon_0 m_e}} \text{ (Equation 3)}$$

where N is the concentration of free electrons, and e and m_e are the electron charge and mass, respectively. This requirement, $\epsilon_m' < -\epsilon_d'$, is fulfilled for frequencies lower than the plasma frequency of the metal. Metals such as gold, silver and aluminum have a negative real part of the dielectric constant

in the visible (Vis) and near infrared (NIR) regime of the light spectrum as depicted in Figure 2^[12].

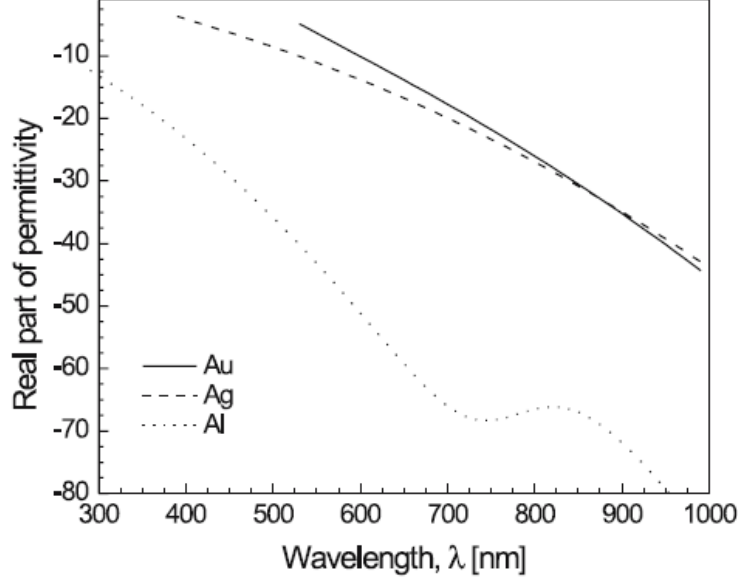


Figure 2. Real part of the dielectric constant of Au, Ag and Al as a function of wavelength^[12].

Among the metals which fulfill the requirement to have a negative real part of the dielectric constant, gold and silver are the most common metals used in SPR experiments due to their strong SPR response in the UV and Vis regime of the light spectrum.

If the real part of the dielectric function of the metal is negative and its magnitude is much larger than the imaginary part $|\epsilon_m'| \gg \epsilon_m''$, the complex propagation of the surface plasmon is given by Equation 1 can be expressed as^[12]:

$$k_{sp} = k'_{sp} + ik''_{sp} = \frac{\omega}{c} \sqrt{\frac{\epsilon'_m \epsilon_d}{\epsilon'_m + \epsilon_d}} + i \frac{\epsilon''_m}{2(\epsilon'_m)^2} \frac{\omega}{c} \left(\frac{\epsilon'_m \epsilon_d}{\epsilon'_m + \epsilon_d} \right)^{3/2} \text{(Equation 4)}$$

Where k'_{sp} and k''_{sp} denote the real and imaginary parts of the propagation constant k_{sp} . The imaginary part of the dielectric function of metal causes propagation constant to have a non-zero imaginary part, which results in attenuation of the surface plasmon. As a surface plasmon propagates along the interface, at a certain distance which is called propagation length, L , the

energy of the surface plasmon is reduced by a factor of $1/e$ and the propagation length is given by $L=1/[2k''_{sp}]$. Propagation length is typically between 10 and 100 μm in the visible regime depending on the metal/dielectric configuration under investigation^[11].

The electromagnetic field of a surface plasmon is confined at the metal/dielectric interface and decays into both media in the direction perpendicular to the interface which is characterized by the penetration depth L_p . The penetration depth is defined as the distance from the interface at which the amplitude of the field decreases by a factor of $1/e$. The penetration depth depends on the wavelength and dielectric constants of the media^[14]. Figure 3 shows the exponential decay of a surface plasmon at a gold/dielectric interface (refractive index of the dielectric is 1.32) into the dielectric and metal at two different wavelengths.

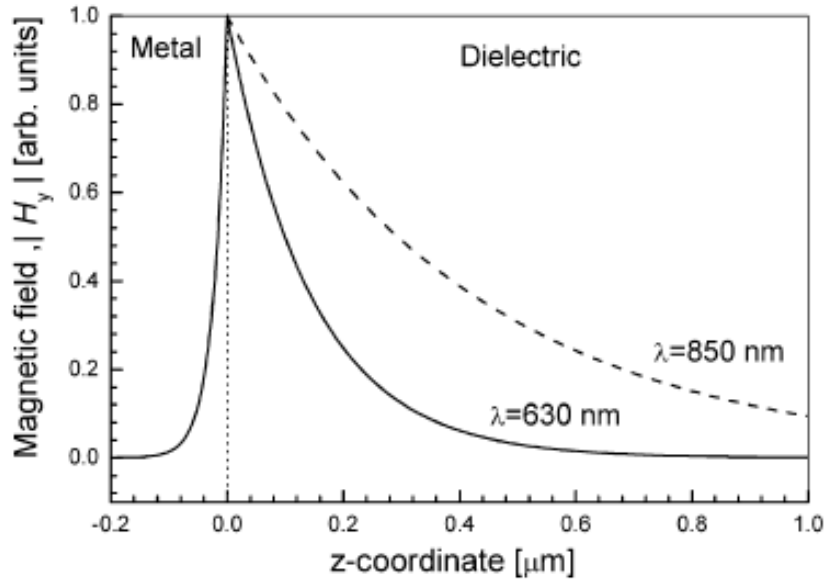


Figure 3. Distribution of the magnetic field amplitude for a surface plasmon at two different wavelengths at the gold/dielectric interface^[15].

Since the most of the electromagnetic field is concentrated in the dielectric medium as depicted in Figure 3, the propagation constant of the surface plasmon is extremely sensitive to the changes in the refractive index of the dielectric layer. Therefore, the changes in the refractive index of the dielectric layer result in changes in the propagation constant of the surface

plasmon, which can be accurately measured by optical means, as discussed in section 2.1.6.

2.1.2 Localized Surface Plasmons (LSPs)

The interaction of the light with particles smaller than the incident wavelength, results in a plasmon which oscillates locally around the particles. This effect is known as localized surface plasmon resonance (LSPR) [13,16,17] and is depicted in Figure 4.

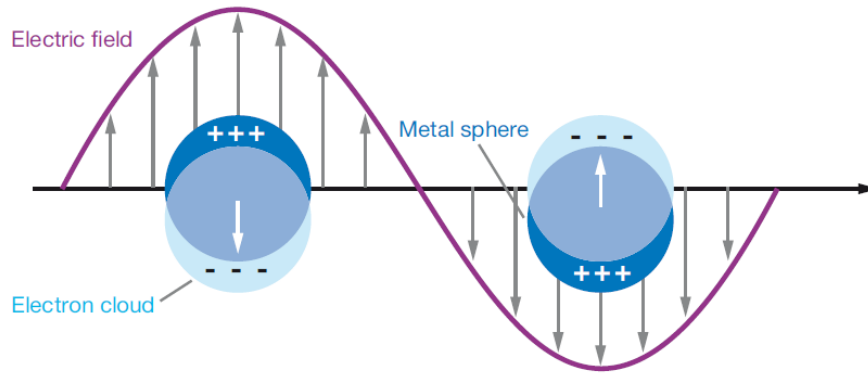


Figure 4. Illustration of a localized surface plasmon resonance (LSPR)[13].

Noble metal nanoparticles have a strong UV-Vis absorption band which is due to LSPR. The extinction coefficient, $E(\lambda)$, in the long-wavelength limit, where the particles are smaller than the incident light wavelength, i.e. $a < \lambda$, is given by Mie theory[16,18-20]:

$$E(\lambda) = \frac{24\pi N a^3 \epsilon_d^{3/2}}{\lambda \ln(10)} x \frac{\epsilon_m''}{(\epsilon_m' + 2\epsilon_d)^2 + (\epsilon_m'')^2} \text{ (Equation 5)}$$

where N is the areal density of the nanoparticles, a is the radius of the nanoparticle, ϵ_d is the dielectric constant of the surrounding medium (here assumed to be a positive, real number), λ is the wavelength, ϵ_m' and ϵ_m'' are the real and imaginary parts of the dielectric function of the metal. This formula provides a resonant peak when $\epsilon_m' = -2\epsilon_d$. For gold and silver this occurs in the visible regime of the spectrum. Moreover, any change in the dielectric constant of the medium, for example when molecules adsorb on

particles, results a shift in the resonance wavelength^[16]. Due to these properties, LSPR can be used to construct sensors which detect the binding of molecules on surfaces.

2.1.3 Excitation of Propagating Surface Plasmons

Surface plasmons cannot be directly excited by light because they have a longer wave vector (parallel to the surface) than wave vector of the photon in air, $k_{ph}=\omega/c$, at the same energy as depicted in Figure 5. Thus, the projection along the interface of the momentum of photons $k_x=k_{ph}\sin\theta$ incident at an angle θ with respect to the surface is always smaller than the SP propagation constant in Equation 1, $k_{sp} = \frac{\omega}{c} \sqrt{\frac{\epsilon_m \epsilon_d}{\epsilon_m + \epsilon_d}}$, preventing momentum matching^[21].

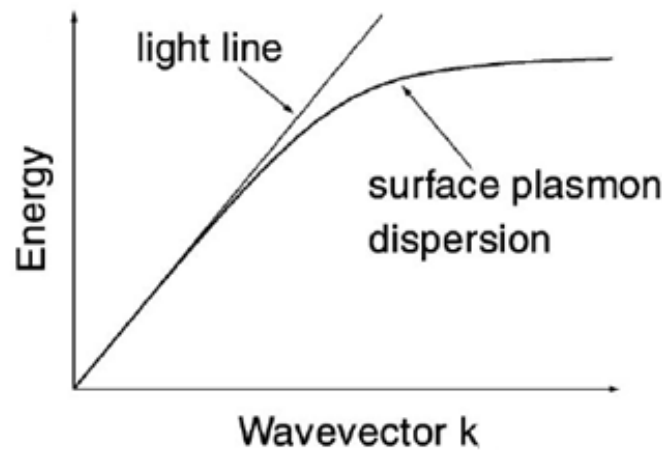


Figure 5. Dispersion curve of light and the surface plasmon on a planar metal-dielectric interface^[21].

For excitation of SPs, the wave vector of photons has to be increased by using either a prism or a grating coupler^[11,21-23].

There are two configurations proposed for excitation of SPs by a prism coupler: the Kretschmann and Otto geometries which are illustrated in Figure 6. These two configurations are based on the attenuated total reflection (ATR) method.

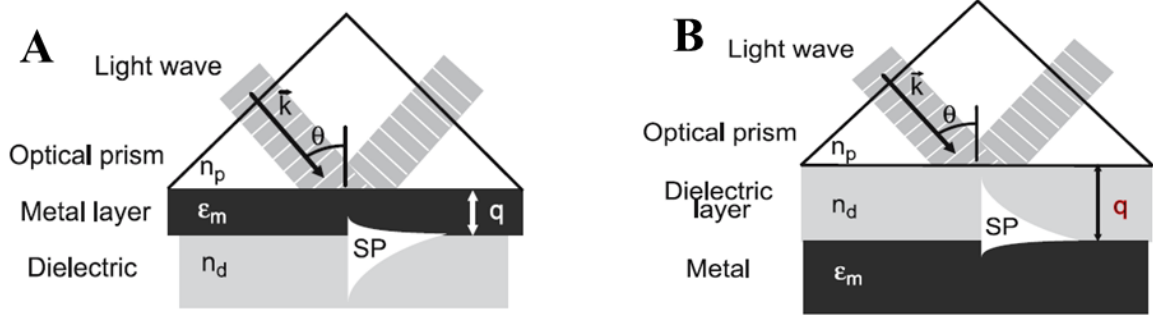


Figure 6. Excitation of surface plasmons in the A) Kretschmann and B) Otto geometry of the attenuated total reflection (ATR) method^[12].

In both of these configurations, the main idea is to use a prism coupler with a refractive index, n_p , which is higher than that of the dielectric layer, n_d , i.e. $n_p > n_d$. The prism is interfaced either above the metal as in Figure 6A or above the dielectric layer as in Figure 6B to fulfill the momentum matching condition for excitation of the SPs. The incident light wave vector in the presence of a prism is given as

$$k_x = \frac{2\pi}{\lambda} n_p \sin \theta \quad (\text{Equation 6})$$

and SP propagation constant is $k_{sp} = \frac{2\pi}{\lambda} \sqrt{\frac{\epsilon_m \epsilon_d}{\epsilon_m + \epsilon_d}}$ where k_x is the incident light wave vector, λ the wavelength of light in vacuum, n_p the refractive index of the prism, θ the incident angle of the light, and ϵ_m the dielectric constant of the metal and ϵ_d the dielectric constant of the dielectric layer. For excitation of surface plasmons the condition $k_x = k_{sp}$ has to be fulfilled. From this relation, to excite the SPs, it follows that one can either change the incident angle of the light (θ) or the wavelength of the light (λ). Based on the parameter that is being changed, SPR can be measured by different methods, such as SPR wavelength-shift, SPR angle-shift and SPR imaging. These methods will be addressed in section 2.1.4.

Another method for excitation of SPs is using a grating coupler which has a periodic structure as illustrated in Figure 7.

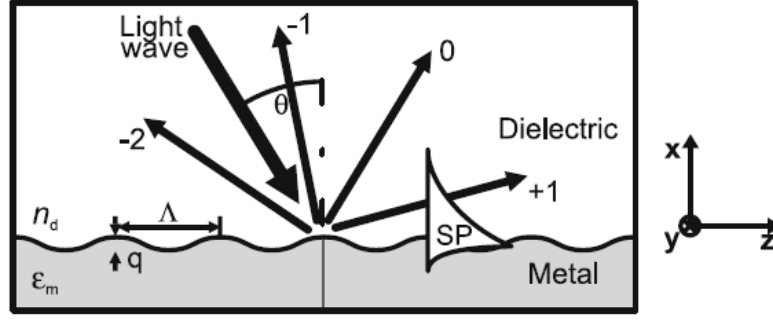


Figure 7. Excitation of surface plasmons by a grating coupler^[12].

Incident light with a given wave vector $k_x = \frac{2\pi}{\lambda} \sin \theta$ generates reflected light of diffraction orders $m=0, \pm 1, \pm 2, \dots$ due to reflection from a grating coupler which acts as a diffraction grating. The generated wave vector, $k_{x,net}$ parallel to the interface can be written as^[12,24]

$$k_{x,net} = k_x + m \frac{2\pi}{\Lambda} \text{ (Equation 7)}$$

where m is the diffraction order and Λ is the periodicity of the grating, respectively. For $m \neq 0$, the additional momentum required to fulfill the plasmon excitation condition is added to the wave vector of the incident light.

In this thesis, dielectric nanoparticles were acting as a grating coupler providing the periodicity required to fulfill the momentum matching condition for excitation of propagating SPs as shown in Figure 8. Therefore, no prism was required to excite SPs.

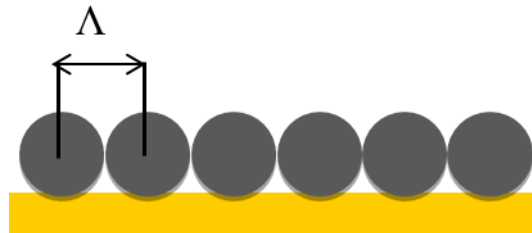


Figure 8. Densely packed monodisperse SiO₂ nanoparticles on a Au film.

2.1.4 Methods of SPR Measurements

When a molecule or an analyte is adsorbed to a metal surface of an SPR sensor, the refractive index of the surface is changed by Δn and, consequently, the propagation constant of the SPs is altered. Here the refractive index of the surface is assumed to be a positive, real number, $n_s = \sqrt{\varepsilon\mu}$ where ε dielectric constant and μ magnetic permeability to be very close to 1 at optical frequencies^[25]. The changes in the propagation constant of the SPs can generally be measured by three methods^[12,26]:

- i) *scanning angle SPR (referred to as SPR angle shift),*
- ii) *scanning wavelength SPR (referred to as SPR wavelength shift),*
- iii) *SPR imaging.*

In SPR angle shift measurements, a monochromatic light source is used for the excitation of SPs and specular reflected light intensity from the surface is followed as a function of incident angle. In SPR wavelength shift, specular reflected light intensity is measured as a function of wavelength at a fixed incident angle. Figure 9 shows an example of both SPR wavelength and SPR angle shift spectra. SPR can be extended to an imaging technique if the surface is illuminated with a monochromatic light source at a fixed incident angle and the reflected light intensity is detected with a charge-coupled device (CCD) camera to generate the SPR image.

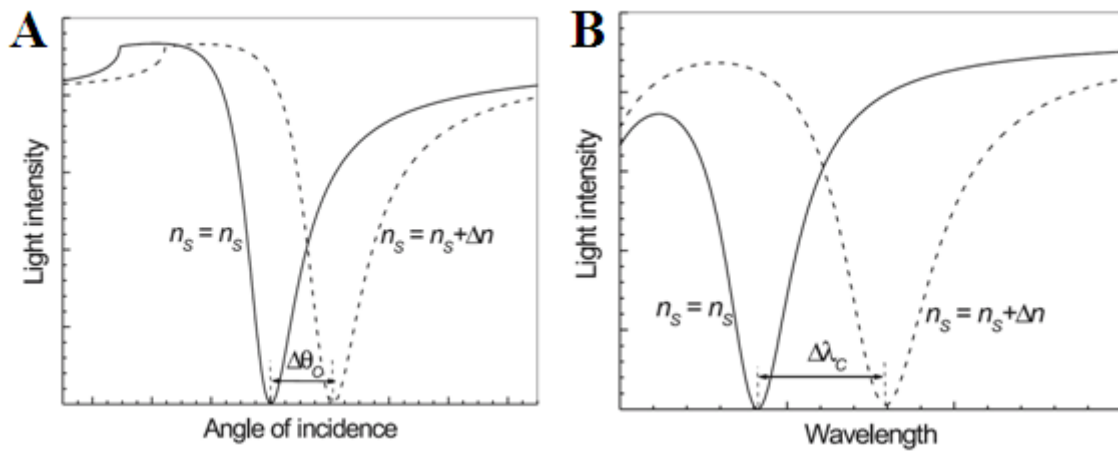


Figure 9. Reflected light intensity as a function of A) wavelength and B) incident angle for a refractive index of n_s and $n_s + \Delta n$ ^[12].

SPR imaging couples the sensitivity of SPR and the spatial capabilities of imaging. As mentioned above, the changes in the reflectivity ($\Delta\%R$) at a fixed angle of incidence and at a fixed wavelength are measured in SPR imaging. Thus, the SPR curve shifts upon adsorption of analyte on the surface as in the exemplarily shown in Figure 10. The change or the difference in the reflectivity ($\Delta\%R$) causes the contrast between coated and non-coated surface areas in the SPR images due to local changes in the refractive index upon analyte adsorption. Experimental examples are discussed in the following sections.

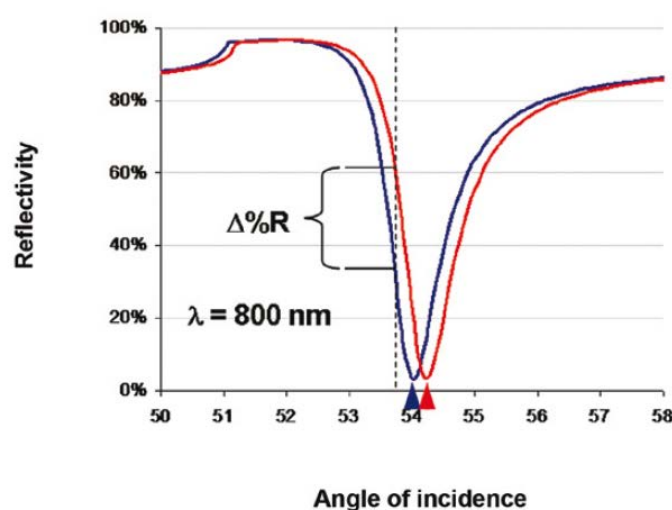


Figure 10. SPR response curves of a plain gold surface (blue curve) and after adsorption of a ~5 nm layer of protein (red curve). In SPR imaging, at a fixed angle and wavelength (dotted line), binding is measured as the local change in reflectivity ($\Delta\%R$)^[27].

In this thesis, SPR wavelength shift and SPR imaging methods were used to follow protein binding on the biosensor surfaces. In wavelength shift measurements, the surface was illuminated with different wavelengths at a fixed incident angle and the reflected intensity of the area of interest was plotted as a function of wavelength to generate SPR curves. At each wavelength, the light reflection from the illuminated surface areas was detected with a CCD camera to generate an SPR image of the surface.

2.1.5 Core-Shell Nanoparticles as SPR Sensor

Metal nanoparticles, such as gold and silver are widely applied in sensing experiments in order to increase the sensitivity of conventional SPR sensors^[28-32]. However, controlling the size and diameter of the nanoparticles had been a difficult task. Moreover, the attachment of the metal nanoparticles and control of their density on the surface without aggregation requires sophisticated fabrication techniques. Furthermore, the detection of larger molecules in size than decay length of the electric field might not be efficient because it depends on the decay length of the electric field which is rather is limited in LSPR. In order to overcome these problems core-shell nanoparticles can be used for excitation of LSP which combine the characteristics of both SPR and LSPR systems as explained in section 2.1.5. The optical characteristics and the sensitivity of core-shell structures can be controlled by the preparation process, such as the core (dielectric) nanoparticle diameter and the metal shell thickness. For instance, by changing the core-to-shell ratio of the structure both the sensitivity and the optical properties of the core-shell nanoparticles can be changed. *Jain et al.* investigated the sensitivity of the core-shell structures in solution and concluded that the sensitivity decreases with decreasing core-to-shell ratio whereas the wavelength of LSPR red-shifts as the thickness of the shell decreases^[29,33].

Exchanging the metal shell from gold to silver affects the sensitivity of the sensor. Silver nanoparticles result in a narrower and sharper SPR peaks than gold nanoparticles. The SPR peak is very sensitive to the real and imaginary part of the dielectric constant of the metal. The real part is responsible for reflection, whereas imaginary part is responsible for absorption of the light in the metal. Narrow resonance is obtained in the SPR spectra due to small damping if $\epsilon_m' \gg 1$ and $|\epsilon_m'| \gg |\epsilon_m''|$ ^[34]. Since the dielectric constant of silver has a higher ratio of $|\epsilon_m'/\epsilon_m''|$ (38.0) than gold (7.33), silver generates sharper SPR peaks than gold. To achieve better sensitivity and to decrease the detection limit of the sensor, the SPR peak of the sensor should have a small bandwidth^[35] which can be achieved by

using silver. Moreover, *Sharma et al.*^[36] proposed that an increase in the concentration of Ag nanoparticles of a Ag-Au alloy structure provides larger shifts in the resonance wavelength.

2.1.6 Sensitivity of Surface Plasmon Resonance Sensors

SPR Response to Bulk Solution

SPR response (R) as either the change in wavelength ($\Delta\lambda$) or incidence angle ($\Delta\alpha$) can be associated with the changes in the refractive index of the medium in contact with the metal surface of the SPR sensor, (Δn). The SPR response to changes in bulk refractive index, in the absence of adsorption from solution, can be defined as^[37]:

$$R = m\Delta n = m(n_{final} - n_{initial}) \text{ (Equation 8)}$$

The magnitude of the slope, m , can be considered as the sensitivity factor for the sensor with respect to RIU (Refractive Index Unit) changes as depicted in Figure 11.

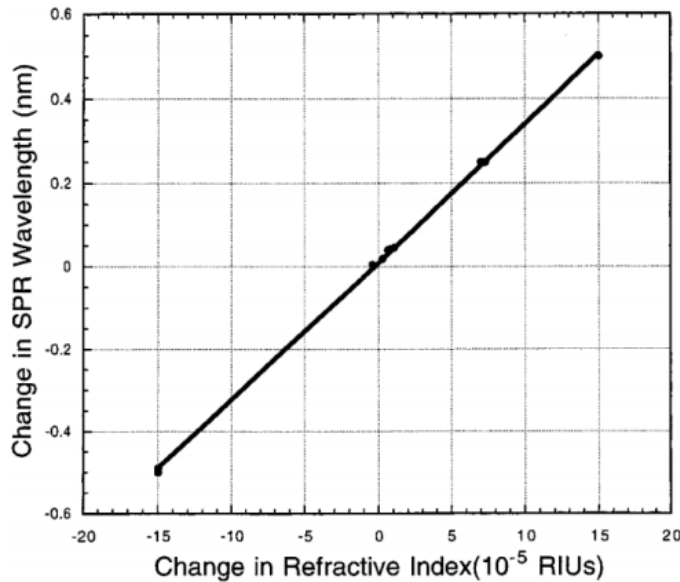


Figure 11. Measured SPR response over a narrow range of n near that for water. ($n=1.330$)^[37]

Over a large range of n the sensor sensitivity could be described by a low-order polynomial equation, in which $m_2\Delta n^2$ is negligible for small Δn ^[37]:

$$R = m\Delta n + m_2\Delta n^2 \text{ (Equation 9)}$$

SPR Response to Adsorbed Layers

If an idealized bilayer structure as shown in Figure 12 is considered, where a thin adsorbed film of uniform thickness d and refractive index n_{ads} is adsorbed to the metal surface of an SPR sensor with a bulk solution above the adsorbate layer, the estimated response is given by^[37]:

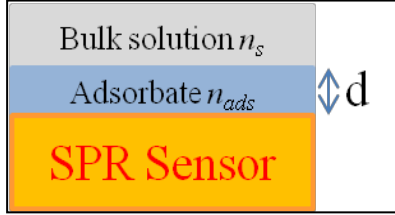


Figure 12. Schematic diagram of a bilayer structure involving an adsorbate thickness d and refractive index n_{ads} on the metal surface of the SPR sensor which is in contact with a solution of refractive index n_s (Scheme was redrawn from Jung et al.^[37])

$$R = m(n_{eff} - n_s) \text{ (Equation 10)}$$

or in case of a quadratic calibration plot:

$$R = m_1(n_{eff} - n_s) + m_2(n_{eff} - n_s)^2 \text{ (Equation 11)}$$

where n_{eff} denotes the effective refractive index of the bilayer, which can be calculated by averaging the refractive index over the depth of the whole bilayer structure:

$$n_{eff} = \left(\frac{2}{l_d}\right) \int_0^\infty n(z) e^{-\frac{2z}{l_d}} dz = n_s + (n_s - n_s) \left[1 - e^{-\frac{2d}{l_d}}\right] \text{ (Equation 12)}$$

where $n(z)$ is the refractive index at height z , d the adsorbate layer thickness and l_d the characteristic decay length of the electromagnetic field perpendicular to the sensor surface^[37].

For a linear calibration curve of SPR response versus bulk solution refractive index, the equation is:

$$R = m(n_{eff} - n_s) = m(n_{ads} - n_s) \left[1 - e^{-\frac{2d}{l_d}}\right] \text{ (Equation 13)}$$

For the more complex nonlinear calibration curve, the effective refractive index of the bilayer is:

$$R = m_1(n_{ads} - n_s) \left[1 - e^{-\frac{2d}{l_d}} \right] + m_2[(n_{ads} - n_s) \left[1 - e^{-\frac{2d}{l_d}} \right]]^2 \text{ (Equation 14)}$$

where the constants m_1 and m_2 are determined from the calibration curve in Figure 13 by fitting the response to the refractive index (RI) of bulk solutions.

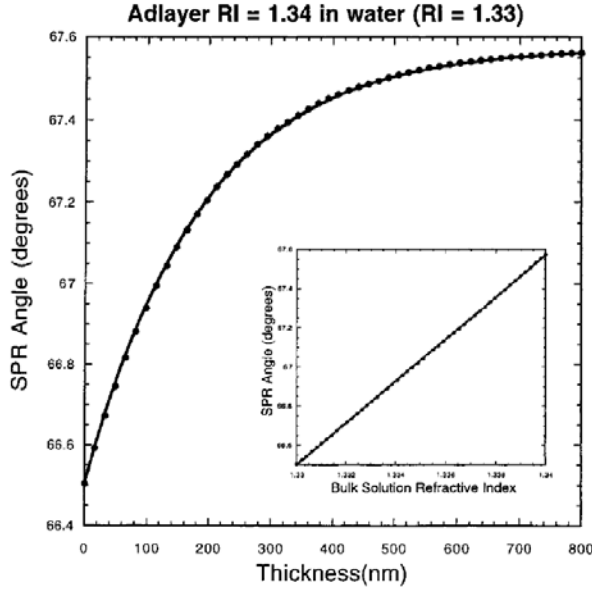


Figure 13. SPR response versus adsorbate thickness, d , where $n_{ads}=1.330$, $n_s=1.340$ and $\lambda=825\text{nm}$. INSET: Calculated SPR response in a homogenous solution for $\lambda=825\text{nm}$ and m was calculated to be 107per RIU^[37].

The same type of relationship as in Equation 12 can be applied to LSPs in spherical objects^[7]. The electric field distribution ($E(kr)$) outside the sphere is^[38]:

$$E(kr) = C e^{\left[-\left[\frac{v^2}{(ka)^2} - 1 + \frac{1}{4(ka)^2} \right]^{\frac{1}{2}} - \frac{1}{2ka} \right] kr} \text{ (Equation 15)}$$

where $v=n+1/2$, $n=1,2,3\dots$, a is the radius of the object, $k=2\pi/\lambda$ the wave vector of the electric field, r the distance from the surface of the sphere and C a constant. Following *Buecker et al.*^[7], LSPs may be considered as low order excitations, so that one may assume $n=0$. Thus, $v=1/2$ and the wave vector of the electric field is given as:

$$E(kr) = C e^{\left[-\left[\frac{1}{2(ka)^2} - 1 \right]^{\frac{1}{2}} - \frac{1}{2ka} \right] kr} \text{ (Equation 16)}$$

For experimental conditions of $a=200\text{nm}$ and $\lambda=400\text{nm}$, $([1/(2(ka)^2)-1]^{1/2})$ becomes an imaginary number describing a radiation field not contributing to the exponential decay^[7]. Therefore, the decay length of electric field strength, l_d , in Equation 12 is found to be $l_d=2a$.

This has been confirmed by sensitivity measurements which show that for the above experimental conditions the decay length of the electric field for core-shell structures exceeds 100 nm which corresponds to LSPR in spheres with a diameter of 100 nm and more^[7]. In contrast, decay length of the electric field for LSPR, when excited in small nanoparticles, is typically in the range of 10 nm and, therefore, lower than the typical decay lengths for propagating plasmons with values of 200-300 nm^[7,18].

In this thesis, the biosensor surfaces described and proposed consist of dielectric nanoparticles, which are adsorbed onto a flat gold surface (or sometimes a plain dielectric film coated onto a flat gold surface) and metallized by gold (silver) nanoparticles prior to electroless gold (silver) plating. Thus, the surfaces contain structural elements which are characteristic of both SPR (flat gold film) and LSPR (gold or silver nanoparticles and metallized dielectric nanoparticles) systems^[7]. The experimental parameters are similar to those used by *Buecker* et al. From the long decay length of the electric field it may, therefore, be concluded that the sensing mechanism was mediated by LSP excitation in the core-shell nanoparticles as a whole not only by LSPR in the small nanoparticles deposited on top of the dielectric cores. In addition, PSPs may contribute to the observed response.

2.1.7 Surface Plasmon Resonance in Biosensing

SPR measurements have been widely used in detection of biological analytes and analysis of biomolecular interactions where SPR offers the advantages of ***label-free*** and ***real-time analysis***. This means in particular^[15]:

1. *Label-free*: Specific binding between the biorecognition element and analyte can be detected or monitored without any radioactive, enzymatic or fluorescent labels.
2. *Real-time*: The time course of the binding event can be instantly monitored due to the rapid response of SPR.

Biosensors are generally classified as label-based or label-free depending on whether the output signal of the molecule binding is obtained by using a labeled compound or not^[39]. The label is designed to be easily measured by its color or its ability to generate photons at a particular energy (wavelength). Enzymes, nanoparticles, radioactive labels and fluorescent dyes are widely used as labels^[15,39]. The main advantage of label-based measurements is their potential to detect lower concentrations. However, the labeling process can alter the native activity and structure surface characteristics of the molecules, which might interfere with the molecule binding and cause distorted results. Moreover, the labeling process is expensive, extensive, and time consuming. Furthermore, incomplete labeling limits the number of molecules being studied^[4,39], and real time monitoring of the molecule binding process onto the sensor surface is often not possible. On the contrary, label-free detection is cheaper, simple to apply and capable of providing information about the kinetics of binding between the surface and the biomolecules in *real time*. For example, direct measurement of the affinity of the interaction and its kinetic parameters enables direct discrimination of a wide variety of protein pairs.

In general, SPR biosensors are used for the detection of binding events between biomolecules such as antigen-antibody^[18,40-42] and DNA-protein^{[43-}

^{46]} interactions or DNA hybridization^[26,47-49], which rely on the specific binding and detection of particular analyte molecules.

In a typical SPR biosensor configuration, one of the interacting molecules is immobilized on the metal surface of the sensor by appropriate surface chemistry which enables immobilization of biorecognition elements while minimizing nonspecific binding to the surface. In general, antibodies are widely used as biorecognition elements because of their high affinity, versatility and commercial availability. To immobilize antibodies, the sensor surface is usually functionalized with a carboxyl (which can be activated by using either *N*-hydroxysuccinimide (NHS) and *N*-(3- dimethylaminopropyl)-*N*-ethylcarbodiimide hydrochloride (EDC) or an aldehyde group to which the antibody can couple via peptide bond formation (i.e. coupling of amine groups with carboxyl groups to give amide groups) as shown in Figure 14. Then the target molecule is introduced to the sensor surface either by incubation of the sensor surface in the target solution and subsequent removal in *ex situ* experiments or by permanent liquid exposure in *in situ* experiments. One can follow the SPR biosensor response at each step of molecule binding to the sensor surface since the refractive index of the surface will change and affect the SPR coupling conditions. In this thesis, the specific binding of antigen-antibody couples was exemplarily investigated on both Au and Ag nanoparticle surfaces which is discussed in section 5.2.1.2.

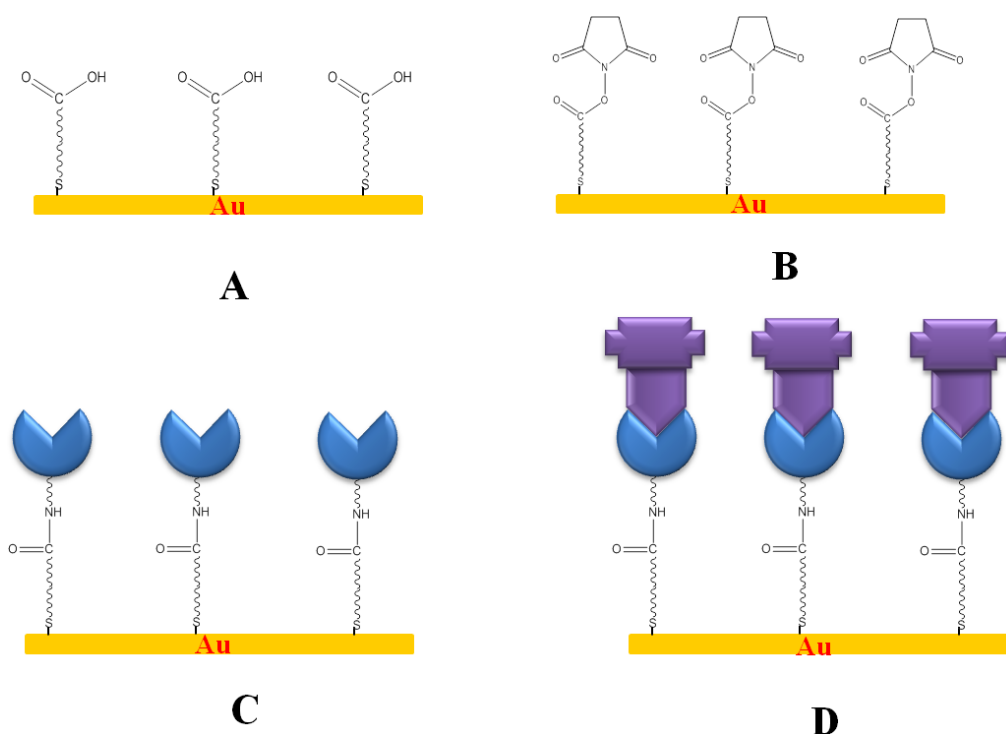


Figure 14. Preparation of a biosensor surface. A) carboxyl functionalization of the biosensor surface, B) activation of carboxyl groups, C) immobilization of antibody via peptide bonding, D) target molecule detection

Beside biosensor development and monitoring of molecular interactions, SPR was also used in this thesis to enhance weak Raman signals in this thesis. Raman signals are amplified in the presence of rough metal surfaces through Electromagnetic Mechanism (EM), a technique which is known as Surface Enhanced Raman Spectroscopy (SERS). In the following part, Raman scattering and the effect of SPR for signal enhancement are briefly discussed.

2.2 Surface Enhanced Raman Scattering (SERS)

Surface Enhanced Raman scattering was first observed in 1974 by *Fleischmann et al.*^[50] when investigating pyridine adsorbed onto a roughened silver electrode surface. Subsequently, *Jeanmarie et al.*^[51] and *Creighton et al.*^[52] independently obtained similar results on roughened silver surfaces. *Jeanmarie et al.*^[51] proposed an electric field enhancement mechanism, whereas *Creighton et al.*^[52] suggested that enhancement is caused by the interaction of molecular electronic states with the metal surface. The effect was called later called *Surface Enhanced Raman Scattering (SERS)*.

Before getting into details of the enhancement mechanisms, a brief introduction to the background of Raman scattering will be given in the following section. Subsequently, two suggested enhancement mechanisms, electromagnetic and chemical mechanism, will be discussed.

2.2.1 Raman Scattering

When light is scattered from a molecule, two processes can occur: elastic and inelastic photon scattering. In elastic scattering, the photons have the same energy (frequency) as the incident photons. The majority of photons undergoes elastic scattering which is also called Rayleigh scattering. However, a small fraction of photons is scattered inelastically, which means that the scattered photons have a different energy than the incident photons. The inelastic scattering has been first observed by *C.V Raman* in 1928 and is therefore called Raman scattering or Raman effect.

Raman scattered photons either gain or lose energy after being scattered from a molecule. When the scattered photons have more energy than the incident photons, the scattering process is called *anti-Stokes scattering*. On the contrary, the scattered photons can lose energy in the scattering process which is denoted as *Stokes scattering*. To obtain the Raman effect, the molecule is excited from ground state to a virtual energy state, and then relaxes into an excited vibrational or rotational state for Stokes Raman scattering. In contrast, in anti-Stokes scattering, the

molecule is excited from an elevated vibrational or rotational energy state and relaxes into a lower energy state as depicted in Figure 15. Both Stokes and anti-Stokes are equally displaced from the Rayleigh feature. Usually, Stokes scattering is followed in Raman Spectroscopy since anti-Stokes scattering is less intense as it occurs from an excited state (n), which according to Boltzman distribution is less populated than the ground state (m)^[53].

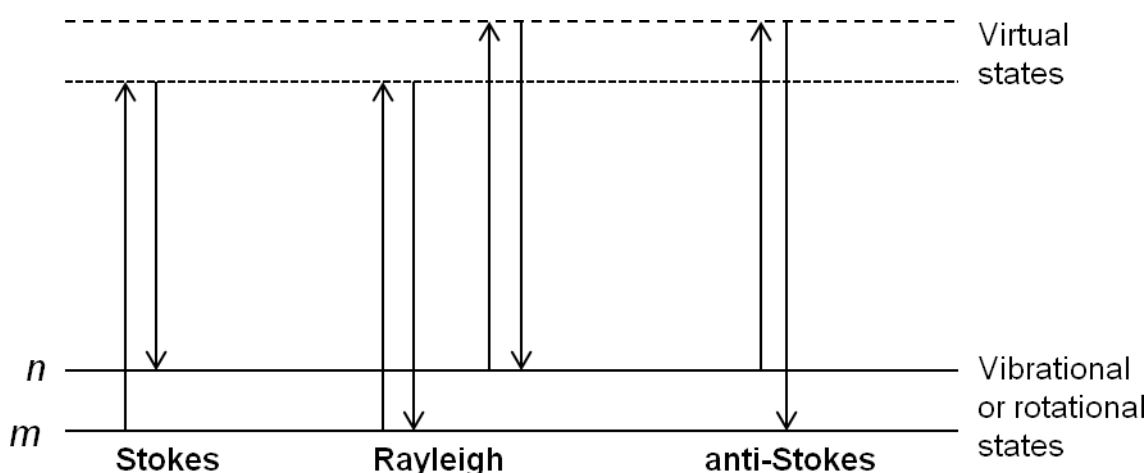


Figure 15. Model for illustration of Stokes, Rayleigh and anti-Stokes Raman scattering

Raman scattering is a powerful analytical tool to investigate molecular composition, structure and interactions both qualitatively and quantitatively. Moreover, since water is a weak Raman scatterer, it is possible to conduct *in situ* experiments in aqueous media. However, there is a certain drawback of Raman scattering: the Raman signals are very weak due to low conversion efficiency of incident photons to Raman scattered photons. To overcome this problem, surface enhanced Raman scattering (SERS) was introduced to amplify the intensity of Raman signals by several orders of magnitude in the presence of a rough metal surface which could generate SPs.

2.2.2 Mechanisms of SERS

There is variety of publications in literature suggesting mechanisms for the enhancement of Raman signals of molecules located in proximity to metal surface. The proposed mechanisms can be divided into two groups: One is the *electromagnetic enhancement (Electromagnetic Mechanism (EM))* in which the enhancement in the field intensity stems from surface plasmons generated on the roughened metal surface. The other is the *chemical enhancement (Chemical Mechanism (CM))* which originates from changes in the adsorbate electronic states due to chemisorption of the analyte^[54].

Campion et al.^[55] explained the CM as a resonance Raman mechanism due to new electronic states which arise from chemisorption and serve as resonant intermediate states in Raman scattering. The highest occupied molecular orbital (HOMO) and lowest unoccupied molecular orbital (LUMO) of the adsorbed molecule can be symmetrically arranged in energy with respect to the Fermi level of the metal as shown in Figure 16^[55]. In this case, charge transfer excitations either from the metal to the molecule or from the molecule to the metal can occur at about half of the energy of the intrinsic intramolecular excitations of the adsorbed molecule^[55]. Molecules commonly studied by SERS typically have their lowest-lying electronic excitations in the near UV which in this model would shift the charge transfer excitations to the visible region of the spectrum. In general, enhancement due to CM has been reported to be in the order of 10^1 - 10^2 to the overall SERS enhancement and is, thus, an important contribution^[55].

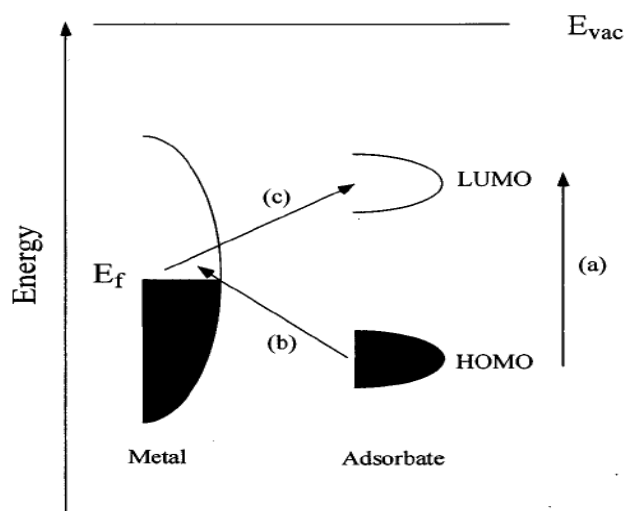


Figure 16. Energy level diagram for a molecule adsorbed on a metal surface. The occupied and unoccupied molecular orbitals are broadened into resonances by their interaction with the metal states; orbital occupancy is determined by the Fermi energy^[55]. Possible charge transfer excitations are from a) HOMO to LUMO, b) HOMO of molecule to metal, c) metal to LUMO of the molecule.

The second frequently proposed mechanism in SERS is EM, which is a result of enhanced electromagnetic fields generated at metal surfaces^[55,56]. EM can be explained as a five step process. In the first step, incident light is applied to a surface at a certain incident angle and can excite a surface plasmon. Second, the large electric field of the plasmon polarizes molecules bound to the surface, creating large effective dipole moments within them. Third, if a molecule now changes its vibrational state then, the molecular polarization will be altered. Fourth, this change in polarization subsequently affects the emitted plasmon, resulting in a new plasmon surface field. Finally the surface plasmon can couple to an outgoing Raman scattered photon^[55-58]. The EM does not depend neither on the nature of specific molecule-metal interactions at the surface, nor on their adsorption properties and is characterized by distances considerably exceeding the atomic size. Its distance dependence is $1/r^{10}$ ^[59]. Therefore, where the EM is operative, the SERS spectra are not different from the Raman spectra of free molecules^[55,56]. The EM contributes in the order of at least 10^5 to 10^6 times to the overall SERS enhancement which makes the most important contribution.

As mentioned above, when the molecules to be studied are adsorbed on a metal surface, their Raman signals are enhanced. The strength of the

enhancement is depending on the chemical nature of the molecule, type of metal and metal structure. Noble metals, such as gold and silver, are widely used as SERS-active substrates because of their strong SPR response in the visible optical range where most of the commonly used lasers (514 nm, 532 nm, 633 nm and 785 nm) operate. For further references and discussion about Raman scattering and SERS, reference is made to the literature^[60].

In both SERS and SPR measurements one of the main aspects of the experiment is the reproducibility of the results which strongly depends on the surface preparation as well as on the experimental conditions. Representative and similar surface preparation plays a key role in the generation of reproducible results. Previous studies by *F.Liu*^[61] and *N. Waly*^[62] in our research group revealed that one of the key steps in the sensor surface preparation is the homogeneous adsorption of dielectric nanoparticles in the form of a densely packed monolayer onto the surface. The monolayer adsorption is followed by consecutive metal seed nanoparticle decoration and growth of the seeds by electroless plating of the metal, respectively. Floating self-assembly of dielectric nanoparticles to achieve high monolayer density is addressed in the following section to introduce the adsorption of dielectric nanoparticles on planar surfaces.

2.3 Floating Self-Assembly

A crucial step in the fabrication of homogeneous biosensor surfaces is the formation of high-densely packed dielectric nanoparticle monolayers on solid surfaces like Si(100) wafers, glass slides, membrane surfaces or plane metal films evaporated on glass slides or Si wafers. There are several methods for nanoparticle deposition on solid surfaces^[63] described in literature such as spin-coating, floating self-assembly, solvent evaporation from the solution containing nanoparticles and electrostatic deposition. The spin coating technique was applied for dielectric nanoparticle deposition in a previous work by *F. Liu* and several deposition parameters were optimized in the scope of the doctoral thesis^[61]. However, dielectric nanoparticle adsorption by spin-coating did not show to be suitable for generation of high-densely packed monolayers on a large surface area like in the case of a standard microscopy slide (25x75mm). To coat large substrates, the floating self-assembly technique is a better and faster approach. It has been applied for the generation of reproducible biosensor surfaces based on polystyrene and silicon dioxide nanoparticles in this current work.

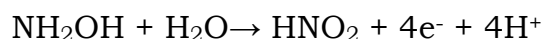
Floating self-assembly has been used in various publications^[63-68] to generate high-densely packed and ordered monolayer structures. It is commonly conducted in two steps: In the first step, nanoparticles are transferred to a liquid/air interface by using a smooth solid support which is immersed into the liquid phase so that the nanoparticles spread on liquid. If necessary, this film can be compacted by adding surfactants or by mechanical means as in the *Langmuir-Blodgett approach*. Compacting is crucial in the preparation of biosensor surfaces to achieve dense and homogeneous nanoparticle layers. In the second preparation step, the nanoparticle layer is lifted off from the air/liquid interface by using appropriate substrates(cf. Figure 31). In general, the first step determines whether a well-ordered monolayer of nanoparticles is formed. The main factors governing the process are the attractive capillary forces (due to the menisci formed around the particles) and convective transport of particles towards the ordered ones^[64]. An experiment by *Denkov et al.*^[64] which

investigated the variation electrolyte concentration, the charge of the particles and their volume fraction showed that neither the electrostatic repulsion nor the van der Waals attraction between the particles is responsible for the formation of ordered monolayer. Moreover, *Kralchevsky et al.*^[68] explained the capillary interaction between colloidal particles floating on a liquid. A detailed discussion on floating self-assembly and capillary forces acting between the particles can be found in publications by *Denkov et al.*^[64,68] and references therein.

2.4 Electroless Metal Plating

Electroless plating of metals is defined as the deposition of metallic ions from solution on a surface and their reduction without applying an electrical potential^[69]. The surface is generally exposed to a plating solution consisting of complexed metal ions and reducing agents, such as formaldehyde^[69-71], hydrazine^[69] or hydroxylamine^[70,72-74]. Since electroless plating has the ability to generate a uniform coating over a large area, it is widely used for deposition of metals such as gold, silver, nickel, etc. Moreover, electroless plating of gold and silver are frequently used to synthesize large colloidal particles because in contrast to the one-step synthesis of large nanoparticles it is capable of producing monodisperse species in high concentration^[72]. To generate large nanoparticles, seeding and electroless plating are applied consecutively for the growth of seed nanoparticles up to a predetermined particle size by adjusting and changing reaction parameters such as plating time, concentration of metal ion solution and reducing agent. Furthermore, electroless plating is also applicable to surface-confined metal nanoparticles. In the following paragraph, electroless plating of gold and silver onto surface-confined gold and silver nanoparticle seeds are discussed in more detail because they have been applied in this thesis.

In general, surface-confined gold nanoparticles are grown in a plating solution consisting of gold tetrachloride (AuCl_4^-) and hydroxylamine (NH_2OH). The seed nanoparticles are generally adsorbed to a functionalized surface via electrostatic interactions. Hydroxylamine is chosen as a reducing agent and is oxidized to nitrite with the four electron oxidation^[69].



While hydroxylamine is in principle thermodynamically capable of reducing Au^{3+} to bulk metal, the reaction is accelerated by gold nanoparticle surfaces^[72] so that bulk metal formation in the bulk is suppressed and only the particle plating grows. In electroless gold plating hydroxylamine is widely chosen over formaldehyde as a reducing agent. *Hrapovic et al.*^[69] showed that the deposition time decreases drastically if hydroxylamine was used

instead of formaldehyde. Moreover, hydroxylamine mediated electroless plating occurs at gold surfaces without new particle nucleation. Therefore, all gold ions participate in the growth of surface-confined nanoparticles as illustrated in Figure 17.

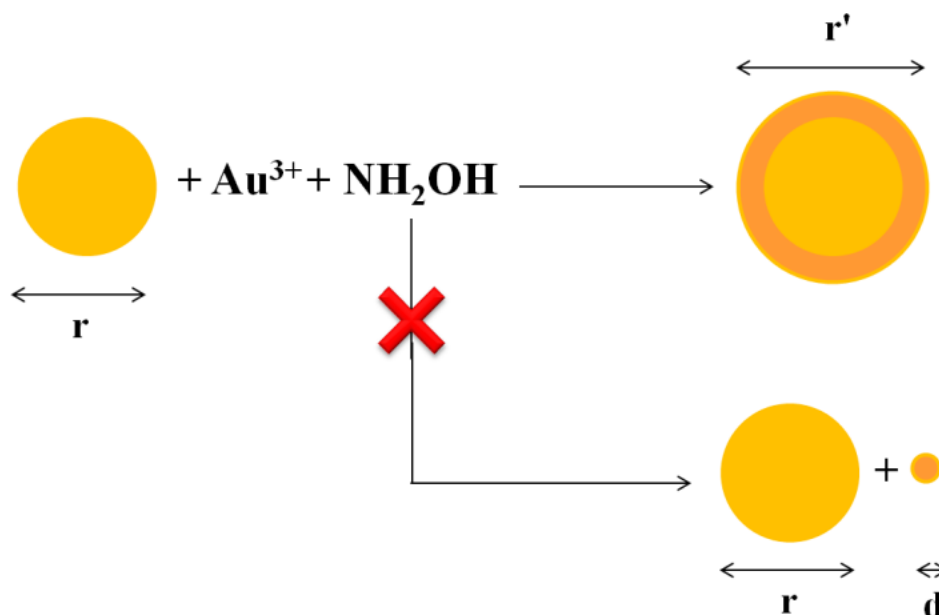
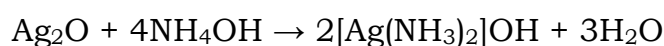
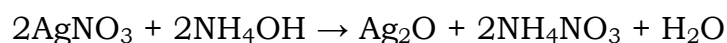


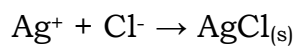
Figure 17. Electroless gold plating with hydroxylamine (redrawn according to the scheme by *Brown et al.*^[72])

In electroless silver plating, likewise electroless gold plating, silver metal nanoparticles are surface-confined to start the autocatalytic reaction acting as surface nucleation site facilitating further silver reduction and silver nanoparticle growth^[75]. Formaldehyde is used as a reducing agent and oxidized to formic acid, whereas silver ions form a complex with ammonia molecules and are then reduced to silver metal by the electrons generated in formaldehyde oxidation. The reaction is generally given as^[76]:



Ammonia molecules form a complex with silver ions and prevent silver oxide precipitation during the reaction. Unlike electroless gold plating, formaldehyde is chosen as a reducing agent over hydroxylamine which

exists in salt form as hydroxylamine hydrochloride ($\text{NH}_2\text{OH}\cdot\text{HCl}$). Due to precipitation of silver cations with chloride anions as silver chloride during the electroless plating,



growth of silver nanoparticles is prevented due to lack of silver cations in the plating solution.

2.5 High Density Peptide Arrays

For the synthesis of high density peptide arrays, our collaboration partner at the German Cancer Research Center in Heidelberg (DKFZ) developed a new method based on amino acid micro particles^[77-79]. The method outperforms similar approaches, such as the lithographic and the SPOT synthesis^[77,78,80] in terms of practicability, feature density and costs. In the following, these three peptide array synthesis techniques will be briefly introduced. For a more detailed insight reference is made to the literature^[77,78].

2.5.1 Lithographic Synthesis

In 1991 *Fodor et al.*^[81] showed for the first time that peptide arrays can be synthesized by a lithographic approach. The principle of lithographic synthesis is shown in Figure 18. Briefly, a lithographic mask determines the first pattern area to be irradiated by light. Second, a photolabile transient protecting group at the end of the oligomer chain is removed due to irradiation. Third, the array is incubated with a solution of pre-activated monomers which react only with the deprotected oligomers in the previously irradiated areas. Forth, an excess of unreacted monomers is removed by washing. Subsequently, a second pattern is defined by another lithographic mask, and a second monomer is coupled in a defined pattern^[77]. The whole procedure is repeated until the desired number of monomers has been added. This promising technique has certain practical drawbacks such as expensive photomasks, time consuming procedure to couple a single kind of monomer and the need for photolabile transient protection groups which are inefficient in terms of repetitive coupling in comparison to conventional *t*-butyloxycarbonyl (Boc) or 9-fluorenylmethoxycarbonyl (Fmoc) protection groups^[77].

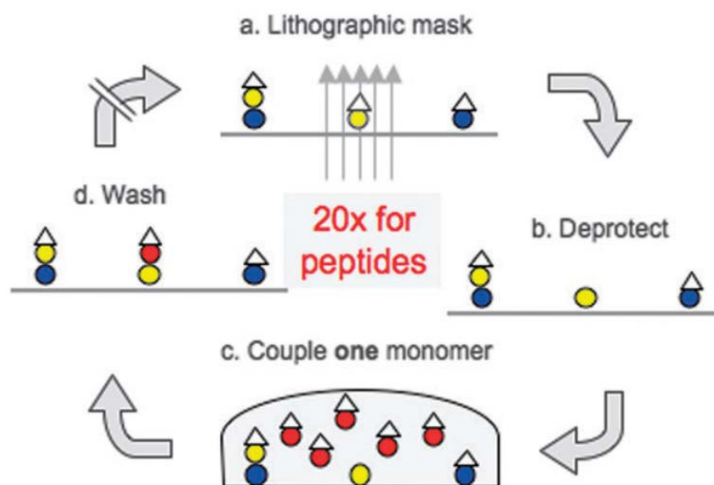


Figure 18. Lithographic peptide array synthesis. a) Lithographic mask defines the area on a 2D solid support. b) Transient protecting group is removed through irradiation. c) C-terminally activated monomers are coupled to the only deprotected structures. d) Excess monomer is washed away^[77].

2.5.2 SPOT Synthesis

Ronald Frank invented the SPOT method to combinatorially synthesize peptide arrays. Figure 19 shows the principle of the SPOT synthesis: At first, small droplets, each containing one of the 20 proteinogenic amino acids, are spotted onto a functionalized cellulose sheet in a selected pattern. Due to C-terminal pre-activation the amino acids couple to functional groups embedded in the solid support. The coupling step is followed by washing to remove the excess monomer. To complete a synthesis cycle, the N-terminal protecting group is removed to provide reactive groups for the next the synthesis cycle^[77]. The SPOT synthesis has been widely used to determine the exact binding motifs, so-called epitopes, of monoclonal or polyclonal antibodies^[82]. However, the SPOT synthesis has the drawback of only low peptide densities around 25 peptide spots per cm² which is mainly due to difficulties in handling amino acid solutions that tend to evaporate or to spread over the array^[77,83,84].

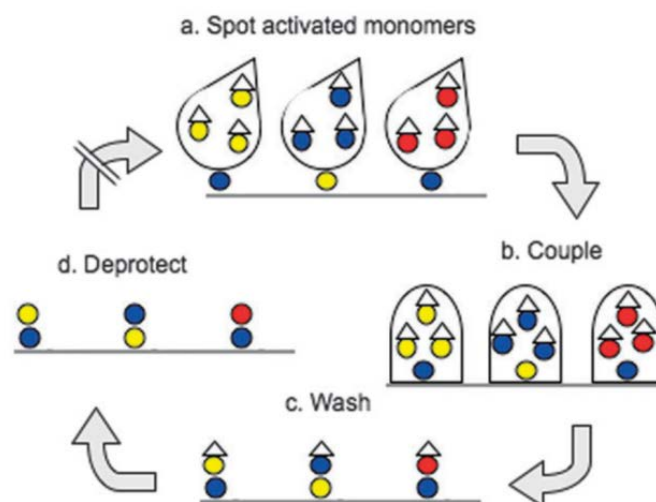


Figure 19. SPOT synthesis^[77]. a) A spotter positions the C-terminally activated amino acid derivatives to defined areas on a solid support. b) They are coupled to the support in parallel. c) Excess monomer is washed away. d) The transient protecting group is removed for the next cycle.

2.5.3 Particle-based Synthesis

High-density peptide arrays can be synthesized by means of a particle-based technique which was developed by *Beyer et al.*^[85]. According to this technique 20 different types of solid amino acid micro particles are used to address the amino acid building blocks onto a solid support in high resolution. Either a custom built laser printer^[82] or a complementary metal oxide semi-conductor (CMOS) chip equipped with an array of pixel electrodes^[85] is used to deposit the micro particles in a defined pattern. Once exactly positioned, the whole layer of amino acid particles is melted to initiate the coupling reaction as shown in Figure 20. Washing and deprotection steps as usual in solid phase peptide synthesis are applied to complete a synthesis cycle. The micro particle-based approach also uses the conventional Fmoc strategy, but compared to the SPOT synthesis the solid polymer matrix (at room temperature) which is used to immobilize the amino acids within particles allows for much higher resolutions in the addressing step without the risk of spreading or evaporation of a solvent^[77,82].

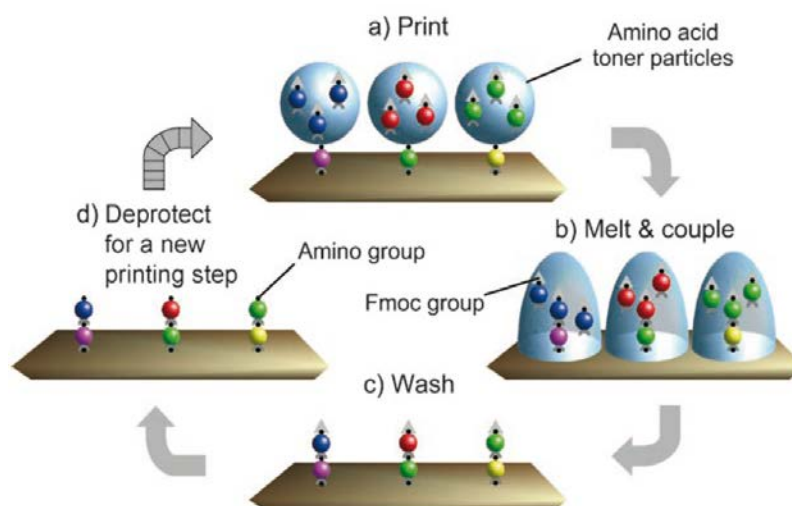


Figure 20. Positioning amino acid particles with a laser printer^[82]. a) A laser printer positions Fmoc-amino acid-OPfp esters embedded within solid toner particles onto a solid support derivatised with free amino acid groups. b) The particles are melted and coupled c) Excess monomer is washed away. d) The Fmoc protecting group is removed.

20 different Fmoc amino acid-OPfp esters (OPfp=pentafluorophenyl) are used to produce the 20 different amino acid micro particles. In general, the particles also contain other components such as the polymer resin (matrix material), pigments and charge control reagents such as Fe(III)- or Al(III) complexes. Due to the right choice of components, each sort of particles can be charged triboelectrically by friction, whereby a negative charge is generated on the surface of the particles^[82], which is required for the addressing step.



Figure 21. The peptide laser printer with 20 different cartridges^[82].

The peptide laser printer depicted schematically in Figure 21 and used for the synthesis of peptide arrays in the context of this thesis, has been developed on the basis of a color laser printer OKI C7400 (OKI systems GmbH, Düsseldorf/Germany). The current generation of the peptide laser printer is equipped with 24 printing cartridges for different particle types and achieves resolution of 700-800 peptide spots per cm^2 ^[86].

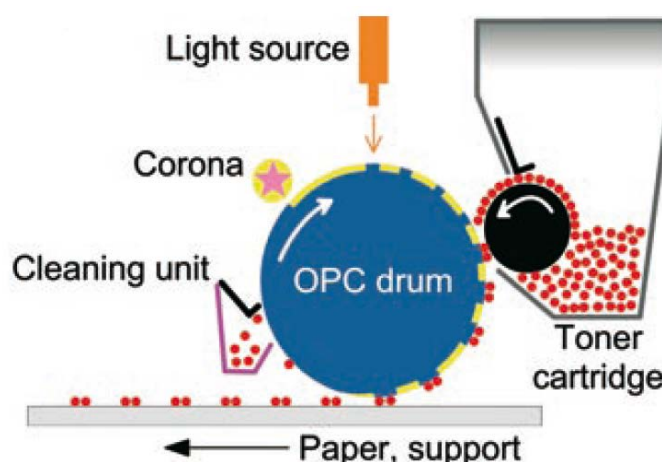


Figure 22. Schematic of a laser printer^[82]. An LED light source illuminates and neutralizes selected areas of the OPC drum, which has been evenly charged by a corona. Triboelectrically charged micro particles (bearing the same charge as the non-neutralized areas of the OPC drum) are transferred only to the neutralized areas. The such generated particle pattern is transferred from the OPC drum to a functionalized glass slide by a strong electrical field applied to the solid support.

To briefly summarize the printing mechanism as described by *Stadler et al.*^[82] as in Figure 22: A row of light-emitting-diodes (LEDs) generates a light pattern on the surface of a uniformly charged organic photoconducting (OPC) drum. Charging of the OPC drum is achieved by a corona. The drum coating is insulating in the dark and becomes conductive upon light irradiation, so that the illuminated areas on the drum are neutralized by grounding. Charged toner particles are selectively transferred to the areas neutralized by light irradiation if OPC drum and particles bear the same charge. Hence, the electrostatic pattern is transformed into the corresponding particle pattern. In the last step, the particle pattern is

printed onto a solid support by means of a strong electric field which is applied to the functional solid support the OPC drum runs over.

3 BIOSENSOR SURFACE ANALYSIS METHODS

3.1 UV-Vis Spectroscopy

Surface plasmons propagating at the interface between a metal and a dielectric can be excited at wavelengths of the light in the UV and visible regime of the electromagnetic spectrum. Detection and analysis of the related extinction spectra can be performed by a UV-Vis spectrometer. Likewise, in general LSPR of nanoparticles is followed by the same spectroscopic technique. The UV-Vis spectrometer used consists of three main components: light source, spectrometer and optical fibers guiding the light to and from the surface or liquid sample.

3.1.1 Light Source

To excite surface plasmons (PSP and LSP), a light source with a continuous spectrum is preferred to cover the whole wavelength regime of plasmon excitation. Moreover, the power of the light source should not change drastically over the whole spectral range. Two different radiation sources, deuterium and tungsten/halogen lamps, are used to generate UV and visible light in the light source. The deuterium lamp emits radiation in the range of 165-350 nm, whereas the tungsten/halogen lamp emits in the range of 350-2500 nm. In common light sources containing both types of the lamps the two light sources are combined in one light path to generate a continuous beam of light at both UV and visible wavelengths.

3.1.2 Spectrometer

In UV-Vis spectroscopy, spectrometers can be classified into different groups based on either the light selecting system used, such as prism- or grating spectrometers, or the number of light paths such as single beam, double beam and multichannel devices. In single beam spectrometers, light

is carried through a single path from the source to the sample and then to the detector. On the other hand, in double beam devices light is splitted into two beams by using mirrors. One of the beams is carried to the detector through the reference cell and the other through the sample cell. Multichannel spectrometers are based on array detectors (photodiode array or CCD). In multichannel devices the dispersive system is a grating spectrograph positioned after the sample or reference cell as shown in Figure 23. The array detector is placed in the focal plane of the spectrograph, where the dispersed radiation strikes it^[87].

In biosensor experiments discussed in this thesis, a multichannel spectrometer based on a grating spectrograph was used to analyze biosensor surfaces in reflection mode by using a special reflection fiber, and for bulk liquid measurements in transmission mode.

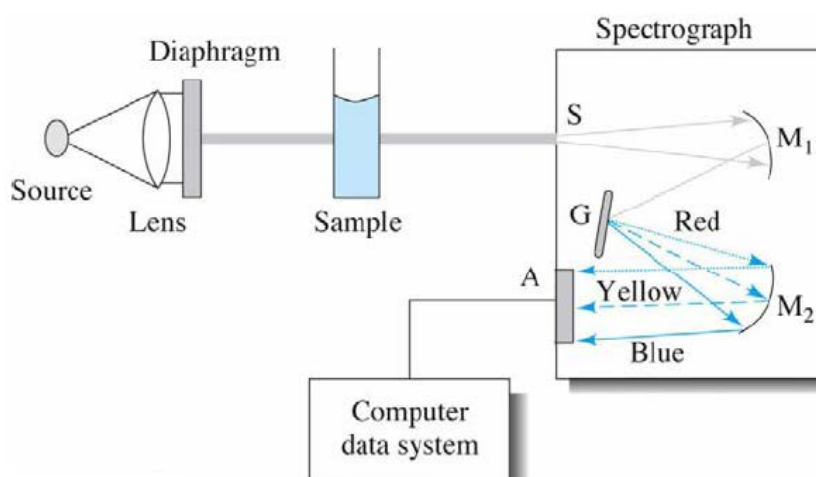


Figure 23. Diagram of a multichannel spectrometer based on a grating spectrograph with an array detector. Radiation from the tungsten or deuterium source is made parallel and reduced in size by the lens and diaphragm. Radiation transmitted by the sample enters the spectrograph through slit S. Collimating mirror M_1 , makes the beam parallel before it strikes the grating G. The grating disperses the radiation into its component wavelengths which are then focused by focusing mirror M_2 onto the photodiode or CCD array A. The output from the array detector is then processed by the computer data system^[87].

3.1.3 Optical Fiber

Optical fibers are used to transmit light waves over nonlinear paths via total internal reflection as shown in Figure 24. To have total internal reflection, the transmitting fiber must be coated with a material (outer cladding material (3)) that has a refractive index which is somewhat smaller than the refractive index of the fiber inner core material (2). By the right choice of materials optical fibers can be designed to transmit UV, visible and NIR light.

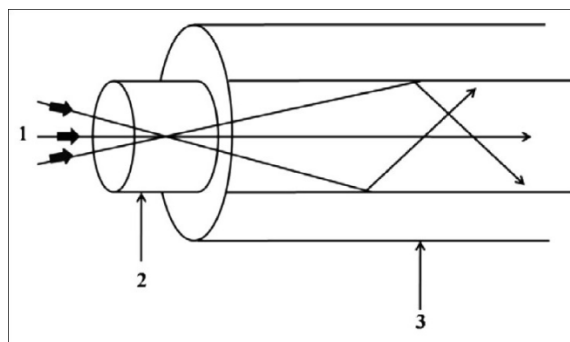


Figure 24. Optical fiber based total internal reflection. Light transmission (1) in an optical fiber occurs by total internal reflection for which the transmitting fiber is coated with outer cladding material (3) that has lower refractive index than the inner core material (2)^[88].

3.2 Surface Plasmon Resonance Imaging (SPRi)

3.2.1 Light Source

In SPRi experiments, either a continuous light source or a single wavelength laser diode is used to excite surface plasmons. A continuous light source is generally used in wavelength scanning SPR and SPRi experiments, whereas a laser diode is used in scanning angle SPR and SPRi experiments.

3.2.2 Monochromator

Monochromators are designed for spectral scanning and continuously vary the wavelength of radiation over a broad range. They are similar in terms of mechanical construction for UV, visible and NIR radiation. The materials of the components, slits, lenses, windows, prisms etc. are adjusted to the desired wavelength regime. Monochromators can be classified into two groups according to the dispersing element used: Czerny-Turner grating and Bunsen prism monochromators. Nowadays almost all commercially available monochromators are based on reflection gratings (cf. Figure 25), because they are cheaper to fabricate, provide better wavelength separation for the same size of dispersing element, and disperse radiation linearly along the focal plane^[87]. Angular dispersion of incoming light, consisting of two wavelengths, occurs in the reflection grating after being collimated (cf. Figure 25). The dispersed radiation is focused on the focal plane *AB* where it appears as two separated rectangular images of the entrance slit (one for λ_1 and one for λ_2). By rotating the dispersing element, one band or the other can be focused on the exit slit^[87].

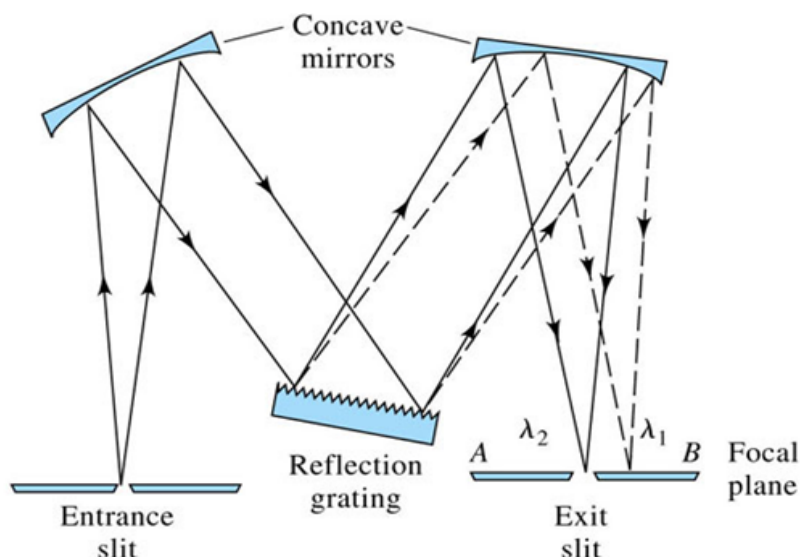


Figure 25. Configuration of the Czerny-Turner grating monochromator ($\lambda_1 > \lambda_2$)^[87].

3.2.3 Charge Coupled Device (CCD) Camera

CCDs are multi-channel silicon array detectors, which are designed using metal oxide semiconductor (MOS) architecture. CCDs detect and measure light in three steps as illustrated in Figure 26^[89]:

1. Absorption of the incident photon energy, followed by the creation of electron-hole pairs proportional to the numbers of adsorbed photons.
2. Transfer of the resulting charge packets within the array from one pixel to the next.
3. Conversion of charge to voltage and subsequent amplification.

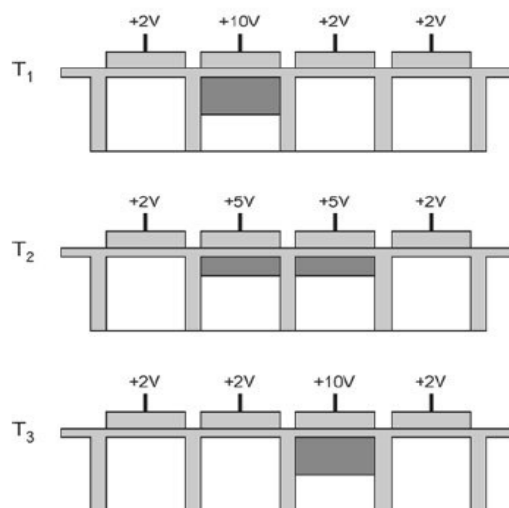


Figure 26. Illustration of the readout operation of a CCD. The charge trapped in one pixel is transferred to the next pixel by changing the voltage levels of neighboring pixels. By repeating this cycle on adjacent pixels, the charges associated with each pixel are sequentially read out into a charge amplifier, which creates a varying output voltage signal^[89].

In order to choose the most appropriate CCD for the desired application, there are three prime parameters to be decided^[89]: the wavelength range of interest, required spectral coverage and resolution, and anticipated light levels. These three parameters determine the chip format, the type of cooling and the individual pixel size.

3.3 X-Ray Photoelectron Spectroscopy (XPS)

X-Ray Photoelectron Spectroscopy is one of the most powerful methods for surface analysis by providing information about the elemental composition, chemical state, stoichiometry and electronic state of elements within the material. XPS is also known as Electron Spectroscopy for Chemical Analysis (ESCA)^[90].

3.3.1 Principles

Each atom in the surface has core electrons with characteristic binding energies that are conceptually, not strictly, equal to the ionization energy of that electron. When an X-ray beam hits to an atom, a possible interaction is that the energy of the X-ray photon is adsorbed completely by a core electron of an atom. If the photon energy, $h\nu$, is large enough, the atom is ionized. The core electron will be ejected from the atom and emitted out of the surface as shown in Figure 27. The emitted electron is referred to as the photoelectron with energy E_{kin} . The binding energy of the core electron is given by the Einstein relationship:

$$E_b = h\nu - E_{kin} - W_f \text{ (Equation 17)}$$

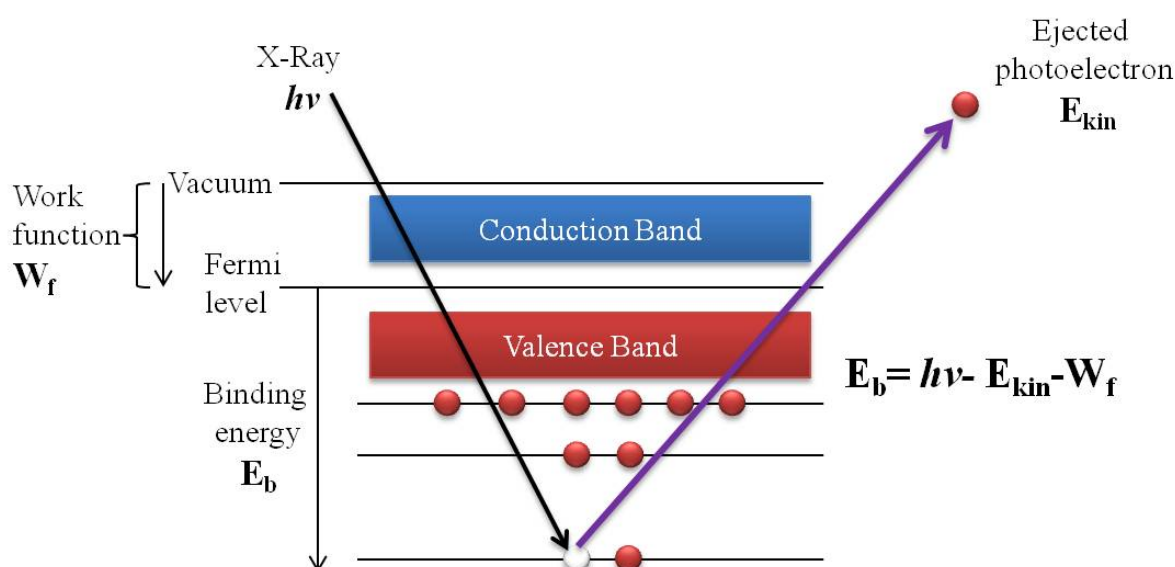


Figure 27. Basic principle of XPS

Since the work function, W_f , can be compensated artificially, the binding energies of photoelectrons are mostly tabulated by their Fermi levels rather than vacuum levels^[91], the binding energy is given as:

$$E_b = h\nu - E_{kin} \text{ (Equation 18)}$$

Characteristic information about the corresponding atoms can be extracted by analyzing the binding energy which corresponds to the kinetic energy of the photoelectrons.

In XPS **chemical shifts** are observed in electron binding energies, in general, any parameter, such as oxidation state, ligand electronegativity and coordination that affects the electron density about the atom is expected to result in a chemical shift in electron binding energy^[92]. Since the binding energies of core-electrons are affected by the valence electrons and, therefore, by the chemical environment of the atom^[92,93]. The attraction of the nuclei for a core-electron is decreased by the presence of the outer electrons. If one of the electrons is removed, the shielding decreases and the effective nuclear charge on the core-electrons increases, which increases the binding energy^[91-93]. Figure 28 shows an example of the C1s signal of fibrinogen adsorbed onto a core-shell nanoparticle surface with Au coating and silica core. With respect to the C-C signal which was normalized to 284.6 eV, the C=O signal is shifted to the highest binding energy (287.8 eV), followed the by C-O signal (285.9 eV).

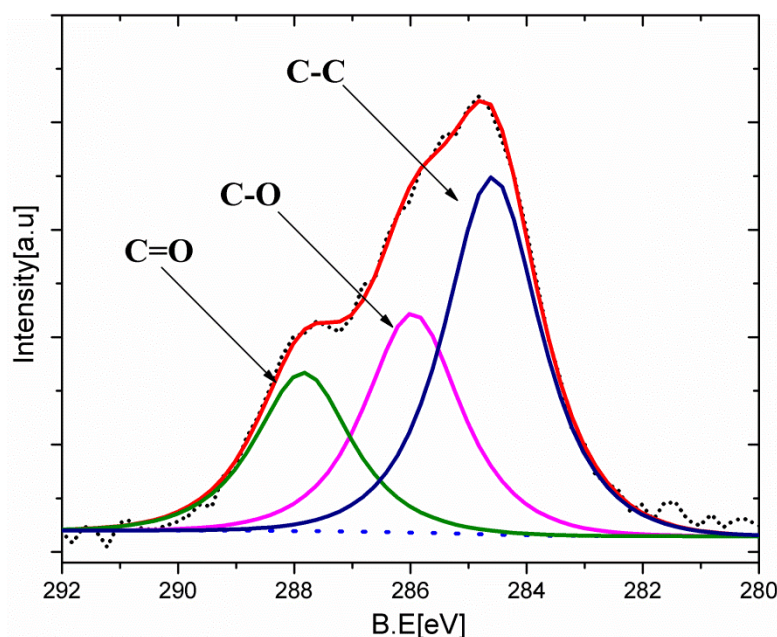


Figure 28. C1s signal in the XP spectrum of fibrinogen on Au shell-silica core surface showing the chemical shifts for C=O (287.9 eV) and C-O (285.9 eV) with respect to C-C normalized to 284.6 eV

XPS signals provide chemical and physical information only about a few outer atomic layers of the surface due to the photoelectric effect. Although X-rays can penetrate 1-20 μm into the sample, only electrons generated within a surface layer of ~ 10 nm depth will be able to leave the substrate^[94]. The exact numbers depend on the type of X-ray source used and the sample surface.

Electrons in XPS can be detected after being ejected unless they lose energy in collisions with other electrons. These electrons, inelastically scattered, appear as additional features in the XPS signals. Electrons originating from higher depth usually do not have the chance to escape unscattered and generally appear in the background at lower kinetic energy. Therefore, the most pronounced signals come from atoms near the surface of the sample and the background from the bulk of the sample^[90].

If I_0 is the flux of electrons originating at depth d , the flux emerging without being scattered, I_d , exponentially decreases with depth according to the formula:

$$I_d = I_0 e^{\frac{-d}{\lambda_e \sin \theta}} \text{ (Equation 19)}$$

where θ is the angle of electron emission with respect to the plane of the surface and $d/\sin\theta$ the distance through the solid at that angle. The quantity λ_e is called the inelastic mean free path length and is defined as the mean distance traveled by an electron between successive inelastic collisions. It determines how surface sensitive the measurement is and depends on kinetic energy of the electron and the material through which it travels 30 Å for organic materials like polymers.

3.3.2 Instrumentation

An XP spectrometer is schematically shown in Figure 29. Usually uses an Al- or Mg-coated anode as an X-ray source which is struck by electrons accelerated by high voltage (10-15 kV) is used as an X-ray source. Beside retardation radiation, characteristic Mg K α (1256.6 eV) or Al K α (1486.6 eV) lines are generated, which is selected for sample analysis. Since XPS is an ultra-high vacuum (UHV) technique, it is equipped with a UHV chamber ($p < 10^{-7}$ mbar). Moreover, XP spectrometers consist of an X-ray monochromator, a movable sample holder and a detector setup (e.g. a hemispherical analyzer as shown in Figure 29)^[90].

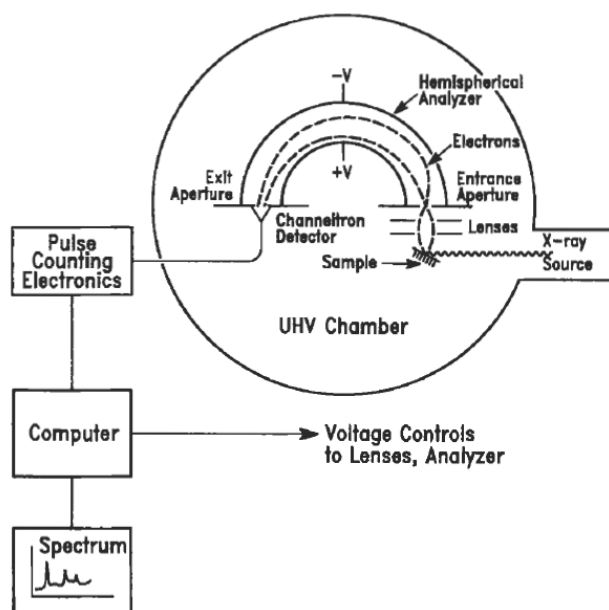


Figure 29. Schematic of a typical electron spectrometer showing all necessary components^[90].

3.4 Scanning Electron Microscopy (SEM)

A Scanning Electron Microscope (SEM) provides a highly magnified image of the surface of a material. The resolution of SEM approaches a few nm and it can operate at high magnifications ranging from about 10x - 300,000x.

3.4.1 Principle of SEM

SEM produces three types of images: secondary electron (SE) images, backscattered electron (BSE) images and elemental X-ray maps. Secondary and backscattered electrons can be separated according to their energies and are generated by different mechanisms. When a high energy primary electron interacts with an atom, the electron can undergo either inelastic scattering with atomic electrons or elastic scattering with the atomic nucleus. In an inelastic scattering process the energy transfer takes place between the atomic electrons and the scattered electrons. When the energy transfer is very small, the emitted electron will not have enough energy to exit the surface. In contrast, when the energy transfer is more than the work function of the material, the emitted electron is able leave the surface. If the energy of the emitted electron is less than 50 eV, it is called secondary electron (SE)^[90]. Most of the SEs are produced within the first few nm of the surface. Since SE electrons can suffer additional inelastic collisions, they can be trapped within the material due to energy loss.

BSEs are considered to be the electrons with energy greater than 50 eV. The energy of BSEs is comparable to the energy of the primary electrons. As the atomic number of the material increases, the chance of backscattering increases, and this increases image brightness. If the primary beam current is denoted as i_0 , the BSE current as i_{BSE} , and the SE current as i_{SE} then

$$i_0 = i_{BSE} + i_{SE} + i_{SC} \text{ (Equation 20)}$$

where i_{SC} is the sample current transmitted through the specimen to ground^[90].

3.4.2 Instrumentation

The main parts of a SEM are the electron source, the magnetic focusing lenses, the sample vacuum chamber, the stage region and the electronics console containing the control panel, electronic power supplies and the scanning modules. The schematic description of SEM operation is shown in Figure 30.

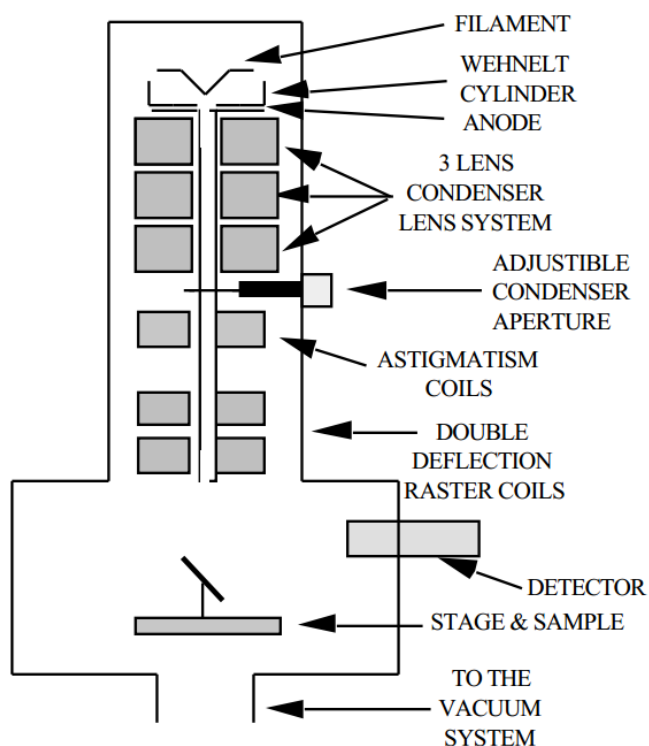


Figure 30. Diagram of SEM column and specimen chamber^[95].

There are three types of electron sources which are thermionic tungsten, LaB₆, and hot and cold field emission elements. In the first case, the electrons are emitted via thermionic emission from a tungsten filament which is heated to high temperatures such as 3000 °C to provide a sufficiently bright source. In comparison LaB₆ can be operated at lower temperatures to yield higher source brightness because its work function is lower than that of tungsten. Moreover, LaB₆ has a longer lifetime and better stability in high vacuum. In newer instruments field emission electron sources are preferred due to their enhanced resolution and low voltage applications of field emission tips^[90]. These tips are very sharp so that the

electrons from the source are extracted at even low temperatures by the strong electric field created at the tip.

To scan a sample in SEM it has to be vacuum stable. Furthermore, if the sample is an insulator it can for example be coated with a thin conducting film of carbon, gold or some other material to avoid charge build up. Electrical grounding helps to prevent this phenomenon in conducting samples which would cause distortion of the image and decrease the resolution.

4 EXPERIMENTAL

4.1 Materials

For substrate preparation clean room cleaned glass slides were purchased from Schott (Jena, Germany). Gold (99.99%), titanium (99.995%) and silicon oxide granulate (99.99%) were obtained from Kelpin (Leimen, Germany).

Amine-terminated silica nanoparticles with diameter of ~500 nm was purchased in solid form from Polysciencies Inc. (USA).

16-mercaptohexadecanoic acid (99%), *N*-hydroxysuccinimide (NHS, 97%), *N*-(3- dimethylaminopropyl)-*N*-ethylcarbodiimide hydrochloride (EDC, 98%), Triton X-100, Hydrogen tetrachloroaurate(III) trihydrate (99.9+%) trisodium citrate dihydrate (99+%), sodium borohydride (99%), hydroxylamine hydrochloride (99.9+%), polyethyleneimine(PEI, MW=25000 Da), phosphate-buffered saline (PBS, pH7.4) tablets, silver nitrate (99%), formaldehyde (37 wt. % in H₂O), sodium thioglycolate(96.5%), *O*-(2-Mercaptoethyl)-*O'*-(2-carboxyethyl)heptaethylene glycol (EG₇-SH), (95%) Disodium phosphate(≥98%), Monopotassium phosphate(≥99%), albumin from bovine serum (BSA) (98%), methylene blue (MB) (Dye content, ≥82%), ethanol (96% and 99.9%), TWEEN 20, sodium chloride (≥99 %), potassium chloride (≥99 %), hydrochloric acid(37%) were purchased from Sigma-Aldrich GmbH (Germany).

The monoclonal rabbit anti-sheep IgG, goat anti-rabbit IgG and mouse anti-human IgG antibodies were received from Dianova GmbH (Hamburg, Germany). The monoclonal mouse-anti-HA 12CA5 IgG antibody (anti-HA) was obtained from *Dr. Gerd Moldenhauer* (DKFZ, Heidelberg/Germany). Fluorescent labels were coupled by *Jürgen Kretschmer* (DKFZ, Heidelberg/Germany) using commercial labeling kits and the respective procedures which were recommended by the manufacturers. Labeling kits for the ATTO 680 dye were obtained from ATTO-TEC GmbH

(Siegen/Germany). All chemicals and solvents were used without further purification.

4.1.1 Preparation of Stock Solutions

Phosphate-buffered Solution (PBS)

PBS solution was prepared by dissolving one PBS tablet in 200 ml MilliQ water and stored in fridge. It was brought to room temperature before use.

PBS-T

0.15 M phosphate buffer saline (PBS) containing additional 0.05 % (v/v) TWEEN 20 (PBS-T) was freshly prepared before use. 8.00 g NaCl (137.0 mmol), 0.20 g KCl (2.7 mmol), 1.44 g Na₂HPO₄ · 2 H₂O (8.1 mmol), and 0.20 g KH₂PO₄ (1.5 mmol) were dissolved in water. The solution was adjusted to pH 7.4 with HCl and then filled up to 1 l. After filtration 500 µl TWEEN 20 was added under constant stirring.

PEI solution

PEI solution was prepared with a concentration of 2mg/ml in 0.5 M NaCl aqueous solution. The solution was stored at fridge and brought to room temperature before use.

4.2 Preparation of Substrates

Consecutive titanium (Ti) and gold (Au) layers of different thicknesses were deposited on different substrates such as polished glass or Si wafers by physical vapor deposition (PVD) by *Georg Albert*^[96]. The Ti layer served as an adhesion promoter between the substrate and the Au layer.

4.3 Adsorption of Dielectric Nanoparticles on Substrate

Dielectric amine terminated SiO₂ nanoparticles were deposited on the substrates which were described in the previous section in three different ways: by incubation, spin coating and self-assembly floating.

4.3.1 By Incubation

In the incubation method, the Au surface was cleaned from organic contaminations under UV radiation (generates O₃) for 2 hours prior to use. Then, the Au surface was immersed in a 1 mM ethanolic solution of 16-mercaptohexadecanoic acid overnight for self-assembled monolayer (SAM) formation of carboxylic acid terminated thiol films. Afterwards, carboxylic groups were activated by a 1:1 (v/v) mixture of 0.2 M *N*-ethyl-*N*-(3-dimethylaminopropyl)carbodiimide hydrochloride (EDC) and 0.05 M *N*-hydroxysuccinimide (NHS) for 7 minutes and the surface was rinsed with water and dried in a stream of N₂. Aqueous 10 wt% amine terminated SiO₂ nanoparticle (Bangs Laboratories Inc., USA) solution (sonicated for 30 min) was deposited on the surface for 1 h to achieve covalent bonding of the nanoparticles to the Au surface via reaction between amine groups of the nanoparticles and activated carboxyl groups of the surface. The surface was carefully rinsed with water to remove unbound nanoparticles and dried in air atmosphere.

4.3.2 By Spin-coating

Like in the incubation method, the Au surface was first cleaned by UV radiation, and functionalized with a SAM of carboxylic acid terminated thiol followed by activation of carboxyl groups using EDC/NHS. The spin coating conditions were optimized by *F. Liu*^[61]: the substrate was placed onto the spin coater (TT 200-8 spin from LP-Thermtech AG, Germany) and covered with 2 ml of 0.1 g/ml aqueous nanoparticle solution for 13 min to facilitate particle adsorption. Then, the sample was rotated with a velocity of 6000 rpm for 300 s. The unbound nanoparticles were removed from the surface during this rotation process. For more information about nanoparticle film

formation by spin coating, the reader is referred to the doctoral thesis by *F. Liu*^[61].

4.3.3 By Self-assembly Floating

The Au surface was cleaned as discussed in the previous sections. For particle adsorption using this method the Au surface can be used as it is or functionalized by a carboxyl terminated thiol for covalent bonding. Since the Au surface is negatively charged, amine terminated silica nanoparticles can also be adsorbed on the surface via electrostatic interactions which are weaker than covalent bonds. A 10 wt% solution of particles was prepared by sonication of 0.1 g in 2 ml of ethanol. 50 μ l of the prepared solution was applied to the surface of a 3 x 4 cm transfer glass slide cleaned in piranha solution (cf. Figure 31). Then, the glass slide was slowly immersed into the vessel which was filled with ~250 ml of Milli-Q water, and particles started to form non-ordered monolayers on the water surface. To consolidate the particles, the water surface tension was changed by addition of 5 μ l of 2 wt% sodiumdodecyl sulfate (SDS) solution and 5 μ l of Triton-X (1:400 in methanol). In such a way a high-densely packed monolayer of particles was obtained on large lateral scales. The particle monolayer was then lifted off by shallow immersion of the Au coated substrate as depicted in Figure 31.

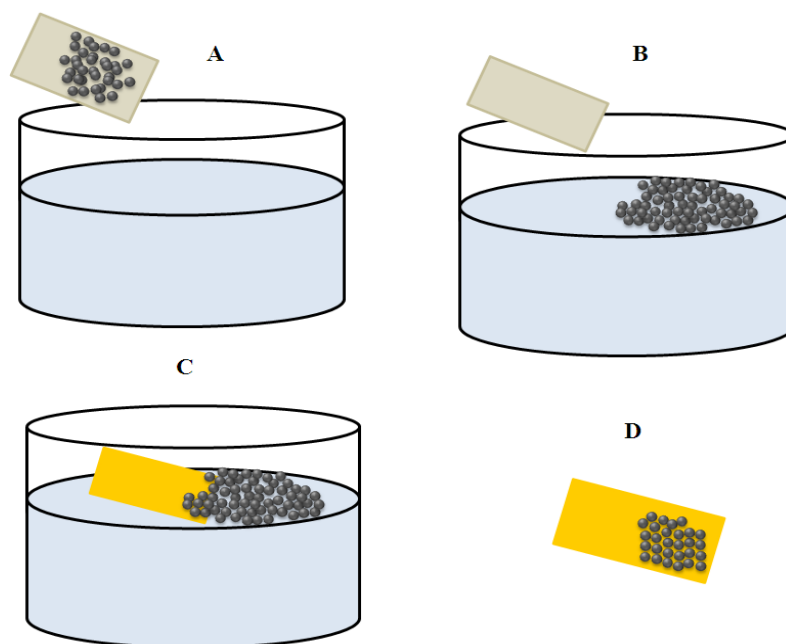


Figure 31. Self-assembly floating of nanoparticles: transfer of the nanoparticles to aqueous media by a transfer glass slide (A), formation of a monolayer of nanoparticles at the air/liquid interface (B), lifting off the monolayer with a Au substrate (C) and densely packed monolayer adsorption on the Au substrate (D)

4.4 Metal Seed Decoration of Dielectric Nanoparticles

Seed nanoparticles were prepared by reduction of the corresponding metal salt with a strong reducing agent (sodium borohydride, NaBH_4) and stabilized by citrate. The synthesized nanoparticles were stable for more than a month and used in several experiments. To coat the amine terminated silica particles with metal seed nanoparticles, the surfaces were first incubated in a 2:1 (v:v) solution of PEI/PBS for 20 min to charge the surface positively. The surfaces were rinsed with Millipore water, dried in air atmosphere and afterwards incubated in seed solutions for 12 h. Then the solution was exchanged with fresh seed solution, in which the substrate was kept for another 12 h. To remove non-bound nanoparticles, the surfaces were gently rinsed with Millipore water and dried in air atmosphere.

4.4.1 Gold Nanoparticle Preparation as Seed Solution

Gold nanoparticles with a diameter of 3-5 nm were prepared according to a well-known procedure^[97]. 6 ml of 1 wt% AuCl_4^- aqueous solution was

diluted to 600 ml (**sol I**) and stirred for 1 min. 6 ml of 1 wt% trisodium citrate dihydrate solution was added to **sol I** and stirred for 10 min vigorously. Then, 4.5 mg of NaBH_4 was added to 6 ml of 1 wt% citrate solution and sonicated for a short time to dissolve NaBH_4 . Citrate/ NaBH_4 solution was added directly to **sol I** resulting in the formation of citrate capped gold nanoparticles, and the solution was kept under vigorous stirring for 1 hour. The color of the solution changed from dark red to wine red with time. The UV-Vis spectrum of the nanoparticles shows a LSPR band around 515 nm as shown in Figure 27. The nanoparticle solution was stored in a fridge and was stable for more than a month.

4.4.2 Silver Nanoparticle Preparation as Seed Solution

Silver nanoparticles were prepared in the same way as gold nanoparticles: reduction of AgNO_3 by NaBH_4 in the presence of citrate as a stabilizer^[98]. Briefly, 1 ml of 0.01 M aqueous AgNO_3 was added to 99 ml of Millipore water containing 3×10^{-5} mol of citrate salt and stirred vigorously for 10 min. 10^{-4} mol of NaBH_4 was added to the solution resulting in a subsequent color change of the solution to yellow due to formation of citrate capped silver nanoparticles. The solution was stirred vigorously for 1 h and stable in the fridge for more than a month. The UV-Vis spectrum of nanoparticles shows LSPR band around 390 nm (cf. Figure 32) which corresponds to an obtained size of less than 10 nm^[98].

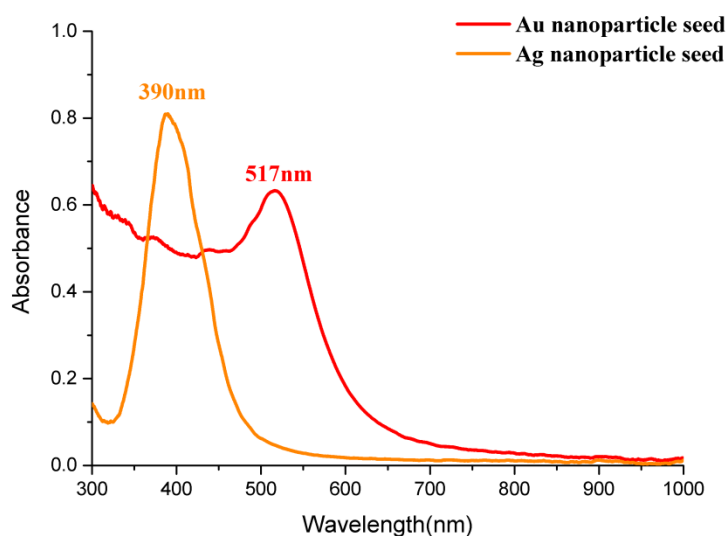


Figure 32. UV-Vis spectra of Au and Ag nanoparticle seeds in aqueous solution.

4.5 Electroless Plating of Surfaces

The growth of the metal seed nanoparticles into a contiguous metal shell was done by electroless plating of the corresponding metal as discussed in section 2.4.

4.5.1 Electroless Gold Plating

In electroless gold plating, the plating solution consists of 0.1 wt% AuCl_4^- and 0.04 M NH_2OH mixed in a ratio of 7:3. The solution was applied to the surface for different periods of time, such as 60 sec, 180 sec, 300 sec and 600 sec to grow the nanoparticle seeds up to the desired size and form a contiguous metal shell around the dielectric. Then the surfaces were rinsed with Millipore water, dried in air atmosphere and either stored in N_2 atmosphere or used immediately.

4.5.2 Electroless Silver Plating

Electroless plating of silver was applied according to the procedure by Zhang et al.^[74] with minor changes. Briefly, the surface was incubated in 5 ml of 5 mM AgNO_3 in a 5 cm diameter petri dish and 1 ml of NH_3 was added. The petri dish was shaken for 10 min on a shaker (Heidolph Promax 1020, Heidolph Instruments GmbH & Co. KG, Schwalbach/Germany). Afterwards 0.75 ml of formaldehyde was introduced into the petri dish and the surface was kept in the solution for 150 sec for growth of the seeds adsorbed on the surface. The surface was then rinsed with Millipore water.

4.6 Protein Adsorption on Biosensor Surfaces for Evaluation of their Performance in UV-Vis Experiments

In order to test the efficiency and the performance of the surfaces as biosensors, biomolecules such as fibrinogen, antibodies and their corresponding antigens were adsorbed on biosensor surfaces. For general performance tests fibrinogen was used as a model protein. To show the capability of SPR measurements to follow antibody-antigen interactions,

homogeneous films of antibodies acting as biospecific probe molecules were first coupled to the biosensor surface followed by non-specific and specific antigen coupling. For SPR imaging experiments, a spotting robot was used to deposit antibodies in an array format on the biosensor surfaces.

4.6.1 Fibrinogen Adsorption

For general sensitivity tests fibrinogen was adsorbed on the biosensor surface and the SPR wavelength shift was followed by taking the extinction spectrum of the biosensor surface before and after fibrinogen adsorption. Fibrinogen was dissolved in PBS by sonication for 30 min and adsorbed on biosensor surfaces by incubating the surface in a 1 mg/ml fibrinogen solution for 180 min in the fridge. The surface was continuously washed in a container with Millipore water to remove non-adsorbed fibrinogen effectively from the solution and dried in air atmosphere.

4.6.2 Covalent Coupling of Antibodies

Peptide bonding between the carboxyl group of the biosensor surface and amine groups of the antibody was used to couple the antibodies covalently to the biosensor surface. The biosensor surface was cleaned for 30 min by UV radiation and then incubated in a 1 mM solution of aqueous sodium thioglycolate for 90 min to functionalize the surface with carboxyl terminated thiol. The carboxyl groups were then activated by incubation with 50 mM EDC/10 mM NHS (1:1 v/v) in 100 mM KPO₄ solution at pH 6.0 for 30 min. The surface was rinsed with Millipore water and dried in air atmosphere. The dried surface was incubated overnight in a solution of 20 µl goat anti-rabbit IgG in 1 ml buffer (100 mM KPO₄/100 mM NaCl) at pH 8.2. After goat anti-rabbit IgG coupling, the surface was washed with a huge amount of water in a container to remove non-bound antibodies and then washed further with PBS buffer solution 3x10 min. In order to prevent nonspecific binding, the surface was blocked with 1 wt% BSA in PBS overnight. To check the efficiency of the blocking step, the surface was treated with 10 µl mouse anti-human IgG in 1 ml PBS overnight on a shaker, an antibody which is not able to specifically bind to goat anti-rabbit

IgG. The washing step was repeated as in the previous antibody coupling step. Specific antibody (rabbit anti-sheep IgG) was coupled to the surface by exposure to 10 µl rabbit anti-sheep IgG in 1 ml PBS solution overnight on a shaker. The washing procedure was repeated as described in the previous steps.

4.6.3 Spotting Antibody Arrays

The antibody arrays were spotted at the German Cancer Research Center (DKFZ) (Heidelberg/Germany) using the BioChip Arrayer (PerkinElmer Life Sciences, Boston/USA) with a single piezo tip. For each spot a certain amount of antibody solution was used which will be specified in each case. Antibody solutions were prepared by C. Schirwitz (DKFZ, Heidelberg/Germany) in filtered PBS-T and filled in Small Volume 384 Well Plates (Greiner Bio-One GmbH, Frickenhausen/Germany).

The array formation on the biosensor surface was checked by using a fluorescence scanner (GenePix 4000B Microarray Scanner, Molecular Devices, Sunnyvale/USA) at appropriate wavelength (633nm). Fluorescence images were analyzed with GenePix Pro image analysis software.

4.7 Peptide Array Synthesis & Layout

The peptide synthesis on was commissioned to the company *PEPperPRINT GmbH* (Heidelberg/Germany) and conducted according to established protocols with the latest laser printer generation^[78].

The layout of the array containing permutations of the HA wildtype epitope is depicted in Table 1. On a substrate in microscopy glass slide format 5 array replicas were arranged in total.

CAAYFYDVFDYAG	GDGA	CAAYFYDVFDAAG	GDGA	CAAYFYDVFPAYAG	GDGA	CAAYFYDVVADYAG	GDGA	CAAYFYDAPDYAG	GDGA	CAAYFYAVFDYAG	GDGA	CAAYFADVFDYAG	GDGA	CAAYAYDVFDYAG	GDGA	CAAAPYDVFDYAG	GDGA
GDGA	GDGA	GDGA	GDGA	GDGA	GDGA	GDGA	GDGA	GDGA	GDGA	GDGA	GDGA	GDGA	GDGA	GDGA	GDGA	GDGA	GDGA
CAAYFYDVFDYCG	GDGA	CAAYFYDVFDCAAG	GDGA	CAAYFYDVFCYAG	GDGA	CAAYFYDVFCDYAG	GDGA	CAAYFYDCCFDYAG	GDGA	CAAYFYCVFDYAG	GDGA	CAAYFCDVFDYAG	GDGA	CAAYCYDVFDYAG	GDGA	CAACFYDVFDYAG	GDGA
GDGA	GDGA	GDGA	GDGA	GDGA	GDGA	GDGA	GDGA	GDGA	GDGA	GDGA	GDGA	GDGA	GDGA	GDGA	GDGA	GDGA	GDGA
CAAYFYDVFDYDG	GDGA	CAAYFYDVFDAG	GDGA	CAAYFYDVFDYAG	GDGA	CAAYFYDVDDYAG	GDGA	CAAYFYDDFDYAG	GDGA	CAAYFYDVFDYAG	GDGA	CAAYFDVFDYAG	GDGA	CAAYDYDVFDYAG	GDGA	CAADFYDVFDYAG	GDGA
GDGA	GDGA	GDGA	GDGA	GDGA	GDGA	GDGA	GDGA	GDGA	GDGA	GDGA	GDGA	GDGA	GDGA	GDGA	GDGA	GDGA	GDGA
CAAYFYDVFDYEG	GDGA	CAAYFYDVFEAG	GDGA	CAAYFYDVFEYAG	GDGA	CAAYFYDVEDYAG	GDGA	CAAYFYDEFDYAG	GDGA	CAAYFYEVFDYAG	GDGA	CAAYFEDVFDYAG	GDGA	CAAYEYDVFDYAG	GDGA	CAAEFYDVFDYAG	GDGA
GDGA	GDGA	GDGA	GDGA	GDGA	GDGA	GDGA	GDGA	GDGA	GDGA	GDGA	GDGA	GDGA	GDGA	GDGA	GDGA	GDGA	GDGA
CAAYFYDVFDYFG	GDGA	CAAYFYDVFDAG	GDGA	CAAYFYDVFFYAG	GDGA	CAAYFYDVFDYAG	GDGA	CAAYFYDFFDYAG	GDGA	CAAYFYFVFDYAG	GDGA	CAAYFFDVFDYAG	GDGA	CAAYFYDVFDYAG	GDGA	CAAFYDVFDYAG	GDGA
GDGA	GDGA	GDGA	GDGA	GDGA	GDGA	GDGA	GDGA	GDGA	GDGA	GDGA	GDGA	GDGA	GDGA	GDGA	GDGA	GDGA	GDGA
CAAYFYDVFDYGG	GDGA	CAAYFYDVFDGAG	GDGA	CAAYFYDVFGYAG	GDGA	CAAYFYDVGDYAG	GDGA	CAAYFYDGFYAG	GDGA	CAAYFYGVFDYAG	GDGA	CAAYFGDVFDYAG	GDGA	CAAYGYDVFDYAG	GDGA	CAAGFYDVFDYAG	GDGA
GDGA	GDGA	GDGA	GDGA	GDGA	GDGA	GDGA	GDGA	GDGA	GDGA	GDGA	GDGA	GDGA	GDGA	GDGA	GDGA	GDGA	GDGA
CAAYFYDVFDYHG	GDGA	CAAYFYDVFDHAG	GDGA	CAAYFYDVPHYAG	GDGA	CAAYFYDVHDYAG	GDGA	CAAYFYDHPDYAG	GDGA	CAAYFYHVFDYAG	GDGA	CAAYFHDVFDYAG	GDGA	CAAYHYDVFDYAG	GDGA	CAAHFYDVFDYAG	GDGA
GDGA	GDGA	GDGA	GDGA	GDGA	GDGA	GDGA	GDGA	GDGA	GDGA	GDGA	GDGA	GDGA	GDGA	GDGA	GDGA	GDGA	GDGA
CAAYFYDVFDYIG	GDGA	CAAYFYDVFDIAG	GDGA	CAAYFYDVFIYAG	GDGA	CAAYFYDVFDYAG	GDGA	CAAYFYDIFDYAG	GDGA	CAAYFYVFDYAG	GDGA	CAAYFIDVFDYAG	GDGA	CAAYIVDVFDYAG	GDGA	CAAIYDVFDYAG	GDGA
GDGA	GDGA	GDGA	GDGA	GDGA	GDGA	GDGA	GDGA	GDGA	GDGA	GDGA	GDGA	GDGA	GDGA	GDGA	GDGA	GDGA	GDGA
CAAYFYDVFDYKG	GDGA	CAAYFYDVFDKAG	GDGA	CAAYFYDVFKYAG	GDGA	CAAYFYDVFDYAG	GDGA	CAAYFYDKFDYAG	GDGA	CAAYFYKVFDYAG	GDGA	CAAYFKDVFDYAG	GDGA	CAAYKYDVFDYAG	GDGA	CAAKFYDVFDYAG	GDGA
GDGA	GDGA	GDGA	GDGA	GDGA	GDGA	GDGA	GDGA	GDGA	GDGA	GDGA	GDGA	GDGA	GDGA	GDGA	GDGA	GDGA	GDGA
CAAYFYDVFDYLG	GDGA	CAAYFYDVFDLAG	GDGA	CAAYFYDVFLYAG	GDGA	CAAYFYDVLDYAG	GDGA	CAAYFYDLFDYAG	GDGA	CAAYFYLVFDYAG	GDGA	CAAYFLDVFDYAG	GDGA	CAAYLYDVFDYAG	GDGA	CAALFYDVFDYAG	GDGA
GDGA	GDGA	GDGA	GDGA	GDGA	GDGA	GDGA	GDGA	GDGA	GDGA	GDGA	GDGA	GDGA	GDGA	GDGA	GDGA	GDGA	GDGA
CAAYFYDVFDYMG	GDGA	CAAYFYDVFDMAG	GDGA	CAAYFYDVFMYAG	GDGA	CAAYFYDVMDYAG	GDGA	CAAYFYDMFDYAG	GDGA	CAAYFYMVFDYAG	GDGA	CAAYFMVFDYAG	GDGA	CAAYMYDVFDYAG	GDGA	CAAMFYDVFDYAG	GDGA
GDGA	GDGA	GDGA	GDGA	GDGA	GDGA	GDGA	GDGA	GDGA	GDGA	GDGA	GDGA	GDGA	GDGA	GDGA	GDGA	GDGA	GDGA
CAAYFYDVFDYNG	GDGA	CAAYFYDVFDNAG	GDGA	CAAYFYDVFNAG	GDGA	CAAYFYDVNDYAG	GDGA	CAAYFYDNFDYAG	GDGA	CAAYFYNVFDYAG	GDGA	CAAYFNDVFDYAG	GDGA	CAAYNYDVFDYAG	GDGA	CAANFYDVFDYAG	GDGA
GDGA	GDGA	GDGA	GDGA	GDGA	GDGA	GDGA	GDGA	GDGA	GDGA	GDGA	GDGA	GDGA	GDGA	GDGA	GDGA	GDGA	GDGA
CAAYFYDVFDYOG	GDGA	CAAYFYDVFDPAAG	GDGA	CAAYFYDVFPYAG	GDGA	CAAYFYDVFDYAG	GDGA	CAAYFYDPPDYAG	GDGA	CAAYFYVPFDYAG	GDGA	CAAYFPDVFDYAG	GDGA	CAAYFDVFDYAG	GDGA	CAAPFYDVFDYAG	GDGA
GDGA	GDGA	GDGA	GDGA	GDGA	GDGA	GDGA	GDGA	GDGA	GDGA	GDGA	GDGA	GDGA	GDGA	GDGA	GDGA	GDGA	GDGA
CAAYFYDVFDYQG	GDGA	CAAYFYDVFDQAG	GDGA	CAAYFYDVFCYAG	GDGA	CAAYFYDVGDYAG	GDGA	CAAYFYDCCFDYAG	GDGA	CAAYFYCVFDYAG	GDGA	CAAYFCDVFDYAG	GDGA	CAAYCYDVFDYAG	GDGA	CAACFYDVFDYAG	GDGA
GDGA	GDGA	GDGA	GDGA	GDGA	GDGA	GDGA	GDGA	GDGA	GDGA	GDGA	GDGA	GDGA	GDGA	GDGA	GDGA	GDGA	GDGA
CAAYFYDVFDYRG	GDGA	CAAYFYDVFDRAAG	GDGA	CAAYFYDVFRYAG	GDGA	CAAYFYDVFDYAG	GDGA	CAAYFYDRFDYAG	GDGA	CAAYFYRVFDYAG	GDGA	CAAYFRDVFDYAG	GDGA	CAAYRYDVFDYAG	GDGA	CAARFYDVFDYAG	GDGA
GDGA	GDGA	GDGA	GDGA	GDGA	GDGA	GDGA	GDGA	GDGA	GDGA	GDGA	GDGA	GDGA	GDGA	GDGA	GDGA	GDGA	GDGA
CAAYFYDVFDYSG	GDGA	CAAYFYDVFDSEAG	GDGA	CAAYFYDVFSYAG	GDGA	CAAYFYDVSDYAG	GDGA	CAAYFYDSPDYAG	GDGA	CAAYFYSVFDYAG	GDGA	CAAYFSVFDYAG	GDGA	CAAYSDVFDYAG	GDGA	CAASFYDVFDYAG	GDGA
GDGA	GDGA	GDGA	GDGA	GDGA	GDGA	GDGA	GDGA	GDGA	GDGA	GDGA	GDGA	GDGA	GDGA	GDGA	GDGA	GDGA	GDGA
CAAYFYDVFDYTG	GDGA	CAAYFYDVFDTAG	GDGA	CAAYFYDVFTYAG	GDGA	CAAYFYDVFDYAG	GDGA	CAAYFYDTFDYAG	GDGA	CAAYFYTVFDYAG	GDGA	CAAYFTDVFDYAG	GDGA	CAAYTYDVFDYAG	GDGA	CAATFYDVFDYAG	GDGA
GDGA	GDGA	GDGA	GDGA	GDGA	GDGA	GDGA	GDGA	GDGA	GDGA	GDGA	GDGA	GDGA	GDGA	GDGA	GDGA	GDGA	GDGA
CAAYFYDVFDYVG	GDGA	CAAYFYDVFDVAG	GDGA	CAAYFYDVFPYAG	GDGA	CAAYFYDVFDYAG	GDGA	CAAYFYDVFDYAG	GDGA	CAAYFYVVFDYAG	GDGA	CAAYFVDVFDYAG	GDGA	CAAYVYDVFDYAG	GDGA	CAAYFYDVFDYAG	GDGA
GDGA	GDGA	GDGA	GDGA	GDGA	GDGA	GDGA	GDGA	GDGA	GDGA	GDGA	GDGA	GDGA	GDGA	GDGA	GDGA	GDGA	GDGA
CAAYFYDVFDYWG	GDGA	CAAYFYDVFDWAG	GDGA	CAAYFYDVFWYAG	GDGA	CAAYFYDVWDYAG	GDGA	CAAYFYDWFDYAG	GDGA	CAAYFYVWFDYAG	GDGA	CAAYFWDVFDYAG	GDGA	CAAYWYDVFDYAG	GDGA	CAAWFYDVFDYAG	GDGA
GDGA	GDGA	GDGA	GDGA	GDGA	GDGA	GDGA	GDGA	GDGA	GDGA	GDGA	GDGA	GDGA	GDGA	GDGA	GDGA	GDGA	GDGA
CAAYFYDVFDYXG	GDGA	CAAYFYDVFDXAG	GDGA	CAAYFYDVFXAG	GDGA	CAAYFYDVFDYAG	GDGA	CAAYFYDXFDYAG	GDGA	CAAYFYXVFDYAG	GDGA	CAAYFXDVFDYAG	GDGA	CAAYXYDVFDYAG	GDGA	CAAXFYDVFDYAG	GDGA
GDGA	GDGA	GDGA	GDGA	GDGA	GDGA	GDGA	GDGA	GDGA	GDGA	GDGA	GDGA	GDGA	GDGA	GDGA	GDGA	GDGA	GDGA

Table 1. Layout of peptide transfer array. The array consist of various HA permutations, all of which are CAA-terminated. The wild type sequence is YPYDVFDYAG.

4.7.1 Peptide Array Transfer & Purification

A sensor surface was placed on top of a circular filter paper inside a petri-dish (cf. Figure 74). The filter paper was soaked with 500 μ l (700 μ l) 50 % (v/v) TFA in toluene. A droplet of the TFA solution was also placed on top of the sensor surface before the peptide array was immediately placed on the sensor surface face down. The rear side of the array was slightly weighted with a small petri dish. The setup was left to react for the desired transfer time (30 min / 2 h). After the transfer sensor and array were carefully separated. The sensor was directly placed in 50 % (v/v) TFA / toluene and rocked for another 30 min to completely cleave the side-chain protecting groups. Subsequently, the samples were washed five times for 5 min each with toluene, two times for 2 min each with EtOH, and then immediately incubated in the blocking solution.

4.7.2 Blocking with EG7-SH

After the transfer and subsequent washing steps, the sensor surfaces were incubated in a 2 mM solution of EG7-SH in EtOH over night. The surfaces were then washed five times for 2 min each with EtOH, and 2 times for 2 min each with water. Subsequently, the surfaces were directly immunostained as described in the following section.

4.7.3 Immunostaining

The sensor surfaces were incubated in PBS-T for 30 min. Meanwhile, a 1:1000 dilution of the monoclonal antibody to HA (12CA5, unconjugated, provided by Dr. Gerd Moldenhauer, NCT Heidelberg) in PBS-T was freshly prepared. After the pre-incubation in PBS-T, the surfaces were gently rocked in this solution for 60 min at room temperature and washed four times for 5 min each with PBS-T. While washing, a 1:5000 dilution of the secondary antibody (goat IgG (H+L) antibody to mouse, conjugated with DyLight680, provided by Thermo Scientific Ltd.) in PBS-T was prepared. The surfaces were gently rocked in the secondary antibody solution for another 30 min, then washed four times for 5 min each with PBS-T, two times for 2 min each

with water, and left to dry in air. Fluorescence scans were performed with the *Odyssey Infrared Imager* (LI-COR Biosciences, Lincoln, NE/USA).

4.8 UV-Vis Spectroscopy Reflection Measurements

UV-Vis measurements to evaluate the efficiency and performance of the nanoparticle-based biosensors were done by illumination of the surface under normal incidence and detection of the reflected light under the same angle with a reflection probe. The reflection probe consists of six optical fibers with a diameter of 600 μm each for illumination of the surface and another optical fiber with the same diameter for collecting the reflected light and guiding it to the spectrometer. The optical set-up consists of a light source (DH-2000-BAL, OceanOptics/USA) equipped with deuterium and halogen lamps that are combined in one light path, a HR 2000 high resolution UV-Vis grating spectrometer (OceanOptics/USA), and a sample stage movable in x-y directions. The optical set-up and the reflection probe are depicted in Figure 33A.

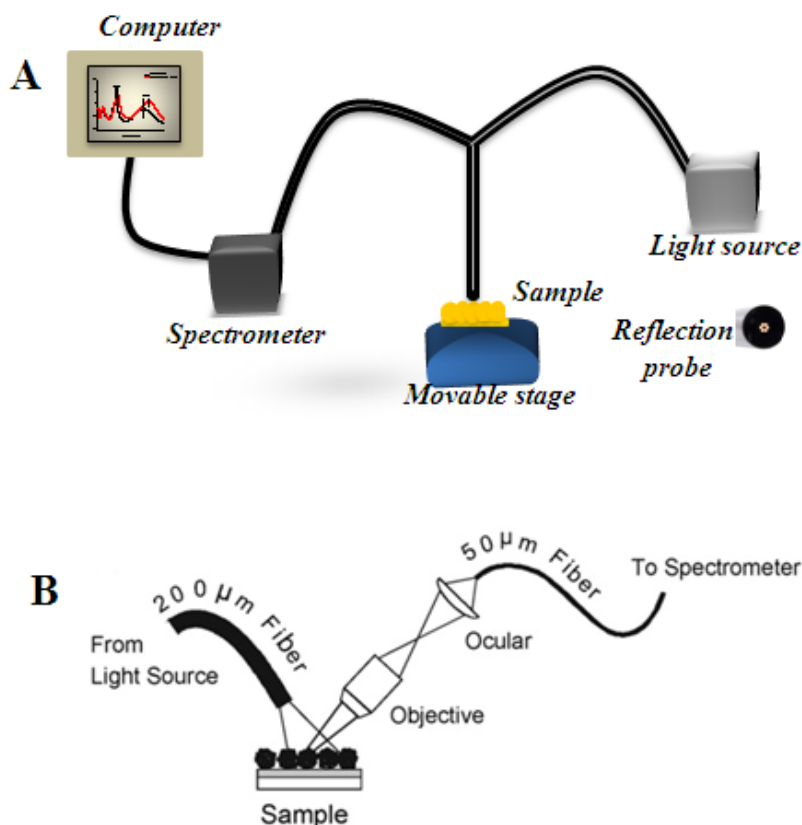


Figure 33. Sketch of the optical set-up for A)UV-Vis reflection measurements. Inset: cross-section of the reflection probe and B) LSPR imaging set-up^[8].

For UV-Vis transmission measurements, the movable stage was exchanged by a transmission stage (OceanOptics/USA) and two optical fibers for input and output. Moreover, a 1 x 1 cm Quartz SUPRASIL cuvette (Hellma GmbH & Co. KG/Germany) was used for liquid phase transmission measurements. All UV-Vis spectra were saved with either Spectra Suite(OceanOptics/USA) or OIbase32(OceanOptics/USA) software and analyzed with Origin (OriginLab/USA).

LSPR imaging experiments were carried out with a homemade set-up shown in Figure 33B which is called as scanning unit. Movements of the translation stage (sample holder) in x- and y-axis directions are controlled by two step motors (OWIS GmbH/Germany) with a minimum step size of 5 μm . The communication and operation between HR 2000 high resolution UV-Vis grating spectrometer (OceanOptics/USA) and the step motors were provided by software developed by *M. Zimmer*^[99]. The sample surface is illuminated with an optical fiber (200 μm in diameter) and the reflected light is guided to the spectrometer with 50 μm diameter optical fiber.

4.9 XPS Measurements

XPS measurements were performed with a MAX200 spectrometer (Leybold-Heraeus, Hanau/Germany) equipped with AlK_{α} (1486.6 eV) and MgK_{α} (1253.6 eV) X-ray sources, and a Specs EA200 multichanneltron detector. All measurements were done with MgK_{α} radiation using the standard parameters displayed in Table 2. All XPS spectra were subsequently normalized with a device specific transmission function because the sensitivity of the detector depends on the energy regime. All spectra measured on Au substrates were normalized to the $\text{Au4f}_{7/2}$ signal at 84.1 eV^[100]. The data were analyzed and fitted by XPSPEAK version 4.1. In quantitative analysis, Shirley background^[101] subtraction was applied. The corresponding signals were fitted and the area under the signals was calculated with XPSPEAK software.

Orbitals	Start Energy (eV)	End Energy (eV)	Step Width (eV)	Dwell time(ms)	Pass Energy (eV)	# of Scans
overview	1000	-4.8	0.4	10	96	3
Au4f	100	72	0.2	40	48	10
Ag3d	385	355	0.2	100	48	10
C1s	310	270	0.2	100	48	20
F1s	710	675	0.2	40	48	20
N1s	410	390	0.2	250	48	24
O1s	545	520	0.2	40	48	16
Si2s	175	140	0.2	100	48	16

Table 2. Standard XPS measurement parameters

4.10 Au Shell Sputter Coating

Au shell and Ti layer were sputter-coated on silica nanoparticle films using a MED 020 Modular High Vacuum System (Bal-Tec AG (Leica Microsystems), Wetzlar/Germany). The samples were placed onto the sample holders and the system was evacuated to less than 2×10^{-4} mbar. For the 5 nm Ti adhesion promoter layer, the Ar pressure was set to 1.3×10^{-2} mbar and sputter-coated for 30 s at 120 mA. Then, Au sputter coating was carried out at either 30 mA or 60 mA and 5×10^{-2} mbar Ar pressure. For different thicknesses of the Au shell sputter coating was performed according to the given durations in Table 3.

Au Shell Thickness (nm)	5	10	15	20	25	30
Current (mA)	30	30	60	60	60	60
Time (s)	20	35	10	22	30	35

Table 3. Au shell sputter coating parameters

4.11 Raman Measurements

A Bruker SENTERRA Raman spectrometer (Bruker Optics, Ettlingen/Germany) based on an Olympus BX-51 microscope (OLYMPUS Co, Tokyo/Japan) was used for the Raman measurements. A red diode laser (wavelength: 785 nm) served as the excitation source. The excitation beam as well as the Raman backscattering radiation was guided through a 20x Olympus MP1 objective (NA 0.45) to the spectrograph. The spectra were obtained with a spectral resolution of 9 cm⁻¹ in the range of 75 cm⁻¹ to 3200 cm⁻¹ at 20 mW laser power. The accumulation time was set different for different measurements with 4 co-additions (4 times accumulation time). The accumulation time is specified for each sample in section 5.5

5 RESULTS AND DISCUSSIONS

In this thesis, label-free biosensor surfaces consisting of core-shell nanoparticles are prepared in a multi-step preparation route. In the first part of this chapter, each step of the core-shell nanoparticle preparation route will be discussed: deposition of core dielectric nanoparticles on different substrates, which is followed by consecutive decoration with sub-10nm metal seed nanoparticles and electroless metal plating.

In the second part, evaluation and comparison of different biosensor surfaces are discussed in terms of optical means and the wavelength shift upon protein adsorption. Moreover, the amount of adsorbed protein on different biosensor surfaces was compared by XPS measurements. Afterwards, as an application of SPR biosensors, the specific antibody-antigen interactions were followed label-free by using different biosensor surfaces.

In the third part, SPR imaging and SPR wavelength shift experiments are introduced with the homemade CCD-based fast read-out system for visualization of protein arrays and detection of protein/peptide interactions. Different biosensor surfaces are discussed in terms of their suitability for SPR imaging and SPR wavelength shift experiments and performance.

In the fourth part, the wavelength averaging process is introduced to achieve better biosensor sensitivity by performing the measurements in longer wavelength regime rather than shorter wavelength regime.

In the last part, different core-shell nanoparticle structures are discussed as SERS substrates to enhance the Raman signals.

5.1 Preparation of Label-free Biosensors

5.1.1 Deposition of Dielectric Nanoparticles on Substrates

Dielectric silica nanoparticle films were deposited on the desired substrates by incubation, spin coating and self-assembly floating methods, respectively. The films were analyzed by SEM in order to control the nanoparticle density and homogeneity. Especially in high-resolution imaging applications, film homogeneity is expected to be a crucial prerequisite to provide good contrast between protein spots and background and to allow for high-sensitivity measurements. In this section, examples of dielectric nanoparticle films prepared by different adsorption methods are shown and discussed.

5.1.1.1 By Incubation

The incubation method to deposit dielectric polystyrene nanoparticles was studied and optimized before in our research group by *U.Konrad*^[102]. Following the established preparation procedures and adapting for silica nanoparticles, the resulting silica nanoparticle film shows incomplete surface coverage and multilayer formation in some parts of the surface as depicted in Figure 34a and Figure 34b. Moreover, while clear extinction peaks are observed when working with the 3 mm fiber bundle of the standard UV-Vis reflection set-up (cf. Figure 34c), only weak and broad resonances are obtained if the surface is analyzed with 50 μm lateral resolution utilizing the scanning unit (cf. Figure 34d). This is a clear disadvantage if biospecific interactions in high density arrays are to be detected.

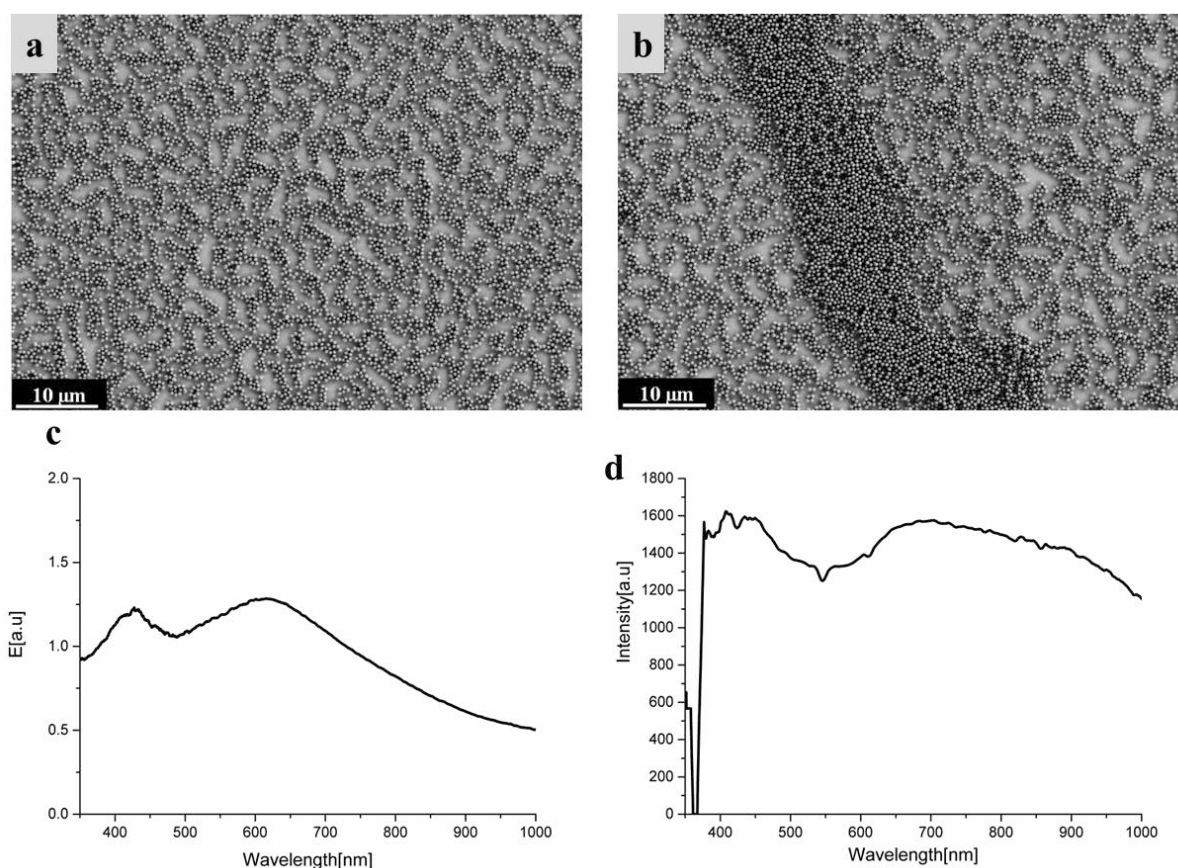


Figure 34. a) and b) are SEM images of silica nanoparticle film deposited on a flat Au film by incubation. Also shown are UV-Vis spectra of the Au shell-silica core nanoparticle film recorded with c) the standard UV-Vis reflection set-up and d) the 50 μm resolution scanning unit. The Au shell was prepared by seeding and consecutive electroless plating.

5.1.1.2 By Spin Coating

The dielectric silica nanoparticles were covalently coupled to flat Au films via peptide bond formation between the amino groups of the nanoparticles and the carboxyl group of substrate-bound alkanethiol SAMs during 13 minutes of incubation. The nanoparticles which were not coupled to the surface were removed from the surface by spin-coating. The resulting film formation is shown by the SEM images in different magnifications in Figure 35. The silica films obtained by spin-coating were not uniform in terms of particle distribution on the surface as depicted in Figure 30a. Moreover, in some areas of the surface multilayer formation was obtained as shown in Figure 35b. Even with optimized parameters, such as rotation speed, type of solvent and incubation time determined by *F. Liu*^[61] the spin-

coating method was not suitable to produce densely packed dielectric nanoparticle films. The optical response from the core-shell nanoparticles were studied in detail by *F.Liu*^[61]. Thus, no UV-Vis spectra are shown here.

In addition, dielectric nanoparticle film formation by spin-coating is an expensive and inefficient method compared to the self-assembly floating method. Using spin-coating, it is possible to prepare about 10 biosensor surfaces (25 x 75 mm microscopy glass slides coated with 100 nm Au) with 1 g of dielectric silica particles. As there are assumedly 10^{13} particles in 1 g of silica powder, and 10^{10} particles are necessary to coat a 25 x 75 mm microscopy glass slide using 500 nm silica nanoparticles in diameter ($\rho=2 \text{ g/cm}^3$) purchased from Polysciences Inc. (Eppelheim/Germany), it becomes obvious that the efficiency to adsorb silica nanoparticles is about 1% for spin-coating. This is due to the fact that most of the particles are removed from the surface during coating.

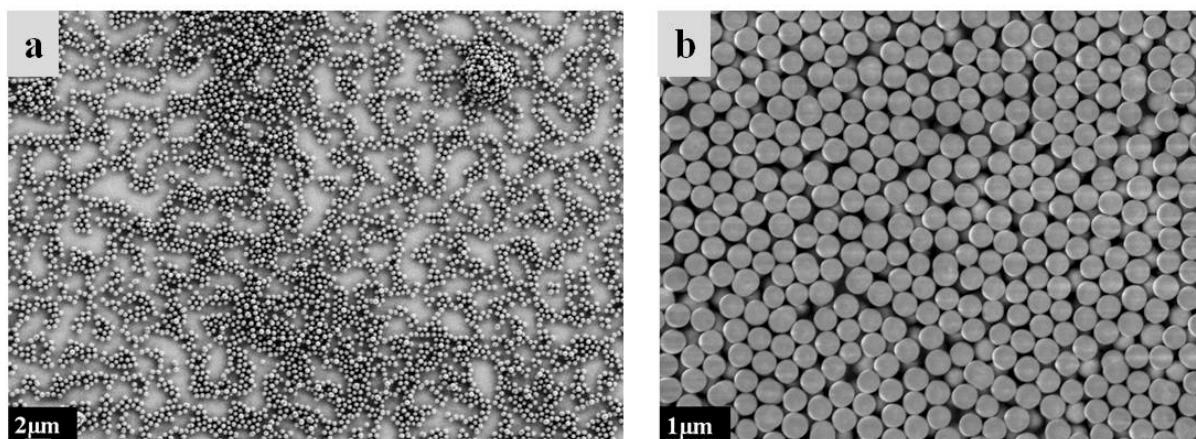


Figure 35. SEM images of dielectric silica particles on a flat Au film prepared by spin-coating.

5.1.1.3 Self-assembly Floating

An alternative method for silica nanoparticle adsorption is the floating self-assembly method which was generally applied for polystyrene and latex nanoparticles in literature^[63,64,66,67]. However, it was also successfully applied in the scope of this thesis for amine-terminated silica particles.

Amine terminated silica particles were distributed in EtOH resulting in a cloudy solution, and transferred to the air/water interface by using a 30 x 40 mm transfer glass slide. When the vessel was illuminated horizontally by a torch, it was possible to see the transfer of the nanoparticles by eye as the transfer glass slide was immersed into the water. After repeated immersion of silica nanoparticles, SDS and Triton-X solutions were added to change the surface tension of water and form a densely packed monolayer of nanoparticles at the air/water interface. Since the nanoparticles are partially positively charged due to their amine groups, they could be transferred to flat Au films, SiO₂ films, glass surfaces, carboxyl/PEI terminated solids and flexible surfaces like membranes. Figure 36a and Figure 36b represent a typical silica nanoparticle film at different magnifications deposited by self-assembly floating.

Figures 36c and 36d display corresponding extinction spectra measured with the standard UV-Vis reflection set-up and the 50 μm resolution scanning unit. In contrast to the core-shell nanoparticle films prepared by incubation (cf. Figure 34), strong and distinct extinction peaks are also obtained at high lateral resolution. This is probably due to the higher particle density resulting in stronger resonances. Thus, for the analysis of high-density arrays, nanoparticle films prepared by floating are clearly preferable.

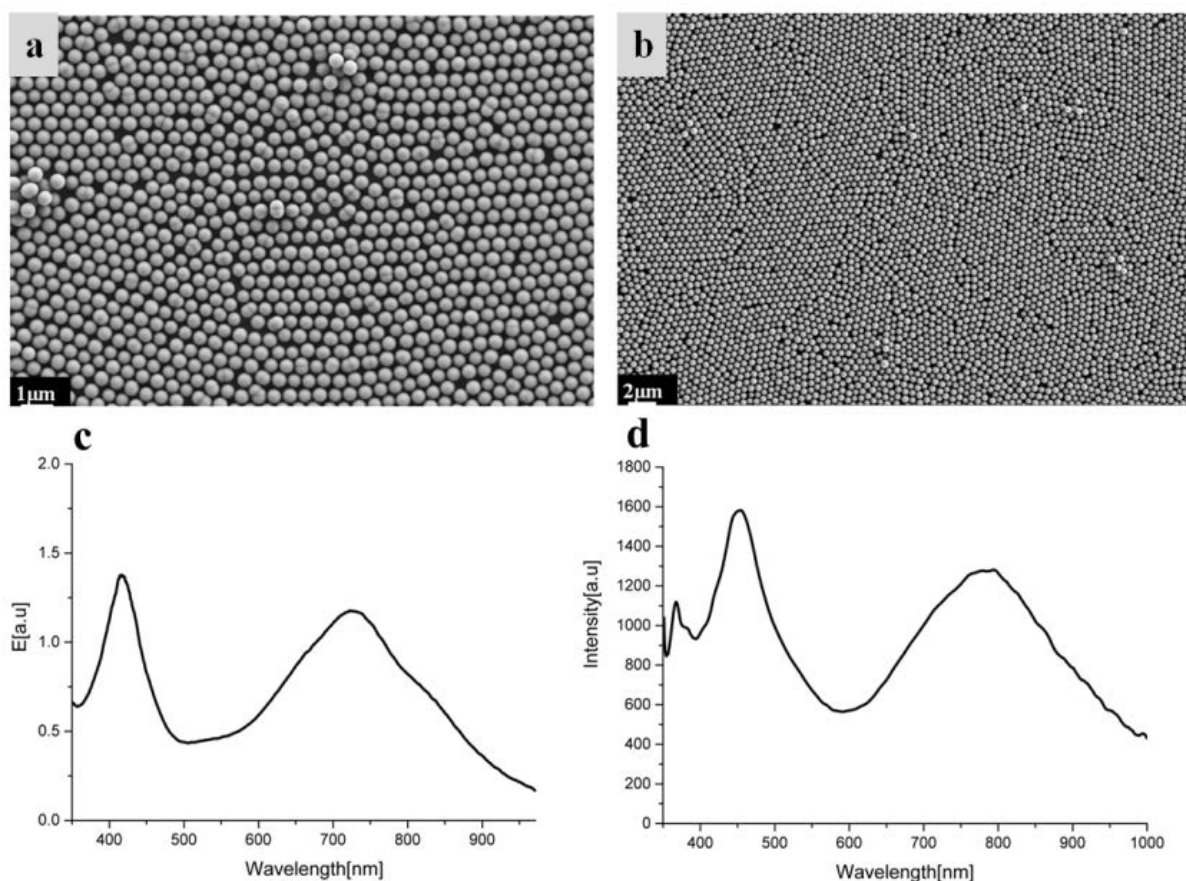


Figure 36. a) and b) are SEM images of a monolayer silica nanoparticle film on a flat Au film deposited by floating assembly. Also shown are UV-Vis spectra of the Au shell-silica core nanoparticle film recorded with c) the standard UV-Vis reflection set-up and d) the 50 μm resolution scanning unit. The Au shell was prepared by seeding and consecutive electroless plating.

Self-assembly floating results in reproducible silica nanoparticle films covering a large surface area. It is even possible coat a complete microscopy glass slide with a high-densely packed nanoparticle monolayer as depicted in Figure 37.

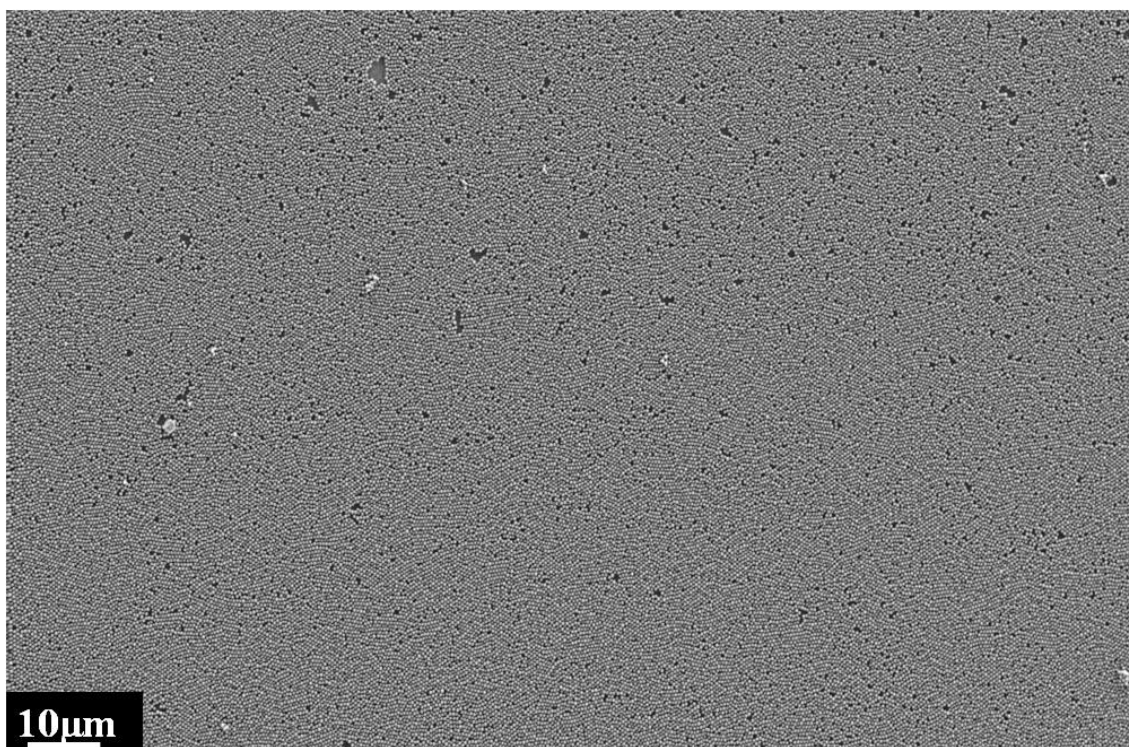


Figure 37. SEM image of monolayer silica nanoparticle film over a large surface area (estimated area 15 x 10 mm).

The experiments show that self-assembly floating is an efficient and cheaper way to deposit silica nanoparticles on surfaces. In general, 0.1 g nanoparticles were used to float at least 10 samples in the size of microscopy glass slides with high-quality nanoparticle films which makes the self-assembly floating method favorable over the other deposition techniques.

In conclusion, by using the self-assembly floating method it was shown that silica nanoparticles could be deposited as a monolayer and high-densely packed over a large surface area. It was, thus, selected as the preferred deposition method and used for the preparation of core-shell nanoparticle layers in the following if not indicated otherwise.

5.1.2 Seed Nanoparticle Decoration on Dielectric Silica Nanoparticles

Seed metal nanoparticles were synthesized according to the procedure described in section 4.4. From the appearance of LSPR peaks at 517 nm for Au nanoparticles and 390 nm for Ag nanoparticles in the UV-Vis spectra of Figure 32 which were similar to the ones reported in literature^[97,98] it can be concluded that nanoparticle preparations for Au and Ag were successful. Since the LSPR peak position of nanoparticles provides information on the size of the metal nanoparticles, further size characterization was not performed. From the respective peak positions, the size of Au and Ag nanoparticles used as seed was estimated to be below 10 nm. As depicted in Figure 38, Au and Ag nanoparticle seeds were successfully decorated on silica nanoparticles which were functionalized with the positively charged polyelectrolyte PEI.

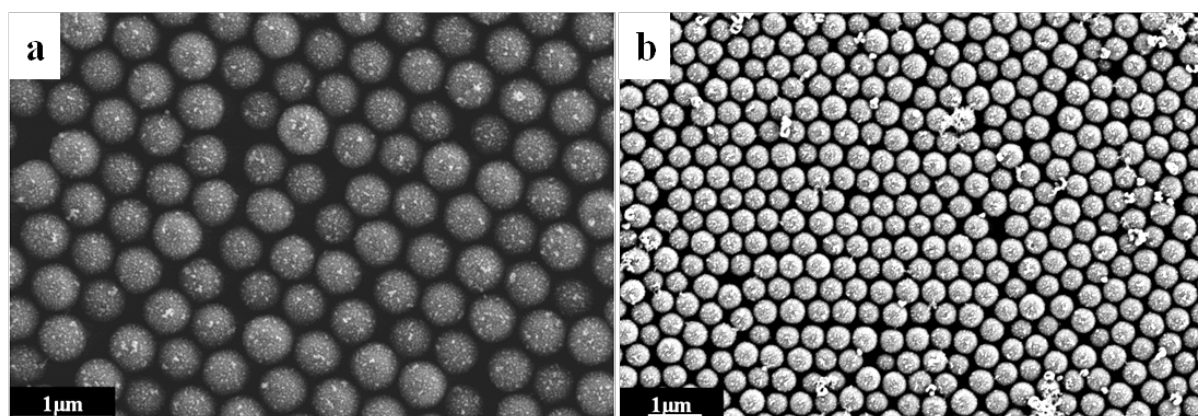


Figure 38. SEM image of silica nanoparticle film on a flat Au film decorated with a) Au nanoparticle and b) Ag nanoparticle seeds, respectively.

Since the seed nanoparticles are citrate capped, they are negatively charged^[103,104] and adsorb to the surface by electrostatic interactions between the negatively charged nanoparticles and the positively charged polyelectrolyte. Decorated metal nanoparticles were grown by electroless plating of the corresponding metal which is discussed in the next section.

5.1.3 Electroless Plating of Surfaces

Seed metal nanoparticle decorated silica nanoparticle surfaces were exposed to plating solutions of the corresponding metal as described in section 4.5. In the following section electroless plating of surfaces will be discussed in terms of the optical response of the surfaces before and after electroless plating supported by SEM images.

5.1.3.1 *Electroless Gold Plating*

Electroless plating was performed in the presence of AuCl_4^- and NH_2OH for different plating times. Surface-confined Au nanoparticle seeds were used as nucleation sites for growth of nanoparticles with the weak reducing agent NH_2OH . No individual gold nanoparticles were formed in the plating solution in agreement with literature^[70,72]. As depicted in Figure 39, surface-confined Au nanoparticle seeds were grown to bigger particles as the plating time increases.

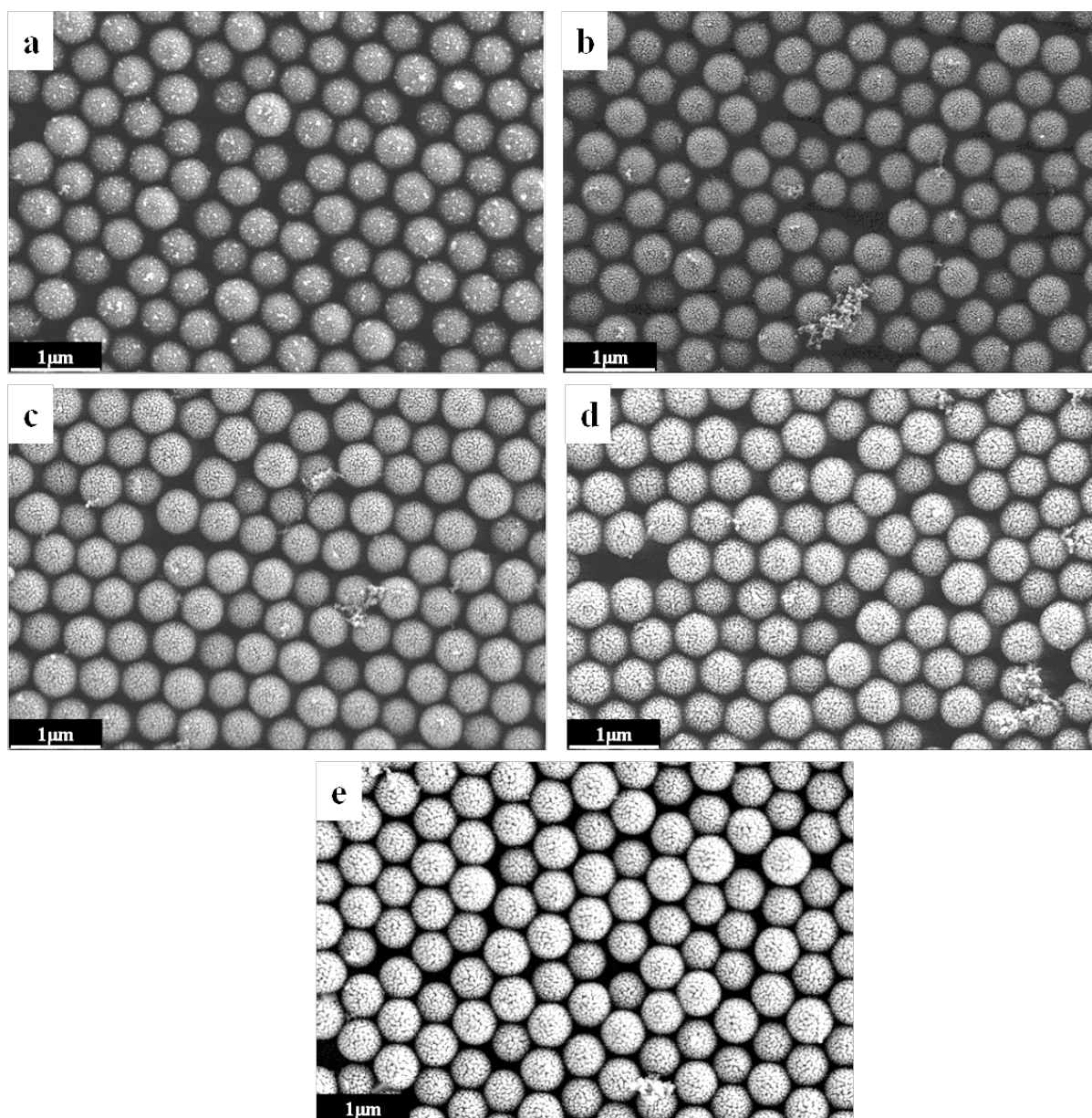


Figure 39. SEM images of silica nanoparticle films deposited on a flat Au film for different plating times: a) no plating (only seeds), b) 1 min plating, c) 3 min plating, d) 5 min plating, and e) 10 min plating.

5.1.3.2 Electroless Silver Plating

Electroless silver plating was applied to silver seed decorated surfaces in the presence of AgNO_3 , NH_3 and CH_2O according to the reactions given in section 2.4. Surface-confined Ag nanoparticles acted as nucleation sites during electroless silver plating. However, also individual Ag nanoparticle formation occurred in the plating solution as observed by a color change of the solution from colorless to dark green after addition of CH_2O to the complex of $\text{Ag}(\text{NH}_3)_2^+$. Individual Ag nanoparticle formation indicates that CH_2O as a reducing agent is strong enough to reduce the complex of $\text{Ag}(\text{NH}_3)_2^+$ in the plating solution. These nanoparticles grew further with time and aggregated to become bigger particles which could be seen by eye. However, as such big particles were not found on the surface it can be concluded that the surface confined nanoparticles were grown on the surface as intended and that possibly adsorbed bigger particles were removed from the surface in the washing step. Figure 40 shows the SEM image of a silica nanoparticle film on a flat Au layer after electroless silver plating for 150 s.

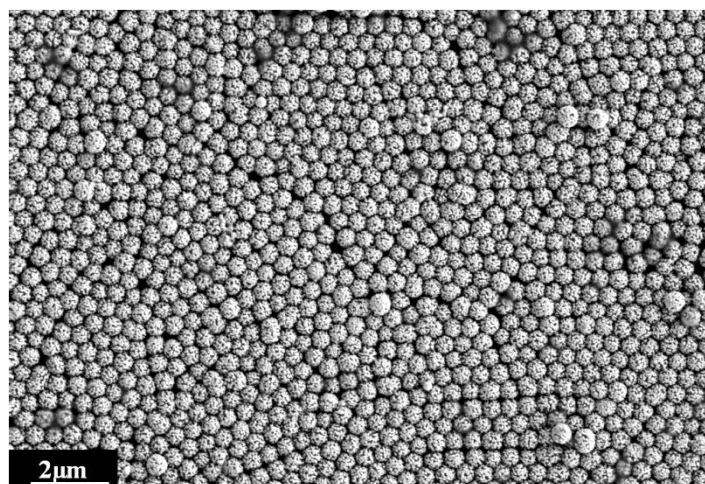


Figure 40. SEM image of silica nanoparticle film after electroless silver plating.

As it is shown in the SEM image in Figure 40, the silica nanoparticle film was coated with Ag nanoparticles successfully after seed nanoparticle decoration. The surfaces were then used in protein adsorption experiments and their performance was followed by the comparing the UV-Vis spectra before and after protein adsorption.

5.2 Optical Response of Biosensor Surfaces upon Protein Adsorption

Optical response of various biosensor surfaces was studied in order to evaluate the performance of the biosensors upon protein adsorption to the surface. Due to the change in the refractive index close to the surface upon protein adsorption, significant changes in the resonant wavelength of LSPs were obtained in the UV-Vis spectra of biosensor surfaces. This part of the thesis is divided into two parts: performance tests by fibrinogen adsorption and the detection of specific antibody-antigen interaction on the biosensor surfaces.

In the first part of the optical response experiments, fibrinogen was used as a model protein to evaluate the performance of the biosensors. Fibrinogen was chosen to compare the results of the experiments with the ones in the past by former members of our research group. Moreover, fibrinogen readily adsorbs to surfaces and is relatively cheaper and easier to work with compared to other high molecular weight proteins like IgGs.

The UV-Vis spectra of the biosensor surfaces were recorded before protein adsorption at least from 3 different coordinates of the biosensor surface with the help of the movable stage shown in Figure 33A. By using the movable stage, almost the same coordinates could be addressed to record the UV-Vis spectra of the surface after protein adsorption. The performance of the surfaces, from now on denoted as *sensitivity*, was evaluated from the difference between the resonant wavelength of the LSPs before and after protein adsorption. All sensitivity tests were carried out on at least 3 different biosensor surfaces by recording 3 different spectra (as explained above) to check the reproducibility and reliability of the measurements. The presented data refer to the whole sample sets of the corresponding experiment. In sensitivity experiments, in order to achieve the highest wavelength shift upon protein adsorption, different configurations of the substrates, different metal nanoparticle morphology, different shell thickness and different types of metal were tested.

As the wavelength shift is also related to adsorbed mass, XPS experiments were carried out to determine the relative amount of protein deposited on the various biosensor surfaces by following the N1s signal before and after protein adsorption.

In the second part of optical response measurements, specific antibody-antigen binding was followed to prove that the prepared biosensor surfaces could be used to detect specific interactions between biomolecules. Likewise, to compare the relative amount of adsorbed molecules on biosensor surfaces, XPS experiments were carried out by following the N1s signal.

5.2.1 Fibrinogen Adsorption on Biosensor Surfaces for Sensitivity Measurements

As described in experimental part, section 4.6.1, prepared biosensor surfaces were incubated in 1mg/ml (w/v) fibrinogen/PBS solution for 180 min and washed in a big container by first diluting the solution with huge amount of water in order to prevent Langmuir-Blodgett-like protein transfer at the air-water interface upon removal of the sample^[105]. In the following section, different biosensor structures are going to be introduced and their sensitivities are going to be discussed.

5.2.1.1 Optical Response from Different Biosensor Structures

In the preparation of biosensor surfaces, different substrate structures and biosensor configurations were tested in order to achieve the highest sensitivity. Figure 41 summarizes the configurations of biosensor surfaces which were tested.

In a UV-Vis spectrum of a biosensor surface consisting of core-shell nanoparticles prepared by seeding and consecutive electroless gold plating (Figure 41I), several prominent SPR peaks are observed. A discussion on the origin of the peaks is beyond the scope of this thesis and can be found in a previous dissertations by *N. Waly*^[62] and *F.Liu*^[61].

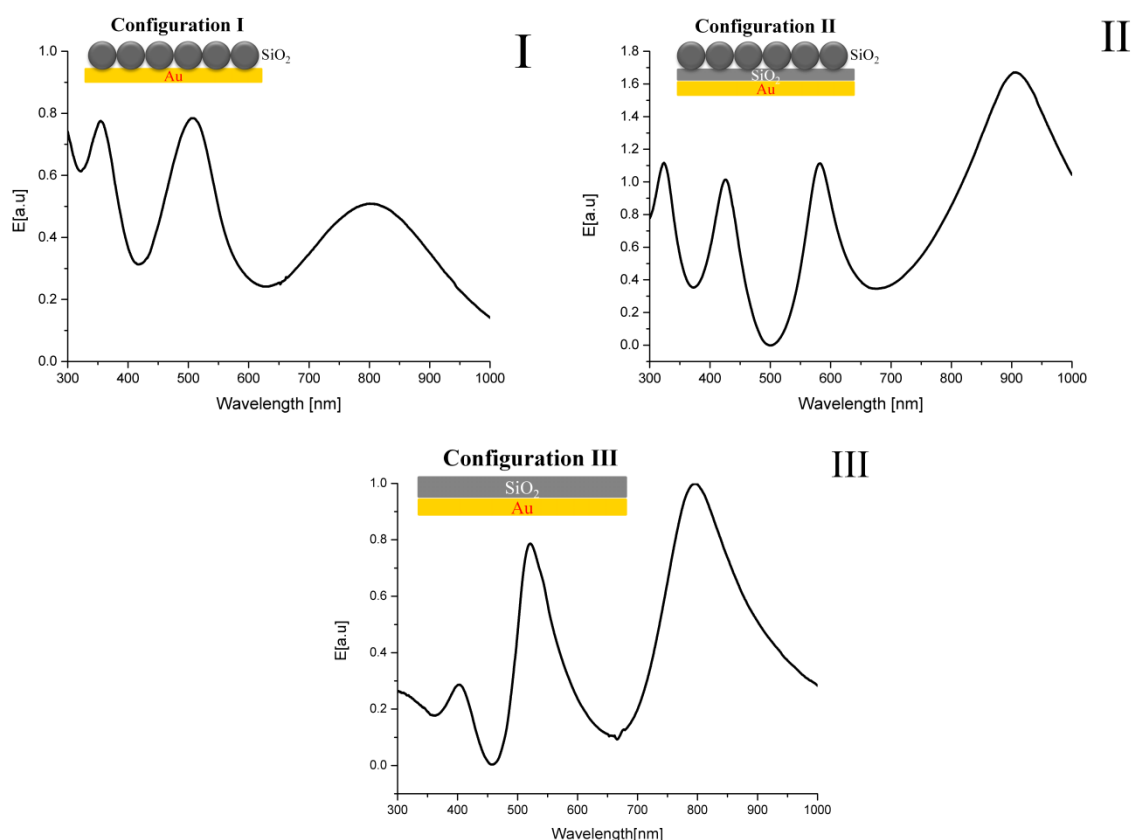


Figure 41. Schematic illustration of substrates used in biosensor configuration variation, focusing on different dielectric layers: I) SiO₂ nanoparticles, II) SiO₂ nanoparticles on a SiO₂ planar film and III) SiO₂ plane film. Corresponding UV-Vis spectra are given below.

In biosensor sensitivity experiments, the change in the resonant wavelength (i.e. the wavelength shift) of the peak between 400-600 nm was followed, due to its good reproducibility. The wavelength position of this peak is much more reproducible within the same sample and from sample to sample than the longer wavelength peak between 700-900 nm. Thus, for the latter, the wavelength shift upon protein adsorption might vary within the same sample from measurement point to measurement point. Therefore, the peak between 400-600 nm was chosen to evaluate the sensitivities of different biosensor surfaces although the peak between 700-900 nm often showed higher wavelength shifts.

The origin of the higher sensitivity of longer wavelength peak was explained by *Homola et al.*^[106] as the sensitivity of a sensor increases

monotonously with wavelength and, consequently, to achieve high sensitivity the sensor should operate at longer wavelengths. To achieve more wavelength shifts (better sensitivity) of the biosensor surfaces, a new approach was generated based on averaging the wavelength maxima of the long wavelength peaks before and upon protein adsorption to the surfaces. This approach and the initial results are discussed in section 5.4.

5.2.1.1.1 Optical Response from Configuration I

In the first configuration (cf. Figure 41I), Au nanoparticles were deposited in different sizes onto dielectric silica nanoparticle films by seeding and electroless gold plating steps consecutively. Note that from now on Au nanoparticle coated silica cores are denoted as “Au shell-silica core”. In order to change the thickness of the Au shell various plating times were applied as shown in Figure 42. The UV-Vis spectra of the corresponding biosensor surfaces are given in Figure 42.

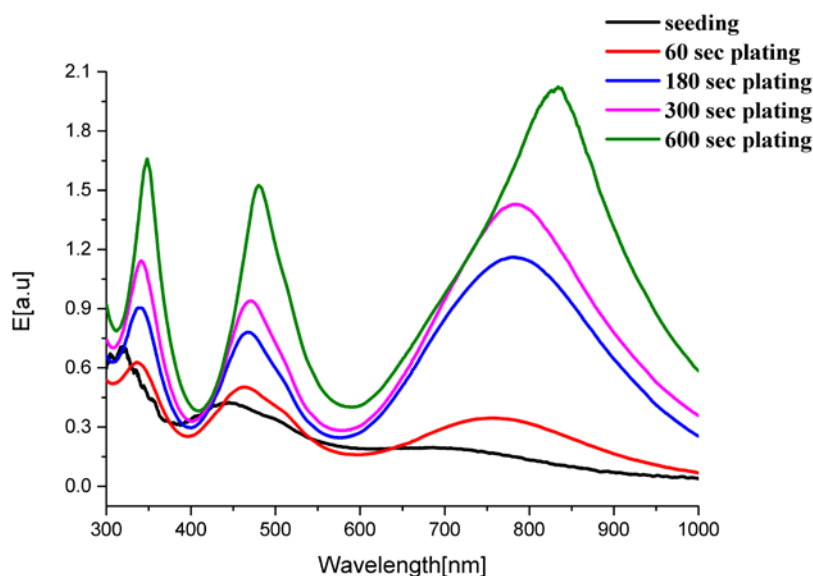


Figure 42. UV-Vis spectra of the biosensor surface (Au shell-silica core) taken after seeding and various times of electroless gold plating

As shown in the UV-Vis spectra in Figure 42, the height of the extinction peaks increases and their wavelength position red-shift as the time of electroless gold plating increases. The resonant frequency of metal nanoparticles is dependent on their size, shape, material properties and surrounding medium^[19,107]. For core-shell structures, *Preston et al.*^[108]

explained the increase in the intensity of the extinction peaks and their red-shift as an examples of a more general phenomenon: the increase of packing density of the randomly deposited Au objects on a surface. Moreover, the peaks get sharper with increasing particle size as observed in the spectra in Figure 42.

Upon fibrinogen adsorption, the extinction maxima were red-shifted as depicted in representative UV-Vis spectra of a biosensor surface before and after fibrinogen adsorption in Figure 43. Since the wavelength position of the extinction maximum is strongly dependent on the dielectric properties of the local environment including adsorbates as discussed in section 2.1.6, adsorption of fibrinogen resulted in a red shift of the extinction maximum due to changes in the refractive index close to the surface.

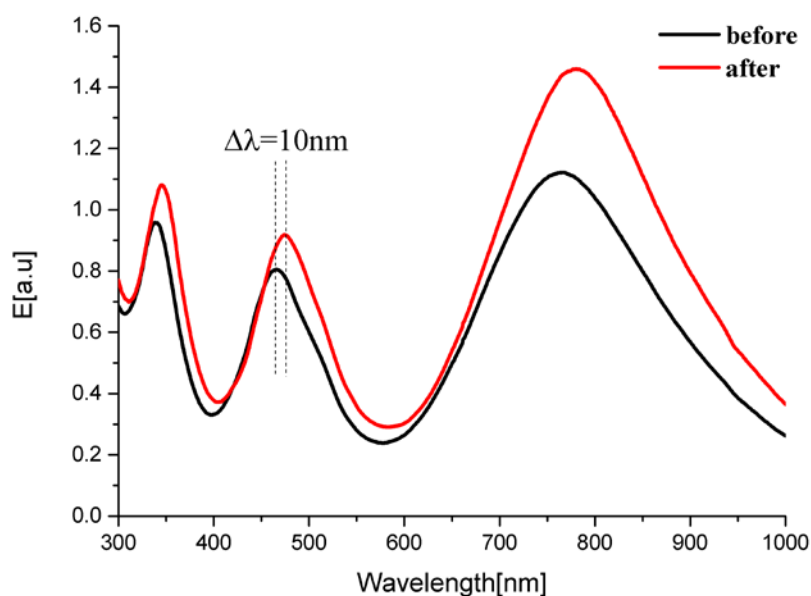


Figure 43. UV-Vis spectra of a biosensor surface (Au shell-silica nanoparticle core) before and after fibrinogen adsorption. The Au shell was prepared by seeding and 180 s electroless plating.

The sensitivity measurement on various biosensor surfaces with different Au shell thickness (regulated by changing the electroless plating time from 0 to 600 s) showed that the wavelength shift upon fibrinogen adsorption decreases as the electroless gold plating time increases (Figure 44).

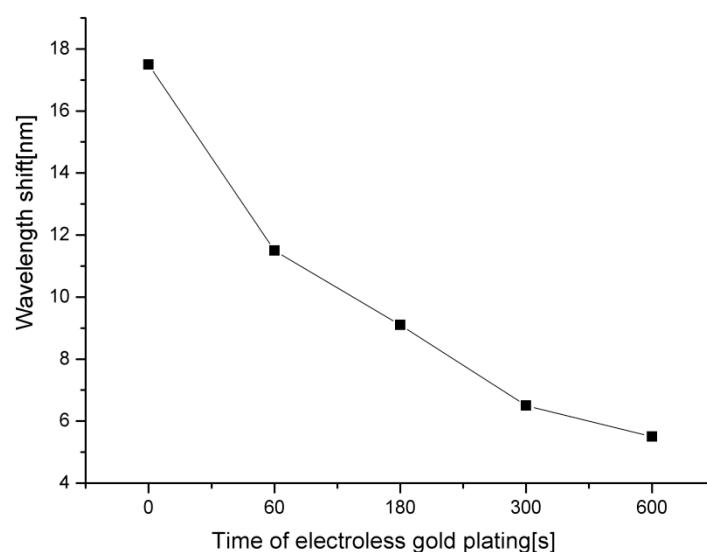


Figure 44. Wavelength shift of various biosensor surfaces upon fibrinogen adsorption for different times of electroless plating.

Jain et al.^[29] observed that the sensitivity (i.e. the change in the wavelength position) of core-shell structures in solution, composed of a dielectric core and a metallic (Au or Ag) shell, decreases near-exponentially with an increase in the shell thickness-to-core radius ratio. *Jain et al.* discussed that as this ratio increases, the field enhancement decreases resulting in a reduction of sensitivity. The same phenomenon was found in our experiments: As the electroless plating time increases, Au shell thickness increases while the size of the dielectric silica cores remains constant, resulting in an increase of the shell thickness-to-core radius ratio. Therefore, sensitivity decreases as this ratio increases.

Another important parameter that affects the sensitivity of SPR biosensors is the surface roughness. Generally, as the surface roughness decreases, the sensitivity of SPR biosensors was found to decrease for both LSP- and PSP-based biosensors^[28,109-111]. From the SEM images of the surfaces in Figure 39, it can be concluded that as the plating time increases the surface roughness decreases, and surface becomes smoother due to the growth of surface confined Au nanoparticles. Accordingly, sensitivity decreases.

In conclusion, the sensitivity of the biosensor surfaces was found to decrease as the time of electroless gold plating increases due to the change in the shell thickness-to-core radius ratio and the surface roughness.

Quantitative Comparison of Adsorbed Protein

As the wavelength shift is also related to adsorbed mass, the presence of an intense XPS N1s signal upon fibrinogen adsorption could be a reliable marker for quantitative comparison of relative fibrinogen amount on different biosensor surfaces. The N1s signal area difference, before and after fibrinogen adsorption, allowed to compare the amount of fibrinogen adsorbed onto each surface presented in Figure 45. As it is shown in Figure 45, the adsorbed amount of fibrinogen on each biosensor surface was similar. Therefore, the differences in sensitivity cannot be attributed to different mass densities of the adsorbate. More detailed information on XPS spectra of surfaces before and after protein adsorption is given in section 5.1.4.2.4.

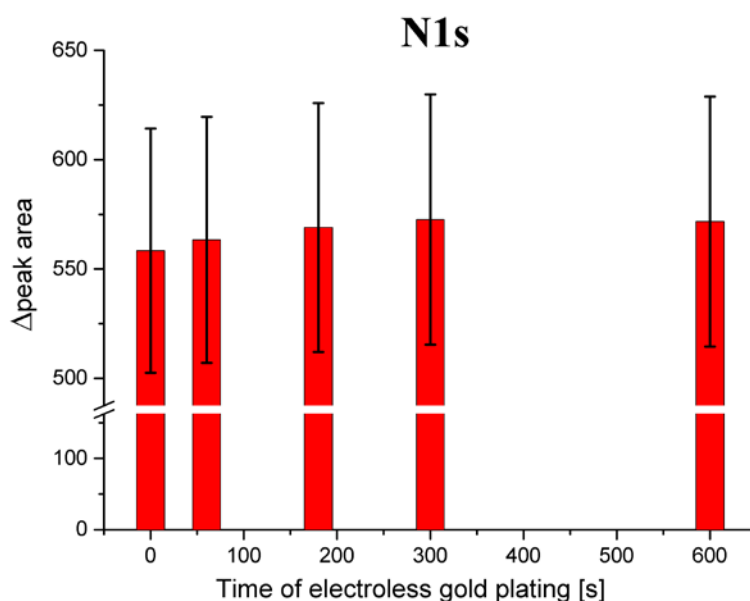


Figure 45. N1s signal area difference in XPS spectra taken before and after fibrinogen adsorption for different biosensor surfaces.

Although the biosensor surface without electroless gold plating, i.e. 0 s plating, showed better sensitivity, the biosensor surface with 180 sec electroless gold plating was used in further experiments, since the former

surface had broader and weaker LSP peaks in the UV-Vis spectrum which complicate the detection of peak position changes. Moreover, it would be advantageous in SPR imaging experiments to have stronger SPR peaks to obtain better contrast difference.

Effect of Different Thickness of Flat Au as a Substrate

In this configuration, substrates with flat Au layers of two different thicknesses, 30 nm and 100 nm, were compared to check the effect of the flat Au layer on the sensitivity of the biosensor surface. As depicted in Figure 46, the wavelength shifts upon fibrinogen adsorption were similar for both thicknesses. Thus, the thickness of the underlying Au layer is no critical parameter. Moreover, changing the substrate from glass to Si wafer did not affect the sensitivity of the biosensor surface either. Therefore, for simplicity and rigidity of the sample, glass was used a substrate for the flat Au layer unless otherwise mentioned in the text. The thickness of flat Au layer will be specified for each experiment under discussion.

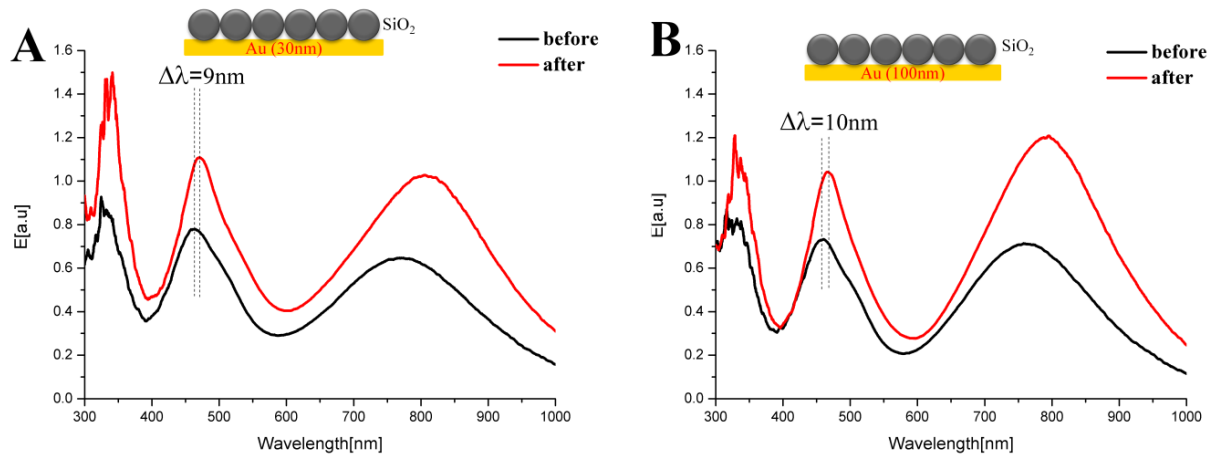


Figure 46. UV-Vis spectra of biosensor surfaces before and after fibrinogen adsorption. Au film thickness A) 30 nm, B) 100 nm.

5.2.1.1.2 Optical Response from Configuration II

In configuration II, Figure 41II, an additional dielectric silica layer (40 nm) was used in between the flat Au layer (30 nm) and the core-shell nanoparticles. The Au shell was deposited by seeding and consecutive electroless gold plating (180 sec) as usual. From a comparison of Figures 43 and 47 it is seen that addition of the dielectric layer increased the wavelength shift of the corresponding extinction maximum by about 40% from 10 nm to 14 nm. This observation is in line with previous experiments by *N. Waly*^[62], who studied the effect of dielectric interlayer thickness on biosensor sensitivity in detail and found that a 40 nm dielectric layer provided the highest sensitivity values. Therefore, no other thicknesses were tested and substrates with a 40 nm silica film deposited on a 30 nm flat Au layer were used in the experiments.

The enhancement mechanism in the sensitivity upon addition of a dielectric layer was discussed by *Lahav et al.*^[112]. They concluded that the origin of the enhancement lies in the combination of the SPR with the guided-wave SPR (GWSPR) which enables the surface plasmons to spread along the dielectric layer. When the dielectric layer (here SiO₂) has a large refractive index ($n=1.54$) it can support guided waves for smaller thickness. Hence the wave vector of surface plasmon k_{sp} increases, a fact that itself enhances the sensitivity through the increase of the penetration depth because the transverse component of the wave vector $k_z=(k_x^2-k_{sp}^2)^{1/2}$ decreases when k_{sp} increases^[112].

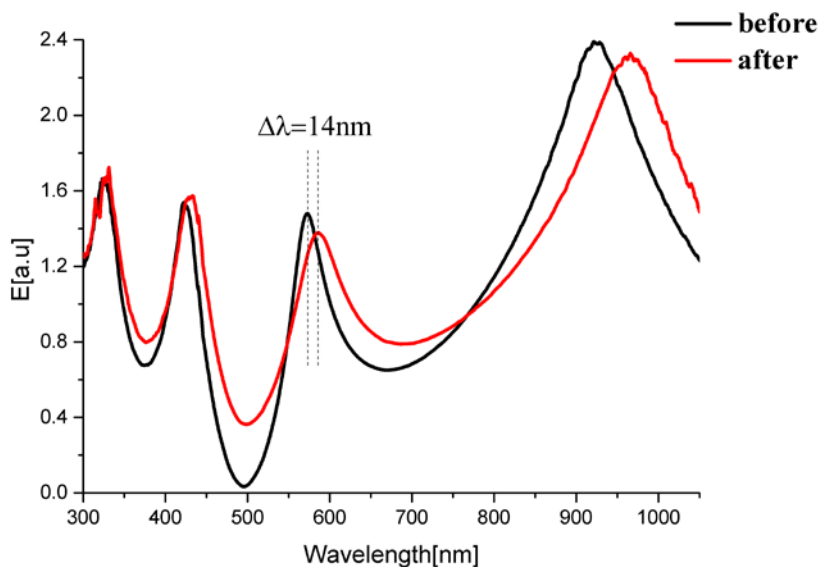


Figure 47. UV-Vis spectra of the biosensor (configuration II in Figure 41) before and after fibrinogen adsorption.

Bhatia et al.^[113] also showed that when a high refractive index dielectric silica layer was deposited on Ag and Au films the sensitivity of the SPR system increases due to the reasons explained above.

In conclusion, one way to enhance the sensitivity of the biosensor is to deposit an additional 40 nm thick dielectric layer in between core-shell particles and flat Au film. A similar positive effect of the additional dielectric layer is going to be discussed and shown in section 5.2.2.

5.2.1.1.3 Optical Response from Configuration III

In the third configuration, which was tested by *F. Liu*^[61] Au nanoparticle seeds were deposited on a PEI functionalized SiO₂ layer of 250 nm thickness and subsequent electroless gold plating was applied for 180 sec for the growth of surface-confined nanoparticle seeds covering the whole surface homogeneously. Due to the change in the refractive index close to the surface, the extinction maximum shifted to longer wavelengths as shown in Figure 48.

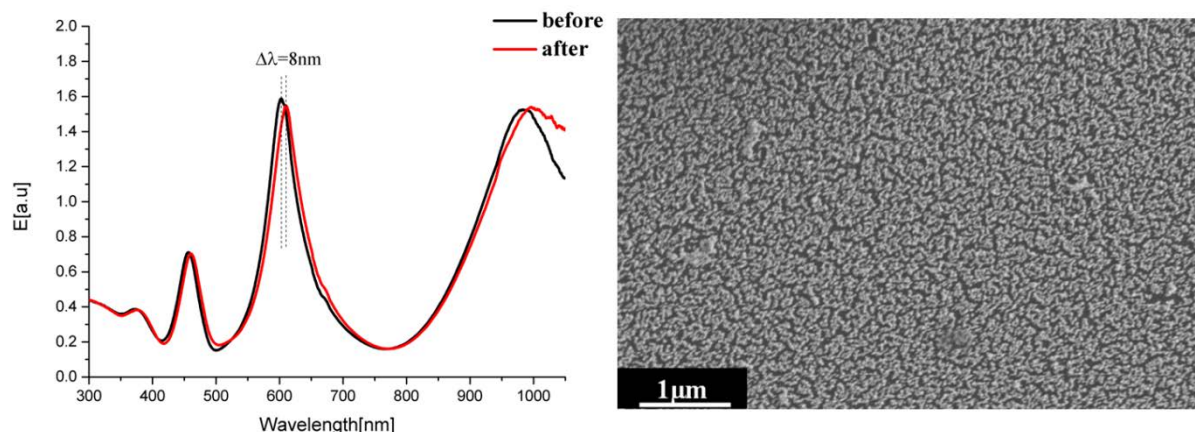


Figure 48. UV-Vis spectra of the biosensor surface (configuration III in Figure 41) before and after fibrinogen adsorption and corresponding SEM image.

In this configuration, the dielectric silica layer acted as a prism to generate and excite surface plasmons in flat Au layer. In addition, Au nanoparticles were used to increase the sensitivity of the system as discussed in section 2.1.5 and widely applied in biosensor configurations for similar purposes^[28-32,114].

Jung et al.^[114] studied a similar configuration in which Au nanoparticles were immobilized on a silica layer on a Au film in comparison with the systems comprising an unmodified Au film and a silica layer on a Au film. Using a silica layer in between Au nanoparticles and the Au film led to changes in the reflectivity of the Au film and increased the sensitivity of the system under investigation. The enhancement of the sensitivity resulted from the coupling of the surface and particle plasmons in the Au film and the Au nanoparticles by the silica layer^[114].

This configuration was proposed as an alternative biosensor structure, in addition to the previously discussed configurations, for SPR imaging and SPR wavelength shift experiments. Since this configuration has a smoother surface compared to the other configurations based on core-shell nanoparticles, this biosensor surface might provide a more homogeneous background.

In summary, three different biosensor configurations were prepared and their sensitivities were evaluated upon fibrinogen adsorption. Although, the biosensor surfaces without electroless gold plating were found to show the best sensitivity, it was not preferred for later experiments since the LSP peaks were broad and had low extinctions. Therefore, 180 s of electroless gold plating time was applied in later experiments which resulted sharper LSP peaks with high extinction. Moreover, addition of a silica layer in between core-shell nanoparticles and the flat Au layer increased the sensitivity of the biosensor. Furthermore, the flat silica layer could also be used as a replacement for the dielectric silica nanoparticle film resulting in similar sensitivity of the biosensor. Out of these three configurations, configuration II had the maximum wavelength shift upon fibrinogen adsorption.

5.2.1.1.4 Effect of Metal Shell Change

One of the ways to improve the sensitivity of the biosensor surface consisting of core-shell nanoparticles is to change the metal shell from Au to Ag. The resulting system of dielectric silica nanoparticle cores and Ag shell is denoted Ag shell-silica core in the following. Ag shell-silica core biosensor surfaces were prepared by a similar method like Au shell-silica cores: first seeding with Ag nanoparticles followed by electroless Ag plating as explained and discussed in section 5.1.2 and 5.1.3.2. Upon fibrinogen adsorption on biosensor surface, the extinction maximum was red shifted due to the change in the refractive index close to the surface as depicted in Figure 49. Compared to Au shell-silica core biosensor surfaces ($\Delta\lambda=11\text{nm}$), Ag shell-silica core biosensor surfaces ($\Delta\lambda=24\text{nm}$) yielded better sensitivity (higher wavelength shift). In order to compare these two biosensor surfaces, the experiments were carried out in parallel and under the same conditions (i.e. same substrate with a 30 nm flat Au film, same incubation time in fibrinogen solution (180 min), etc.).

Fibrinogen adsorption on biosensor surfaces could be confirmed by the wavelength shift of the surface plasmon as well as by XPS spectra of the surfaces. Mainly, there were two remarkable changes in the C1s and N1s signals upon fibrinogen adsorption. Both signals could confirm fibrinogen adsorption qualitatively and the N1s signal was used for quantitative analysis of relative fibrinogen amount on the two different biosensor surfaces.

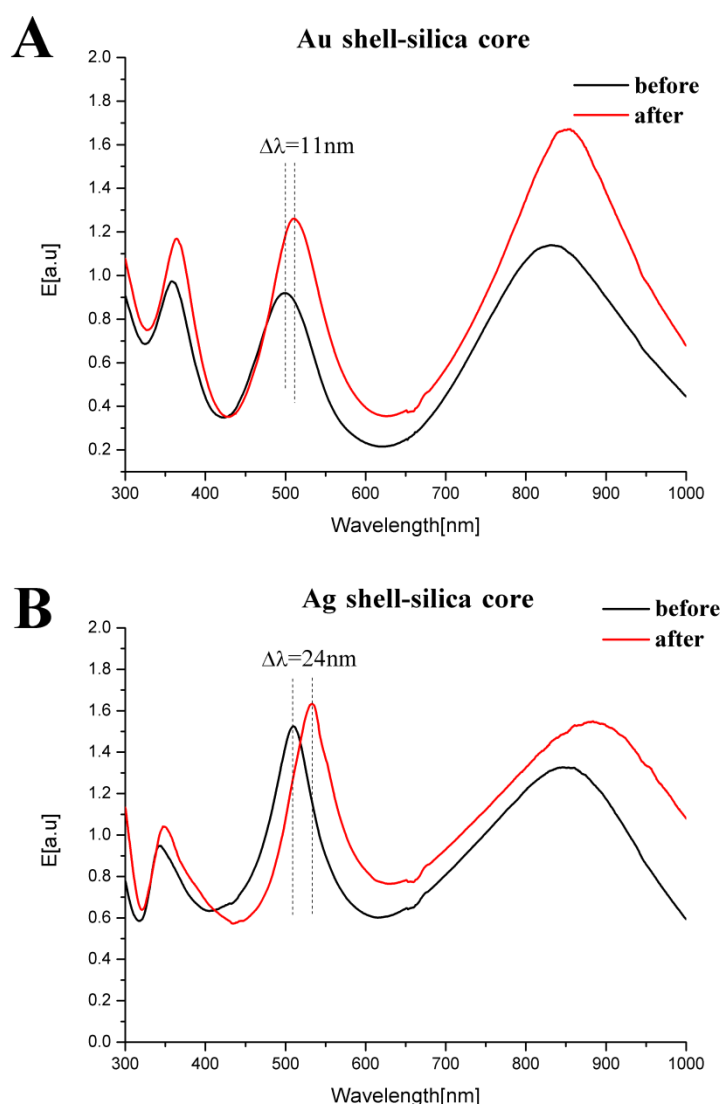


Figure 49. UV-Vis spectra of a A) Au shell-silica core, B) Ag shell-silica core nanoparticle film biosensor surface before and after fibrinogen adsorption.

Before getting into details it should be noted that the binding energies shifted to higher values due to a *surface charging* effect. Since silica nanoparticles are not able to conduct the electrons resulting from the

photoelectric process (cf. Figure 27), positive net charge accumulation on the biosensor surface is inevitable and caused 3.6 eV shift in the binding energy. This shift could be confirmed by the position of the $\text{Ag}3d_{5/2}$ signal. There are two different Ag nanoparticle environments on the biosensor surface: one of them was Ag nanoparticles on silica cores and the other Ag nanoparticles on the flat Au film. Since the latter one was grounded, there was no shift in its binding energy, so that the $\text{Ag}3d_{5/2}$ signal is observed at 368.2 eV (green curve in Figure 50). In contrast, since Ag nanoparticles on silica cores are not grounded, the corresponding $\text{Ag}3d_{5/2}$ peak was shifted to a higher binding energy of 371.8 eV (blue curve in Figure 50) due to charge accumulation. Therefore, there were two different duplets in XPS spectrum of the $\text{Ag}3d$ signal as shown in Figure 50.

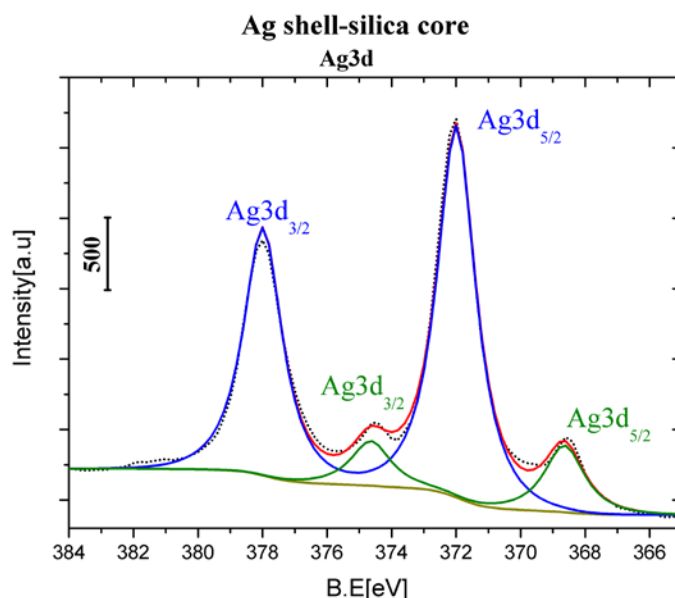


Figure 50. XPS spectrum of the $\text{Ag}3d$ signal of a Ag shell-silica core biosensor surface.

The elemental analysis indicated a significant increase of the carbon and nitrogen content due to fibrinogen adsorption. In XPS spectra of $\text{C}1s$ signals of the biosensor surfaces before fibrinogen adsorption C-C and C-H moieties (289.2 eV), -C-O (290.7 eV) and -C=O (292.8 eV) were observed. These peaks arose mainly from the polyelectrolyte, PEI, and amine terminated silica nanoparticles. After fibrinogen adsorption, these signals increased in intensity and the shoulder at 292.8 eV (-C=O) was more pronounced than before fibrinogen adsorption as depicted in Figure 51. The

increase in the intensity of the C-C, -C-O -C=O signals indicated the adsorption of fibrinogen on the surface.

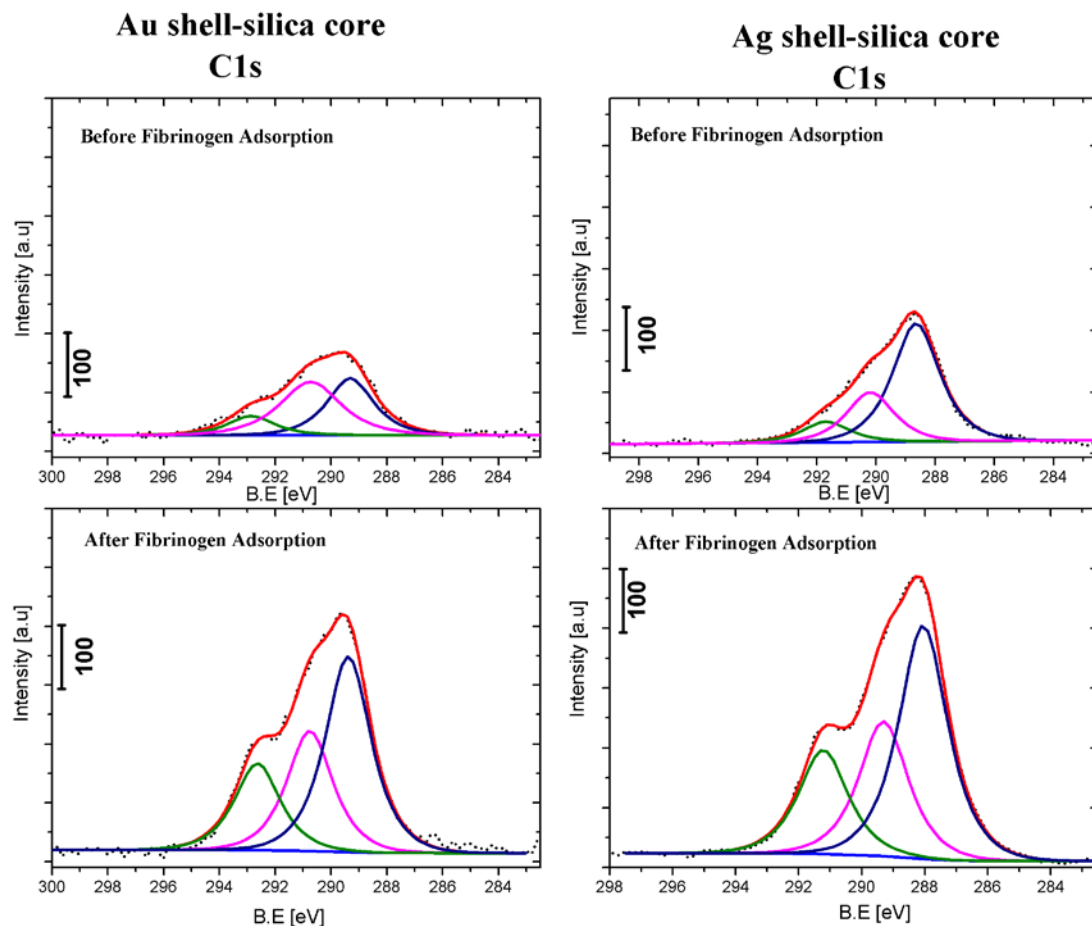


Figure 51. XPS spectra of C1s signal of Au shell-silica core and Ag shell-silica core biosensor surfaces before and after fibrinogen adsorption.

The presence of an intense XPS N1s signal upon fibrinogen adsorption can serve as a reliable marker for quantitative comparison of relative fibrinogen amount on different biosensor surfaces. The N1s signal of the biosensor surface before protein adsorption (Figure 52) had a binding energy of 403.4 eV which might be due to -NH_3^+ of PEI and protonated amine groups of amine-terminated silica nanoparticles^[115]. Upon fibrinogen adsorption the signal intensity increased due to an increase in the nitrogen content originating from fibrinogen, and the binding energy shifts to a lower energy of 402.6 eV, which could be attributed to amino groups of the fibrinogen molecule^[115,116]. For comparison of the amount of fibrinogen on Ag-shell and

Au-shell biosensor surfaces, the area under N1s signal was calculated. The comparison indicated that the amount of adsorbed fibrinogen on both of these biosensor surfaces was similar as depicted in Figure 52.

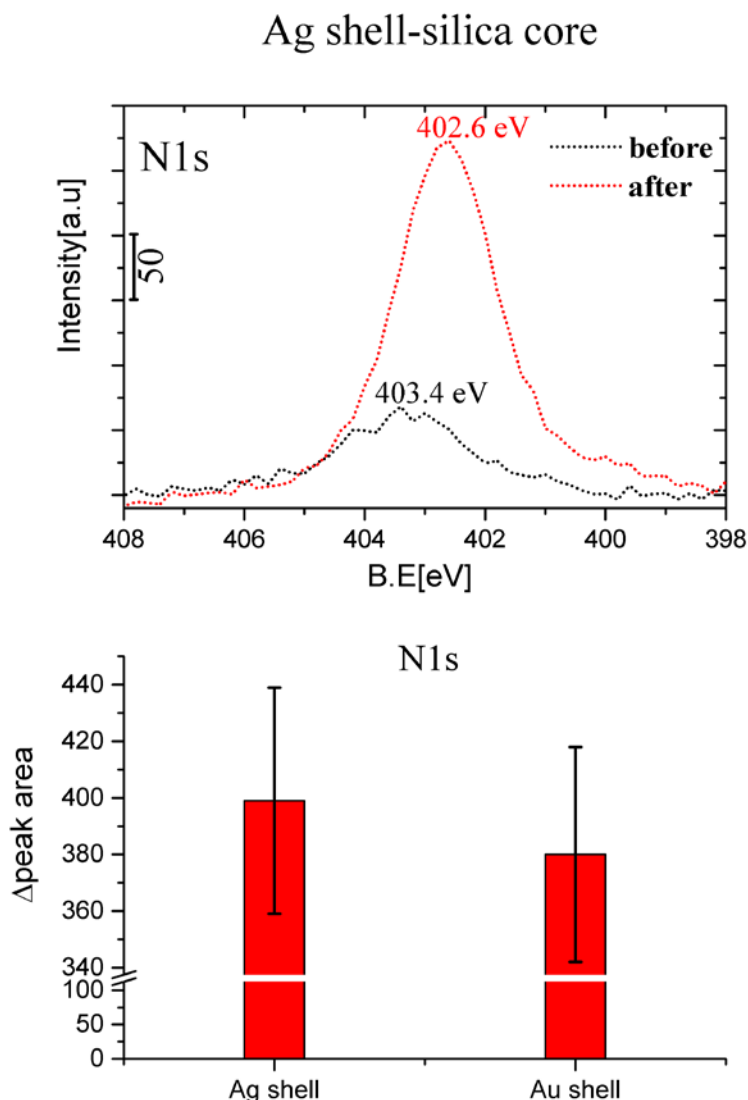


Figure 52. XPS spectra of the N1s signal of a Ag shell-silica core nanoparticle film before and after fibrinogen adsorption and comparison of the N1s signal area for Au shell- and Ag shell-silica core nanoparticle films. Shown is the difference in peak area with respect to the situation before and after fibrinogen adsorption.

In summary, the sensitivity of the biosensor surface was significantly improved when the Au shell was replaced with a Ag shell. Biosensor surfaces with Ag shell showed better optical response and a higher wavelength shift than biosensor surfaces with Au shell upon similar amount of fibrinogen adsorption. Independent XPS measurements were used to determine amount of adsorbed protein. The higher sensitivity in case of Ag

shells may be attributed to the fact that Ag has a larger real part of dielectric constant ($|\epsilon_m'|$) than Au^[106]. Therefore, the improvement in sensitivity was due to the favorable optical properties of the Ag shell.

5.2.1.2 Specific Antibody-Antigen Binding on Biosensor Surfaces

One of the applications of SPR measurements is monitoring the specific binding events between antibodies and antigens by following the wavelength shifts of the SPR peaks. Specific antibody-antigen binding experiments were carried on in parallel with both Ag shell-silica core and Au shell-silica core biosensor surfaces in order to evaluate the performance of these surfaces.

As explained in section 4.6.2, the biosensor surfaces were functionalized with carboxylic thiol before antibody coupling. For evaluation, the optical response of the biosensor surfaces was followed with UV-Vis spectroscopy for each step of binding as shown in Figure 53 and Figure 54. In the first step, goat anti-rabbit IgG was covalently coupled to the biosensor surfaces via peptide bonding between carboxylic groups of the functionalized biosensor surface and amine groups of the antibody.

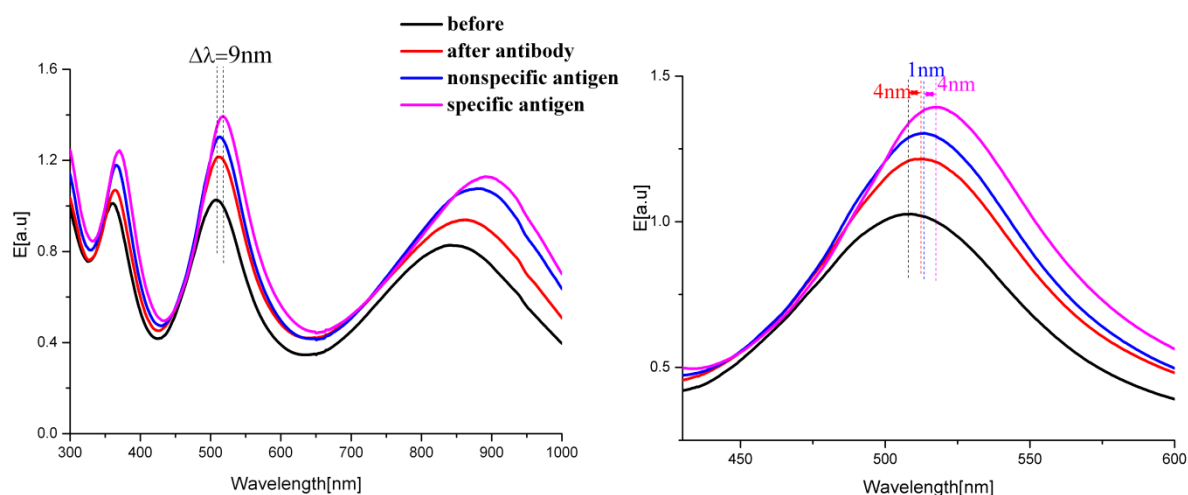


Figure 53. UV-Vis spectra of Au shell-silica core nanoparticle film before antibody binding, after antibody binding, after nonspecific antigen binding and after specific antigen binding.

As shown in Figure 53 and Figure 54, 4 nm wavelength shift for Au shell-silica core and 8 nm for Ag shell-silica core biosensor were obtained, respectively. Then the surfaces were blocked with BSA to prevent nonspecific binding, which was successful according to the wavelength shifts of only 1 nm for each surface upon nonspecific antigen (mouse anti-human IgG) incubation. When the specific antigen (rabbit anti-sheep IgG) was coupled to the antibody on the biosensor surface the corresponding wavelength shifts were 4 nm for Au shell-silica core and 8 nm for Ag shell-silica core biosensor surfaces. The wavelength shifts for each step (after antibody coupling and after specific antigen binding) were almost similar for both of the biosensor surfaces. Taken into account that antibody and antigen have almost the same molecular weight, the response indicates that on average one antigen binds to one antibody for both Au and Ag shells.

As it is shown in the UV-Vis spectra of the biosensor surfaces, the total wavelength shifts are 9 nm for Au shell-silica core and 19 nm for Ag shell-silica core biosensor surfaces which is in agreement with the sensitivity ratio observed in previous experiments on fibrinogen adsorption.

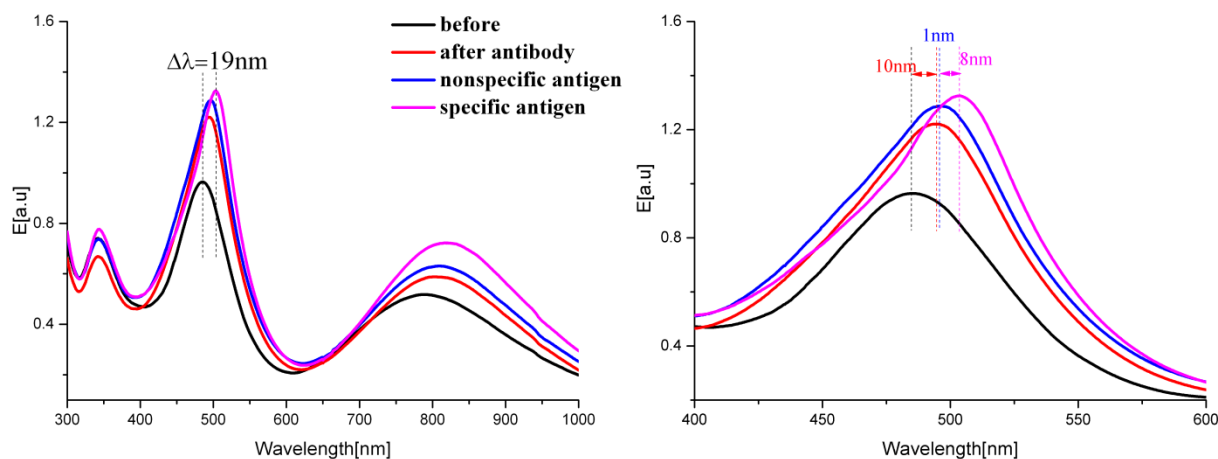


Figure 54. UV-Vis spectra of Ag shell-silica core nanoparticle film before antibody binding, after antibody binding, after nonspecific antigen binding and after specific antigen binding.

XPS measurements were carried out on biosensor surfaces to compare the relative total amount of coupled biomolecules on each surface. XPS measurements were done before mouse anti-rabbit IgG coupling and after

rabbit anti-sheep IgG binding by following the N1s signal. XPS results revealed that the total amount of biomolecules coupled to each surface was almost similar as shown in Figure 55.

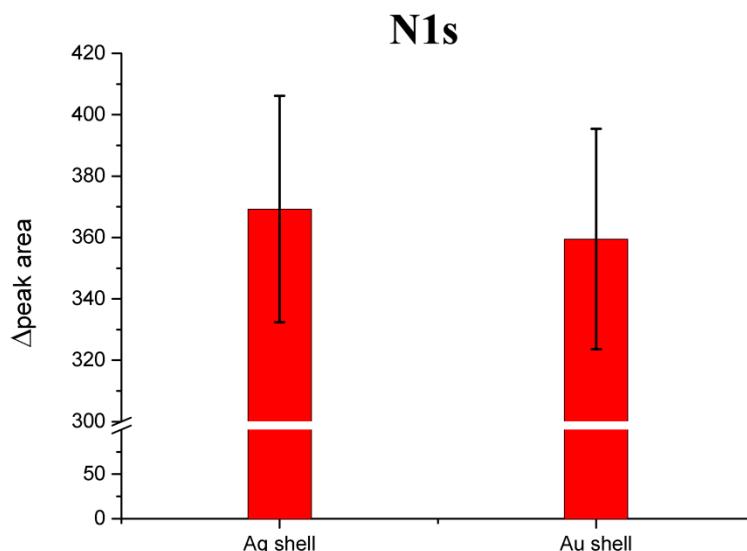


Figure 55. N1s signal area difference between before antibody coupling and after specific antigen coupling for Ag shell-silica core and Au shell-silica core biosensor surfaces.

5.2.1.3 Alternative Biosensor Configurations

In addition to the biosensor configurations discussed above, different biosensor configurations were prepared by selecting more flexible substrates than glass slides. The selected materials were polyvinylidene fluoride (PVDF) membranes (pore size 500 nm) and polyimide (PI) foils which could be advantageous in the next step of experiments such as peptide transfer from a solid synthesis surface to the biosensor surface (section 5.3.2). Therefore, dielectric silica nanoparticles were deposited on these flexible substrates by self-assembly floating and coated with a Au shell by seeding and consecutive electroless gold plating. Initially, the flexible substrates were coated with a flat Au layer. For PVDF membranes Au coating was done via sputter coating since the membrane was not stable at the temperatures required for PVD deposition. Figure 56 shows the bare and silica nanoparticle coated membrane surfaces.

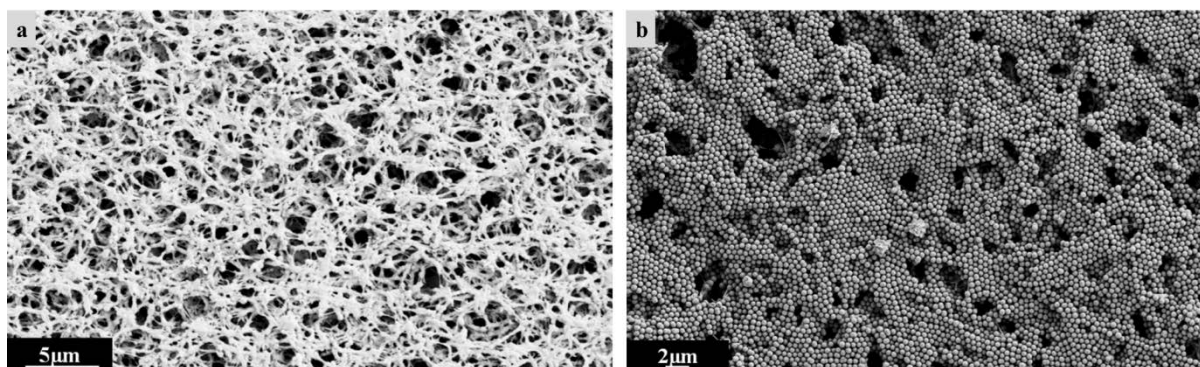


Figure 56. SEM images of a) a Au-coated PVDF membrane and b) the same substrate with a dielectric silica nanoparticle film deposited on it.

Since the membrane itself does not have a smooth surface it looks as if silica nanoparticles were not deposited as a monolayer. However, closer inspection reveals that the silica particles were adsorbed as a homogenous monolayer. Figure 57 shows the UV-Vis spectra of a Au shell-silica core nanoparticle film on a PVDF membrane before and after fibrinogen adsorption.

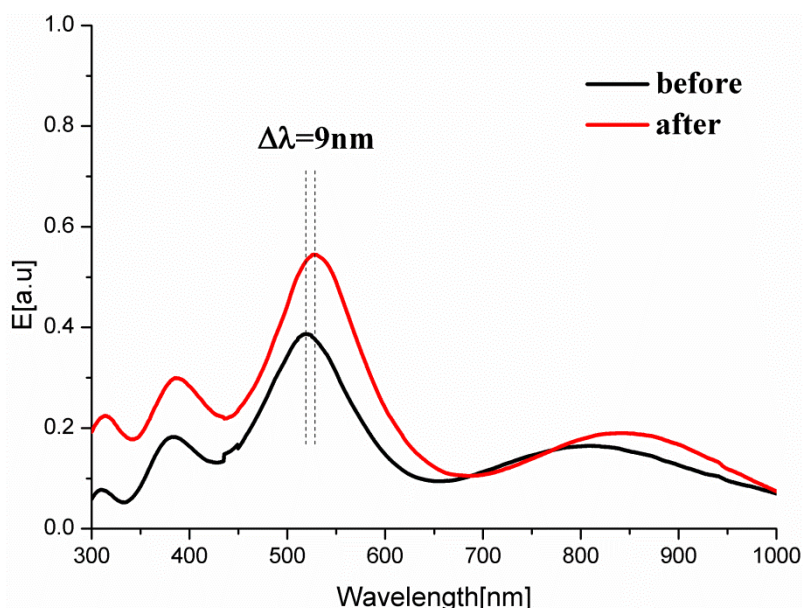


Figure 57. UV-Vis spectra of a Au shell-silica core nanoparticle film on a PVDF membrane before and after fibrinogen adsorption.

Onto the second alternative substrate, the PI foil, a flat Au layer was evaporated by Georg Albert using PVD. A Au shell-silica core nanoparticle film was prepared as described before. As shown in Figure 58, the silica nanoparticles were again deposited as a homogenous monolayer on the PI

foil. Figure 58 shows the UV-Vis spectra of the Au-core-silica-shell nanoparticle film on the PI film before and after fibrinogen adsorption.

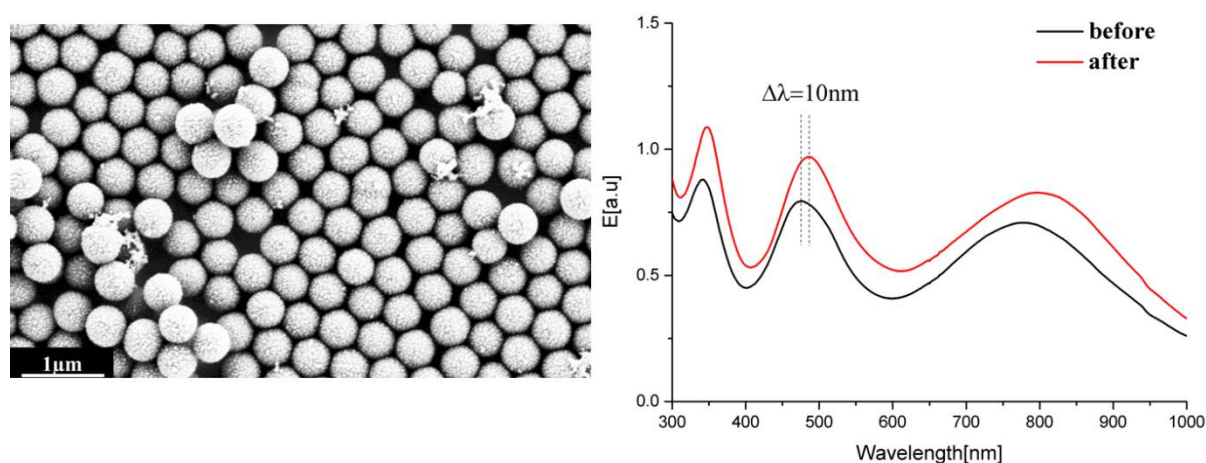


Figure 58. SEM image of a Au shell-silica core nanoparticle film deposited on a PI foil (left) and UV-Vis spectra of Au shell-silica core the nanoparticle film before and after fibrinogen adsorption.

In collaboration with *Christiane Antoni* the sensitivity of these types of biosensor surfaces was measured and compared upon fibrinogen adsorption in the scope of a student physical chemistry research project. It was concluded that the biosensor surfaces prepared on these flexible substrates are a promising alternative to the ones prepared on solid substrates with a similar sensitivity (wavelength shift) upon fibrinogen adsorption. Furthermore, the stability of the biosensor surfaces was evaluated in TFA, DMF and toluene solutions and it was found that the surfaces were stable. The compatibility of these surfaces with further experiments (SPR imaging and SPR wavelength shift) will be discussed in the following chapters.

5.2.2 Sputter Coating of a Au shell on Dielectric Nanoparticles

A Au shell can be deposited on dielectric silica particles by sputter coating as well as seeding and consecutive electroless plating. In the scope of a student physical chemistry research project by *Christina Lehrer*, core-shell nanoparticles were prepared by sputter coating of a Au shell on dielectric silica nanoparticles in order to obtain optically homogeneous surfaces. A corresponding SEM image is shown in Figure 59. It has been possible to prepare different thicknesses of the Au shell by changing the time of sputter coating. In order to find the optimum Au shell thickness, 5, 10, 15, 20, 25, 30 nm of Au was sputter coated on the silica cores using 5 nm of Ti as an adhesion promoting layer. For shell thickness optimization, configuration I in Figure 41I was used as the substrate.

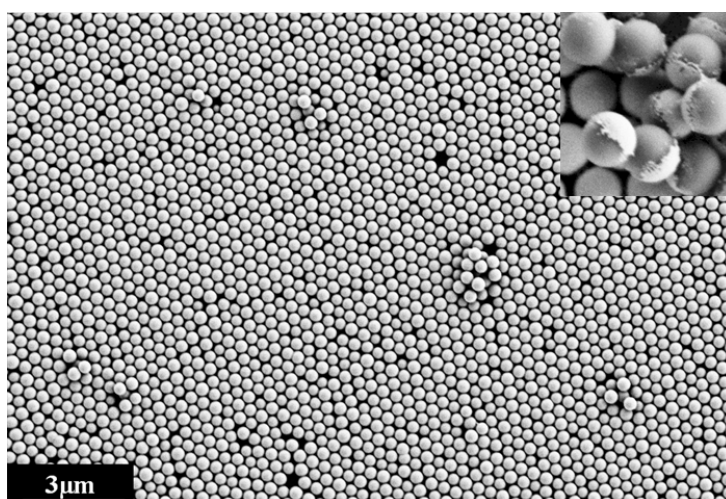


Figure 59. SEM image of a Au shell-silica core nanoparticle film prepared by sputter coating the Au shell (20 nm thickness). Inset: Au shell coated silica nanoparticles which were removed from the surface.

As depicted in Figure 60, a 20 nm Au shell thickness yielded the best sensitivity (the highest wavelength shift) upon fibrinogen adsorption. Moreover, the UV-Vis spectrum of the surface with a 20 nm Au shell thickness had either more symmetrical or more intense SPR peaks than the other surfaces with different thickness as shown in Figure 61. 20 nm was chosen to be the optimum Au shell thickness. As discussed in the previous section 5.2.1.1.1, the sensitivity decreases starting from 20 nm shell thickness as the shell thickness-to-core ratio increases. The lower sensitivity

values for Au shell thicknesses of 5, 10 and 15 nm might be related to the surface roughness of the shell, because sputter coating of these thicknesses resulted in cracks on the shell which prevents continuous shell formation. Therefore, surface roughness could affect the sensitivity in addition to the shell-thickness-to-core ratio.

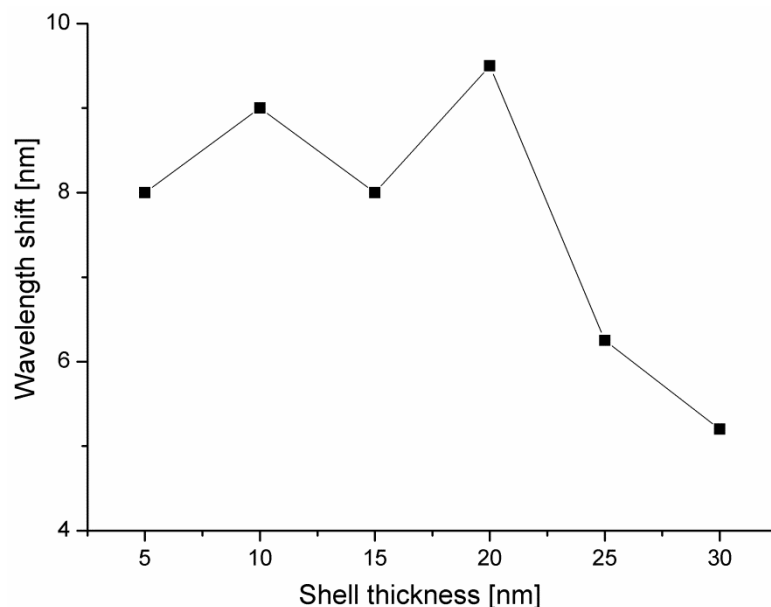


Figure 60. Wavelength shift of biosensor surfaces for different shell thickness.

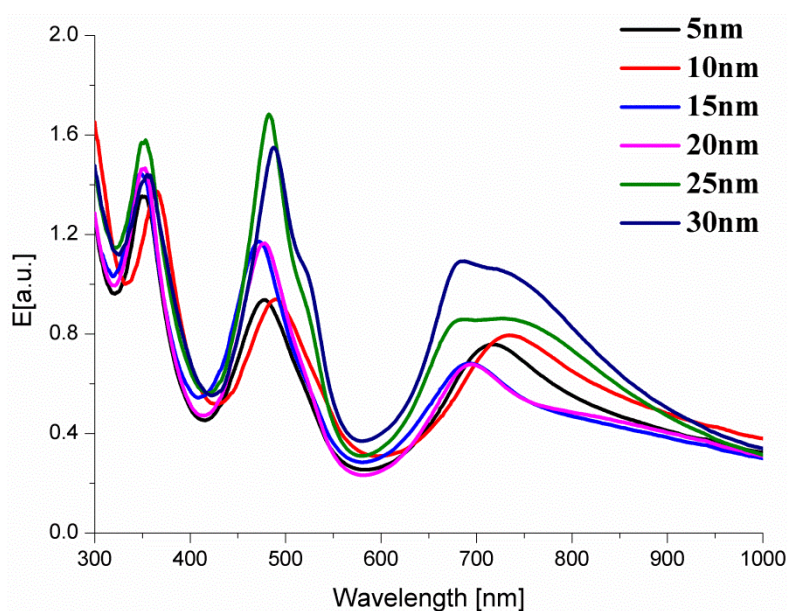


Figure 61. UV-Vis spectra of biosensor surfaces prepared by sputter coating of the Au shell at different shell thickness.

In section 5.2.1.1.2, it was shown that using a 40 nm dielectric silica layer, deposited in between the core-shell nanoparticles and flat Au film, improved the sensitivity of the biosensor surface. The same modification was

applied to the biosensor surface prepared by sputter coating of the Au shell (configuration II in Figure 41). Again, the introduction of this dielectric silica layer improved the sensitivity of the biosensor upon fibrinogen adsorption, as shown in Figure 62.

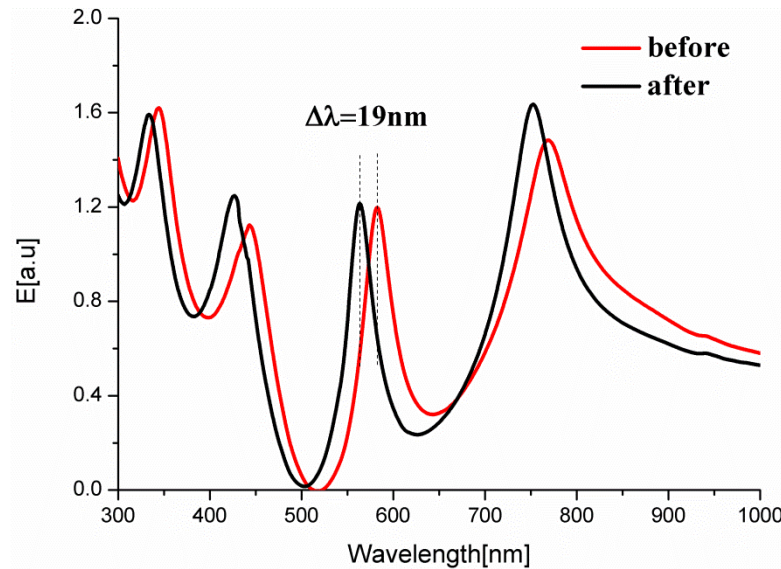


Figure 62. UV-Vis spectra of the biosensor (configuration II in Figure 33) prepared by sputter coating of Au shell before and after fibrinogen adsorption.

In general, the main advantage of the biosensor surfaces prepared by sputter coating the Au shell is the homogenous shell coating which results in better optical homogeneity in SPR imaging and SPR wavelength shift experiments. The optical homogeneity of the biosensor is important to obtain a reliable contrast difference within the SPR image at different wavelengths.

5.3 Label-free Detection of Protein Binding on Biosensor Surfaces by SPR Imaging and SPR Wavelength Shift

The Fast Read-out System

In this part of the thesis, the biosensor surfaces discussed and proposed in previous sections were analyzed with a homemade fast read-out system which was set up within the context of this thesis and is schematically shown in Figure 63. It extends the detection capabilities of the previously used UV-Vis spectroscopy and the scanning unit set-up as detailed in what follows. The fast read-out set-up consists of the following parts: DH-2000-BAL light source (OceanOptics/USA) equipped with deuterium and halogen lamps that are combined in one light path, stainless-steel jacketed fiber optic with 600 μ m core diameter (OceanOptics/USA), 74-UV Collimating Lens (OceanOptics/USA), Cornerstone 260 1/4m Monochromator (Newport Spectra-Physics GmbH/Germany) equipped with motorized slits, telescope system including concave, PLCC-lens, with FL=-100mm (Laser Components GmbH/Germany) and convex, PLCX-lens, FL=250mm, (Laser Components GmbH/Germany) to expand the beam diameter, rotational sample holder (Thorlabs GmbH/Germany), a high resolution Sensicam UV CCD camera (PCO AG/Germany) equipped with two different imaging lenses: Makro Planar 2/100mm ZF (Carl Zeiss/Germany) operating between 400-1000nm and UV-VIS CoastalOpt® SLR Lens (Coastal Optics/USA) operating between 250-650nm.

The resolution of the monochromator was controlled by setting the slit width to 3 nm in all experiments. In the telescope system the beam diameter was expanded 2.5 times with respect to the diameter of fiber optic (600 μ m) and to approximately 1.6 cm² in diameter (calculated by the pixel size and the number of pixels illuminated) as the area illuminated by the light source. The resolution of the images was adjusted to be around 20 μ m/pixel. In order to prevent the system from stray light exposure, the set-up was covered with a black box which was built in the machine shop of the Physical Chemistry Department, Heidelberg. For the solidity of the set-

up, an optical breadboard (Thorlabs GmbH /Germany) was used to mount all the pieces of the set-up. Moreover, this breadboard provides vibrational stability as well.

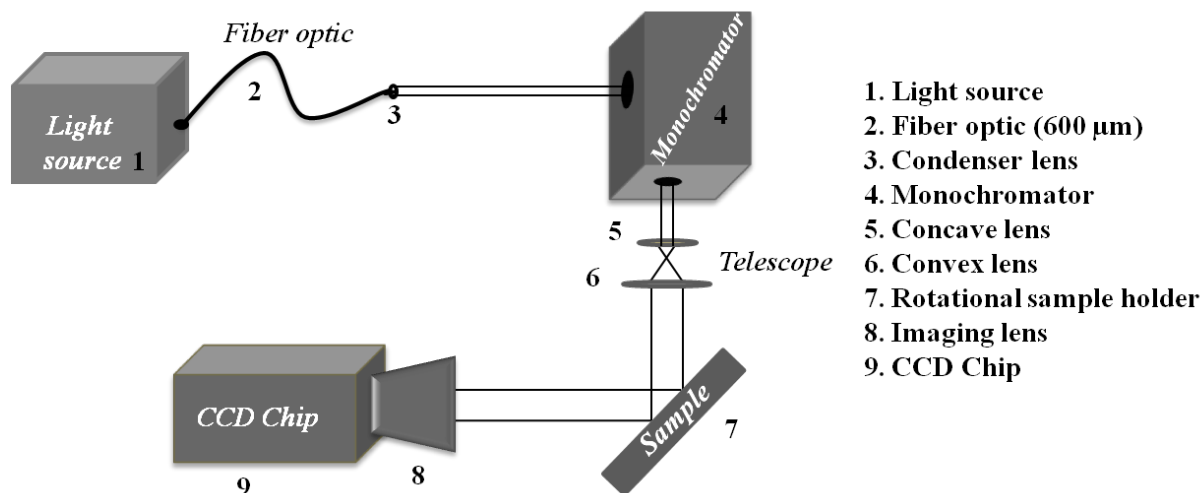


Figure 63. Fast read-out set-up and its components.

The spectral range covered with the set-up is between 300 and 900nm which gives the opportunity to do label-free detection in UV and Visible regime of the light spectrum as well as in the Near-IR regime. This allows to use different extinction peaks for biosensing depending on the specific application. Moreover, in *in situ* measurements a wavelength regime with minimum adsorption of the solvent used can be selected. All parts of the set-up were chosen to be compatible with the requirements of light transmission and detection in the mentioned wavelength regime. The quantum efficiency of the CCD camera was measured by the company as given in Figure 64A covering the UV regime. The concave and convex lenses used for the telescope system for expanding the beam diameter, and condenser lens are made of fused silica which is almost transparent at the desired wavelengths as shown in Figure 64B. The imaging lenses, Makro Planar 2/100mm ZF (Carl Zeiss/Germany) and UV-VIS CoastalOpt® SLR Lens (Coastal Optics/USA) are compatible and overlap each other in terms of light transmission as shown in Figure 65.

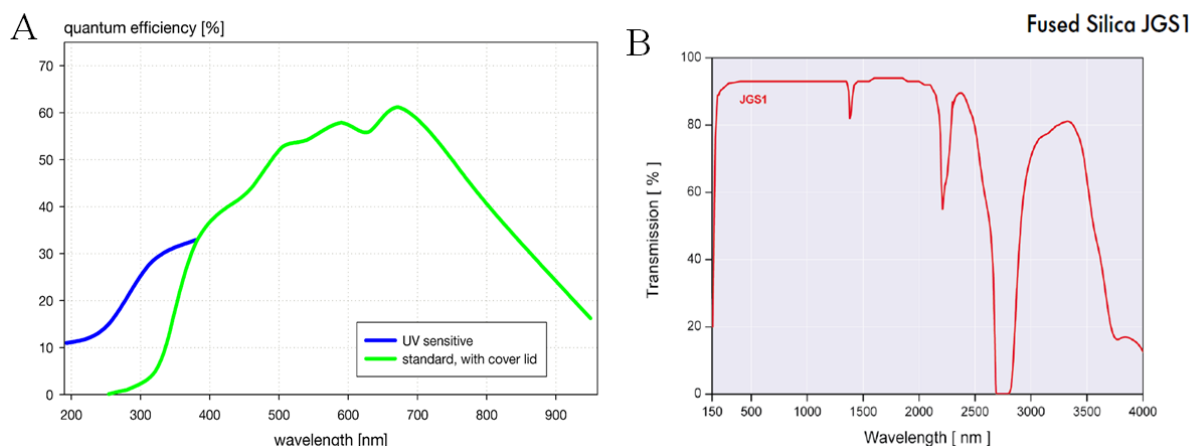


Figure 64. Quantum efficiency curve for A) Sensicam UV measured by PCO and B) transmission curve for fused silica measured by Laser Components.

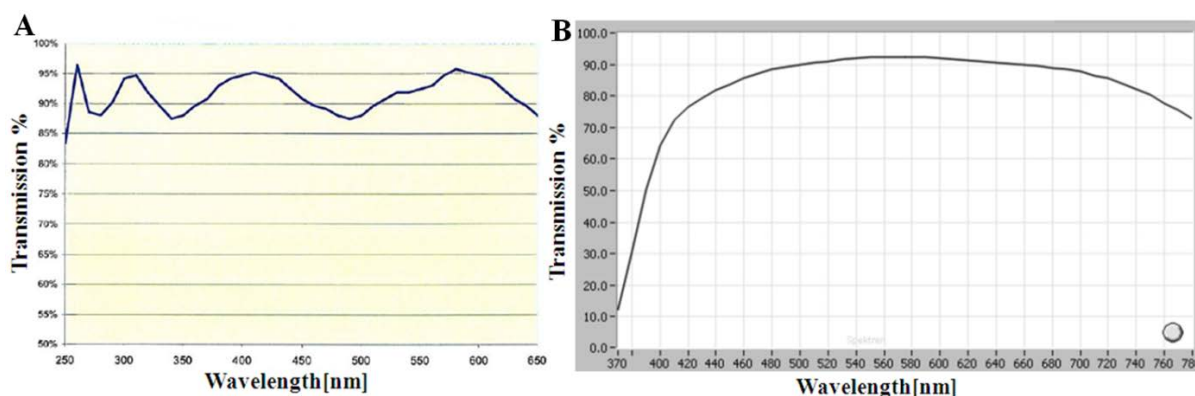


Figure 65. Transmission curves of A) UV-VIS CoastalOpt® SLR Lens and B) Makro Planar 2/100mm ZF provided by the companies.

For label-free imaging of protein arrays using the fast read-out set-up shown in Figure 63, monochromatic light illuminates the biosensor surface at a fixed angle and the reflected light is detected using the CCD camera. The image obtained shows the intensity distribution of the reflected light with lateral resolution (“intensity image”). However, sometimes even more meaningful is the wavelength position of the extinction peaks for each spot of the surface. For this purpose, the measurement is repeated for a range of wavelengths around the expected peak position. For each spot, the intensity can now be plotted as a function of wavelength to extract the wavelength position of the extinction peak (“wavelength image”). Measurements which compare the wavelength positions at two different locations will be referred to as “wavelength shift measurements”.

In our research group three different experimental set-ups are used to follow and evaluate the biomolecular interactions on the biosensor surfaces; (i) a UV-Vis reflection set-up, (ii) a LSPR imaging set-up (the scanning unit) and (iii) a CCD-based fast read-out set-up. The UV-Vis reflection set-up, shown in Figure 33A, is used to evaluate the performance of the proposed and prepared biosensor surfaces by non-specific adsorption of proteins whereas the others are used to detect biomolecular reactions in an array format. The CCD-based fast read-out set-up was developed to replace the existing scanning unit in our research group which was shown in Figure 33B. In the scanning unit, the biosensor surface is placed on a motorized sample holder which can move in x-y directions with 5 μm step size while the sample surface is illuminated with an optical fiber (200 μm in diameter) and the reflected light is guided to the spectrometer with 50 μm diameter optical fiber. The lateral resolution of the scanning unit is determined by the step size selected in the scanning process and the diameter of the optical fibers used in the measurements. The wavelength resolution is determined by the resolution of the spectrometer used. The main drawback of the scanning unit is that the measurement takes too long to achieve good resolution over a large scanning area. On the contrary, the CCD-based fast read-out set-up can perform faster measurements than the scanning unit. Moreover, the fast read-out set-up is proposed to be more convenient to follow the binding kinetics of biomolecules.

The protein arrays were deposited on the biosensor surfaces by two different techniques which are direct spotting on the biosensor surface by a spotting robot and the transfer of the array from a synthesis surface to the biosensor surface. For initial tests of the biosensor surfaces and the fast read-out set-up, only the spotting robot was used to generate protein arrays on the biosensor surface due to simplicity of the technique. The purpose of the test experiments was to find the most suitable biosensor surface parameters for transfer of the protein arrays from the synthesis surface and subsequent detection of biospecific interactions in following experiments.

To compare different biosensor surfaces, fibrinogen was spotted on the surface by pipetting the protein directly onto the surface by hand. This method generally yields spots in millimeter size and was used for its simplicity. Moreover, results of different analysis techniques, such as UV-Vis reflection spectroscopy and SPR wavelength shift measurements, could be directly compared using the same set of samples as discussed in section 5.3.1.2.

5.3.1 Detection Protein Arrays on Biosensor Surfaces by SPR Intensity Imaging

The fast read-out set-up was first used to detect antibody arrays spotted at DKFZ. Alexa Fluor 647 goat anti-rabbit IgG (2mg/ml) was the selected protein and spotted onto a biosensor surface (configuration III in Figure 41 with Au nanoparticles deposited by seeding and consecutive electroless gold plating). The surface was first scanned with a fluorescence scanner to approve the correct spotting of the antibody array as depicted in fluorescence image Figure 66A. An array of 25x25 spots was formed with a spot size of 250 μm (2nl antibody solution/spot) and a center-to-center distance of 600 μm as shown in Figure 66A. Afterwards, the surface was imaged with the fast read-out set-up at different wavelengths to select optimum intensity contrast between spots and background. The intensity image obtained for 600 nm wavelength is shown in Figure 66B.

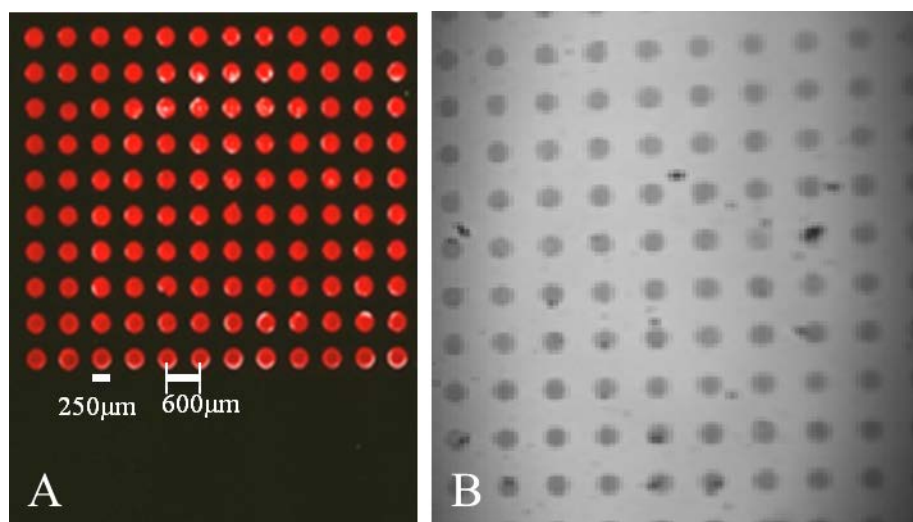


Figure 66. A) Fluorescence image and B) SPR intensity image (2.5s exposure time) of the antibody array spotted on biosensor surface as measured at 600 nm wavelength.

Based on the spot size of the arrays as determined by fluorescence imaging, the lateral resolution of the fast read-out system was calculated to be $\sim 20 \mu\text{m}/\text{pixel}$ (The same pixel size was calculated in another set of experiment in which the array was spotted with a diameter of 400 μm and the diameter of the spot was confirmed with an optical microscope, too). To calculate the wavelength shift of the system upon antibody adsorption, the surface was imaged at different wavelengths between 400-700 nm, with a

scanning interval of 10 nm at a fixed incident angle. By following the intensity of specific certain pixels as a function of wavelength at different locations which correspond to the antibody spots and the background (i.e. where there are no antibody spots), SPR curves were generated as shown in Figure 67. The wavelength shift was calculated as 9 nm with an intensity contrast in reflectivity, $\Delta R/R$ of 14% at 600 nm wavelength. For this sample the mass density of adsorbed antibody for this sample was 16 ng/mm² as calculated from the spot size and the amount of protein deposited per spot.

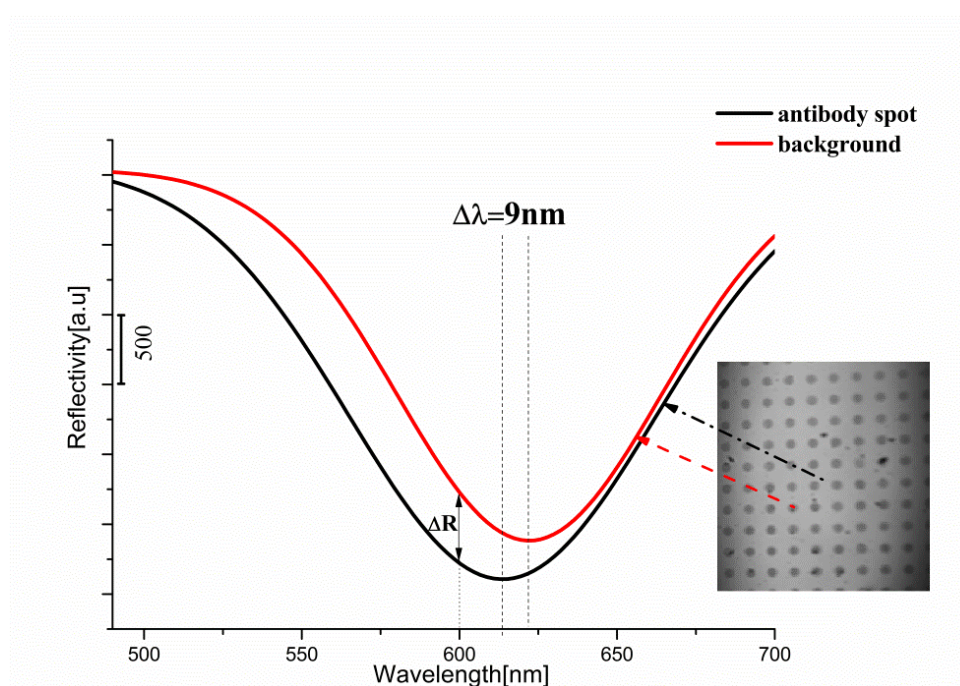


Figure 67. SPR curves for antibody spots and background generated from the SPR images at different wavelengths.

The first attempt to detect antibody arrays with the fast read-out set-up was successfully achieved by SPR intensity imaging and SPR wavelength shift measurements. It was shown that the fast read-out set-up could be used for label-free detection of protein arrays.

5.3.1.1 SPR Intensity Imaging Experiments by Fast Read-out Set-up Using Core-Shell Nanoparticle Films

For label-free detection of antibody arrays, different configurations of biosensor surfaces as discussed in section 5.2.1.1 and 5.1.3.2 were used for SPR intensity imaging and SPR wavelength shift measurements. For SPR intensity imaging, FITC dye conjugated anti-HA IgG antibody (1mg/ml) was spotted onto different sensor configurations (Au shell-silica core and Ag shell-silica core) in different concentrations in order to figure out the detection limit on these surfaces. 0.5 nl of antibody solution were used for each spot, by dilution of 1mg/ml antibody solution from 1:5 to 1:100 v/v dilution).

It was found out that 2.6 ng/mm² protein could be detected on Au shell-silica core films (Figure 68A) while 0.13 ng/mm² protein could be detected on Ag shell-silica core biosensor surfaces (Figure 68B).

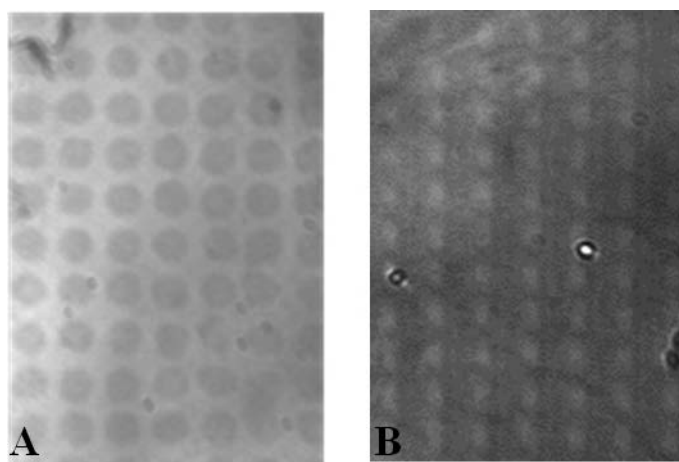


Figure 68. SPR intensity images of an antibody array on an A) Au shell-silica core film (2.6 ng/mm² protein) and B) Ag shell-silica core film (0.13 ng/mm² protein) measured at at 650 nm wavelength. (5 s integration time for A and 7.5 s for B)

One of the advantages of the fast read-out set-up in combination with core-shell nanoparticle films is the opportunity to perform SPR imaging measurements in different regimes of the light spectrum such as UV and Vis. For this purpose, FITC dye conjugated anti-HA IgG antibody was spotted on the biosensor (configuration I in Figure 41) with a spot size of 250 μ m and a center-to-center distance of 400 μ m. Since the biosensor

surface has resonance peaks in both the UV and Vis regime of the light spectrum, it was possible to obtain information from the surfaces by using two different lenses which were compatible to these regimes of the light spectrum. The SPR images at different wavelengths are given in Figure 69. The SPR images show that the fast read-out set-up could be used to perform SPR imaging measurements in different regimes of the light spectrum which are compatible with the optical properties of core-shell nanoparticles.

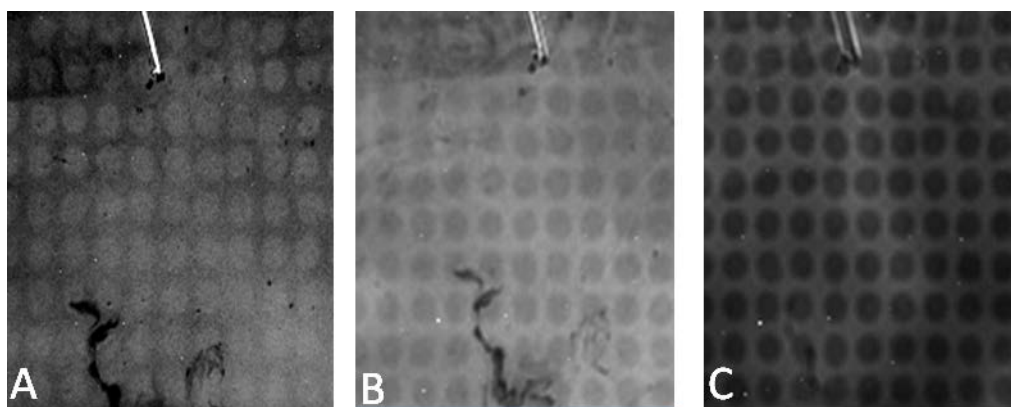


Figure 69. SPR images of an antibody array spotted on a biosensor surface (same sample) measured at different wavelengths A) 360 nm B) 600 nm and C) 800 nm (5 s integration time). (A Au core-silica-shell nanoparticle layer on 30 nm flat Au film was used in the experiments.)

5.3.1.2 SPR Wavelength Shift Measurements on Biosensor Surfaces

After SPR intensity imaging had been performed on different biosensor surfaces at different wavelengths, SPR wavelength shift measurements were carried out to compare the results to the wavelength shifts obtained by UV-Vis reflection spectroscopy (cf. section 4.8). Accordingly, 10 μ l of fibrinogen solution was pipetted on the biosensor surface (configuration III in Figure 41) to generate fibrinogen spots. The SPR spectra of the spot and the background were measured with the UV-Vis reflection set-up, and the wavelength shift was found to be 7 nm upon protein adsorption as shown in Figure 70B. The same sample was used in SPR wavelength shift experiments for recording SPR images between 400-600 nm with a 5 nm scanning interval. An area of 30x30 pixels in the center of the spot (darker areas with

black borders) and in the background area (red circle) was used to calculate the reflected light intensity at different wavelengths to generate the SPR peaks for the fibrinogen spot and the background, respectively (Figure 70A).

Such obtained wavelength shift of 8 nm is similar to the one found by UV-Vis reflection spectroscopy so that it may be concluded that both techniques yield consistent results.

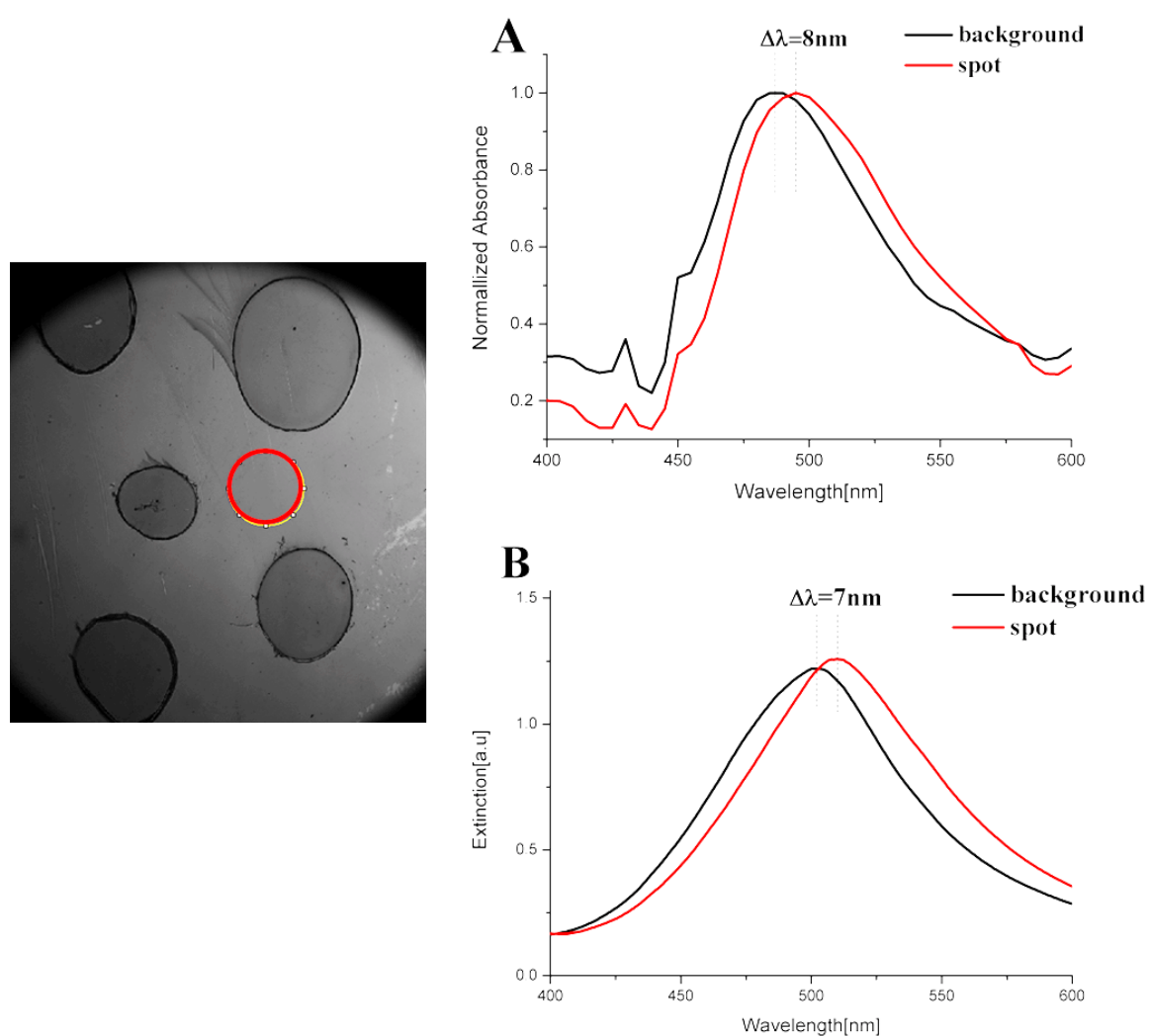


Figure 70. SPR image of biosensor surface at 500nm and A) SPR wavelength shift and B) UV-Vis reflection spectra of the protein spot and background.

Comparison of Ag shell-silica core and Au shell-silica core Biosensors by SPR Wavelength Shift Measurements

Ag shell-silica core and Au shell-silica core biosensor surfaces were prepared as described before and for simplicity 10 μ l of fibrinogen solution was pipetted on each surface to form protein spots. Both surfaces were scanned between 400-750 nm wavelength with 10 nm scanning interval. SPR images of both surfaces at 550 nm are given in Figure 71.

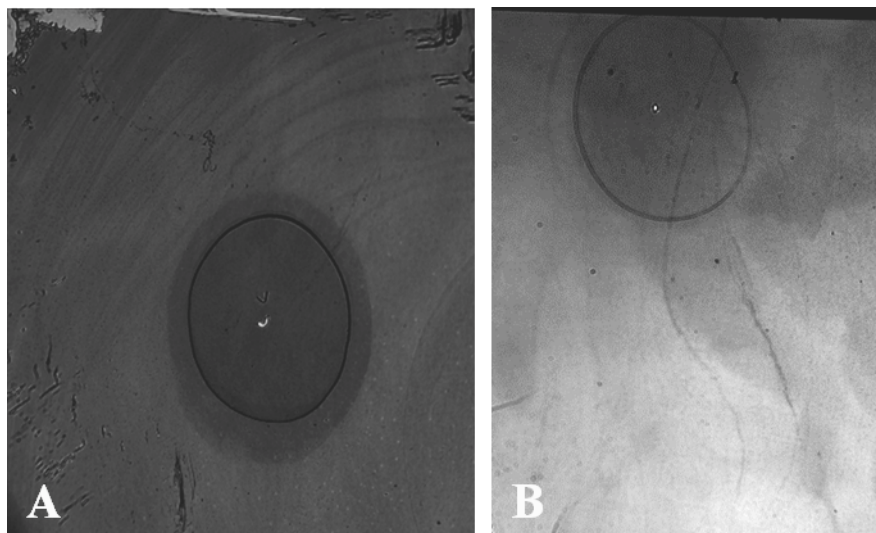


Figure 71. SPR images of fibrinogen spots on A) Au shell-silica core and B) Ag shell-silica core at 550 nm (2 s integration time for each)

First the corresponding UV-Vis reflection spectra from each fibrinogen spot were collected and the background spectra were recorded from the area closest to the fibrinogen spots. Based on the comparison of UV-Vis reflection spectra of fibrinogen spots and background, 19 nm wavelength shift was obtained for Ag shell-silica-core whereas 9 nm for Au shell-silica core biosensor as shown in Figure 72. These obtained wavelength shifts were comparable to previous experiments. To calculate the SPR wavelength shift, the average reflected intensity of a 30x30 pixel area from the fibrinogen spot and the background was followed as a function of wavelength in the same wavelength regime. As shown in Figure 72, the wavelength shifts determined for both biosensor surfaces were similar to the ones obtained by UV-Vis reflection measurements. Based on both measurement methods, the Ag-core-silica-shell biosensor surface showed better response, i.e. higher

wavelength shift, to fibrinogen adsorption than the Au-core-silica-shell biosensor.

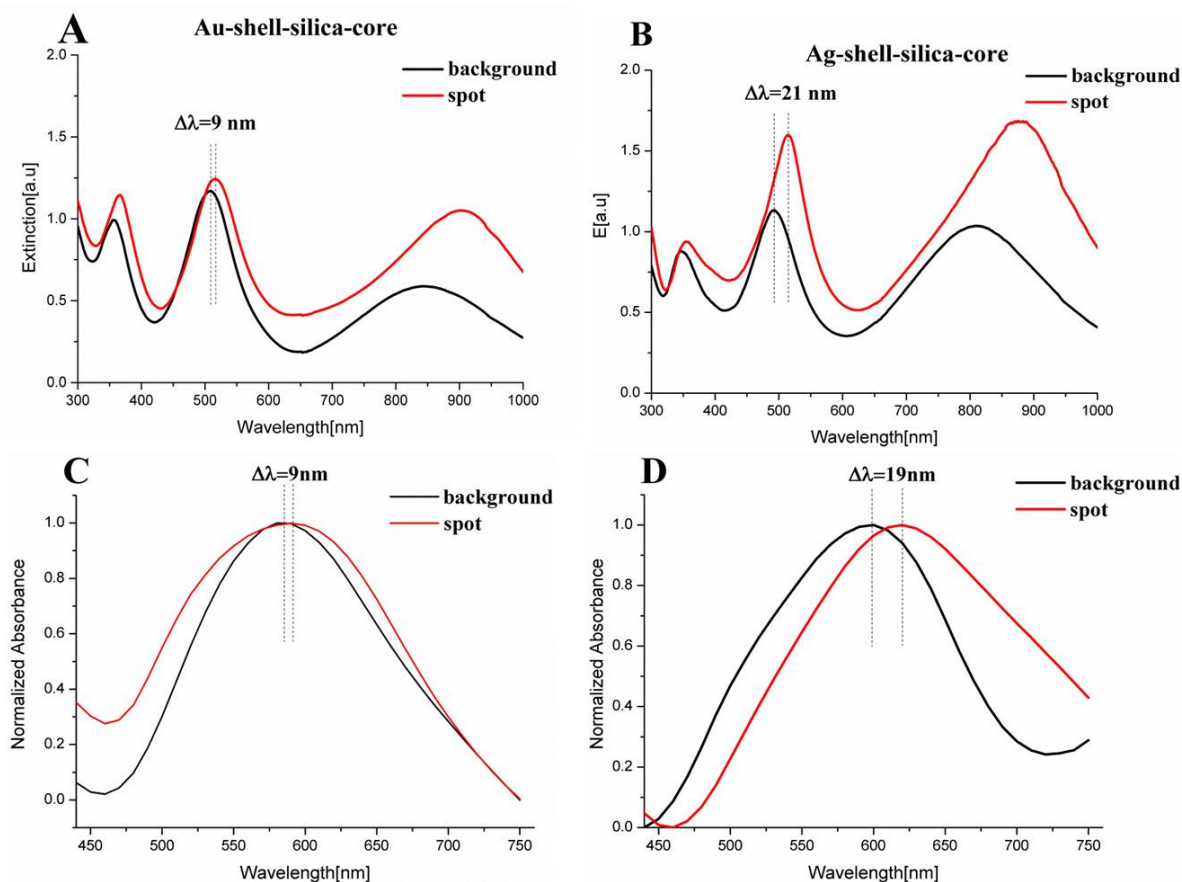


Figure 72. UV-Vis reflection spectra of fibrinogen spot and background on A) Au shell-silica core and B) Ag shell-silica core, and SPR wavelength shift spectra of fibrinogen spot and background on C) Au shell-silica core and D) Ag shell-silica core.

In summary, biosensor surfaces consisting of core-shell nanoparticle films prepared by seeding and consecutive electroless metal plating were used in SPR imaging and SPR wavelength shift measurements with a CCD-based fast read-out detection set-up. In both types of measurements Ag shell-silica core nanoparticle surfaces showed better response (i.e. higher wavelength shift and lower detection limit) than Au shell-silica core nanoparticle surfaces. However, as seen in the SPR images shown in Figures 68, 69 and 71, the biosensor surfaces were not optically homogeneous in SPR imaging experiments. I.e. the light intensity reflected from different locations within one protein spot or within the background varies. This causes severe problems as optical homogeneity is crucially important in

array analysis to clearly distinguish between protein spots and their background. Its importance even increases if only small amounts of biomolecules are detected.

5.3.1.3 SPR Imaging Measurements on Alternative Biosensor Surfaces

In SPR imaging measurements, one of the most important features is the effective reflectivity of light from the biosensor surface which was mainly dominated by the choice of the substrate. Based on SPR imaging measurements it was concluded that configurations shown in Figure 41, could be used as biosensor surfaces for the detection of spotted antibody arrays. However, since these substrates were not thought to be flexible enough for high density peptide array transfer experiments (*cf.* chapter 5.3.2.2) which were done in cooperation with C.Schirtwitz (DKFZ/Heidelberg), alternative biosensor surfaces were also evaluated for their suitability in SPR imaging measurements. For this purpose, PI-foils and PVDF membranes were used as substrates as discussed in section 5.2.1.3.

The biosensor surfaces were prepared as explained in section 5.2.1.3 and for simplicity 10 µl fibrinogen solution was pipetted on the surface and adsorbed for 3 h to generate millimeter size protein spots instead of spotting antibody arrays. Unfortunately, the light intensity reflected from the Au membrane based biosensor surface was very low so that a long acquisition time (10 s/image, see Fig. 73A) was required for SPR imaging even though the wavelength shift upon fibrinogen adsorption was consistent with the one found for the biosensor surface in Figure 41 configuration I. The low reflected light intensity could be due to the porous structure of the membrane which traps the light inside. This observation was confirmed by UV-Vis reflection measurements which required 2000 ms/spectrum integration time for the Au coated PVDF membrane based biosensor surface whereas only 75 ms/spectrum were necessary for the Au coated glass

substrate based biosensor surface. Note, that in general 10 spectra were averaged for one measurement in UV-Vis reflection experiments.

A biosensor surface based on a PI-foil with an evaporated Au film on top was found to be more suitable in terms of its reflected light intensity and its wavelength shift (9 nm) upon fibrinogen adsorption in UV-Vis reflection experiments. Almost the same integration time (80 ms/spectrum) could be used for collecting the spectra as for Au coated glass substrates. However, in SPR imaging measurements as shown in Figure 73B, the optical properties of the biosensor surface were inhomogeneous due to the rough surface of the PI-foil. Actually, the stripes in the images originate from the PI-foil itself. Therefore, it was concluded that the flat Au film evaporated PI-foil based biosensor surface was also not suitable for SPR imaging measurements on protein arrays.

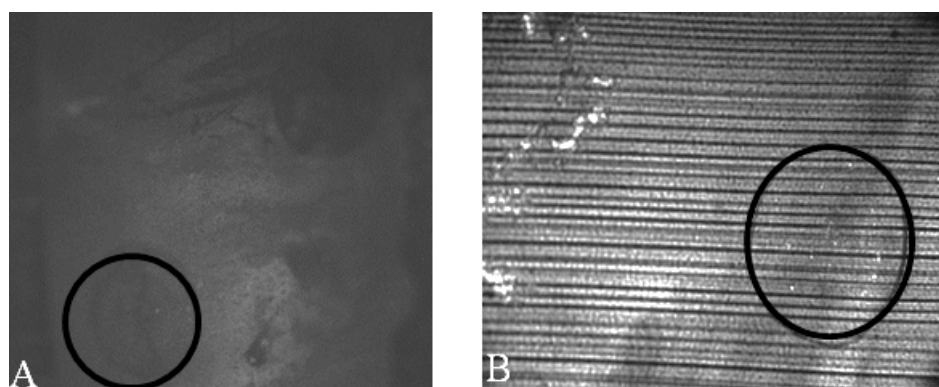


Figure 73. SPR images of fibrinogen spots on a A) Au coated PVDF membrane based and B) PI-foil based biosensor. (10 s exposure for A and 1.5 s exposure for B)

In summary, the alternative biosensor surfaces discussed in section 5.2.1.3 were found to be incompatible with SPR imaging measurements to detect proteins in array format due to either low reflectivity or surface roughness causing inhomogeneous background.

5.3.2 Label-free Detection of High Complexity Peptide Arrays

5.3.2.1 *Synthesis of Peptide Arrays*

The method which was applied to synthesize the peptide arrays for the experiments in this chapter is explained in more detail in the literature^[78,79]. Briefly summarized, the peptide arrays used in transfer experiments were synthesized with the laser printer, particle based synthesis technique (introduced in section 2.5.3), on glass slides which have a functional coating consisting of poly(ethylene glycol) methacrylate (PEGMA) and methyl methacrylate (MMA)^[117]. As a synthesis layout an array containing permutations of the wild type HA (hemagglutinin A) epitope (YPYDVPDYA-OH) was chosen. The content of the array is listed in Table 1. In the resulting array, the peptide spots were approximately 512 μm in diameter with 1024 μm center-to-center spacing which was achieved by inserting GDGA as a “spacer” in every second line and column of the pre-defined pattern.

5.3.2.2 *Transfer of Peptide Arrays*

In order to generate high-density (i.e. highly resolved) peptide arrays on biosensors, the arrays were transferred to the sensor surfaces from the original synthesis surfaces. The transfer method has recently been developed and optimized to also purify the peptide arrays from synthesis artifacts by C. Schirwitz^[78,79]. For the transfer, the entire peptide array is synthesized on surfaces bearing a cleavable linker. Furthermore, the peptide spots which shall be transferred obtain AA followed by cysteine as a key-sequence in the last step of the combinatorial array synthesis. As soon as the synthesis surface is exposed to the cleavage medium while being placed face-down onto the biosensor surface the transfer of peptide spots is initiated. Thereby, close contact as depicted schematically in Figure 74 and only small volumes of the cleavage medium are essential to prevent lateral diffusion. Moreover, a circular filter paper soaked with the cleavage medium is placed under the sensor surface to generate an atmosphere of cleavage medium in the petri dish. In this case, the acid-labile Rink amide linker^[118]

and TFA in toluene (50 % v/v) were applied to simultaneously cleave the peptides and the side-chain protecting groups. At the same time, the re-binding of the peptide due to cysteine-gold interaction was achieved in this medium. The transfer time was set from 30 min up to 2 h. After each transfer experiment, the surfaces were carefully separated lifting the synthesis surface from the sensor surface. Due to capillary forces, complete evaporation of the solvent was beneficial for the slide separation which could be achieved by opening the petri-dish a few minutes before the end of the transfer time. To prevent nonspecific protein adsorption in the subsequent immunostaining with the specific antibody to HA, the biosensor surface was additionally blocked with 2 mM solution of O-(2-mercaptoethyl)-O'-methylhexaethyleneglycol (EG₇-SH) for 1 h up to 24h. Thiols like EG₇-SH are known to form SAMs on the free binding sites on the gold surfaces, whereby EG moieties provide protein repelling properties^[105].

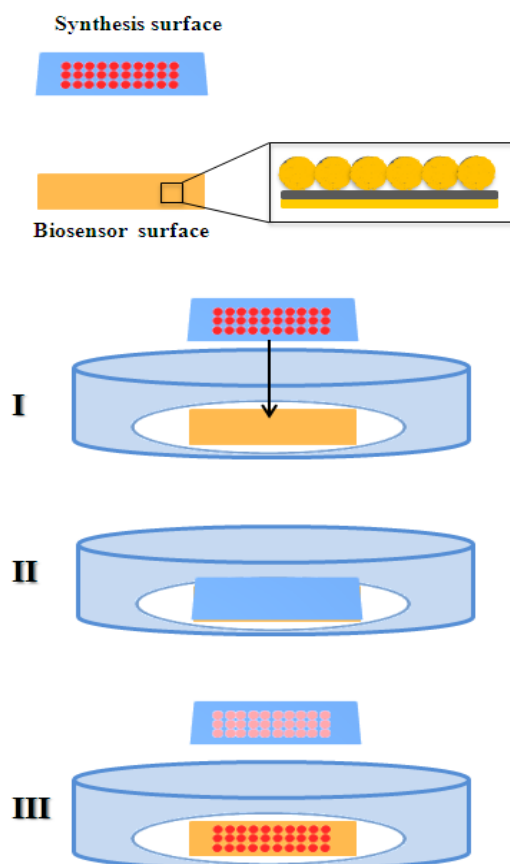


Figure 74. Transfer of peptide arrays. I) The synthesis surface is placed face-down on the biosensor surface. II) The synthesis surface is left on the biosensor for the desired transfer time. III) Separation of the surfaces. (Redrawn according to experimental set up by C. Schirwitz^[78])

Figure 75 shows an immunostaining with the mouse anti-HA IgG and subsequent exposure to goat anti-mouse IgG, conjugated with DyLight680, on the biosensor surface. The fluorescence pattern on the biosensor surface indicated that the specific transfer of the cysteine-terminated peptides was successfully achieved.



Figure 75. Fluorescence image of the transferred array on a biosensor surface. The image was obtained by staining the array with the DyLight 680 conjugated antibody. The biosensor surface consists of an Au shell silica-core nanoparticle film. A glass slide coated with a 30 nm flat Au film and 40 nm SiO₂ served as the substrate.

For label-free detection of the peptide array, the biosensor surface in Figure 75 was analyzed with the fast read-out set-up at various wavelengths. Figure 76 presents SPR images of the biosensor surface at three different wavelengths.

As shown in Figure 76, SPR images of Au shell-silica core nanoparticle films at different wavelengths exhibited inhomogeneously reflected light over the entire illuminated area. It is obviously challenging to detect protein arrays on such an inhomogeneous background by following the reflected light intensity. Therefore, it is necessary to prepare optically homogeneous core-shell nanoparticle-based biosensor surfaces for detection of proteins in array format in both SPR imaging and SPR wavelength shift measurements.

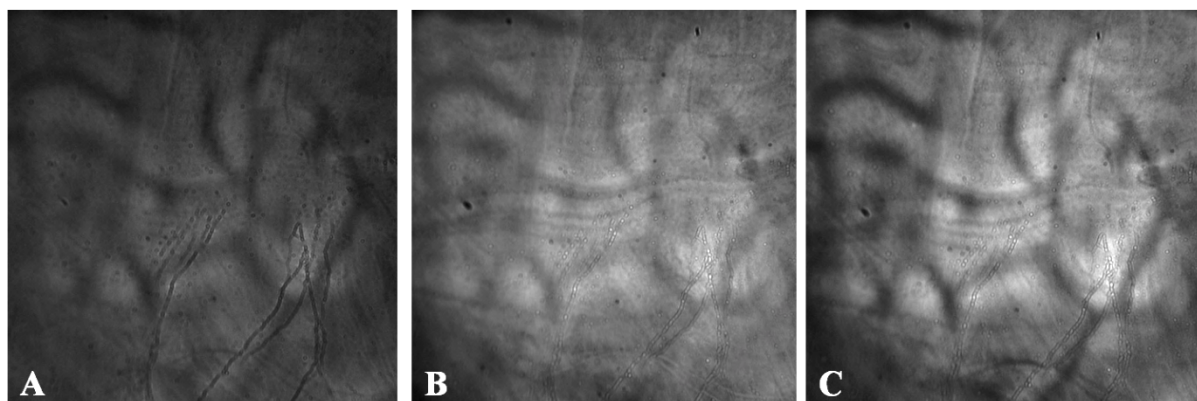


Figure 76. SPR images of the Au shell silica-core nanoparticle film on the biosensor surface to which the peptide array in Table 1 was transferred. Wavelengths: A) 550 nm, B) 600 nm and C) 650 nm. A glass slide coated with a 30 nm flat Au film and 40 nm SiO₂ served as the substrate.

To apply SPR imaging as a label-free detection method for binding events in peptide arrays it is important to have a good contrast between the background (unoccupied areas on the sensor surface) and the protein (peptide with bound antibody) array since the reflected light intensities at different wavelengths are used to generate SPR peaks of the background and the protein array. Thus, the biosensor surface has to be optically homogeneous prior to protein deposition which means that the reflected light intensity of the surface should not change drastically for different pixels (areas) of the surface at single wavelength illumination. Therefore, this biosensor surfaces prepared by seeding and consecutive electroless gold plating was not suitable for biosensing applications in array format.

Figure 77 depicts the LSPR intensity image of the same biosensor surface as in Figure 76 scanned over the corresponding wavelength regime (680-710nm). The LSPR intensity image was recorded by using the scanning unit introduced in section 4.7 with a step size of 100 μ m. LSPR intensity images are based on color coding of each pixel corresponding to the intensity of maxima of the extinction peak. As shown in the LSPR intensity image in Figure 77, the surface was found to be inhomogeneous at microscopic scale which makes it difficult to detect protein arrays.

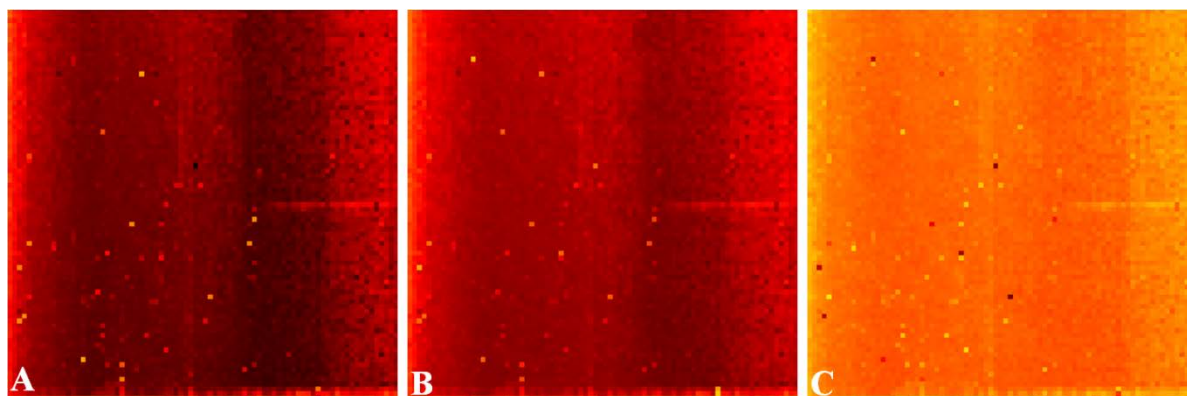


Figure 77. LSPR image of an Au shell-silica core nanoparticle film after antibody staining of the transferred peptide array taken at a step size of 100 μm . The color indicates the intensity of the extinction peak observed at wavelengths: A) 550 nm, B) 600 nm and C) 650 nm. A glass slide coated with a 30 nm flat Au film and 40 nm SiO_2 served as the substrate.

In the first experiments in which the protein array was directly spotted to the biosensor surface, configuration III in Figure 41 was found to be optically more homogeneous over the entire surface area. However, this configuration showed to be unstable with respect to TFA/toluene treatment which was used as a reaction medium for the peptide array transfer to the biosensor surface. The surface-confined Au nanoparticles were ripped off from the surface during the transfer of the protein array as indicated by the Au particle aggregates in the transfer medium. Thus, for an application of the surface as a biosensor for binding events in peptide arrays, there are two criteria which should be met: stability and optical homogeneity. Higher stability of the biosensor surfaces could be achieved by the use of core-shell nanoparticles instead of adsorbing nanoparticles on flat surfaces because on core-shell nanoparticles metal shell nanoparticles are anchored to the dielectric core. However, the more stable core-shell nanoparticles prepared by seeding and consecutive electroless plating were not optically homogeneous enough to detect small contrast changes in SPR imaging measurements. The inhomogeneous surfaces properties could be due to shell preparation by seeding and consecutive electroless plating since it is hard to control adsorption of Au nanoparticle seeds, the shell thickness and surface roughness by this technique. Therefore, shell deposition on the

dielectric core particles was intended to be improved in order to have an optically homogeneous background in SPR measurements.

One of the most common ways to deposit a metal shell on dielectric core nanoparticles is the sputter coating technique, which provides high flexibility in terms of controlling the shell thickness. In general, it provides a smoother shell surface than seeding and consecutive electroless metal plating (cf. Figure 39 and Figure 59). Therefore, the sputter coating technique was thought to produce optically more homogeneous core-shell nanoparticle films. In the next chapter, the application of such biosensor surfaces consisting of nanoparticles sputter-coated with an Au shell for SPR imaging and SPR wavelength shift measurements will be discussed.

5.3.2.3 *SPR Imaging and SPR Wavelength Shift Measurements on Core-Shell Nanoparticles with Sputter-Coated Metal Shell*

Au shell-silica core nanoparticle surfaces were prepared and optimized in sensitivity experiments upon fibrinogen adsorption as discussed in section 5.2.2. In SPR imaging measurements, the biosensor surfaces prepared by sputter coating were found to be optically more homogeneous than the biosensor surfaces prepared by seeding and electroless metal plating (cf. Figure 76 and 78). The SPR images of the Au shell-silica core nanoparticle film prepared by sputter coating the Au shell are shown in Figure 78 and indicate an optically homogeneous biosensor surface.

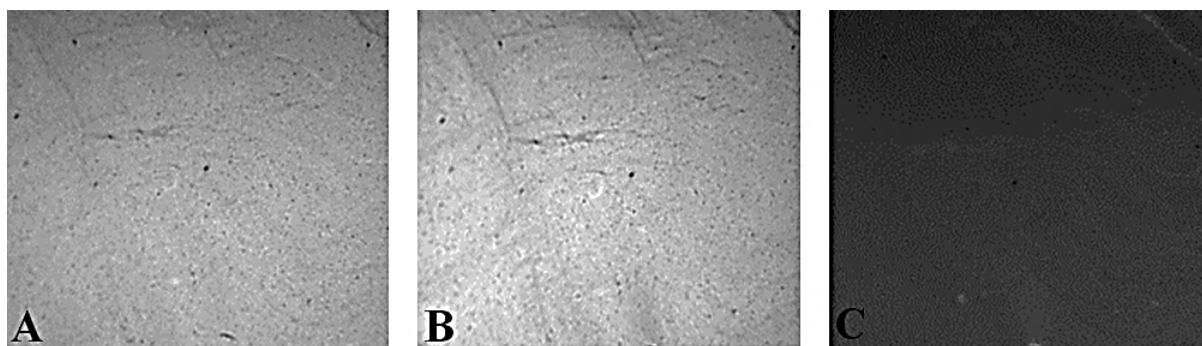


Figure 78. SPR images of a Au shell-silica core nanoparticle film on 30 nm flat Au with sputter-coated Au shell (~20nm) at different wavelengths A) 550 nm, B) 600nm and C) 650nm

The optical homogeneity of the biosensor surface was also checked in the LSPR images which are depicted in Figure 79. The LSPR image of the Au shell-silica core nanoparticle film prepared by sputter coating shows better optical homogeneity than the film prepared by seeding and plating (Figure 77). Therefore, Au shell-silica core nanoparticle biosensor surfaces prepared by sputter coating of the Au shell were considered to be favorable for the label-free detection of binding events in peptide arrays.

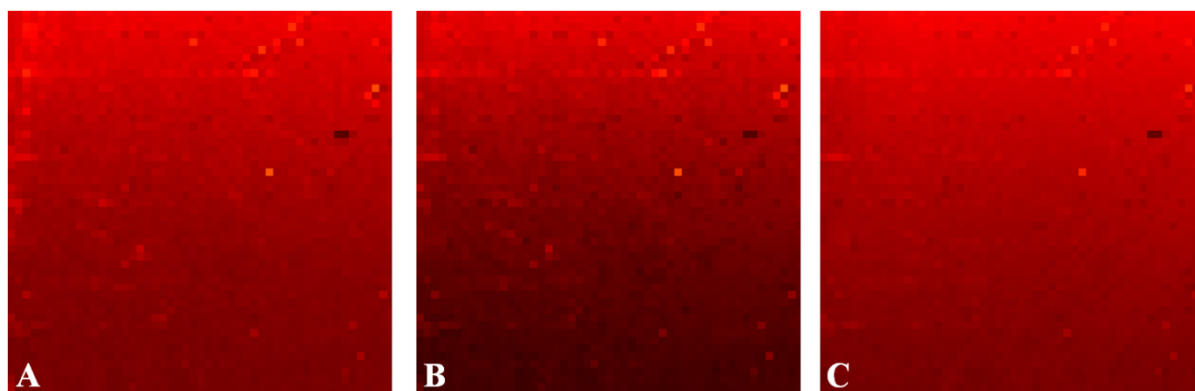


Figure 79. LSPR image of a Au shell-silica core nanoparticle film (taken at a step size of 100 μm) with sputter-coated Au shell (~ 20 nm) on 30 nm flat Au at wavelengths A) 550 nm, B) 600 nm and C) 650 nm in comparison to Figure 78.

A peptide array was transferred from the synthesis surface to the biosensor surface for 30 min as explained in section 5.3.2.2. Figure 80A shows a fluorescence image after immunostaining the biosensor surface with mouse anti-HA IgG and goat anti-mouse IgG, conjugated with DyLight680. The fluorescence pattern on the biosensor surface indicates the specific transfer of the cysteine-terminated peptides to the biosensor surface with good lateral resolution. Moreover, when the biosensor surface was analyzed with the fast read-out set-up at different wavelengths, the protein array could be detected in a label-free format as shown in Figure 80B. Thus, in principle it is possible to detect transferred protein arrays in a label free format by using the fast read-out set-up after the peptides had been transferred to the biosensor surface and reacted with specific antibodies. The SPR imaging measurements and fluorescence scan are proving the label-free and label-based detection of the protein array.

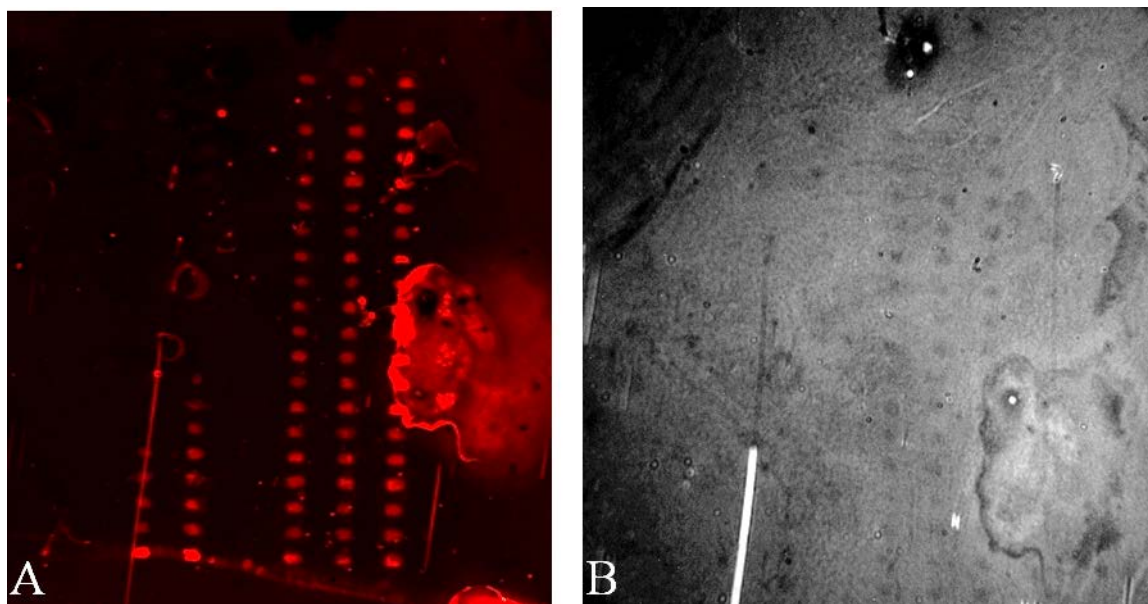


Figure 80. A) Fluorescence image of a peptide array stained with dye-labeled secondary antibody on an Au shell-silica core nanoparticle film and B) SPR image at 535 nm. A 40 nm SiO₂ layer on a 30 nm flat Au film served as the substrate (4 s integration time for B)

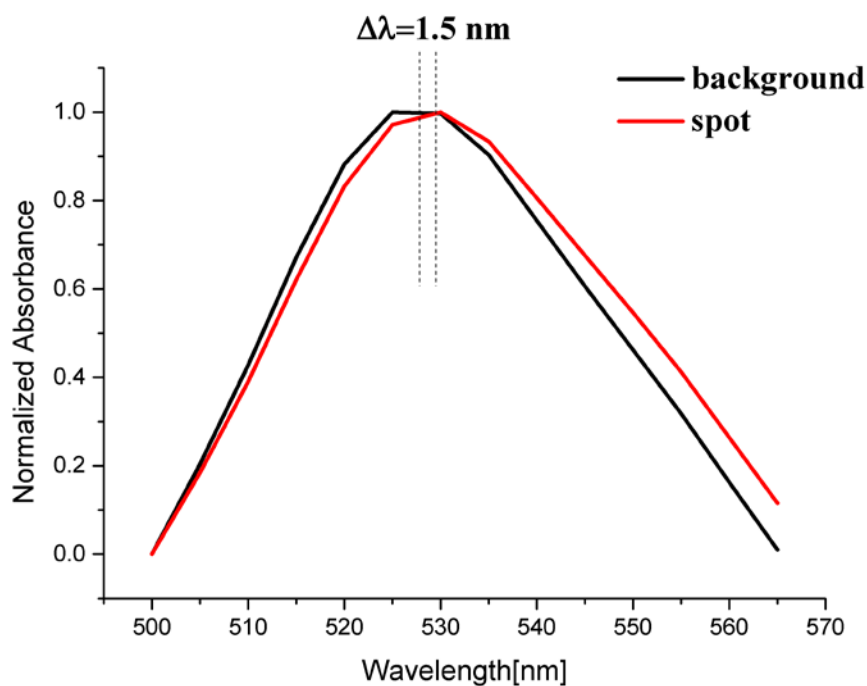


Figure 81. SPR wavelength shift spectra of background and protein spot

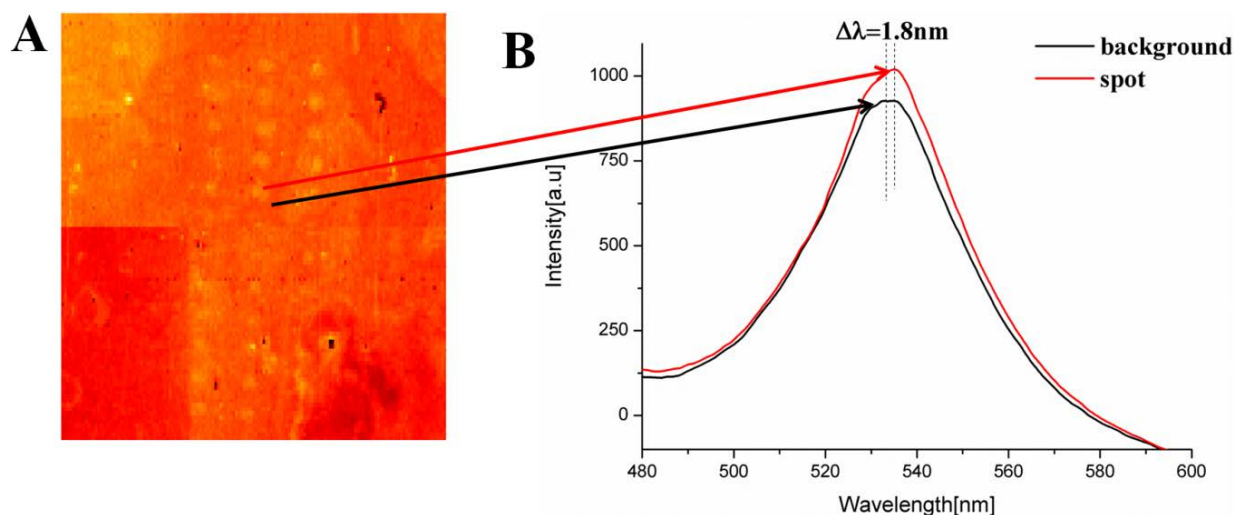


Figure 82. A) LSPR intensity image of Au shell-silica core nanoparticle film after peptide array transfer and antibody staining. B) UV-Vis spectra of protein spot and corresponding background. (The step size was 50 μm)

The biosensor surface was analyzed at different wavelengths (between 500 and 565 nm) with a scanning interval of 5 nm to determine the wavelength shift upon protein array binding to the biosensor surface. Figure 81 shows the SPR peak of a protein spot and the corresponding background between which 1.5 nm wavelength shift was obtained. In addition to this, the same surface was scanned for the LSPR image which is shown in Figure 82A. The corresponding wavelength shift was found to be 1.8 nm.

To increase protein density, the peptide array was transferred in an experiment from the synthesis surface to the biosensor surface with a prolonged incubation time of 2 h (instead of 30 min) as explained in section 5.3.2.2. Figure 83A shows a fluorescence image after immunostaining the biosensor surface with mouse anti-HA IgG and goat anti-mouse IgG, conjugated with DyLight680. The fluorescence pattern on the biosensor surface indicates the specific transfer of the cysteine-terminated peptides to the biosensor surface with good lateral resolution and the reproducibility of the transfer experiment. Furthermore, when the biosensor surface was analyzed with the fast read-out set-up at different wavelengths, the protein array was detected in a label-free format as shown in Figure 83B.

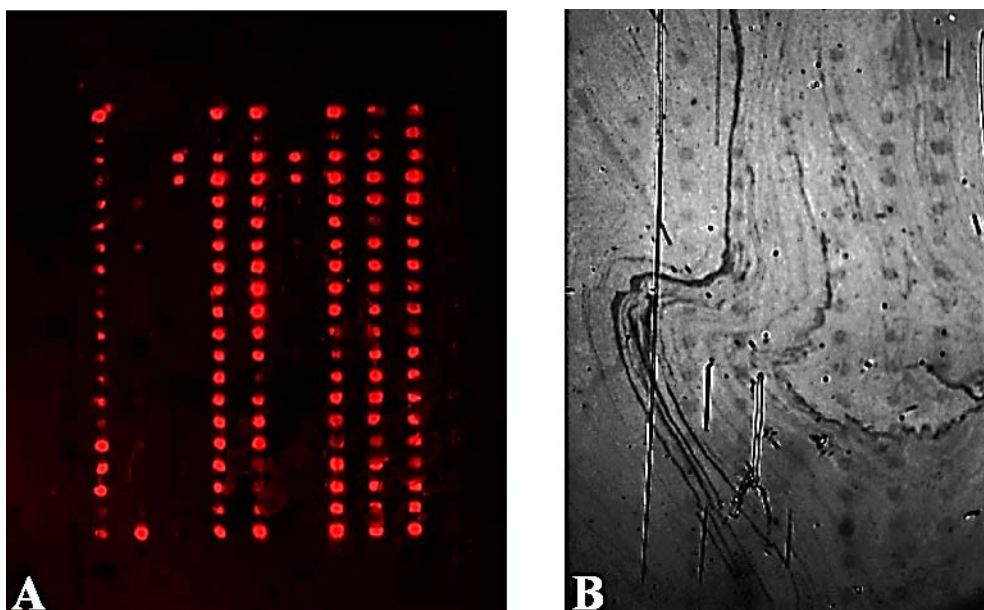


Figure 83. A) Fluorescence image of a peptide array stained with dye-labeled secondary antibody on a Au shell-silica core nanoparticle film and B) SPR image at 530 nm. A 40 nm SiO₂ layer on a 30 nm flat Au film served as the substrate (10 s integration time for B)

The biosensor array was analyzed at different wavelengths (480-565 nm) with a scanning interval of 5 nm to determine the wavelength shift upon protein binding to the surface. Figure 84 shows the SPR peak of a protein spot and the corresponding background in which the wavelength shift was displayed as 3.6 nm. Longer transfer of the peptide array caused an increase in the protein mass density on the biosensor surface by providing more binding sites for the antibodies.

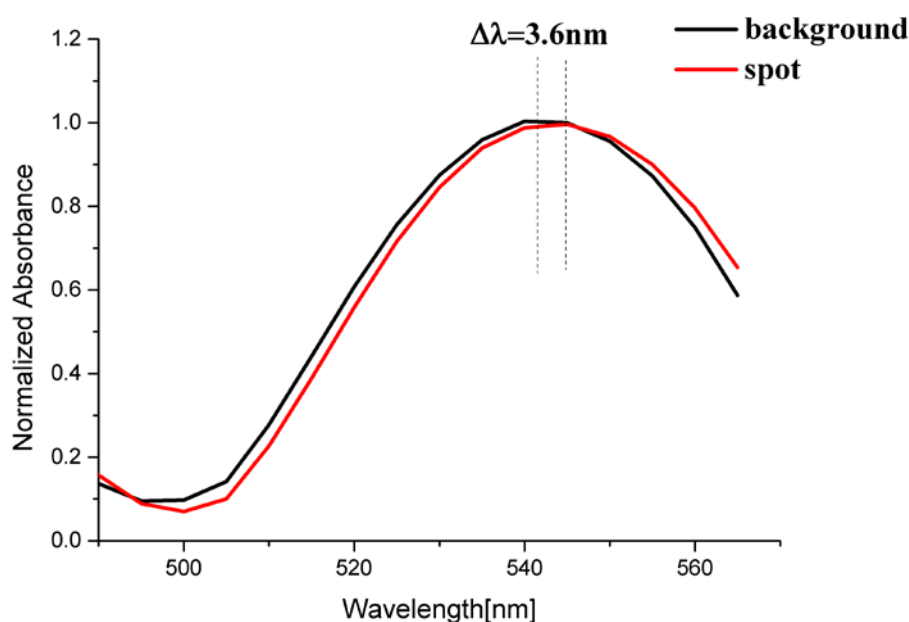


Figure 84. SPR wavelength shift spectra of background and protein spot

The same biosensor surface was scanned for the LSPR image with the scanning unit as shown in Figure 85. The corresponding wavelength shift was found to be 4 nm as shown in the UV-Vis spectra of the spot and background in Figure 85.

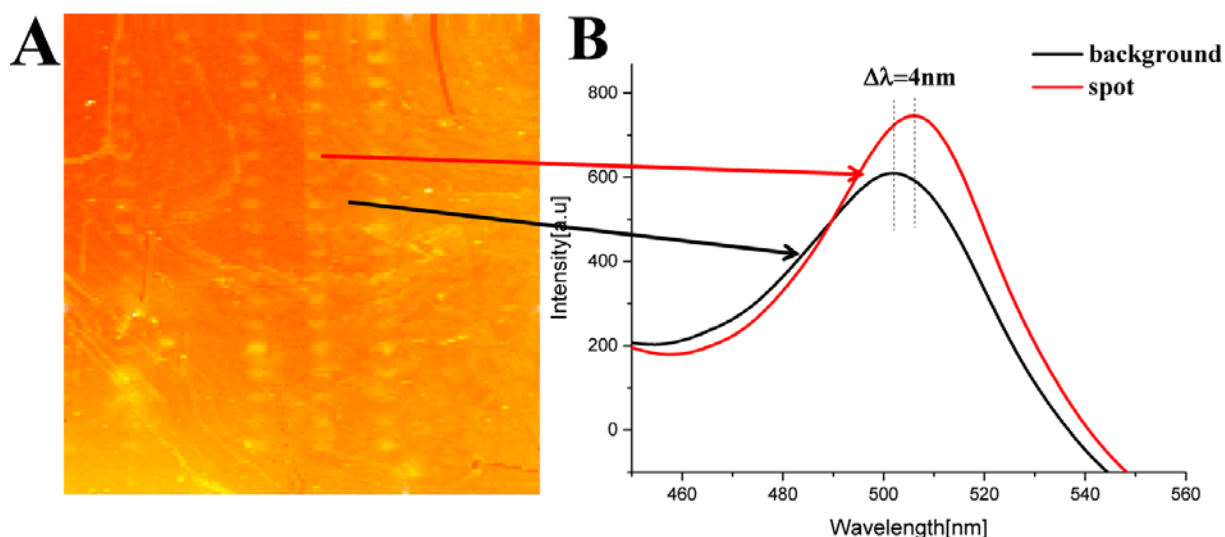


Figure 85. A) LSPR image of a Au shell-silica core nanoparticle film after peptide array transfer and antibody staining. B) UV-Vis spectra of protein spot and corresponding background. (The step size was 50 μm)

The surface density of protein of the label-free detected protein array on the biosensor surface is not exactly known since the amount of transferred peptide per spot and the amount of coupled antibody could not be quantified. Therefore, a spotting method was used to deposit a determined amount of protein (antibody) on the same kind of biosensor surface in order to figure out the detection limit in wavelength shift measurements. Moreover, such data should help to estimate the total deposited protein density in the peptide array transfer experiments. For this purpose, ATTO 680 conjugated anti-HA IgG (1mg/ml) was spotted at different concentrations (v/v 1:5, 1:25, 1:50, 1:100, 1:250 in PBS) onto the biosensor surface in a 9x25 array format. Each spot was formed from 0.5 nl antibody solution with 250 μm diameter and 400 μm center-to-center distance. Figure 86A shows the fluorescence image of the antibody arrays at different concentrations on the same biosensor surface which confirms the

presence of antibody array on the surface. The SPR image of the nanoparticle film at 500 nm is shown in Figure 86B.

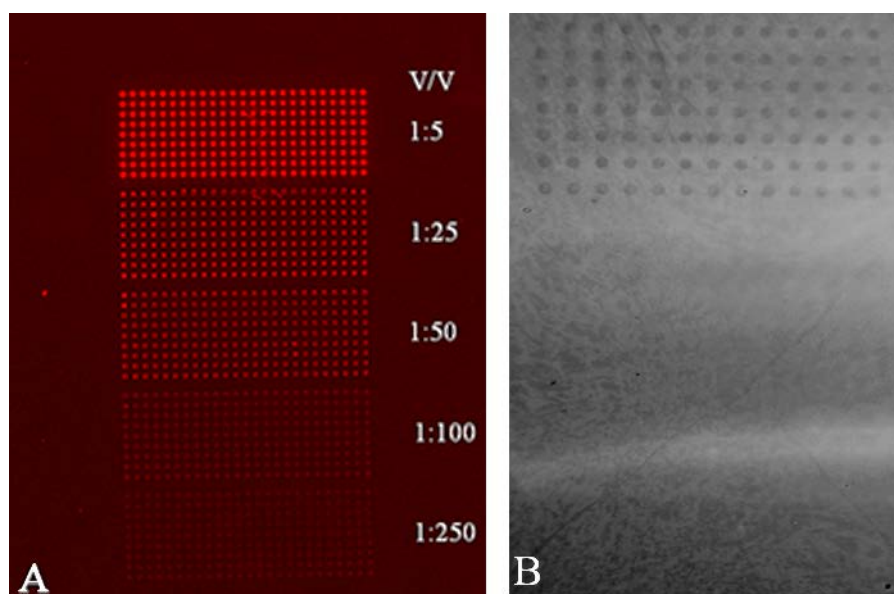


Figure 86. A) Fluorescence image of antibody array at different concentrations and B) SPR image of the nanoparticle film with the same antibody array at 500nm.

In the SPR image of the nanoparticle film only the array spotted with the highest antibody concentration was observed which corresponds to 1 ng/mm^2 protein on the biosensor surface. Unfortunately, lower concentrations were not detected with SPR imaging measurements. When the nanoparticle film was scanned at different wavelengths for wavelength shift measurements, the observed antibody spot and the background yielded the SPR peaks given in Figure 87. The wavelength shift was found to be 2 nm upon 1 ng/mm^2 protein adsorption to the surface. The obtained wavelength shift of 2 nm was found to be similar to the wavelength shift in peptide transfer experiments, which amounted to 1.5 nm and 3.6 nm for 30 min and 2 h transfer time, respectively.

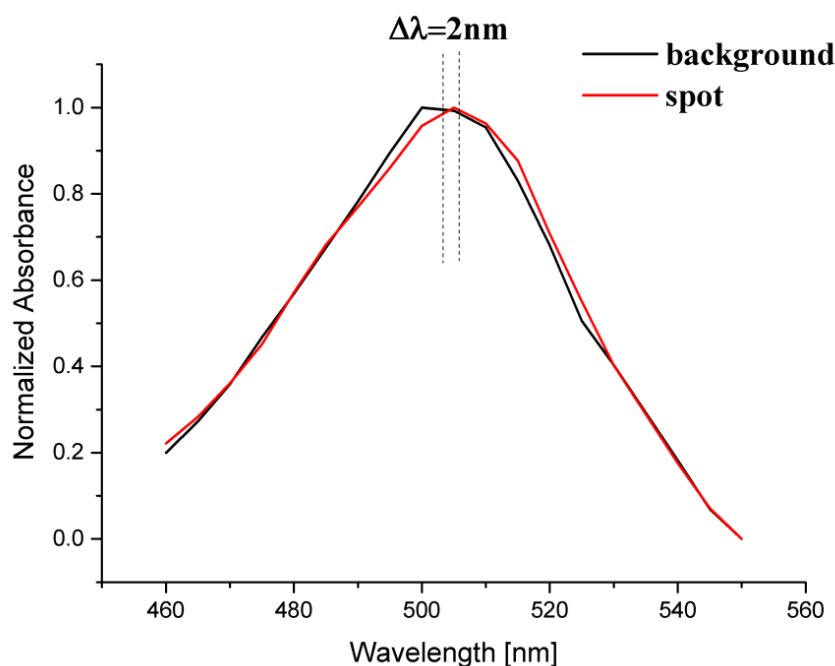


Figure 87. SPR wavelength shift spectra of background and protein spot

The same surface was analyzed with the LSPR scanning unit for cross-checking the results with another technique. Figure 88 shows the LSPR image of the nanoparticle film with the antibody array (1 ng/mm^2) and the corresponding UV-Vis spectra of the antibody spot and the background. 2.5 nm shift was obtained upon 1 ng/mm^2 antibody adsorption to the nanoparticle film. The wavelength shifts from two different set-ups (scanning unit and the fast read-out set-up) were found to be similar and confirming the validity of the obtained wavelength shifts.

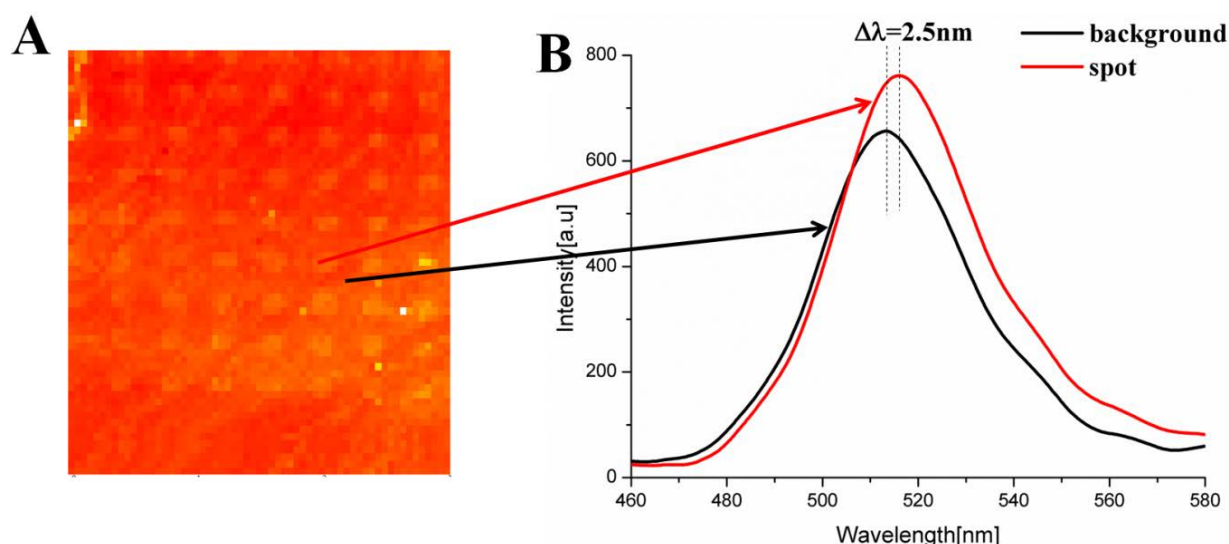


Figure 88. A) LSPR intensity image of an Au shell-silica core nanoparticle film with spotted antibody array (1ng/mm² protein). B) UV-Vis spectra of protein spot and corresponding background are shown (The step size was 50μm).

The sensitivity factor for the core-shell nanoparticle film (Au shell-polystyrene core) was reported to be 2.7 nm/(ng/mm²) by Buecker et al.^[7] which is comparable to the value of 2 nm/(ng/mm²) derived from the wavelength shift of 2nm for 1 ng/mm² protein adsorption on core-shell nanoparticle film in this thesis. After comparison the sensitivity results of earlier experiments^[62] polystyrene as core nanoparticle, it can be stated that the choice of the core nanoparticle material (either silica or polystyrene) does not significantly affect the wavelength shift (sensitivity) of core-shell nanoparticle film. In these experiments, the nanoparticle films were prepared by adsorbing the core nanoparticles by floating self-assembly. The shell formation was formed by seeding and consecutive electroless gold plating. The sensitivity of the nanoparticle films was evaluated as discussed in section 4.6.1. As a consequence of the earlier experiments, silica was chosen as core nanoparticle because polystyrene is not stable with respect to TFA and toluene treatment. In contrast, silica as core material is chemically inert to the peptide microarray transfer conditions.

In summary, the fast read-out set-up could be successfully implemented to detect spotted protein arrays and transferred peptide microarrays after the corresponding immunostaining in a label-free format. However, the immunostained peptide microarray showed only low

wavelength shifts which was traced back to a low amount of surface-bound protein. The resulting wavelength shift upon protein adsorption on an optically homogeneous Au shell-silica core nanoparticle film was found to be in the range of 1.5 nm. The LSPR imaging set-up based on the scanning unit confirmed the wavelength shift obtained in the wavelength shift measurements using the fast read-out set-up.

In order to determine the amount of protein in a transferred and immunostained peptide microarray, the antibody which was used in the immunostaining was spotted on the same nanoparticle film. As a result, the detection limit of the nanoparticle film was found to be in the range of 1 ng/mm² resulting in about 2 nm wavelength shift with the fast read-out set-up and about 2.5 nm with the scanning unit. Therefore, the protein mass density in the transfer experiments could be estimated to be about 1 ng/mm² for 30 min transfer time and almost double that value for 2 h of incubation with transfer solution.

5.4 Wavelength Averaging of Long Wavelength Peak for Better Sensitivity

A crucial parameter for detection of the protein interactions is the sensitivity of the biosensor surface. Based on the experiments discussed in previous sections, the detection limit of the biosensor was found to be around 1 ng/mm² protein mass density resulting in 2.5 nm wavelength shift, which may not be enough to identify low affinity protein binding reactions. Therefore, the sensitivity of the biosensor surface should be improved. However, the parameters discussed in previous sections to enhance the sensitivity which are inter alia (i) introduction of a dielectric layer in between core-shell particles and the flat metal film, (ii) changing the metal shell from Au to Ag and (iii) changing the metal shell deposition method from seeding and consecutive electroless plating to sputter coating, did not have an impact of more than a factor of two (cf. section 5.2.1 and 5.2.2).

Homola et al.^[106] reported the sensitivity factor, S_n , with the following expression:

$$S_n = \frac{d\lambda}{dn_s} = \frac{n_p \varepsilon_{mr}}{\frac{n_p}{\lambda} n_s^3 \left(\frac{1}{\varepsilon_{mr}} - 1 \right) + \frac{dn_p}{d\lambda} n_s (n_s^2 + \varepsilon_{mr})} \quad (\text{Equation 21})$$

where λ is the resonant wavelength, n_s is the refractive index of the sensed medium, ε_{mr} is the real part of the dielectric constant of the metal and n_p is the refractive index of the prism. Theoretical calculations and experimental studies^[106,119-121] suggested that the sensitivity with respect to the changes of the resonant wavelength and the refractive index of the bulk sensed medium increases monotonously with wavelength for gold and silver as shown in Figure 89.

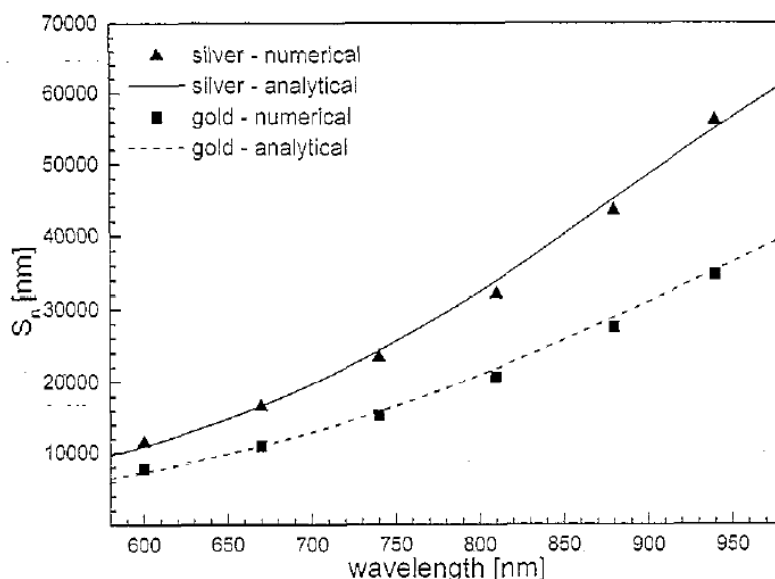


Figure 89. Sensor sensitivity, S_n , as a function of wavelength for the structure: BK7 glass prism, surface plasmon active metal layer (gold and silver with 50 nm thickness), gaseous sensed medium ($n_s=1$)^[106].

In the UV-Vis spectrum of a biosensor surface (cf. Figure 41), which was described in section 5.2.1.1.1, there are two distinct peaks at shorter and longer wavelength as discussed in section 5.2.1.1. The shorter wavelength peak was chosen to analyze and optimize the biosensor sensitivity with the UV-Vis reflection set-up (cf. Figure 33A) upon nonspecific protein adsorption because its wavelength shift upon protein adsorption was much more reproducible. Moreover, the optical homogeneity of the sensor surfaces was much better for the short than the long wavelength peak on the same sample with full-width at half maximum (FWHM) values of 3.4 nm and 28.2 nm, respectively, for the variation in peak position as shown in the histograms in Figure 90.

The histograms were obtained from an LSPR image taken with the scanning unit and display the number of positions on the surface for which a specific peak position has been recorded. Note that the LSPR image recorded with the scanning unit can be presented in two formats: as an intensity image (cf. Figure 88), and as a data file including the x-y-coordinates and wavelength maximum for each step. The histograms in Figure 90 were prepared using the latter file format for a specific area on the biosensor surface.

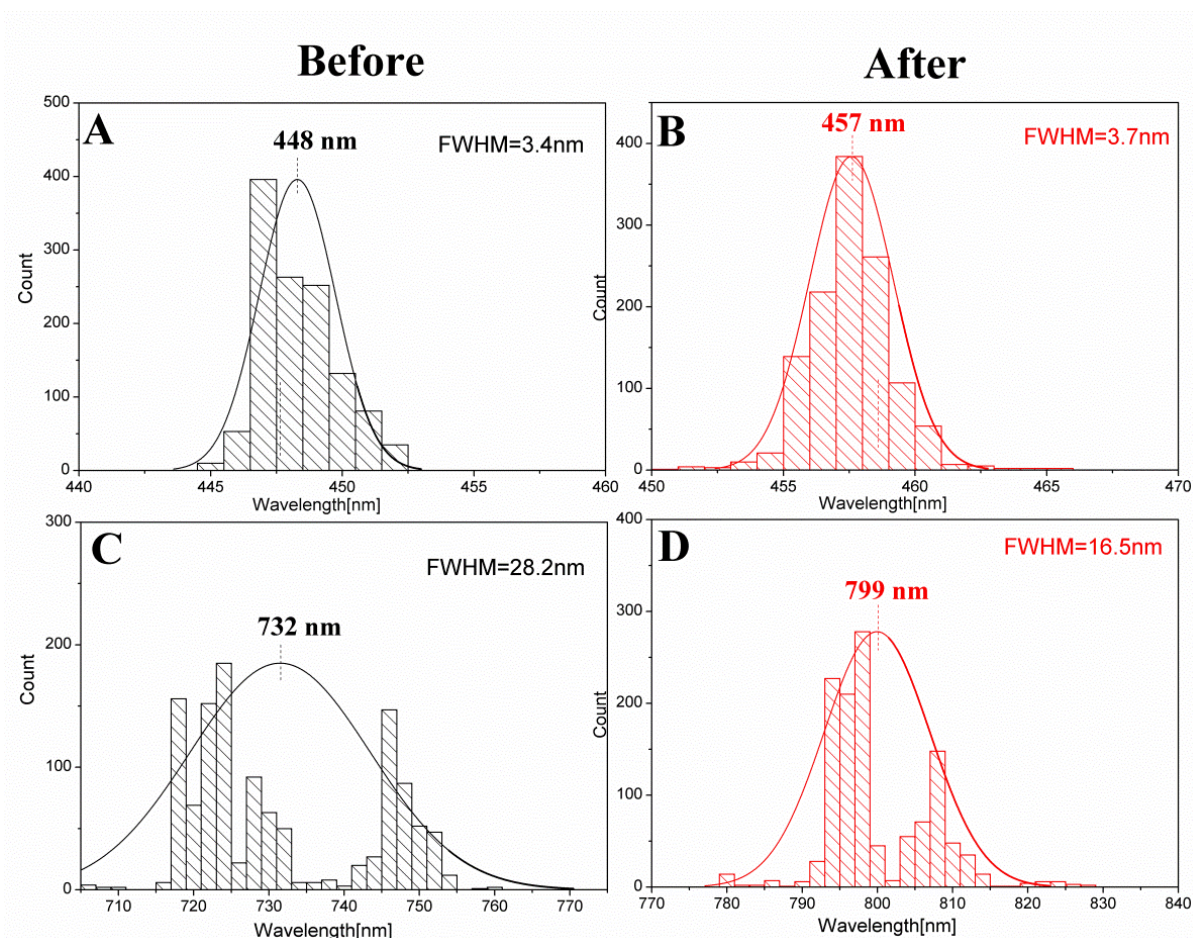


Figure 90. Distribution of the wavelength maxima of a biosensor surface for A) the short wavelength peak before protein adsorption, and B) the short wavelength peak after protein adsorption, C) the long wavelength peak before protein adsorption and D) the long wavelength peak after protein adsorption. (Configuration I in Figure 41 was used with a Au metal shell prepared by seeding and 180 s electroless gold plating) The histograms were generated from the LSPR image of the biosensor surface recorded by the scanning unit. The scanned area was 1x1 mm with 25 μ m step size. Full Width at Half Maximum (FWHM) values were calculated to be A) 3.4 nm B) 3.7 nm, C) 28.2 nm and D) 16.5 nm. They were determined from the histograms by fitting the data with a Gaussian function. Bin size was set to 1 nm for A and B, 2 nm for C and D.

To calculate the wavelength shift due to fibrinogen adsorption (c.f. section 4.6.1), the biosensor surface was scanned with the scanning unit over a particular area before and after protein adsorption. Subsequently, the histograms for before and after protein adsorption were plotted as in Figure 90 and the averaged wavelength maxima were determined for both histograms. The difference between the averaged wavelength maxima in the

two histograms was taken as the wavelength shift. This procedure is called from now on **wavelength averaging**.

Wavelength averaging was first applied to the short wavelength peak to obtain the wavelength shift upon protein adsorption (cf. Figure 90A and 90B). As displayed in Figure 91, the wavelength shift (9 nm) for the short wavelength peak was found to be similar to the ones obtained in section 5.2.1.1.1. Then, the wavelength averaging was performed for the long wavelength peak as shown in Figure 90C and 90D. As shown in Figure 91, the wavelength shift upon protein adsorption was found to be higher by about a factor of seven for the long wavelength peak compared to the short wavelength peak.

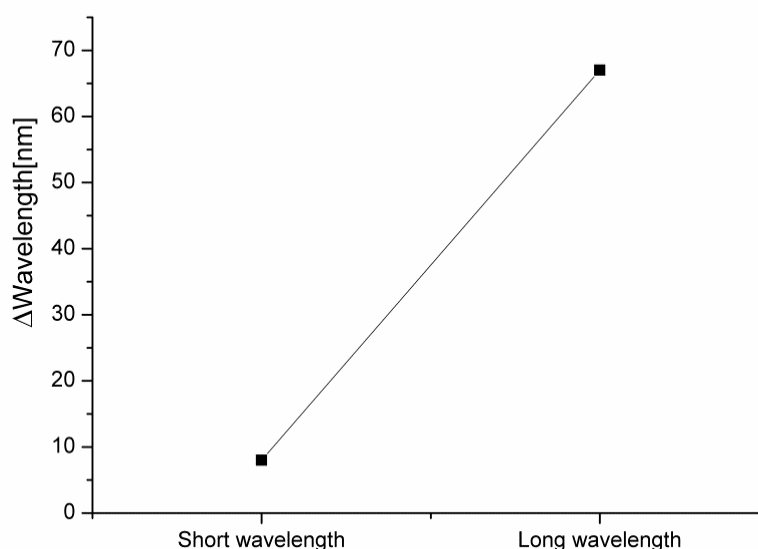


Figure 91. Wavelength shifts of the short and the long wavelength peak upon protein adsorption on the biosensor surface as deduced from Figure 90.

The wavelength averaging was carried out in order to compensate the optical inhomogeneity of the long wavelength peak during the measurements. When the protein was adsorbed on the biosensor surface homogeneously, the wavelength averaging process produced reliable results for short wavelength and long wavelength peaks. As explained above, the sensitivity of a biosensor, which is a crucial parameter for detection of protein interactions as explained above, is significantly higher for long wavelengths than for

short wavelengths. Therefore, the wavelength averaging process was also applied to the label-free detection of spotted antibody arrays to achieve a better sensitivity.

For this purpose, ATTO 680 conjugated anti-HA IgG antibody (1mg/ml) was spotted in 1:1 v/v dilution in PBS-T) onto the biosensor surface in a 20x20 array format with $\sim 300\ \mu\text{m}$ diameter and $1000\ \mu\text{m}$ center-to-center distance. Each spot was formed from 0.5 nl antibody solution resulting in a protein density of about $4\text{ng}/\text{mm}^2$ on the surface. Figure 92 shows the fluorescence image of the antibody array on the biosensor surface which confirms the presence of the proteins. The corresponding LSPR intensity image recorded with the scanning unit at 610 nm after antibody adsorption is shown in Figure 93.

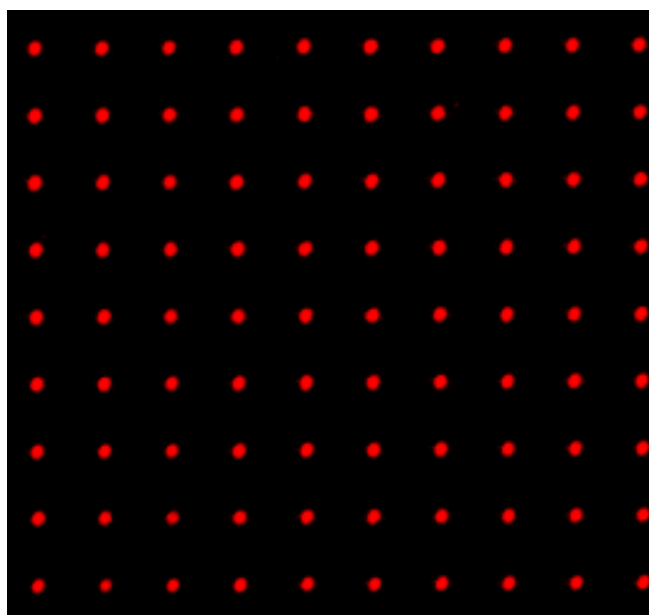


Figure 92. Fluorescence image of ATTO 680 conjugated anti-HA IgG antibody

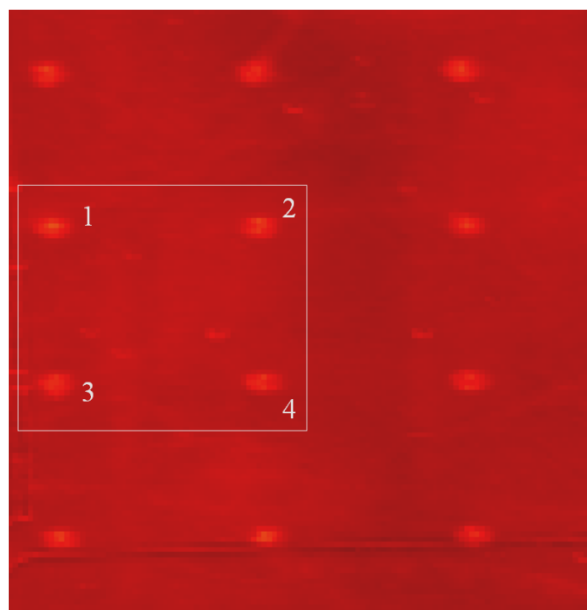


Figure 93. LSPR intensity image of Au shell-silica core nanoparticle film after antibody adsorption at 610 nm, and the four selected antibody spots for wavelength averaging. (The step size of the scan is 25 μ m)

The wavelength averaging was carried out for four selected antibody spots, as shown in Figure 93, for both scanning the biosensor surface before and after antibody adsorption. For this purpose, reflectivity data obtained for a 4x4 matrix of adjacent measurement steps in the center of the antibody spots was chosen for wavelength averaging. The histograms of the 16 peak positions evaluated in each spot are displayed in Figure 94. The corresponding LSPR intensity and wavelength images of the core-shell nanoparticle film before and after antibody adsorption are displayed in Figure 95 for the four antibody spots. The LSPR wavelength image was generated using the wavelength maximum of each pixel within an antibody spot and plotted with Origin (OriginLab/USA) as a color coded map as shown in Figure 95.

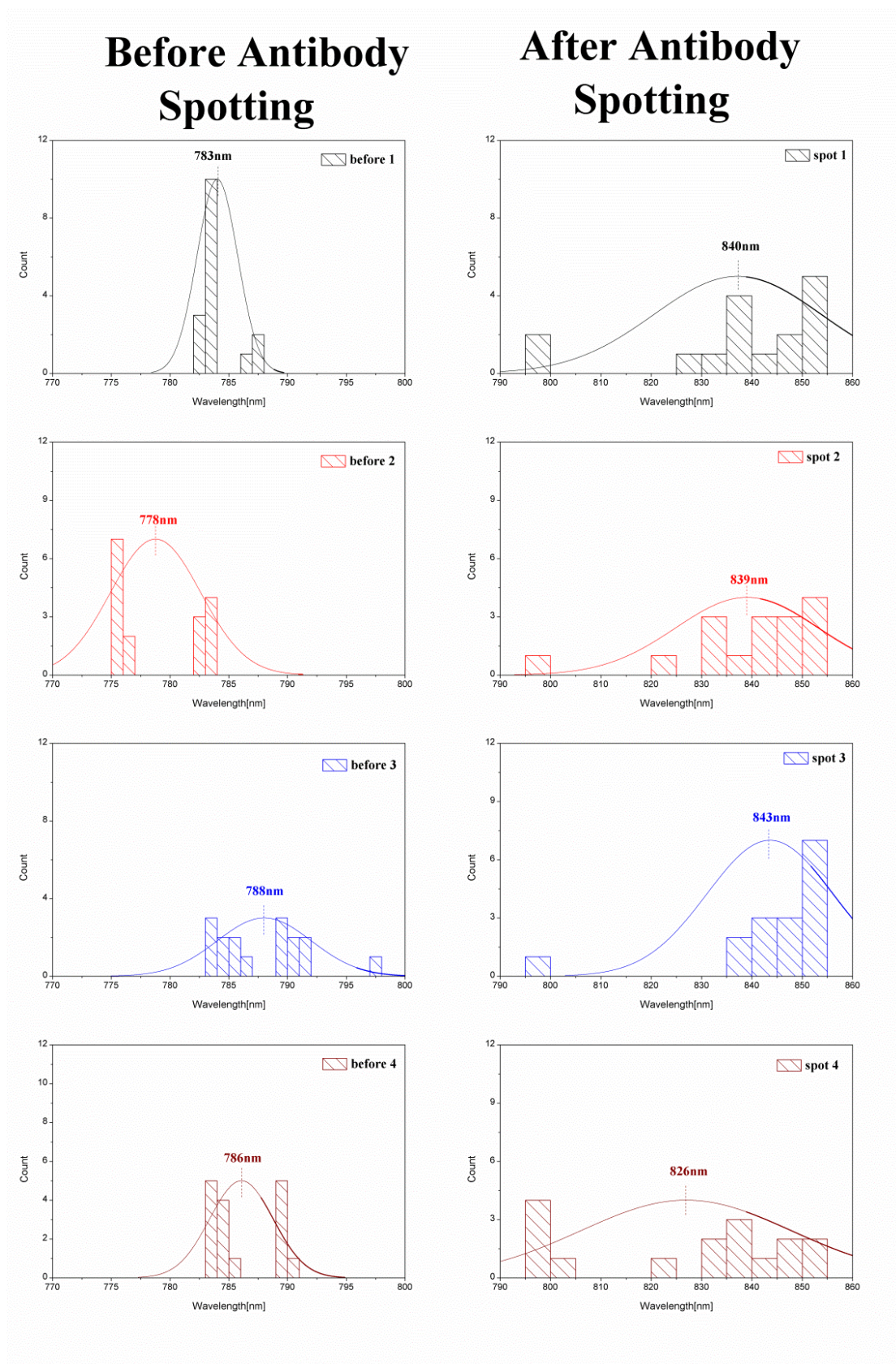


Figure 94. Distribution of the wavelength maxima of a biosensor surface after antibody adsorption for four different spots and their corresponding area before antibody adsorption. (16 pixels for each histogram, bin size is 5 nm for after antibody adsorption column and 1 nm for before antibody adsorption column)

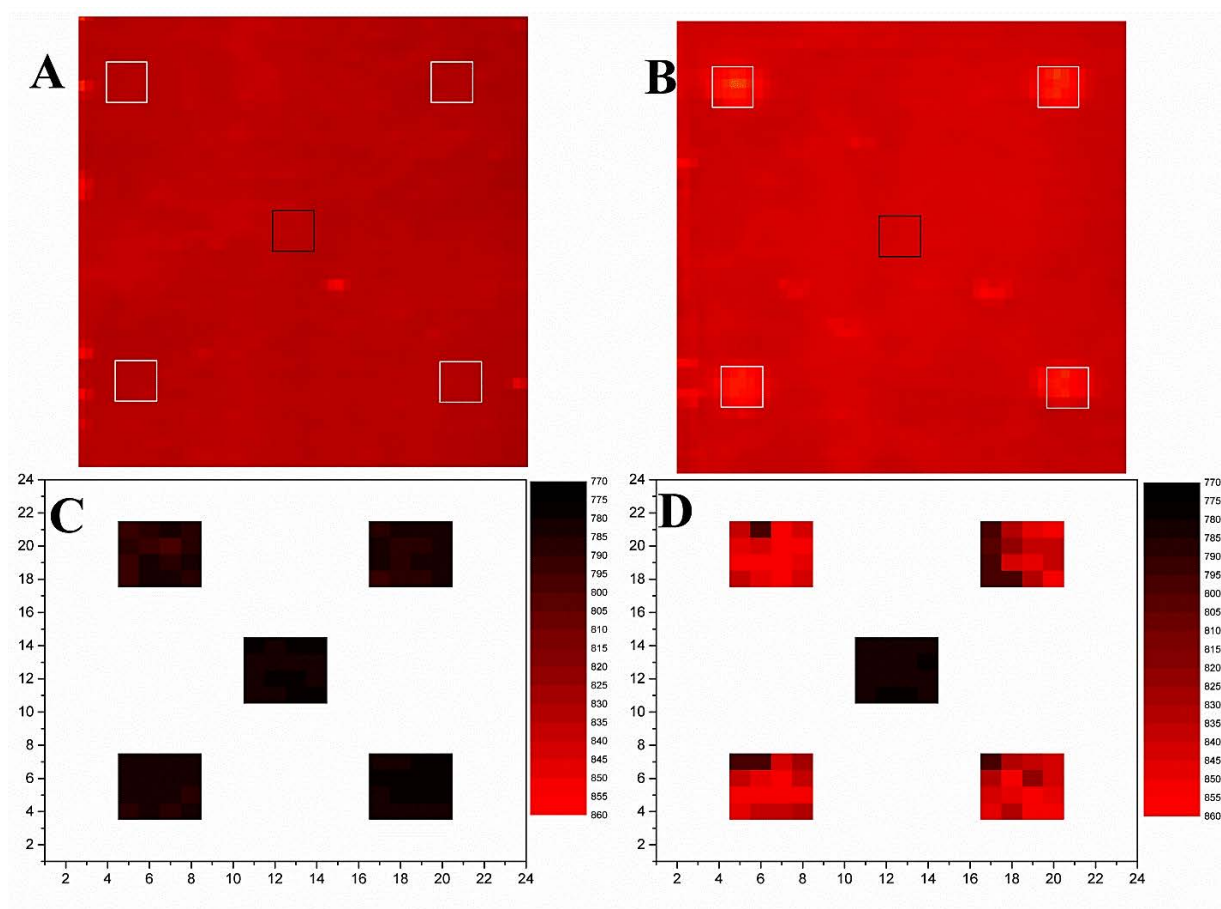


Figure 95. LSPR intensity images of the Au shell-silica core nanoparticle film A) before antibody spotting, B) after antibody spotting, and LSPR wavelength images C) before antibody spotting for the marked areas of image A and D) after antibody spotting for the marked areas of image B. The LSPR wavelength images were obtained from the histograms in Figure 94. Color codes in A and B show the peak intensity, in C and D the peak position determined for each step of scanning. LSPR intensity images were recorded at 610 nm with a step size of 25 μm . (White squares correspond to areas before and after antibody adsorption and black square corresponds to background where there was no antibody present)(Center to center distance in C and D was reduced and the images were magnified to show the details of the analysis)

As displayed in Figure 95, the wavelength position of the extinction peak varies within each spot due to the optical inhomogeneity of the samples, which is particularly pronounced for the long wavelength peak. Therefore, for each spot the obtained wavelength positions were averaged and the individual wavelength positions were replaced by the averaged one and its corresponding color (“wavelength averaging”). The same procedure was applied to a 4x4 array in the center of Figure 95 A) and B) (marked black) to account for the averaged peak position of matrix material in between the

spots, the so-called background. This background peak position was attributed to all areas of the image except the antibody spots. Figure 96 shows the corresponding wavelength images together with the color code for the individual wavelengths.

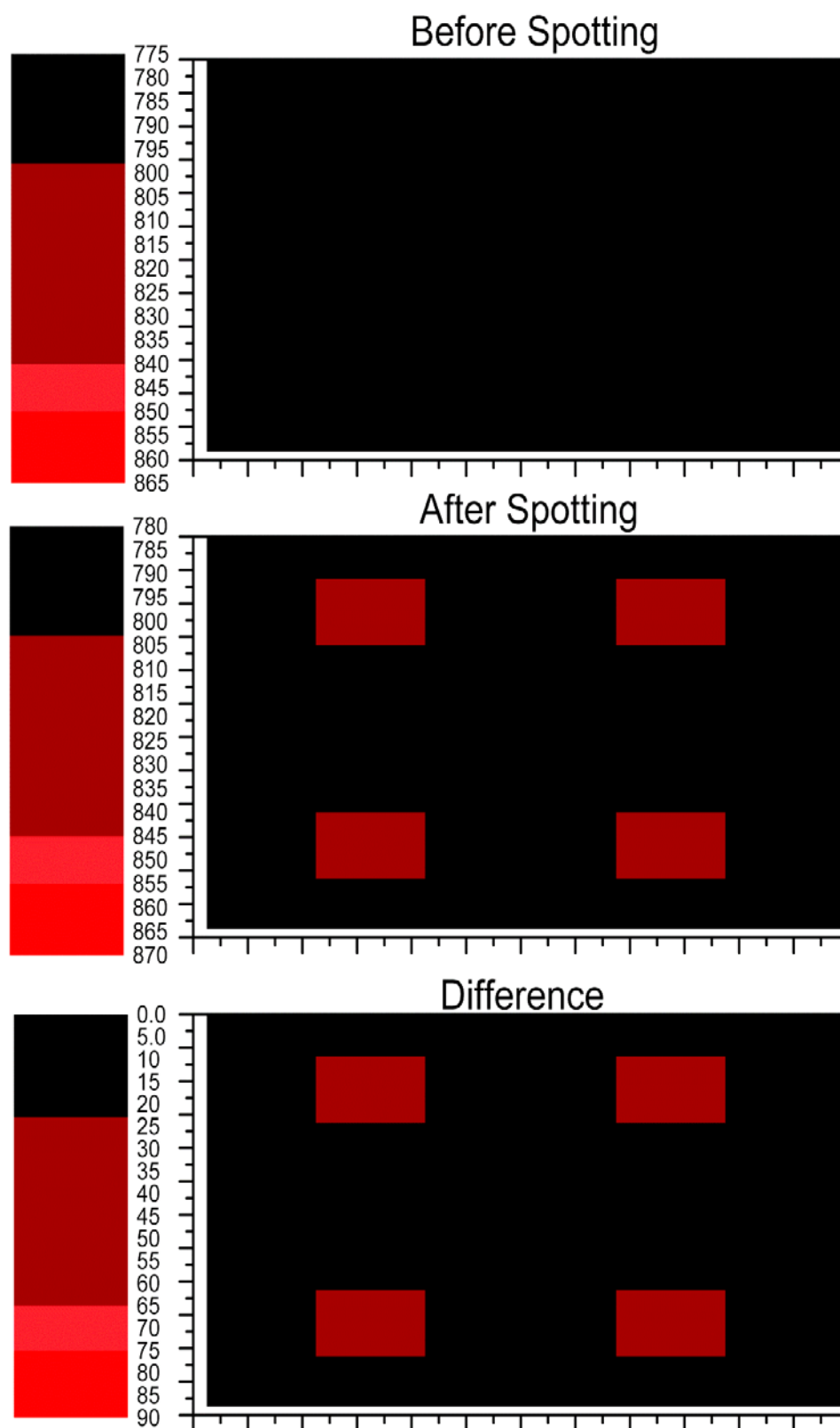


Figure 96. LSPR wavelength images after the wavelength averaging process for A) before antibody spotting and B) after antibody spotting. C) displays the difference between B) and A). (Center to center distance in images was reduced and the images were magnified to show the details of the analysis as in Figure 95)

The calculated wavelength shifts for the difference in Figure 96 were 57, 61, 55 and 40 nm for the four antibody spots, resulting in an average value of 54 ± 9 nm. As mentioned in section 5.3.2.3, the sensitivity factor for the core-shell nanoparticle film was reported to be 2.7 nm/(ng/mm²) by Buecker et al.^[7]. The sensitivity of core-shell nanoparticle film after wavelength averaging was calculated $54\text{nm}/(4\text{ng}/\text{mm}^2)=13.5 \text{ nm}/(\text{ng}/\text{mm}^2)$. Thus, the sensitivity of the core-shell structure can be improved by a factor of five when the measurements are done using the long wavelength peak of the core-shell structure.

Figure 97 compares the LSPR intensity and wavelength images of the four protein spots. The wavelength image shows the presence of protein spots more distinctive than the intensity image. Therefore, it would be advantageous to work with the wavelength image in the detection of low affinity binding events and/or interactions in high density peptide arrays.

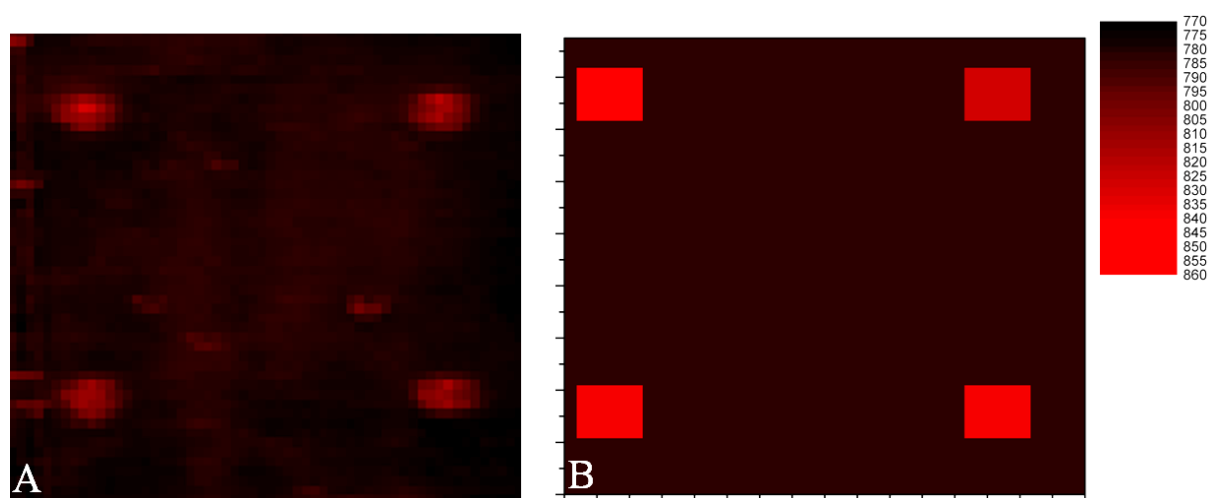


Figure 97. A) LSPR intensity image and B) LSPR wavelength image of the four protein spots. The color code is only valid for B.

The wavelength averaging can also be applied to the detection of interactions in high density peptide arrays to achieve higher sensitivity and reproducibility using the long wavelength peak. However, there are certain criteria to be fulfilled for interaction analysis in high density peptide arrays with improved sensitivity. First, the long wavelength peak only shows higher

wavelength shifts than the short wavelength peak when the metal shell is prepared by seeding and consecutive electroless metal plating. In case of sputter-coated metal shells, the wavelength shifts were found to be similar for both peaks.

Second, the biosensor surface should be blocked after peptide array transfer with a blocking agent molecule. In experiments with sputter-coated metal shells (cf. section 5.3.3) EG7-SH was used to prevent nonspecific antibody binding. The blocking step with EG7-SH has not been successful for the core-shell nanoparticles when the metal shell is prepared by seeding and consecutive electroless metal plating due to heterogeneous chemistry of the biosensor surface: As metal coverage is incomplete, it consists of both SiO₂ and Au surface areas together with a rough metal surface (cf. Figure 39). For successful detection of interactions in high density peptide arrays the biosensor surface should be properly blocked to prevent nonspecific antibody binding. One strategy might be to block the Au shell with EG7-SH and the non-metallized SiO₂ areas with an EG-functionalized silane. Corresponding experiments are still in progress.

Another crucial parameter is to carry out the measurements at exactly the same positions before and after protein adsorption, particularly in case of protein adsorption in array format. Two possible instruments could be used to conduct these measurements: the scanning unit (cf. Figure 33B) and the CCD-based fast read-out set-up (cf. Figure 63). The scanning unit produces two different kinds of LSPR images, intensity and wavelength images, the latter of which were used for the wavelength averaging process. However, the measurements with the scanning unit are inefficient for high-resolution scans on large surface areas due to the low scanning speed and still existing software problems with respect to data handling. On the other hand, the CCD-based fast read-out set-up can be an alternative to overcome these obstacles. It can be used to generate SPR intensity images at different wavelengths, which can next be converted into SPR wavelength images for wavelength averaging. Considering the high number of pixels in the CCD chip, all of which contribute individual peak positions for further analysis,

an automated data analysis software is presently developed in collaboration with *J. Wagner*.

In summary, wavelength averaging was successfully applied to achieve significantly enhanced sensitivity ($\sim 13.5 \text{ nm}/(\text{ng}/\text{mm}^2)$) for detection of proteins in array format. After certain improvements in the experimental procedure and data analysis discussed above, the wavelength averaging procedure will also be applicable to interaction analysis in high density peptide arrays.

5.5 Use of Core-shell Nanoparticles as Surface Enhanced Raman Scattering (SERS) Substrates

One of the applications of core-shell nanoparticle films is the enhancement of weak Raman signals due to their strong SPR response in Surface Enhanced Raman Scattering (SERS). As explained in section 2.2.2 two types of mechanism are responsible for the enhancement of Raman signals, namely the electromagnetic and the chemical mechanism. SERS enhancement is dependent on nanoparticle structure, size and their dielectric constant. In chemical enhancement, there should be an interaction between the metal surface and the molecule which might lead to a wavenumber shift in the SERS spectrum^[122,123].

In the first part, SERS enhancement of Au shell-silica core nanoparticles having different Au shell thickness is going to be discussed by adsorbing methylene blue (MB) as an analyte molecule. Moreover, the SERS enhancement of MB on Ag shell-silica core nanoparticles is compared to the enhancement on Au shell-silica core nanoparticles.

In the second part, SERS spectra of fibrinogen were recorded on both Au shell-silica core and Ag shell-silica core nanoparticle films.

5.5.1 SERS of MB on Core-Shell Nanoparticles

Core-shell nanoparticle films were prepared as discussed in section 4.3.3, 4.4 and 4.5 on a 30 nm flat Au film deposited on a Si wafer. The 785 nm excitation line was used to excite SPs. The surfaces were exposed to an UV lamp for 30 min for removal of potential impurities prior to analyte adsorption. 10 μ l of a 10^{-4} M MB solution was adsorbed onto a core-shell nanoparticle film on a 10x10 mm substrate without further washing steps in order to keep the number of analyte molecules ($\sim 6 \times 10^{10}$ molecule/mm²) constant for all constant for all samples..

Au shell-silica core nanoparticle films with different shell thickness were prepared by changing the time of electroless plating as discussed in section 4.5.1 resulting in the UV-Vis spectra shown in Figure 98.

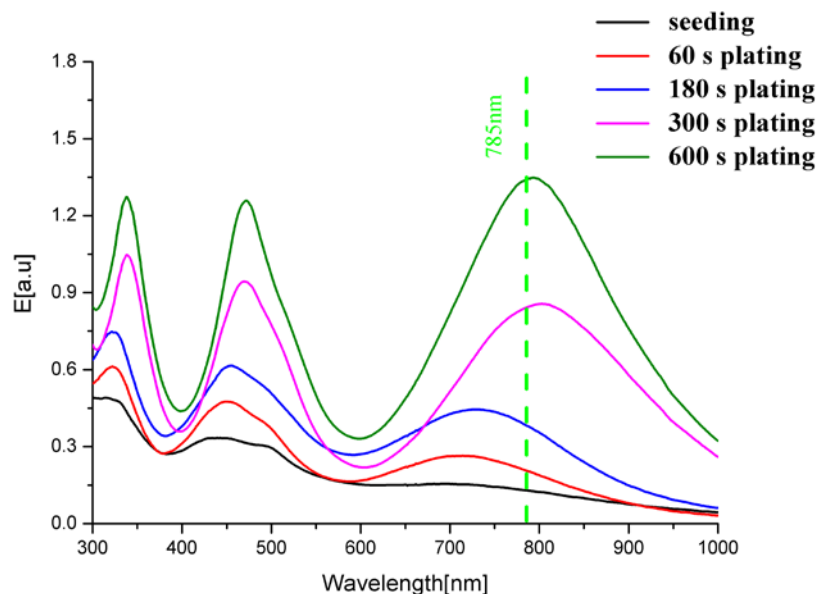


Figure 98. UV-Vis spectra of Au shell-silica core nanoparticle films taken after seeding and various times of electroless gold plating and the wavelength of the Raman excitation line.

The Raman spectrum of dissolved MB molecules was not recorded at higher concentrations such as 0.01 M by using the 785 nm excitation line because there was no signal from the molecule. Therefore, the Raman spectrum of the molecule could not be provided for peak assignments. However, MB was already studied in literature^[124-129] and tentative peak assignments are summarized in Table 4.

Raman Frequency[cm ⁻¹]	Tentative assignment
1621	$\nu(\text{CC})_{\text{ring}} + \nu(\text{CNC})_{\text{ring}}$
1503	$\nu(\text{CC})_{\text{ring}}$
1432	$\nu(\text{CC})_{\text{ring}}$
1399	$\nu(\text{CC})_{\text{ring}} + \nu(\text{CNC})_{\text{ring}}$
1332	$\nu(\text{CC})_{\text{ring}}$
1132	$\nu(\text{CN})$
1040	$\nu_{\text{as}}(\text{CSC})$

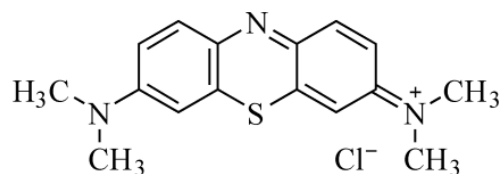


Table 4. Tentative peak assignment of Raman frequencies observed in the SERS spectrum of MB and the structure of MB.(ν =symmetric stretching, ν_{as} = asymmetric stretching)^[127].

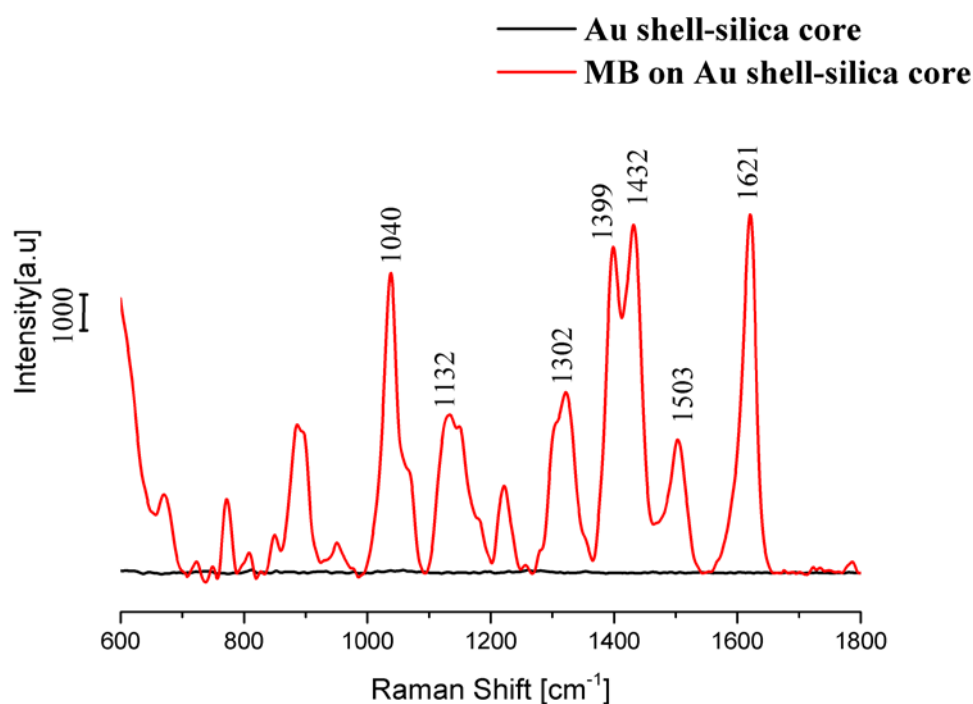


Figure 99. SERS spectrum of 10^{-4} M MB on a Au shell-silica core nanoparticle film (600s electroless gold plating) and Raman spectrum of background prior to molecule adsorption. (10 s accumulation time for each spectrum)($\sim 6 \times 10^{10}$ molecule/mm²)

Raman frequencies of the assigned peaks are also shown in Figure 99 together with the Raman spectrum of the MB film on Au shell-silica core nanoparticle particle film. The Raman spectrum of the Au shell-silica core nanoparticle particle film had no significant peaks, thus, the obtained SERS spectrum after MB incubation consisted only of MB originated peaks.

The same amount of MB was adsorbed on Au shell-silica core nanoparticle films with different Au shell thickness and the SERS spectra of the molecule were recorded. The area of the intense 1621 cm^{-1} $\nu(\text{CC})_{\text{ring}} + \nu(\text{CNC})_{\text{ring}}$ peak was calculated for different times of electroless gold plating and is shown in Figure 100. As the time of electroless plating increases, the intensity of the peak and, thus, the area increases. As shown in Figure 98, the longer wavelength SPR peak overlaps with the excitation line as the time of electroless plating increases. The same kind of trend was obtained by Lee et al.^[130] for Au nanosphere surfaces which were grown by electroless gold plating. They found that the longer wavelength peak increases in intensity as the time of electroless plating increases and shows better enhancement of signals.

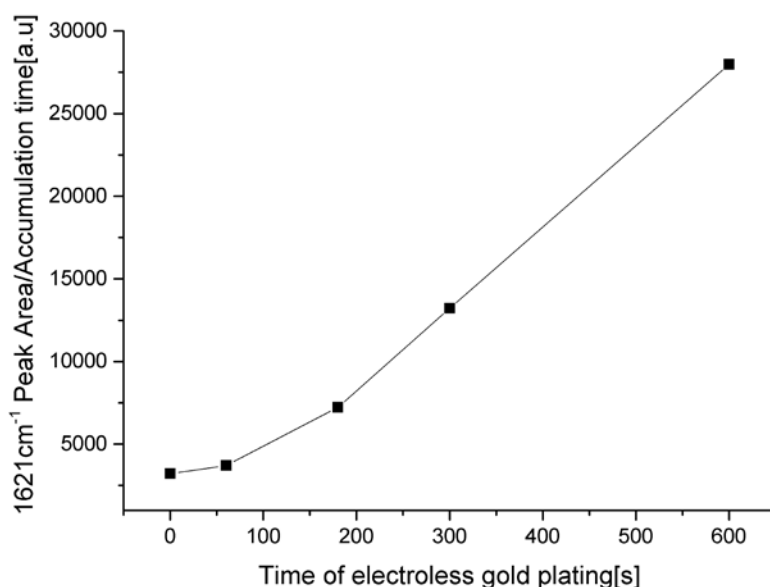


Figure 100. 1621cm^{-1} peak peak area/accumulation time for different time of electroless gold plating.

The enhancement factor (EF) for each core-shell nanoparticle film could not be calculated since the Raman spectrum of MB could not be recorded at the given excitation line. However, the peak area determined for each electroless gold plating time gave a clue about how much the signals are enhanced. According to the data, the strongest signal enhancement was achieved for 600 s electroless gold plating, where the longer wavelength peak overlaps more with the excitation line.

In a similar experiment, the SERS spectra of 10 μ l of 10^{-4} M MB deposited on a 10 x 10 mm substrate were recorded on both Au shell-silica core and Ag shell-silica core nanoparticle films as shown in Figure 102 in order to compare the SERS enhancement of these core-shell structures. Au shell-silica core and Ag shell-silica core nanoparticle films were prepared as discussed in section 5.2.1.1.4. As shown in Figure 102, the SERS enhancement of MB signals on Ag shell-silica core films was higher than on Au shell-silica core layers. Furthermore, the area of the 1621 cm^{-1} $\nu(\text{CC})_{\text{ring}} + \nu(\text{CNC})_{\text{ring}}$ peak of MB on Ag shell-silica core films was around 5 times higher than on Au shell-silica core films as shown in Figure 103.

The more pronounced SERS enhancement of Ag is well-known and the explanation is based on the parameter χ (the contribution of the interband transition to the dielectric function). If χ is large, the width of the resonance increases and the SERS enhancement decreases^[131,132]. The complex valued interband transition is wavelength dependent and contributes to the dielectric function of the metal as the following^[132,133]:

$$\varepsilon_m = \chi + 1 - \frac{\omega_p^2}{\omega^2 + i\omega\gamma} \quad (\text{Equation 22})$$

where ε_m is the dielectric function of a metal modified for interband transitions, ω_p is the metal's plasma frequency and γ is the electronic-scattering rate. *Pinchuk et al.*^[132,133] calculated real and imaginary part of the dielectric functions of Au and Ag decomposed into the Drude, $\varepsilon_{\text{Drude}}$, and interband, χ , contributions as shown in Figure 101. As could be seen in

Figure 101A and 101C, the interband transition is larger for gold than silver; therefore, the SERS enhancement of Ag is higher than Au.

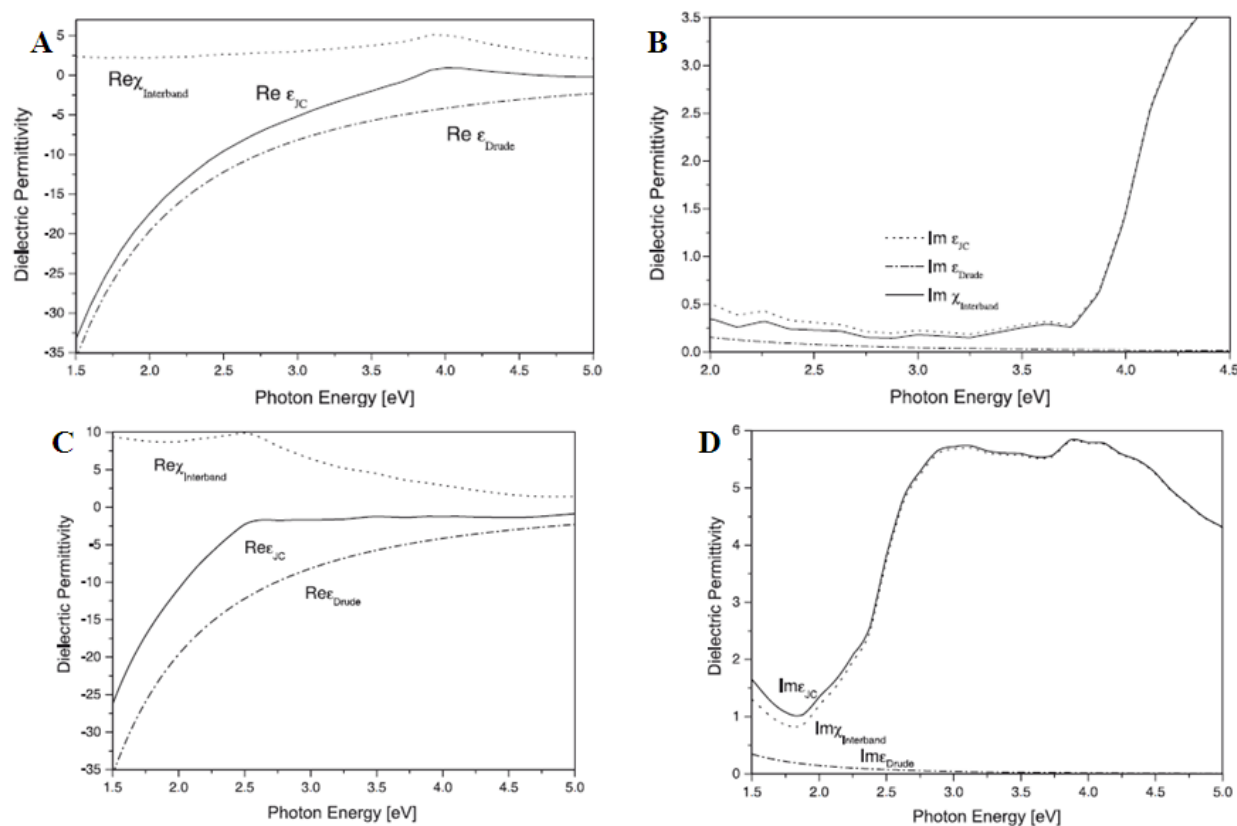


Figure 101. A) Real and B) imaginary part of the dielectric permittivity of Ag, C) Real and D) imaginary part of the dielectric permittivity of Au. Values are decomposed into the Drude, ϵ_{Drude} , and interband, χ , contributions.

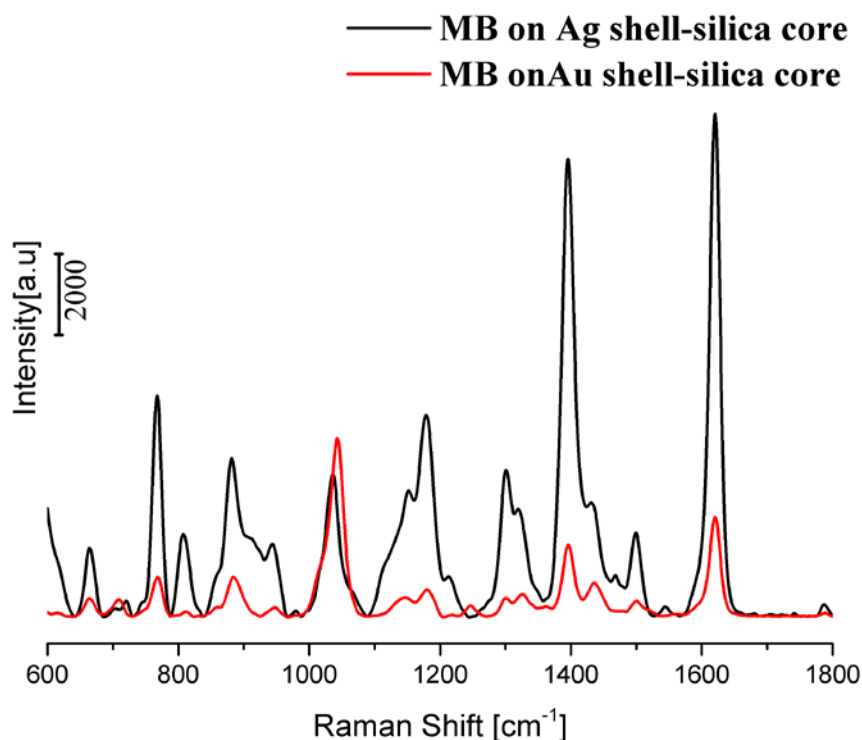


Figure 102. SERS spectra of 10^{-4} M MB on Au shell-silica core and Ag shell-silica core nanoparticle films. 10 s accumulation time were selected for each spectrum and a baseline correction was performed. ($\sim 6 \times 10^{10}$ molecule/mm²)

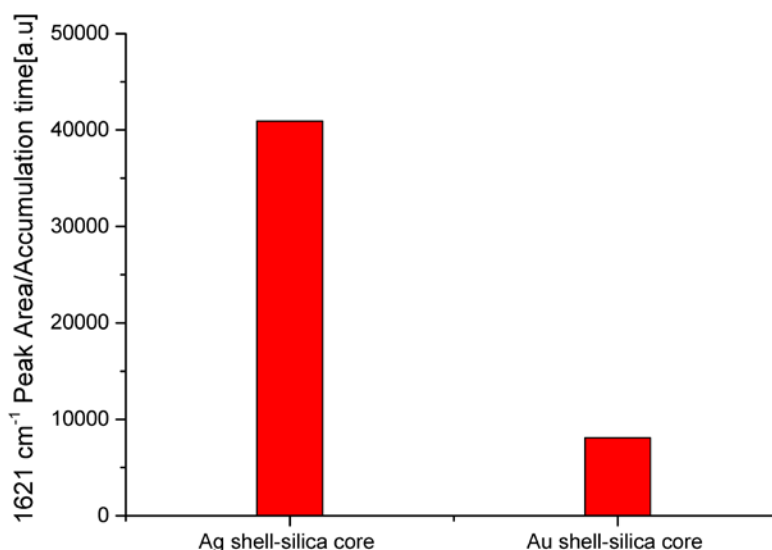


Figure 103. 1621cm⁻¹ peak area/accumulation time for Au shell-silica core and Ag shell-silica core nanoparticle films.

Another difference in Figure 102, except the signal intensities, is that the 1040 cm⁻¹ peak, which was assigned to asymmetric stretching vibrations

of C-S-C, had a higher intensity on the Au shell-silica core nanoparticle film than on the Ag shell-silica core nanoparticle film. According to literature the intensity of the SERS signals increases as the molecule gets in closer proximity to the metal surface^[134]. Therefore, the more intense $\nu_{as}(CSC)$ peak on the Au shell-silica core nanoparticle film indicated that the C-S-C bond of MB was closer to the Au surface than to the Ag surface. This could also be observed from the intensity ratio of $\nu_{as}(CSC)$ peak to $\nu(CC)_{ring} + \nu(CNC)_{ring}$ peak which is higher for the Au surface than for the Ag surface.

The second observed difference is the relative red shift of the asymmetric stretching vibrations of the C-S-C bond on the Au shell-silica core nanoparticle film. As it was mentioned in section 2.2.2, among the enhancement mechanism of SERS chemical enhancement may lead to wavenumber shifts of some of the molecular Raman vibrations, whereas electromagnetic mechanism does not^[122,123]. Since the Raman spectrum of MB is not available, the amount of wavenumber shift could not be evaluated for neither Au shell-silica core nor Ag shell-silica core films. However, from the relative frequency shift of the asymmetric stretching vibrations of the C-S-C bond it could also be concluded that the C-S-C bond of MB was in closer proximity to the Au surface than to the Ag surface.

In summary, both Au shell-silica core and Ag shell-silica core nanoparticle films were evaluated for their SERS enhancement upon MB adsorption. The Ag shell-silica core nanoparticle film had higher SERS enhancement than the Au shell-silica core nanoparticle film. Moreover, MB was found to be in closer proximity to the Au shell-silica core nanoparticle surface with respect to its C-S-C bond whereas the C-N-C bond is in closer proximity to Ag shell-silica core surface. Furthermore, the relative wavenumber shift of the asymmetric stretching vibrations of the C-S-C bond indicated that the chemical enhancement mechanism might play a role in SERS enhancement of MB in addition to the electromagnetic enhancement mechanism.

5.5.2 SERS of Fibrinogen

Fibrinogen was adsorbed on the Au shell-silica core and Ag shell-silica nanoparticle films for evaluation of these surfaces in terms of their SERS enhancement upon protein binding. Adsorption took place as discussed in section 4.6.1 and was followed by UV-Vis reflection measurements, which resulted in similar wavelength shifts as in section 5.2.1.1.4. The corresponding SERS spectra of fibrinogen on core-shell nanoparticle films are shown in Figure 104. The SERS spectra were recorded by using the 532 nm excitation line since no spectra were obtained with 785 nm excitation line. The assignment of the corresponding peak positions is given in Table 5[135-137].

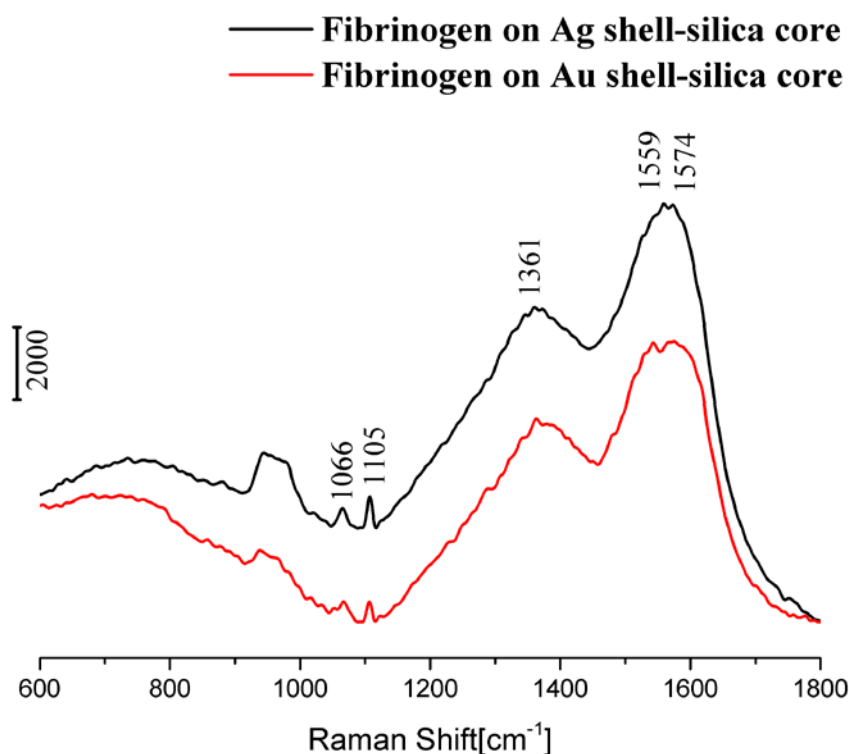


Figure 104. SERS spectra of fibrinogen on Ag shell-silica core and Au shell-silica core nanoparticle films (20 s accumulation time were selected for each spectrum and a baseline correction was performed)

The obtained SERS spectra of fibrinogen displayed more intense peaks for the Ag shell-silica core nanoparticle film. It was not possible to record Raman spectrum of fibrinogen with either the 532 nm or the 785 nm

excitation line, since proteins have low Raman cross section^[56]. Therefore, no further quantitative analysis can be performed based on the obtained spectra.

Raman Frequency[cm ⁻¹]	Tentative assignment
1574	C=C stretching
1559	Amide II
1361	C-H deformation
1105	C-N stretching
1066	C-C/C-N stretching

Table 5. Tentative peak assignment of Raman frequencies observed in SERS spectrum of fibrinogen^[135-137].

In summary, SERS spectra of fibrinogen were obtained on Au core-shell and Ag shell-silica core nanoparticle films. The latter showed better SERS enhancement.

6 SUMMARY AND CONCLUSIONS

The aim of this work was to develop a bioanalytical system which facilitates the label-free read-out of biospecific binding events in high-density peptide arrays on a novel nanostructured material with mutually coupled optical and biological functionalities.

The optical properties of metal-coated dielectric nanoparticle monolayers led to a red shift of the plasmonic extinction peaks upon protein adsorption due to the change in the refractive index close to the surface. In order to optimize the adsorption-induced wavelength shift upon protein (with fibrinogen serving as a model protein) different features were changed in the biosensor configuration and the impact of these parameters on biosensor performance was tested.

First, the metal surface roughness and the shell thickness were changed by tuning the electroless gold plating time. The sensitivity of the biosensor surfaces was found to decrease as the time of electroless gold plating increases due to the change in the shell thickness-to-core radius ratio and the altered surface roughness.

Second, the metallized substrate configuration, on which core-shell nanoparticles were adsorbed, was varied. Changing the thickness of the flat Au film covering the glass or silicon substrate from 30 nm to 100 nm did not have an influence on the sensitivity of the biosensor. On the other hand, an additional 40 nm SiO₂ film on top of the flat Au layer increased the sensitivity of the biosensor surfaces by 40%. This increase in sensitivity was even higher for biosensor surfaces metallized by sputter coating the Au shell and amounted to about 90%.

Third, alternative biosensor configurations were evaluated in terms of their performance upon protein adsorption. One of the alternative biosensor

surfaces was prepared by replacing the dielectric nanoparticles with a plane dielectric film, and was found to be similar in sensitivity upon protein adsorption to the core-shell nanoparticle films. Moreover, flexible substrates such as PI-foils and PVDF membranes were also used as an alternative to the rigid glass and silicon carriers for the deposition of core-shell nanoparticle films.

Changing the metal shell from Au to Ag increased the sensitivity of the biosensor surfaces significantly. The increase in sensitivity was attributed to larger real part of the dielectric constant of Ag. Both Au and Ag shell biosensor surfaces were used to follow specific antibody-antigen reactions in which Ag shell structures showed better sensitivity than Au shell ones.

As the measured wavelength shift is related to the amount of adsorbed protein, it has to be normalized to the mass density of the protein layer to evaluate the actual sensitivity of the nanoparticle surfaces. For this purpose XPS measurements were carried out to determine the relative amount of protein deposited on the various biosensor surfaces by following the N1s signal before and after protein adsorption. The protein density was found to be similar on all biosensor surfaces which were compared in this thesis.

The optical properties of the biosensor surfaces were analyzed with three different instrumental set-ups; (i) a UV-Vis reflection set-up, (ii) a LSPR imaging set-up (the so-called scanning unit) and (iii) a homemade CCD-based fast read-out set-up. The UV-Vis reflection set-up was used to evaluate the performance of the proposed and prepared biosensor surfaces by nonspecific adsorption of proteins whereas the others served to detect biomolecular reactions in an array format, in particular in high density peptide arrays.

SPR intensity imaging and SPR wavelength shift measurements were used to compare and evaluate the biosensor surfaces with the CCD-based fast read-out system. In a first attempt, both techniques were successfully applied to detect a spotted antibody array with good lateral resolution and contrast. Furthermore, SPR intensity imaging measurements were utilized to

quantify the detection limit of Au-shell (2.6 ng/mm² protein) and Ag-shell (0.13 ng/mm² protein) based biosensor surfaces. SPR wavelength shift measurements confirmed the higher sensitivity of Ag-shell based biosensors. In addition, the obtained values by UV-Vis reflection and SPR wavelength shift measurements were found to be consistent, which again confirms the excellent performance of the new set-up.

Biosensor surfaces prepared by seeding and consecutive electroless metal plating were found to be optically too inhomogeneous for the detection of biomolecular interactions in array format. Therefore, sputter coating was used to deposit the Au metal shell on dielectric silica nanoparticles. This way, a much better optical homogeneity was obtained. To use the core-shell nanoparticle films as a biosensor for the detection biospecific interactions in high density peptide libraries, the peptide arrays were transferred to the nanoparticle film preserving spot size and lateral distances. Both the CCD-based fast read-out system and the scanning unit were used to detect protein/peptide interactions in these arrays and yielded consistent results in terms of wavelength shift. By increasing the incubation time for peptide array transfer from 30 min to 2 h more than doubled the amount of transferred peptide as indicated by the observed wavelength shifts. The detection limit of the optically homogeneous nanoparticle film was found to be approximately 1 ng/mm² resulting in a 2 nm wavelength shift with the fast read-out set-up and 2.5 nm with the scanning unit by analyzing well-defined amounts of protein spotted onto the nanoparticle film in an array. Therefore, the amount of protein detected in the transfer experiments could be estimated to vary between 1 and 2 ng/mm² depending on incubation time.

One of the most promising options to further increase the sensitivity of the core-shell nanoparticle films was found to perform the measurements in the long wavelength instead of the short wavelength regime. Here, the sensitivity of nanoparticle film was found to be five to seven times higher for Au shell formation by seeding and consecutive electroless plating. No such

pronounced effects were observed nanoparticle films metallized by sputter coating.

Unfortunately, experiments utilizing seeded and plated core-shell nanoparticles in the long wavelength regime seriously suffered from a lack of reproducibility due to significant sample-to-sample variation and even strong variation in the optical response at different locations of a single sample. This problem has to a large extent been solved by suitable averaging procedures, denoted as wavelength averaging. With this approach, the sensitivity of the biosensor surface was found to be $\sim 13.5 \pm 2 \text{ nm}/(\text{ng}/\text{mm}^2)$ by analyzing well-defined amounts of protein spotted onto the nanoparticle film in an array with the scanning unit. This value is five times higher than the sensitivity reported in literature for the short wavelength regime utilizing similar core-shell nanoparticle systems^[7].

Thus, the optimized conditions for the most sensitive biosensor response are the use of core-shell nanoparticle films consisting of dielectric silica core nanoparticles deposited on a metalized substrate by self-assembly floating, and metal shell formation by seeding and consecutive electroless plating. Moreover, performing the measurements in the long wavelength regime is crucial for high sensitivity.

The core-shell nanoparticle films were also used to enhance the intensity of weak Raman signals of methylene blue (MB) and fibrinogen due to their strong SPR response in Surface Enhanced Raman Scattering (SERS). Both electromagnetic and chemical enhancement mechanisms were found to be responsible for the Raman signal enhancement of MB. Moreover, Ag shell-silica core nanoparticle films enhanced the Raman signals more than Au shell-silica core nanoparticle films.

7 REFERENCES

1. Schroeder, H., et al., *Generation of live-cell microarrays by means of DNA-directed immobilization of specific cell-surface ligands*. Angewandte Chemie-International Edition, 2007. **46**(22): p. 4180-4183.
2. Stears, R.L., T. Martinsky, and M. Schena, *Trends in microarray analysis*. Nature Medicine, 2003. **9**(1): p. 140-145.
3. Li, P.Y., et al., *A new method for label-free imaging of biomolecular interactions*. Sensors and Actuators B-Chemical, 2004. **99**(1): p. 6-13.
4. Ray, S., G. Mehta, and S. Srivastava, *Label-free detection techniques for protein microarrays: Prospects, merits and challenges*. Proteomics, 2010. **10**(4): p. 731-748.
5. Wu, G.H., et al., *Bioassay of prostate-specific antigen (PSA) using microcantilevers*. Nature Biotechnology, 2001. **19**(9): p. 856-860.
6. Haes, A.J., et al., *A nanoscale optical biosensor: The long range distance dependence of the localized surface plasmon resonance of noble metal nanoparticles*. Journal of Physical Chemistry B, 2004. **108**(1): p. 109-116.
7. Buecker, P., et al., *Label-free biosensors based on optically responsive nanocomposite layers: Sensitivity and dynamic range*. Langmuir, 2008. **24**(15): p. 8229-8239.
8. Dahint, R., et al., *Optically responsive nanoparticle layers for the label-free analysis of biospecific interactions in array formats*. Biosensors & Bioelectronics, 2007. **22**(12): p. 3174-3181.
9. Himmelhaus, M. and H. Takei, *Cap-shaped gold nanoparticles for an optical biosensor*. Sensors and Actuators B-Chemical, 2000. **63**(1-2): p. 24-30.
10. Smith, E.A. and R.M. Corn, *Surface plasmon resonance imaging as a tool to monitor biomolecular interactions in an array based format*. Applied Spectroscopy, 2003. **57**(11): p. 320A-332A.
11. Maier, S.A. and H.A. Atwater, *Plasmonics: Localization and guiding of electromagnetic energy in metal/dielectric structures*. Journal of Applied Physics, 2005. **98**(1): p. 10.
12. Homola, J., *Surface Plasmon Resonance Based Sensors*. Springer Series on Chemical Sensors and Biosensors, 2006. **4**.
13. Willets, K.A. and R.P. Van Duyne, *Localized surface plasmon resonance spectroscopy and sensing*, in *Annual Review of Physical Chemistry* 2007, Annual Reviews: Palo Alto. p. 267-297.

14. Homola, J., *Surface plasmon resonance sensors for detection of chemical and biological species*. Chemical Reviews, 2008. **108**(2): p. 462-493.
15. Homola, J., *Present and future of surface plasmon resonance biosensors*. Analytical and Bioanalytical Chemistry, 2003. **377**(3): p. 528-539.
16. Haes, A.J., et al., *Plasmonic materials for surface-enhanced sensing and spectroscopy*. Mrs Bulletin, 2005. **30**(5): p. 368-375.
17. Kelly, K.L., et al., *The optical properties of metal nanoparticles: The influence of size, shape, and dielectric environment*. Journal of Physical Chemistry B, 2003. **107**(3): p. 668-677.
18. Haes, A.J. and R.P. Van Duyne, *A unified view of propagating and localized surface plasmon resonance biosensors*. Analytical and Bioanalytical Chemistry, 2004. **379**(7-8): p. 920-930.
19. Kreibig, U. and M. Vollmer, *Optical Properties of Metal Clusters*. 1995. **25**.
20. Mayer, K.M. and J.H. Hafner, *Localized Surface Plasmon Resonance Sensors*. Chemical Reviews, 2011. **111**(6): p. 3828-3857.
21. Schroter, U. and D. Heitmann, *Grating couplers for surface plasmons excited on thin metal films in the Kretschmann-Raether configuration*. Physical Review B, 1999. **60**(7): p. 4992-4999.
22. Pitarke, J.M., et al., *Theory of surface plasmons and surface-plasmon polaritons*. Reports on Progress in Physics, 2007. **70**(1): p. 1-87.
23. Zayats, A.V., Smolyaninov, II, and A.A. Maradudin, *Nano-optics of surface plasmon polaritons*. Physics Reports-Review Section of Physics Letters, 2005. **408**(3-4): p. 131-314.
24. Kooyman, R.P.H., *Physics of Surface Plasmon Resonance*. Handbook of Surface Plasmon Resonance, 2008: p. 15-33.
25. Shvets, G. and Y.A. Urzhumov, *Electric and magnetic properties of sub-wavelength plasmonic crystals*. Journal of Optics a-Pure and Applied Optics, 2005. **7**(2): p. S23-S31.
26. Brockman, J.M., B.P. Nelson, and R.M. Corn, *Surface plasmon resonance imaging measurements of ultrathin organic films*. Annual Review of Physical Chemistry, 2000. **51**: p. 41-63.
27. Kodoyianni, V., *Label-free analysis of biomolecular interactions using SPR imaging*. Biotechniques. **50**(1): p. 32-40.
28. Chen, S.J., et al., *Enhancement of the resolution of surface plasmon resonance biosensors by control of the size and distribution of nanoparticles*. Optics Letters, 2004. **29**(12): p. 1390-1392.
29. Jain, P.K. and M.A. Ei-Sayed, *Surface plasmon resonance sensitivity of metal nanostructures: Physical basis and universal scaling in metal nanoshells*. Journal of Physical Chemistry C, 2007. **111**(47): p. 17451-17454.

-
30. Lyon, L.A., M.D. Musick, and M.J. Natan, *Colloidal Au-enhanced surface plasmon resonance immunosensing*. Analytical Chemistry, 1998. **70**(24): p. 5177-5183.
 31. Lyon, L.A., et al., *Surface plasmon resonance of colloidal Au-modified gold films*. Sensors and Actuators B-Chemical, 1999. **54**(1-2): p. 118-124.
 32. Lyon, L.A., D.J. Pena, and M.J. Natan, *Surface plasmon resonance of Au colloid-modified Au films: Particle size dependence*. Journal of Physical Chemistry B, 1999. **103**(28): p. 5826-5831.
 33. Jain, P.K. and M.A. El-Sayed, *Plasmonic coupling in noble metal nanostructures*. Chemical Physics Letters, 2010. **487**(4-6): p. 153-164.
 34. Mitsushio, M., K. Miyashita, and M. Higo, *Sensor properties and surface characterization of the metal-deposited SPR optical fiber sensors with Au, Ag, Cu, and Al*. Sensors and Actuators a-Physical, 2006. **125**(2): p. 296-303.
 35. Roh, S., T. Chung, and B. Lee, *Overview of the Characteristics of Micro- and Nano-Structured Surface Plasmon Resonance Sensors*. Sensors, 2011. **11**(2): p. 1565-1588.
 36. Sharma, A.K. and B.D. Gupta, *Fibre-optic sensor based on surface plasmon resonance with Ag-Au alloy nanoparticle films*. Nanotechnology, 2006. **17**(1): p. 124-131.
 37. Jung, L.S., et al., *Quantitative interpretation of the response of surface plasmon resonance sensors to adsorbed films*. Langmuir, 1998. **14**(19): p. 5636-5648.
 38. Oraevsky, A.N., *Whispering-gallery waves*. Quantum Electronics, 2002. **32**(5): p. 377-400.
 39. Rapp, B.E., F.J. Gruhl, and K. Lange, *Biosensors with label-free detection designed for diagnostic applications*. Analytical and Bioanalytical Chemistry, 2010. **398**(6): p. 2403-2412.
 40. Karlsson, R., *SPR for molecular interaction analysis: a review of emerging application areas*. Journal of Molecular Recognition, 2004. **17**(3): p. 151-161.
 41. Karlsson, R. and A. Falt, *Experimental design for kinetic analysis of protein-protein interactions with surface plasmon resonance biosensors*. Journal of Immunological Methods, 1997. **200**(1-2): p. 121-133.
 42. McDonnell, J.M., *Surface plasmon resonance: towards an understanding of the mechanisms of biological molecular recognition*. Current Opinion in Chemical Biology, 2001. **5**(5): p. 572-577.
 43. Brockman, J.M., A.G. Frutos, and R.M. Corn, *A multistep chemical modification procedure to create DNA arrays on gold surfaces for the study of protein-DNA interactions with surface plasmon resonance imaging*. Journal of the American Chemical Society, 1999. **121**(35): p. 8044-8051.
-

-
44. Houseman, B.T. and M. Mrksich, *Carbohydrate arrays for the evaluation of protein binding and enzymatic modification*. Chemistry & Biology, 2002. **9**(4): p. 443-454.
 45. Schuck, P., *Use of surface plasmon resonance to probe the equilibrium and dynamic aspects of interactions between biological macromolecules*. Annual Review of Biophysics and Biomolecular Structure, 1997. **26**: p. 541-566.
 46. Wegner, G.J., H.J. Lee, and R.M. Corn, *Characterization and optimization of peptide arrays for the study of epitope-antibody interactions using surface plasmon resonance imaging*. Analytical Chemistry, 2002. **74**(20): p. 5161-5168.
 47. He, L., et al., *Colloidal Au-enhanced surface plasmon resonance for ultrasensitive detection of DNA hybridization*. Journal of the American Chemical Society, 2000. **122**(38): p. 9071-9077.
 48. Nelson, B.P., et al., *Surface plasmon resonance imaging measurements of DNA and RNA hybridization adsorption onto DNA microarrays*. Analytical Chemistry, 2001. **73**(1): p. 1-7.
 49. Peterson, A.W., R.J. Heaton, and R.M. Georgiadis, *The effect of surface probe density on DNA hybridization*. Nucleic Acids Research, 2001. **29**(24): p. 5163-5168.
 50. Fleischmann, M., P.J. Hendra, and A.J. McQuillan, Chem. Phys. Lett., 1974. **26**: p. 163.
 51. Jeanmarie, D.L. and R.P. Van Duyne, *Surface Raman spectroelectrochemistry, part 1: heterocyclic, aromatic, and aliphatic amines adsorbed on the anodized silver electrode*. J. Electroanal. Chem, 1977. **84**: p. 1-20.
 52. Albrecht, M.G. and J.A. Creighton, *Anomalously intense Raman spectra of pyridine at a silver electrode*. Journal of American Chemical Society, 1977. **99**: p. 5215-5217.
 53. Petry, R., M. Schmitt, and J. Popp, *Raman Spectroscopy - A prospective tool in the life sciences*. Chemphyschem, 2003. **4**(1): p. 14-30.
 54. Weaver, M.J., S.Z. Zou, and H.Y.H. Chan, *The new interfacial ubiquity of surface-enhanced Raman spectroscopy*. Analytical Chemistry, 2000. **72**(1): p. 38A-47A.
 55. Champion, A. and P. Kambhampati, *Surface-enhanced Raman scattering*. Chemical Society Reviews, 1998. **27**(4): p. 241-250.
 56. Kneipp, K., et al., *Surface-enhanced Raman scattering and biophysics*. Journal of Physics-Condensed Matter, 2002. **14**(18): p. R597-R624.
 57. Moskovits, M., *Surface-enhanced Spectroscopy* Rev. Mod. Phys., 1985. **57**: p. 783-826.
-

-
58. Schatz, G.C., M.A. Young, and R.P. Van Duyne, *Electromagnetic mechanism of SERS*. Surface-Enhanced Raman Scattering: Physics and Applications, 2006. **103**: p. 19-45.
 59. Kennedy, B.J., et al., *Determination of the distance dependence and experimental effects for modified SERS substrates based on self-assembled monolayers formed using alkanethiols*. Journal of Physical Chemistry B, 1999. **103**(18): p. 3640-3646.
 60. Guvenc, H.O., *Surface enhanced Raman scattering from Au and Ag nanoparticle coated magnetic microspheres*, Master Thesis, 2008.
 61. Liu, F.C., *Development of LSPR-based Optical Biosensor for the Label-free Detection of Biomolecular Interaction in High-Density Peptide Arrays*, PhD. Dissertation, 2011.
 62. Waly, N., *Optimization of core-shell nanoparticle layers for optical biosensing*, PhD. Dissertation, 2011.
 63. Rybczynski, J., U. Ebels, and M. Giersig, *Large-scale, 2D arrays of magnetic nanoparticles*. Colloids and Surfaces a-Physicochemical and Engineering Aspects, 2003. **219**(1-3): p. 1-6.
 64. Denkov, N.D., et al., *Mechanism of Formation of 2-dimensional Crystals from Latex-particles on Substrates*. Langmuir, 1992. **8**(12): p. 3183-3190.
 65. Dimitrov, A.S. and K. Nagayama, *Steady-State Unidirectional Convective Assembling of Fine Particles into 2-Dimensional Arrays*. Chemical Physics Letters, 1995. **243**(5-6): p. 462-468.
 66. Liu, Y.F., et al., *A floating self-assembly route to colloidal crystal templates for 3D cell scaffolds*. Chemistry of Materials, 2005. **17**(20): p. 4918-4924.
 67. Wang, X.D., C.J. Summers, and Z.L. Wang, *Large-scale hexagonal-patterned growth of aligned ZnO nanorods for nano-optoelectronics and nanosensor arrays*. Nano Letters, 2004. **4**(3): p. 423-426.
 68. Kralchevsky, P.A. and K. Nagayama, *Capillary Forces Between Colloidal Particles*. Langmuir, 1994. **10**(1): p. 23-36.
 69. Hrapovic, S., et al., *New strategy for preparing thin gold films on modified glass surfaces by electroless deposition*. Langmuir, 2003. **19**(9): p. 3958-3965.
 70. Brown, K.R., et al., *Hydroxylamine seeding of colloidal au nanoparticles. 3. Controlled formation of conductive Au films*. Chemistry of Materials, 2000. **12**(2): p. 314-323.
 71. Cheng, W.L., S.J. Dong, and E.K. Wang, *Gold nanoparticles as fine tuners of electrochemical properties of the electrode/solution interface*. Langmuir, 2002. **18**(25): p. 9947-9952.
 72. Brown, K.R. and M.J. Natan, *Hydroxylamine seeding of colloidal Au nanoparticles in solution and on surfaces*. Langmuir, 1998. **14**(4): p. 726-728.
-

-
73. Jin, Y.D., et al., *Controlled nucleation and growth of surface-confined gold nanoparticles on a (3-aminopropyl)trimethoxysilane-modified glass slide: A strategy for SPR substrates*. Analytical Chemistry, 2001. **73**(13): p. 2843-2849.
74. Zhang, J.H., et al., *Facile methods to coat polystyrene and silica colloids with metal*. Advanced Functional Materials, 2004. **14**(11): p. 1089-1096.
75. Cui, J.Q. and I. Kretzschmar, *Surface-anisotropic polystyrene spheres by electroless deposition*. Langmuir, 2006. **22**(20): p. 8281-8284.
76. Koura, N., *"Electroless Plating Of Silver", Electroless Plating Fundamentals & Applications*. 1985(Chapter 17): p. 441-462.
77. Breitling, F., et al., *High-density peptide arrays*. Molecular Biosystems, 2009. **5**(3): p. 224-234.
78. Schirwitz, C., *Purification of Peptides in High Complexity Arrays*. PhD. Dissertation, 2012.
79. Schirwitz, C., et al., *Purification of High-Complexity Peptide Microarrays by Spatially Resolved Array Transfer to Gold-Coated Membranes*. Advanced Materials, 2013: p. n/a-n/a.
80. Min, D.H. and M. Mrksich, *Peptide arrays: towards routine implementation*. Current Opinion in Chemical Biology, 2004. **8**(5): p. 554-558.
81. Fodor, S.P.A., et al., *Light-Directed, Spatially Addressable Parallel Chemical Synthesis*. Science, 1991. **251**(4995): p. 767-773.
82. Stadler, V., et al., *Combinatorial synthesis of peptide arrays with a laser printer*. Angewandte Chemie-International Edition, 2008. **47**(37): p. 7132-7135.
83. Frank, R., *The SPOT synthesis technique - Synthetic peptide arrays on membrane supports - principles and applications*. Journal of Immunological Methods, 2002. **267**(1): p. 13-26.
84. Hilpert, K., D.F.H. Winkler, and R.E.W. Hancock, *Peptide arrays on cellulose support: SPOT synthesis, a time and cost efficient method for synthesis of large numbers of peptides in a parallel and addressable fashion*. Nature Protocols, 2007. **2**(6): p. 1333-1349.
85. Beyer, M., et al., *Combinatorial synthesis of peptide arrays onto a microchip*. Science, 2007. **318**(5858): p. 1888-1888.
86. Schirwitz, C., et al., *Sensing Immune Responses with Customized Peptide Microarrays*. Biointerphases, 2012. **7**(1-4).
87. Skoog, D.A., F.J. Holler, and S.R. Crouch, *Principles of Instrumental Analysis*. 2006. **6th ed.** .
88. Shah, R.Y. and Y.K. Agrawal, *Introduction to fiber optics: Sensors for biomedical applications*. Indian Journal of Pharmaceutical Sciences. **73**(1): p. 17-22.
-

89. Clarke, A.R. and C.N. Ebenhardt, *Microscopy techniques for materials science*. CRC Press, 2002.
90. Brundle, C.R., C.A. Evans, and S. Wilson, *Encyclopedia of materials characterization: surfaces, interfaces, thin films*. Gulf Professional Publishing, 1992.
91. Briggs, D. and M.P. Seah, *Practical Surface Analysis by Auger and Photoelectron Spectroscopy*. Wiley: Chichester, 1996. **1**(2nd Edition).
92. Swartz, W.E.J., *X-ray photoelectron spectroscopy*. Anal. Chem., 1973. **45**(9): p. 788A-800a.
93. Hollander, J.M. and W.L. Jolly, *X-Ray Photoelectron Spectroscopy*. Acc. Chem. Res., 1970. **3**(6): p. 193-200.
94. Stamm, M., *Polymer Surfaces and Interfaces: Characterization, Modification and Applications*. Springer, Berlin /Heidelberg (Germany), 2008. **1. ed.**
95. Dunlap, M. and J.E. Adaskaveg, *Introduction to the Scanning Electron Microscope: Theory, Practice and Procedures*. Facility for Advanced Instrumentation, U.C Davis, 1997.
96. Albert, G., *Herstellung und Charakterisierung polykristalliner Goldschichten zur Verwendung in der Nanolithographie*. University of Heidelberg.
97. Grabar, K.C., et al., *Two-dimensional arrays of colloidal gold particles: A flexible approach to macroscopic metal surfaces*. Langmuir, 1996. **12**(10): p. 2353-2361.
98. Zhang, S.Z., et al., *Formation of gold and silver nanoparticle Arrays and thin shells on mesostructured silica nanofibers*. Advanced Functional Materials, 2007. **17**(16): p. 3258-3266.
99. Zimmer, M., *Aufbau und Evaluierung eines orts aufgelosten UV-Vis-Spektrometers*. Diplom Thesis, 2005.
100. Turner, N.H. and A.M. Single, *Determination of Peak Positions and Areas from Wide-Scan XPS Spectra*. Surface and Interface Analysis, 1990. **15**(3): p. 215-222.
101. Smith, G.C., *Surface Analysis by Electron Spectroscopy: Measurement and Interpretation*. Plenum Press, 1994.
102. Konrad, U., *Markierungsfreier Proteinnachweis auf optisch aktiven Nanopartikel-Oberflächen*. Diplom Thesis, 2005.
103. Garcia-Aonso, J., et al., *Cellular Internalization of Silver Nanoparticles in Gut Epithelia of the Estuarine Polychaete Nereis diversicolor*. Environmental Science & Technology, 2011. **45**(10): p. 4630-4636.
104. Ivanov, M.R., H.R. Bednar, and A.J. Haes, *Investigations of the Mechanism of Gold Nanoparticle Stability and Surface Functionalization in Capillary Electrophoresis*. Acs Nano, 2009. **3**(2): p. 386-394.
105. Herrwerth, S., et al., *Covalent coupling of antibodies to self-assembled monolayers of carboxy-functionalized poly(ethylene glycol): Protein*

- resistance and specific binding of biomolecules*. Langmuir, 2003. **19**(5): p. 1880-1887.
106. Homola, J., *On the sensitivity of surface plasmon resonance sensors with spectral interrogation*. Sensors and Actuators B-Chemical, 1997. **41**(1-3): p. 207-211.
107. Su, K.H., et al., *Interparticle coupling effects on plasmon resonances of nanogold particles*. Nano Letters, 2003. **3**(8): p. 1087-1090.
108. Preston, T.C. and R. Signorell, *Growth and Optical Properties of Gold Nanoshells Prior to the Formation of a Continuous Metallic Layer*. ACS Nano, 2009. **3**(11): p. 3696-3706.
109. Byun, K.M., S.J. Yoon, and D. Kim, *Effect of surface roughness on the extinction-based localized surface plasmon resonance biosensors*. Applied Optics, 2008. **47**(31): p. 5886-5892.
110. Chen, X., M. Pan, and K. Jiang, *Sensitivity enhancement of SPR biosensor by improving surface quality of glass slides*. Microelectronic Engineering, 2010. **87**(5-8): p. 790-792.
111. Kanso, M., S. Cuenot, and G. Louarn, *Roughness effect on the SPR measurements for an optical fibre configuration: experimental and numerical approaches*. Journal of Optics a-Pure and Applied Optics, 2007. **9**(7): p. 586-592.
112. Lahav, A., M. Auslender, and I. Abdulhalim, *Sensitivity enhancement of guided-wave surface-plasmon resonance sensors*. Optics Letters, 2008. **33**(21): p. 2539-2541.
113. Bhatia, P. and B.D. Gupta, *Surface-plasmon-resonance-based fiber-optic refractive index sensor: sensitivity enhancement*. Applied Optics, 2011. **50**(14): p. 2032-2036.
114. Jung, J., et al., *Enhanced surface plasmon resonance by Au nanoparticles immobilized on a dielectric SiO₂ layer on a gold surface*. Analytica Chimica Acta, 2009. **651**(1): p. 91-97.
115. Longo, L., et al., *New insights from X-ray photoelectron spectroscopy into the chemistry of covalent enzyme immobilization, with glutamate dehydrogenase (GDH) on silicon dioxide as an example*. Analytical and Bioanalytical Chemistry, 2006. **385**(1): p. 146-152.
116. Vanea, E., K. Magyari, and V. Simon, *Protein attachment on aluminosilicates surface studied by XPS and FTIR spectroscopy*. Journal of Optoelectronics and Advanced Materials, 2010. **12**(5): p. 1206-1212.
117. Stadler, V., et al., *PEGMA/MMA copolymer graftings: Generation, protein resistance, and a hydrophobic domain*. Langmuir, 2008. **24**(15): p. 8151-8157.
118. Rink, H., *Solid-Phase Synthesis of Protected Peptide-Fragments Using a Trialkoxy-Diphenyl-Methylester Resin*. Tetrahedron Letters, 1987. **28**(33): p. 3787-3790.

119. Karlsen, S.P., et al., *First-order surface plasmon resonance sensor system based on a planar light pipe*. Sensors and Actuators B-Chemical, 1996. **32**(2): p. 137-141.
 120. Yuk, J.S., et al., *Sensitivity enhancement of spectral surface plasmon resonance biosensors for the analysis of protein arrays*. European Biophysics Journal with Biophysics Letters, 2006. **35**(6): p. 469-476.
 121. Yuk, J.S., et al., *Sensitivity of ex situ and in situ spectral surface plasmon resonance sensors in the analysis of protein arrays*. Biosensors & Bioelectronics, 2005. **20**(11): p. 2189-2196.
 122. Arenas, J.F., et al., *Complete analysis of the surface-enhanced Raman scattering of pyrazine on the silver electrode on the basis of a resonant charge transfer mechanism involving three states*. Journal of Chemical Physics, 2000. **112**(17): p. 7669-7683.
 123. Fleger, Y., et al., *SERS as a probe for adsorbate orientation on silver nanoclusters*. Journal of Raman Spectroscopy, 2009. **40**(11): p. 1572-1577.
 124. Hao, Q.Z., et al., *Surface-Enhanced Raman Scattering Study on Graphene-Coated Metallic Nanostructure Substrates*. Journal of Physical Chemistry C, 2012. **116**(13): p. 7249-7254.
 125. Merlen, A., et al., *Surface enhanced spectroscopy with gold nanostructures on silicon and glass substrates*. Surface Science, 2011. **605**(13-14): p. 1214-1218.
 126. Naujok, R.R., R.V. Duevel, and R.M. Corn, *Fluorescence and Fourier Transform Surface-Enhanced Raman Scattering Measurements of Methylene Blue Adsorbed onto a Sulfur-Modified Gold Electrode*. Langmuir, 1993. **9**(7): p. 1771-1774.
 127. Nicolai, S.H.A. and J.C. Rubim, *Surface-enhanced resonance Raman (SERR) spectra of methylene blue adsorbed on a silver electrode*. Langmuir, 2003. **19**(10): p. 4291-4294.
 128. Nicolai, S.H.D., et al., *Electrochemical and spectroelectrochemical (SERS) studies of the reduction of methylene blue on a silver electrode*. Journal of Electroanalytical Chemistry, 2002. **527**(1-2): p. 103-111.
 129. Xiao, G.N. and S.Q. Man, *Surface-enhanced Raman scattering of methylene blue adsorbed on cap-shaped Silver nanoparticles*. Chemical Physics Letters, 2007. **447**(4-6): p. 305-309.
 130. Lee, W., et al., *Self-Assembled SERS Substrates with Tunable Surface Plasmon Resonances*. Advanced Functional Materials, 2011. **21**(18): p. 3424-3429.
 131. Fleger, Y. and M. Rosenbluh, *Surface Plasmons and Surface Enhanced Raman Spectra of Aggregated and Alloyed Gold-Silver Nanoparticles*. Research Letters in Optics, 2009. **2009**.
 132. Kneipp, K., M. Moskovits, and H. Kneipp, *Surface-Enhanced Raman Scattering: Physics and Applications*. Springer, Berlin, Germany, 2006.
-

133. Pinchuk, A., G. von Plessen, and U. Kreibig, *Influence of interband electronic transitions on the optical absorption in metallic nanoparticles*. Journal of Physics D-Applied Physics, 2004. **37**(22): p. 3133-3139.
134. Kovacs, G.J., R.O. Loutfy, and P.S. Vincett, *Distance Dependence of SERS Enhancement Factor from Langmuir-Blodgett Monolayers on Metal Island Films: Evidence for the Electromagnetic Mechanism*. Langmuir, 1986. **2**(6): p. 689-694.
135. Marx, J., et al., *Laser Raman Spectroscopy Study of Bovine Fibrinogen and Fibrin*. Biochimica et Biophysica Acta, 1979. **578**(1): p. 107-115.
136. Poon, K.W.C., et al., *Quantitative reagent-free detection of fibrinogen levels in human blood plasma using Raman spectroscopy*. Analyst, 2012. **137**(8): p. 1807-1814.
137. Strehle, M.A., et al., *A Raman spectroscopic study of the adsorption of fibronectin and fibrinogen on titanium dioxide nanoparticles*. Physical Chemistry Chemical Physics, 2004. **6**(22): p. 5232-5236.

8 APPENDIX

8.1 Abbreviations

AFM	Atomic Force Microscopy
ATR	Attenuated Total Reflection
Boc	<i>t</i> -butyloxycarbonyl
BSE	Back Scattered Electrons
CCD	Charged Coupled Device
CM	Chemical Mechanism
CMOS	Complementary Metal-oxide Semiconductor
DKFZ	German Cancer Research Center
EDC	N-(3-Dimethylaminopropyl)-N'-ethylcarbodiimide hydrochloride
EF	Enhancement Factor
EG7-SH	O-(2-mercaptoethyl)-O'-methylhexaethyleneglycol
EM	Electromagnetic Mechanism
FL	Focal Length
Fmoc	Chloroformic acid 9H-fluoren-9-ylmethyl ester
FWHM	Full Width at Half Maximum
IgG	Immunoglobulin G
HA	Hemagglutinin A
HOMO	Highest Occupied Molecular Orbital
LED	Light-emitting Diode
LSPR	Localized Surface Plasmon Resonance
LUMO	Lowest Unoccupied Molecular Orbital
MMA	Methyl methacrylate
NHS	N-hydroxysuccinimide
NIR	Near Infrared
OPC	Organic photoconductor
OPfp	Pentafluorophenyl ester
PBS	Phosphate Buffer Saline
PBS-T	Phosphate Buffer Saline Tween
PEGMA	Poly(ethylene glycol) methacrylate
PEI	Poly ethylene imine
PI	Poly imide
PLCC	Plano-Concave
PLCX	Plano-Convex
PSP	Propagating Surface Plasmon
PVD	Physical Vapor Deposition
PVDF	Polyvinylidene fluoride
RI	Refractive Index

RIU	Refractive Index Unit
SAM	Self Assembled Monolayer
SDS	Sodium monododecyl sulfate
SE	Secondary Electron
SEM	Scanning Electron Microscopy
SERS	Surface Enhanced Raman Scattering
SP	Surface Plasmon
SPR	Surface Plasmon Resonance
SPRi	Surface Plasmon Resonance Imaging
TFA	Trifluoroacetic acid
UHV	Ultra High Vacuum
UV	Ultraviolet
Vis	Visible
XPS	X-ray photoelectron spectroscopy

8.2 List of Aminoacids

Ala	A	Alanine
Arg	R	Arginine
Asn	N	Asparagine
Asp	D	Aspartic acid
Cys	C	Cysteine
Glu	E	Glutamic acid
Gln	Q	Glutamine
Gly	G	Glycine
His	H	Histidine
Ile	I	Isoleucine
Leu	L	Luecine
Lys	K	Lysine
Met	M	Methionine
Phe	F	Phenylalanine
Pro	P	Proline
Ser	S	Serine
Thr	T	Thyreonine
Trp	W	Tryptophan
Tyr	Y	Tyrosine
Val	V	Valine

8.3 Acknowledgement

This thesis would not have been possible without the guidance and the help of several people who in one way or another contributed their valuable assistance in the preparation and completion of this study.

Foremost, I would like to express the deepest appreciation to my supervisor *Prof.(apl.) Dr. Reiner Dahint* for his persistent support, patience, motivation and encouragement to hurdle all the obstacles in the completion of this study.

Besides my supervisor, I wish to thank *Prof. Dr. Michael Grunze* for the opportunity to be part of his research group, the scientific discussions in the group seminars and the meetings with him.

I would like to thank the current and past members of Biosensor and Bioelectronics Research group for their help and scientific discussions. Namely; *Dr. Andrea Seehuber, Dr. Fanny Liu, Dr. Noha Waly, Anna Grab*, my office mate and dear friend *Mustafa Sayin*.

Special gratitude to *Dr. Christopher Schirwitz* for his corrections of this thesis, help during the high density peptide transfer experiments, fluorescence measurements and discussions.

I am thankful to *PD. Dr. Ralf Bischoff, Dr. Felix Loeffler* and *Juergen Kretschmer* for their help and technical assistance during peptide transfer experiments, who are members of our collaboration partner, *Chip Based Peptide Array Group* in Cancer Research Center (DKFZ) in Heidelberg. Moreover, I thank *Christian Schmidt, Markus Spath, Sandra Manthey* and *Dr. Rene Meyer* for their assistance during protein spotting experiments.

I am grateful to many colleagues in Applied Physical Chemistry Institute for their support and collaboration during my study. Particularly, *Dr. Nikolaus Meyerbroeker* for introducing MAX 200 and discussions about

XPS results.

I thank *Prof. Dr. Christoph Woell* from Karlsruhe Institute of Technology for letting me use his laboratory and *Stefan Heissler* for helping with the Raman measurements.

Finally, I want to express my deepest gratitude to my parents, brother, sister and friends for their support and encouragement during my study.

8.4 Eidesstattliche Erklärung

Eidesstattliche Versicherung gemäß § 8 der Promotionsordnung der Naturwissenschaftlich-Mathematischen Gesamtfakultät der Universität Heidelberg

1. Bei der eingereichten Dissertation zu dem Thema

Label-free Detection of Biospecific Interactions in Peptide Arrays Using Core-shell Nanoparticles

handelt es sich um meine eigenständig erbrachte Leistung.

2. Ich habe nur die angegebenen Quellen und Hilfsmittel benutzt und mich keiner unzulässigen Hilfe Dritter bedient. Insbesondere habe ich wörtlich oder sinngemäß aus anderen Werken übernommene Inhalte als solche kenntlich gemacht.

3. Die Arbeit oder Teile davon habe ich ~~wie folgt~~/bislang nicht¹⁾ an einer Hochschule
des In- oder Auslands als Bestandteil einer Prüfungs- oder Qualifikationsleistung vorgelegt.

Titel der Arbeit: _____

Hochschule und Jahr: _____

Art der Prüfungs- oder Qualifikationsleistung: _____

4. Die Richtigkeit der vorstehenden Erklärungen bestätige ich.

5. Die Bedeutung der eidesstattlichen Versicherung und die strafrechtlichen Folgen einer unrichtigen oder unvollständigen eidesstattlichen Versicherung sind mir bekannt.

Ich versichere an Eides statt, dass ich nach bestem Wissen die reine Wahrheit erklärt und nichts verschwiegen habe.

Heidelberg, den 29.01.2013

Ort und Datum

Unterschrift

¹⁾Nicht Zutreffendes streichen. Bei Bejahung sind anzugeben: der Titel der andernorts vorgelegten

